

PREPARACIÓN DE NUEVOS
MATERIALES FOTOCATALIZADORES
PARA LA DESCONTAMINACIÓN DE
GASES NO_x



UNIVERSIDAD DE CÓRDOBA

FACULTAD DE CIENCIAS

Instituto Universitario de Investigación en Química Fina y Nanoquímica

Departamento de Química Inorgánica e Ingeniería Química

Memoria de Tesis presentada por:

José Balbuena Jurado

Para aspirar al grado de “*Doctor por la Universidad de Córdoba*”

TITULO: *Preparación de nuevos materiales fotocatalizadores para la descontaminación de gases NOx*

AUTOR: *José Balbuena Jurado*

© Edita: UCOPress. 2017
Campus de Rabanales
Ctra. Nacional IV, Km. 396 A
14071 Córdoba

www.uco.es/publicaciones
publicaciones@uco.es



TÍTULO DE LA TESIS:

Preparación de nuevos materiales fotocatalizadores para la descontaminación de gases NO_x

DOCTORANDO/A: JOSÉ BALBUENA JURADO

INFORME RAZONADO DEL/DE LOS DIRECTOR/ES DE LA TESIS

El trabajo científico que se recoge en la memoria que presenta el Licenciado en Química D. José Balbuena Jurado ha sido realizado bajo nuestra dirección en los laboratorios del departamento de Química Inorgánica e Ingeniería Química.

Este trabajo ha permitido abrir una nueva línea de investigación en el grupo FQM-175, dedicada al estudio de nuevos materiales fotocatalizadores para la eliminación de gases NO_x del entorno urbano. La puesta a punto de nuevas técnicas de medida, así como la intensa labor investigadora realizada por el Ldo. Balbuena ha permitido obtener una gran cantidad de resultados novedosos, como se constata en el hecho de que de este trabajo se han escrito 5 artículos, 3 de ellos ya publicados en revistas

internacionales, 3 artículos en libros científicos y 19 comunicaciones a congresos nacionales e internacionales. Además, como complemento a su formación investigadora, el Ldo. Balbuena realizó una estancia investigadora en un laboratorio de una institución europea de prestigio; Biomolecular Engineering Lab, Faculdade Ciências e Tecnologia, Universidade Nova de Lisboa (FCT-UNL).

En nuestra opinión, la memoria que se presenta reúne los requisitos necesarios para optar al grado de Doctor por la Universidad de Córdoba.

Por todo ello, se autoriza la presentación de la tesis doctoral.

Córdoba, 2 de mayo de 2017

Firma del/de los director/es

Fdo: Luis Sánchez Granados



Fdo: Manuel Cruz Yusta



Index

1. Preámbulo	1
Preamble.....	4
2. Hipótesis y objetivos.....	7
Hypothesis and objectives.....	13
3. Design of advanced De-NO _x photocatalysts	19
3.1. Introduction – Nanomaterials to combat NO _x pollution	21
3.2. Enhanced activity of α -Fe ₂ O ₃ for the photocatalytic NO removal.....	77
3.3. Advances in photocatalytic NO _x abatement through the use of Fe ₂ O ₃ /TiO ₂ nanocomposites.....	113
3.4 Mesoporous and visible light active anatase: a high selectivity De-NO _x photocatalyst.	157
4. Preparation of new De-NO _x photocatalysts through the valorisation of industrial waste	203
4.1. Introduction	205
4.2. Preparation of self-cleaning and de-polluting building materials through the valorization of industrial wastes.....	217
4.3. Synthesis of α -Fe ₂ O ₃ on rice husk as efficient De-NO _x photocatalyst.	237
5. Resumen general.....	275

Overall summary.	278
6. Experimental techniques.	281
A) Physical and morphological characterization.....	281
B) Chemical and electronic characterization	291
C) Characterization of photocatalytic processes.	302
7. Producción y Difusión Científica.	311
7.1. Artículos publicados en revistas y libros científicos.....	312
7.2. Comunicaciones a congresos	319
7.3. Referencias de los diferentes actos de difusión realizados en prensa y otros medios de comunicación.....	329

1. Preámbulo

Respirar aire limpio y sin riesgos para la salud es un derecho inalienable de todo ser humano. La calidad del aire, o mejor dicho su degradación o contaminación, es el resultado de fenómenos complejos derivados de una pluralidad de causas y efectos asociados, en general, a la actividad humana y a la emisión de contaminantes a la atmósfera. Teniendo en cuenta sus importantes efectos en la salud y el medioambiente, disponer de un aire limpio se ha convertido en un objetivo prioritario de la política ambiental y de las estrategias de desarrollo sostenible, ya que es un factor determinante de la calidad de vida y que se percibe como una demanda social creciente.

Hoy en día las ciudades hacen frente a serios problemas de contaminación en su atmósfera urbana, debida a las emisiones de los sistemas de transporte y, de las industrias que hay en ellas. De hecho, los sistemas de transporte se están convirtiendo en la principal fuente de emisión contaminante. Así se detectan episodios de contaminación en ciudades poco industrializadas. Por otra parte, en las grandes urbes se realizan restricciones del tráfico rodado los días en que se detectan altos niveles de contaminación.

Los gases de óxidos de nitrógeno ($\text{NO} + \text{NO}_2$; gases NO_x) son junto con el CO_2 y la fracción BTEX (Benceno, Tolueno, Etanol y Xileno) de los compuestos orgánicos volátiles (COV's) las principales emisiones nocivas generadas por los medios de transporte. Los

óxidos de nitrógeno tienen una toxicidad muy elevada, incluso superior a la del monóxido de carbono (CO), que origina serios problemas de salud. La respiración continuada de aire contaminado con gases NO_x afecta directamente a los pulmones originando enfisemas y bronquitis, entre otras afecciones. En España, como en otros países de Europa o del resto del Mundo, existen importantes capas de población en las ciudades expuestas a elevados niveles de contaminación atmosférica por NO_x. Así, son muchos los días del año que, en ciudades como Madrid, Barcelona, Zaragoza, Murcia, etc, se supera el límite máximo de 40 µg/m³ establecido como saludable por la legislación nacional e internacional. También, los gases NO_x son responsables de otros serios problemas medioambientales como se detallarán en el capítulo 3.1 titulado “Nanomaterials to combat NO_x pollution”. Por otra parte, los COV’s, fruto de actividades químicas, fabricación de pinturas o de la combustión incompleta de la gasolina, son considerados como compuestos carcinogénicos. Entre ellos, la mayor preocupación medioambiental se centra en la eliminación de la fracción BTEX.

La Industria Química es uno de los sectores que en mayor medida contribuyen a alcanzar el Desarrollo Sostenible. Éste abarca aspectos sociales, ambientales y económicos. En nuestra sociedad, gracias a su contínuo trabajo en innovación y desarrollo, esta industria es capaz de proponer nuevos materiales y soluciones. En lo que respecta a la descontaminación atmosférica, se proponen día a día nuevos catalizadores y últimamente está surgiendo con fuerza

el empleo de la fotocatalisis como técnica de remediación in-situ en el ambiente urbano. Esta tecnología es sencilla de implementar y sus primeros resultados son muy prometedores, tanto en los productos comerciales que existen, como en los entornos en los que han sido aplicados.

No obstante, como toda tecnología de nueva implementación, presenta ciertos inconvenientes y desventajas que hacen que en la actualidad su uso no sea tan amplio como se desea.

En este contexto, este trabajo de investigación aborda la preparación y caracterización de nuevos materiales con propiedades fotocatalíticas, al objeto de suponer un avance en el conocimiento de los mismos y facilitar su futura implementación comercial como materiales a ser usados para la descontaminación atmosférica urbana.

Preamble

Breathing clean, safe air for health is an inalienable right of every human life. Air quality, or in other words its degradation or pollution, is the result of complex phenomena derived from a plurality of causes and effects generally associated with human activity and the emission of pollutants into the atmosphere. Taking the important effects on health and the environment into account, having a clean air has become a priority objective of environmental policy and sustainable development strategies, as it is a determining factor in the quality of life being perceived as a growing social demand.

Currently, cities fight against serious pollution problems in their urban atmosphere, due to emissions from transport systems and the industries in them. In fact, transport systems are becoming the main source of pollutant emissions. This is how pollution episodes are detected in less industrialized cities. On the other hand, road traffic restrictions in the big cities account on days when high pollution levels are detected.

Nitrogen oxides gases (NO + NO₂; NO_x gases) together with CO₂ and the BTEX fraction (Benzene, Toluene, Ethanol and Xylene) of the volatile organic compounds (VOC's) are the main harmful emissions generated by transport systems. Nitrogen oxides have a very high toxicity, even higher than carbon monoxide (CO), which causes serious health problems. The continuous breathing of NO_x

polluted air directly affects the lungs causing emphysema and bronchitis, among other diseases. In Spain, as in other countries of Europe or the rest of the World, there are important population groups in cities exposed to high levels of NO_x. Thus, many days of the year, in cities such as Madrid, Barcelona, Zaragoza, Murcia, etc., the maximum limit of 40 µg/m³ established as healthy by national and international legislation is exceeded. Also, NO_x gases are responsible for other serious environmental problems as detailed in Chapter 3.1 entitled "Nanomaterials to combat NO_x pollution". On the other hand, VOC's, resulting from chemical activities, the manufacture of paints or the incomplete combustion of gasoline, are considered as carcinogenic compounds. Among them, the main environmental concern is the elimination of the BTEX fraction.

The Chemical Industry is one of the sectors with major contributions to achieve Sustainable Development. It covers social, environmental and economic aspects. In our society, thanks to its continuous work in innovation and development, this industry can propose new materials and solutions. Regarding atmospheric decontamination, new catalysts are being proposed day by day and the use of photocatalysis as an in-situ remediation technique in the urban environment has recently been emerging. This technology is simple to implement and the first results are very promising, both in the commercial products and in the environments in which they have been applied.

However, because it is a technology of new implementation, there are certain disadvantages limiting its widespread use.

In this context, this research deals with the preparation and characterization of new materials with photocatalytic properties, with the purpose of advance in their knowledge and facilitate their future commercial implementation as materials to be used for urban atmospheric depollution.

2. Hipótesis y objetivos.

El objetivo principal de esta Tesis Doctoral (de aquí en adelante, Tesis) es el desarrollo de materiales para combatir la contaminación atmosférica urbana, específicamente, el desarrollo de nuevos materiales con capacidad descontaminante De-NO_x. Se pretende preparar nuevos materiales que, siendo de bajo coste, puedan actuar efectivamente en los agentes tóxicos del aire de la atmósfera urbana, en concreto contra los óxidos de nitrógeno (NO_x), reduciendo su concentración y dejando un aire mas limpio en los centros urbanos. La aplicación a gran escala de este tipo de materiales permitirá ayudar a mitigar los efectos de la contaminación urbana.

Actualmente, el material fotocatalítico mas usado para procesos De-NO_x es el TiO₂ (principalmente en fase anatasa), el cual bajo la irradiación de luz solar induce la degradación (procesos de oxidación-reducción) tanto de la materia orgánica como de los contaminantes inorgánicos en su superficie (CO₂, NO_x, BTEX ...). Las propiedades inherentes del TiO₂ tales como alta estabilidad, baja toxicidad y alta actividad fotocatalítica comparada a otros óxidos metálicos, lo convierten en el material mas adecuado para esta finalidad.¹

Sin embargo, el coste de este material es tan alto que, solamente es usado en aplicaciones muy específicas de elevado presupuesto, lo que implica una seria limitación en el caso de ser

aplicado a gran escala para combatir la contaminación urbana. Además, su producción implica un alto coste energético y genera un gran número de residuos, algunos de ellos con trazas de elementos radiactivos.² Por otra parte, la actividad fotocatalítica del TiO_2 solamente ocurre con luz ultravioleta de longitud de onda inferior de 387 nm debido a su elevado band gap (3.2 eV), por lo que solamente puede utilizar un 4.5% del total de la luz solar y limitando así su utilización en áreas donde la luz solar tiene una intensidad más baja, como por ejemplo los países Nórdicos.³

Con el propósito de avanzar en el conocimiento, el objetivo de esta Tesis es proponer nuevas acciones de investigación, las cuales han sido estructuradas en dos bloques interrelacionados, pero bien diferenciados.

A) *Diseño de materiales fotocatalizadores avanzados De- NO_x* . El objetivo de este bloque es conseguir el desarrollo de nuevos fotocatalizadores avanzados De- NO_x de bajo coste. En este sentido, el principal material fotocatalítico estudiado será el óxido de hierro en fase hematita. La hematita ($\alpha\text{-Fe}_2\text{O}_3$) es el óxido de hierro con propiedades semiconductoras de tipo n más estable bajo condiciones ambientales. Este óxido presenta buen rendimiento como material fotocatalítico, es fácil de obtener usando métodos de síntesis simples y es considerado un material de bajo coste.⁴ Aunque la actividad fotocatalítica de la hematita es inferior a la del TiO_2 en fase anatasa, puede absorber luz visible (2.2 eV de band gap)

Además, será analizada la combinación de $\text{TiO}_2/\alpha\text{-Fe}_2\text{O}_3$ cuya sinergia resultaría en un mayor rendimiento en procesos fotocatalíticos.⁵ Finalmente, también será estudiada la optimización del TiO_2 como un fotocatalizador de bajo coste con mejoradas propiedades De- NO_x será estudiada.

B) *Preparación de nuevos fotocatalizadores De- NO_x a través de la valorización de residuos industriales.* El objetivo de este bloque es la valorización de residuos industriales cuya transformación/adecuación mejora la actividad fotocatalítica de los materiales. En este sentido, considerando la preparación de productos medioambientalmente sostenibles, es importante estudiar la preparación de semiconductores a partir de co-productos industriales. Los residuos con un alto contenido en óxidos de hierro serían de potencial interés, por ejemplo, los provenientes del corte de granito, acerías, limpieza de barcos, etc. Por otro lado, serán objeto de estudio los residuos cuya transformación permita usarlos como soporte apropiado de un material fotocatalizador, mejorando su actividad.

Con el fin de poder conseguir estos objetivos, son usadas las siguientes hipótesis de partida (por favor, ver también capítulos 3.1 y 4.1):

- La capacidad de los metales de transición para actuar como fotocatalizadores De- NO_x . Mas específicamente, la capacidad de la fase hematita de realizar este proceso

fotoquímico, como previamente fué descrita con éxito por el grupo de investigación “Química Inorgánica, FQM-175”.

- La capacidad de modificar las características químicas, electrónicas y morfológicas de los óxidos de hierro y óxidos de titanio con el fin de mejorar su actividad fotocatalítica, como ha sido descrita ampliamente por numerosos grupos de investigación nacionales e internacionales.
- La existencia de residuos industriales con alto contenido en óxidos de metales de transición.
- La capacidad de los residuos transformados, una vez enriquecidos en algunos metales de transición (por ejemplo, óxidos de hierro), de llevar a cabo en su superficie reacciones redox activadas por la luz, como ha sido demostrado previamente de forma pionera por el grupo de investigación “Química Inorgánica, FQM-175”. También, el hecho de que algunos residuos procesados presentan altos valores de superficie específica.

Las hipótesis previas soportan la expectativa de éxito en todo el objetivo general de esta investigación.

Este objetivo es presentado en las dos siguientes secciones en relación a los objetivos específicos de esta Tesis. Cada sección consta de una introducción al objeto de estudio y después los artículos de investigación, que presentan los resultados y discusión científica en relación con cada objetivo principal. El contenido, estructura y formato de cada artículo publicado o enviado para su

publicación ha sido mantenido. Todos los artículos fueron publicados (o enviados) en revistas internacionales de relevancia en la correspondiente área de conocimiento.

Referencias

1. Chen, H.; Nanayakkara, C. E.; Grassian, V. H., Titanium dioxide photocatalysis in atmospheric chemistry. *Chem. Rev.* **2012**, *112* (11), 5919-5948.
2. McNulty, G. S., *Production of titanium dioxide*. IAEA Proceedings Series: Sevilla, 2007.
3. Folli, A.; Bloh, J. Z.; Strøm, M.; Pilegaard Madsen, T.; Henriksen, T.; Macphee, D. E., Efficiency of solar-light-driven TiO₂ photocatalysis at different latitudes and seasons. Where and when does TiO₂ really work? *J. Phys. Chem. Lett.* **2014**, *5* (5), 830-832.
4. Mishra, M.; Chun, D.-M., α -Fe₂O₃ as a photocatalytic material: a review. *Appl. Catal. A: Gen.* **2015**, *498*, 126-141.
5. Sugrañez, R.; Cruz-Yusta, M.; Mármol, I.; Morales, J.; Sánchez, L., Preparation of sustainable photocatalytic materials through the valorization of industrial wastes. *ChemSusChem* **2013**, *6* (12), 2340-2347.

Hypothesis and objectives

The main objective of this *Philosophiæ Doctor Thesis* (from here on out, Thesis) is the development of materials to combat the atmospheric urban pollution, more specifically, the development of new materials with De-NO_x depolluting ability. It is intended to prepare new materials that, being of low cost, can act effectively on the harmful agents of the air in the urban atmosphere, specifically in the nitrogen oxides (NO_x), minimizing them and leaving a cleaner air in the urban centres. The large-scale application of this type of material will help to mitigate the effects of urban pollution.

Nowadays, the photocatalytic material most used for De-NO_x processes is TiO₂ (mainly in the anatase phase), which under sunlight irradiation induces the degradation (oxidation-reduction processes) of both organic matter and inorganic pollutants on its surface (CO₂, NO_x, BTEX ...). The inherent properties of TiO₂ such as high stability, low toxicity and high photocatalytic activity compared to other metal oxides, make it the most appropriate for this purpose.¹

However, the cost of this material is high so, it is only used in very specific applications with a high budget, which implies a serious limitation in the case to be applied at large scale to combat urban pollution. In addition, its production implies a high energetic cost generating great number of residues, some of them being radioactive traces elements.² In addition, the photocatalytic activity

of TiO_2 only occurs with ultraviolet light of wavelength lower than 387 nm due to its large band gap (3.2 eV), which only allows to take advantage of 4.5% of the total sunlight and limiting its use in areas where the intensity of light is lower, v.g. the Northern countries.³

With the purpose of advance in the knowledge, the aim of this Thesis is to propose new research actions, which has been structured into two interrelated but well differentiated blocks.

A) *Design of advanced De- NO_x photocatalyst materials.* With this action the objective is to achieve the development of new and low-cost advanced De- NO_x photocatalyst. In this sense, the main photocatalytic material studied will be the iron oxide in its hematite phase. The hematite ($\alpha\text{-Fe}_2\text{O}_3$) is the iron oxide with n-type semiconductor properties, more stable under environmental conditions. This oxide presents good performance as a photocatalytic material, it is easy to obtain by using of simple synthesis methods and it is considered a low cost material⁴. Although the photocatalytic activity of hematite is lower than that of TiO_2 in the anatase phase, in contrast, it can absorb visible light (2.2 eV band gap).

Furthermore, it will be analysed a combination of $\text{TiO}_2/\alpha\text{-Fe}_2\text{O}_3$ whose synergy would result in catalytic processes with better performance.⁵ Finally, the optimization of TiO_2 as enhanced low-cost De- NO_x photocatalyst will be studied.

B) *Preparation of new De-NO_x photocatalyst through the valorisation of industrial waste.* The objective of this action is the valorization of the industrial wastes whose transformation/adequacy enhance the photocatalytic activity of materials. In this sense, considering the preparation of environmentally sustainable products, it is important to study the preparation of semiconductors from industrial co-products. The residues with a high content of iron oxides would be of potential interest, i.e. sludge from granite cutting, steelworks, cleaning of ships, etc. On the other hand, it will be object of study the wastes whose transformation let use them as proper support of a photocatalyst material, enhancing their activity.

In order to achieve these objectives, the following starting hypotheses are used (please, see also chapters 3.1 and 4.1):

- The ability of transition metal oxides to act as De-NO_x photocatalysts. More specifically, the ability of the hematite phase to perform this photochemical process, as previously was successfully described by the research group "Inorganic Chemistry, FQM-175".
- The capability to modify the chemical, electronic and morphological characteristics of iron oxides and titanium oxides in order to improve their photochemical activity, as has been widely described by several national and international research groups.

- The existence of industrial wastes with high contents of transition metal oxides.
- The ability of the transformed residues, once enriched in some transition metal oxides (e.g. iron oxides), to carry out light-activated redox reactions on their surface, as it has previously demonstrated in a pioneering way by the "Inorganic Chemistry, FQM-175" research group. Also, the fact that some processed wastes present high values of specific surface area.

The previous hypotheses support the expectation of success in the overall objective of the research.

The same is presented below in two sections in relation to the specific objectives of this Thesis. Each section consists of an introduction to the subject of study and, later, the research articles presenting the results and scientific discussion in relation with each main objective. The content, structure and format of each published or drafted article has been maintained. All articles were published (or submitted) in international journals of relevance in the corresponding area of knowledge.

References

1. Chen, H.; Nanayakkara, C. E.; Grassian, V. H., Titanium dioxide photocatalysis in atmospheric chemistry. *Chem. Rev.* **2012**, *112* (11), 5919-5948.
2. McNulty, G. S., *Production of titanium dioxide*. IAEA Proceedings Series: Sevilla, 2007.
3. Folli, A.; Bloh, J. Z.; Strøm, M.; Pilegaard Madsen, T.; Henriksen, T.; Macphee, D. E., Efficiency of solar-light-driven TiO₂ photocatalysis at different latitudes and seasons. Where and when does TiO₂ really work? *J. Phys. Chem. Lett.* **2014**, *5* (5), 830-832.
4. Mishra, M.; Chun, D.-M., α -Fe₂O₃ as a photocatalytic material: a review. *Appl. Catal. A: Gen.* **2015**, *498*, 126-141.
5. Sugrañez, R.; Cruz-Yusta, M.; Mármol, I.; Morales, J.; Sánchez, L., Preparation of sustainable photocatalytic materials through the valorization of industrial wastes. *ChemSusChem* **2013**, *6* (12), 2340-2347.

3. Design of advanced De-NO_x photocatalysts

3.1. Introduction – Nanomaterials to combat NO_x pollution



Copyright © 2015 American Scientific Publishers
All rights reserved
Printed in the United States of America

Review

Journal of
Nanoscience and Nanotechnology
Vol. 15, 6373–6385, 2015
www.aspbs.com/jnn

Nanomaterials to Combat NO_x Pollution

J. Balbuena, M. Cruz-Yusta, and L. Sánchez*

*Departamento de Química Inorgánica, Facultad de Ciencias–Universidad de Córdoba,
Campus de Rabanales, Edificio Marie Curie, 14071–Córdoba, Spain*

The presence of NO_x gases (NO+NO₂) in the atmosphere is a major concern of society because of their associated adverse and harmful effects. In order to remove the NO_x gases from the air, photocatalysis arises as an innovative and promising technique. Through the use of photochemical oxidation processes the NO and NO₂ gases are oxidised to NO₃⁻ form and thus removed from the air. In recent years new nanomaterials are being developed by researchers with the aim to enhance their photocatalytic activity to combat the NO_x pollution. The main focus is devoted to preparing new TiO₂ based compounds with the highest specific surface area (SSA), different morphology and chemical modifications. In order to increase the SSA, different substrates were used to disperse the TiO₂ nanoparticles: organic and carbon fibres, mesoporous materials, clays composites and nanoporous microparticles. In the other hand, high photocatalytic performances were obtained with nanotubes, self-orderer nano-tubular films and nanoparticles with the lowest size. Conversely, when TiO₂ is doped with ions the oxide exhibited a better photocatalytic performance under visible light, which is related to the creation of intermediate energy states between the conduction band and the valence band. Alternatively, visible light photocatalysts different from titanium oxide have been studied, which exhibit a good De-NO_x efficiency working under $\lambda > 400$ nm visible light irradiation.

Keywords: Photocatalytic Oxidation, Nitrogen Oxides, Titanium Dioxide, Nanomaterials.

3.1.1. Introduction

Atmospheric pollution has been recognised as one of the most serious environmental problems, causing a major concern for modern society. The air pollutants — substances that may harm humans, animals, vegetation and materials — reach the atmosphere from these main sources: natural sources, such as volcanic eruptions, soil erosion, forest fires; and anthropogenic sources, in particular emissions resulting from human actions.¹ Conversely, air pollutants can be classified according to their origin as primary or secondary pollutants. Primary pollutants are those emitted directly by the sources to the atmosphere: CO, SO₂, nitrogen oxides (NO_x) and particles (PM10 and PM2.5). Secondary pollutants are formed from chemical reactions occurring in the atmosphere: tropospheric ozone (O₃), HNO₃ and H₂SO₄.²⁻³

In that concerning to the NO_x gases, several adverse and harmful effects are associated with the presence of NO_x in the atmosphere and decreasing the nitrogen oxides (NO_x = NO + NO₂) concentration of the atmosphere, De-NO_x action, has become an obligatory and necessary task. They are responsible for such environmental problems as photochemical smog, tropospheric ozone, ozone layer depletion, even global warming caused by N₂O and, together with sulphur oxides, NO_x contributes to the generation of acid rain. On the other hand, human health is affected in several ways when the amount of NO_x interacting with lung tissues increases: emphysemas, bronchitis, etc. Another

problem is the interplay and interdependence of NO_x with other air pollutants, mainly volatile organic compounds (VOC). The co-created by-products (e.g., nitrous acid or peroxyacyl nitrate (PAN)) can be 10 times more toxic to humans than NO_x. Moreover, the presence of ozone in the troposphere can also damage the eyes and lungs.⁴⁻⁸ Therefore, limiting the amount of breathable NO_x in working and urban atmospheres is an important priority. For this reason, policies have been implemented by the USA (US Environmental Protection Agency; EPA) and European (European Environmental Agency; EEA) communities which limit the hourly NO_x air concentration at 0.1 ppm and 0.2 ppm, respectively. However, the recommended maximum amount of breathable NO_x in working and urban atmospheres is usually surpassed in the centre of the big cities.⁹⁻¹⁰ Moreover, some statements urge to the administrators to promulgate a new short-term NO_x standard in the range of 50 to 75 ppb.⁹ This concern has raised the interest of the research community to study new actions to effectively combat the NO_x pollution, which is the focus of this review.

NO_x inlets come from industry and the transportation sector, the latter being the most important source of NO_x in urban environments. There are three basic mechanisms leading to the formation of nitrogen oxides during combustion and thus three types of NO_x are identified: thermal, prompt and fuel NO_x.¹¹ Thermal NO_x is formed by the high-temperature reaction of nitrogen with oxygen, while prompt NO_x occurs by the relatively fast reaction between nitrogen, oxygen, and hydrocarbon radicals.

Otherwise, fuel NO_x is formed by the direct oxidation of organo-nitrogen compounds, with N–H and C–N bonds, present in the fuel. During combustion, the ring structures are broken and species such as HCN, NH₃ or •NH₂ and •CN are formed, which by reaction with O₂ originate NO_x. Some methods have been developed and implemented in order to control NO_x emissions, which are divided into primary and secondary methods.¹²⁻¹³ Primary methods refer to preventing the formation of NO_x, being the NO_x removal carried out inside a combustion zone (e.g. furnace) without the need for another reactor. The secondary methods are applied to reducing the already formed NO_x, being the most common between them: selective catalytic reduction (SCR), selective non-catalytic reduction (SNCR) and others like absorption of NO_x, phase separation, NO_x storage and reduction (NSR); ozone injection or NO conversion into HNO₃.¹⁴⁻¹⁶ However, none of them are applicable to directly remove the NO_x breathable by the residents located in the urban centres. To this aim, the photocatalysis is an innovative and promising technique for the removal of undesirable gaseous compounds.

Over the past ten years, the photocatalytic oxidation (PCO) of NO_x emissions has proven to be a powerful and simple technology.¹⁷⁻²² By using TiO₂ as an efficient photocatalyst, NO_x oxidation is easily promoted by using only atmospheric oxygen, water, and UV-A radiation.²³ This simple mechanism is the basis for the preparation of de-polluting building materials such as photocatalytic pavements, cement, mortars, and paints, an interesting strategy to combat the NO_x pollution in our cities.^{20, 24-31}

Considering the difficulty of decreasing NO_x levels in large urban centres with certain characteristics (lack of wind or rain, intense road traffic, proximity to industrial zone, etc.), the construction of city architectural elements (roadways and building fronts) using photocatalytic materials begins to attract the attention of governments, industry and researchers. In recent years, an intense effort has been devoted to understanding and enhancing the PCO of NO_x gases by using TiO₂-containing cementitious materials focusing on: i) the study of factors affecting the PCO process (amount, phase, particle size, and surface area of TiO₂,²⁰ NO_x flow rate, light intensity, surface chemistry, humidity, and environmental conditions);^{18, 20, 23, 26-27, 32-33} ii) the use of recycled materials;^{20, 27, 34} iii) the NO_x photocatalytic oxidation mechanism;^{19, 24} iv) the evaluation of the microstructure, mechanical properties and durability of TiO₂-materials;³⁵⁻³⁶ and v) the study of practical conditions.³⁷⁻³⁸

Bearing in mind that the future implementation of De-NO_x materials in our cities would be a large-scale operation, increasing as maximum their photocatalytic efficiency would be a desired goal in order to reach competitive costs for their commercialisation and to remove the largest amount of NO_x gases from the urban atmosphere. Nanoscience is considered a key area to the development of enhanced catalytic processes.³⁹ The studies in this area have been motivated by the work of Haruta et al., reporting that Au nanoparticles smaller than 5 nm supported on α -Fe₂O₃ are very active for CO oxidation.⁴⁰ Considering that most

heterogeneous catalytic processes take place at the active surface sites of the bulk catalyst, it seems reasonable to propose that the smaller the particle size, the higher the surface area and activity. Although the consequences of the nanosize in catalysis seem quite obvious, in some cases the scenario is more complex, being an object of study by the research community.⁴¹

The aim of this review is to present the current state and importance of nanomaterials in their specific use to remove NO_x gases through the use of PCO processes. In a few years this has become a flourishing research activity, which was not summarised in previous and important reviews on the subject of NO_x abatement.^{13, 41-47}

3.1.2. NO_x removal by photochemical oxidation process

The photocatalysis research and application on the atmospheric environment is mainly based in the use of titanium dioxide, TiO₂. This oxide is the most promising photocatalyst due to its non-toxicity, strong oxidation power and chemical inertness. TiO₂ has three major stable polymorphs being the anatase phase which showing the highest photocatalytic activity.⁴⁸ As semiconductor material, the anatase phase exhibits a large band gap of 3.2 eV being its photocatalytic property activated by ultraviolet light (UV) of wavelengths shorter than 387 nm. Even though for the best cases the UV radiation is only 4-5% of the overall energy of sunlight,⁴⁹⁻⁵⁰

the photon energies in this region (10^{13} quanta·cm⁻²·s⁻², at high noon) are sufficient to activate TiO₂ with the formation of separated electron-hole pairs, as discussed below.⁵¹

Based on this titanium dioxide polymorph, the industry Evonik commercialises the *TiO₂-P25* product (hereafter designated as P25) composed of 75% anatase and 25% rutile. This product is the typical commercially available material used in De-NO_x building materials and also by the research community as standard.⁵²⁻⁵³ A synergy effect between both phases has been suggested for the increased photocatalytic activity of this product.⁵⁴

The photochemical reaction of TiO₂ with NO_x gases is presented in Figure 1. When the TiO₂ semiconductor material is activated with light of wavelength equal to or greater than the band gap energy, the electrons in the valence band are transferred to the conduction band leaving electron holes – h^+ – (1). The pair of mobile charges produced can reach the surface of the semiconductor particle and initiate the redox process.⁵⁵ Thus, photogenerated electrons and holes can react with H₂O (2) and O₂ (3) molecules, leading to the formation of reactive oxygen species (ROS) acting as strong oxidants. Subsequently, the oxygen radical O₂^{•-} assists the oxidation of NO to NO₃⁻ (4). Simultaneously, the participation of hydroxyl radicals – OH• – lead also to the formation of NO₃⁻ through the intermediate oxidation steps NO → HNO₂ → NO₂ (5,6), being the nitrate ions the major product deposited on the catalyst (7).^{18-19, 23, 31-32} Obtaining nitrate as the major product is quite

important, as NO_2 is more toxic than NO ,⁵⁶ being necessary to observe the photocatalyst selectivity towards the above reactions.⁵⁷

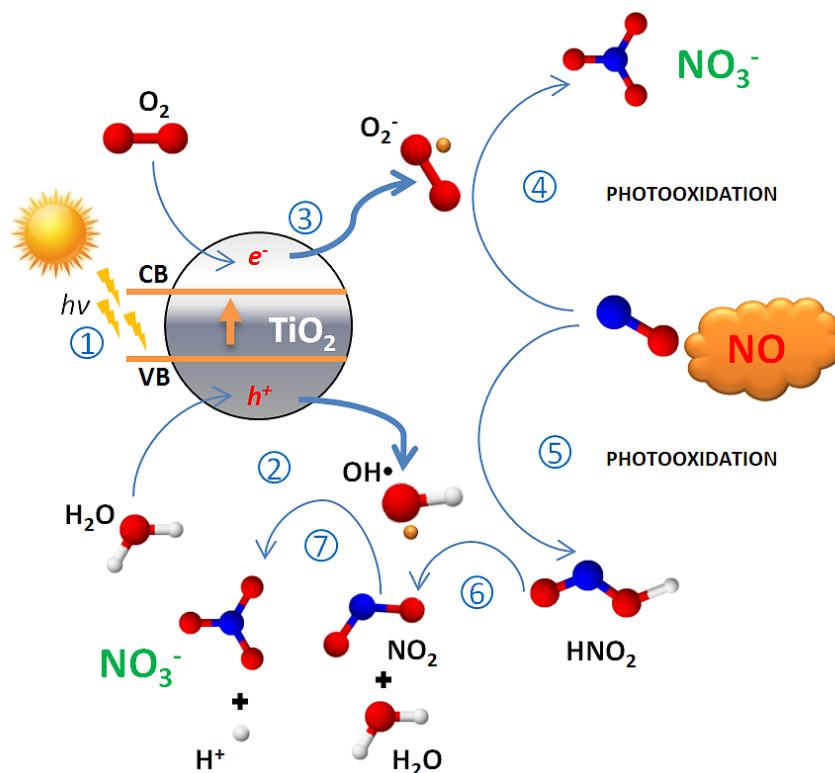


Figure 1. Mechanism of NO photocatalytic oxidation.

The PCO mechanism showed in Figure 1 was summarised with the aim to enhance understanding of it. Even though the photocatalytic oxidation of NO on TiO_2 particles has shown the formation of nitrate as the final product,^{18-19, 58} many studies demonstrated the complexity of the overall mechanism. Thus, it was reported that several kinds of ROS species such as atomic oxygen (O), O^- , $\text{OH}\cdot$ radical and $\text{HO}_2\cdot$ radical are produced through reactions among O_2^- , h^+ , O^- , $\text{H}^+/\text{H}_2\text{O}$ and OH^- on the TiO_2 surface

and, based on the gas-chemistry concerning to NO_x, other simultaneous reactions take place.⁵²

The NO adsorption on TiO₂, an important stage, has shown the formation of surface adsorbed NO⁻, N₂O₂²⁻ and nitrate.⁵⁹ In similar way, the physisorbed/chemisorbed NO₂ plays an important role and some findings suggest HNO₃ formation by physisorbed NO₂ and H₂O vapour, while chemisorbed NO₂ and NO₃⁻ are less reactive toward H₂O vapour.⁶⁰ On the other hand, the pathways leading to the HNO₂ and HNO₃ formation seem to be conditioned by the NO₂ concentration.⁶¹⁻⁶⁴ At high NO₂ levels, the formation of N₂O₄ intermediate leads to NO⁺, and NO₃⁻, which further react with H₂O to form HNO₂ and HNO₃. Also, at high NO₂ levels, chemisorbed NO₂ is not present on the surface due to its oxidation to adsorbed nitrate. At low NO₂ levels, surface chemisorbed NO₂ (nitrite) reacts with H⁺ and OH• originated from photocatalytic H₂O dissociation on TiO₂, leading to HNO₂ and HNO₃ formation.

The efficiency of the PCO mechanism, represented in Figure 1, depends mainly on the UV-A radiation, increasing with the intensity of the radiation.¹⁹ However, the role of water seems to be very important and controversial. Some authors conclude that increasing relative humidity values reduces the oxidation rate as the water molecules compete with the NO_x molecules at the photocatalyst active surface.^{31-32, 65-66} On the other hand, it has been reported that water plays an important role in the generation of hydroxyl radicals – OH• –, improving the efficiency of heterogeneous photocatalysis.^{18-19, 67-68} Thus, the hydroxyl groups

present on the photocatalyst surface play an important role because adsorption of NO occurs mainly through interaction with them.⁶⁹

Finally, two main factors were considered for the photocatalyst deactivation: water consumption on its surface (if not continuously supplied) and adsorbed NO₃⁻ species. Nevertheless, the photocatalyst is easily regenerated by washing with water.^{52, 70}

3.1.3. TiO₂ nanoparticles as efficient De-NO_x photocatalyst

As mentioned above, TiO₂ has been reported as an effective De-NO_x material by oxidising NO and NO₂ into nitrate. At this point we survey the different strategies followed by the researchers in order to improve the photocatalytic efficiency for this application under the nanoscience prism. Because the photocatalysts exhibit different selectivity to the NO and NO₂ photochemical oxidation, the terms “photocatalytic efficiency” or “photocatalytic performance” are hereafter used to refer the changes in total NO_x concentration during the photocatalytic test. However, the studies of some authors are only devoted to the photocatalytic oxidation of NO gas, usually referred as “NO conversion”, being this mentioned on this work.

Surface area and morphology

The photocatalytic activity exhibited by titanium dioxide can be easily increased with the preparation of compounds exhibiting a high specific surface area (SSA). For this, two main strategies are adopted: i) the use of a variety of substrates with the higher specific surface area, on which titanium dioxide nanoparticles are dispersed, and ii) to control the TiO₂ morphology and size through the use of different synthetic techniques. A schematic illustration concerning the different scenarios followed to disperse TiO₂ is represented in Figure 2.

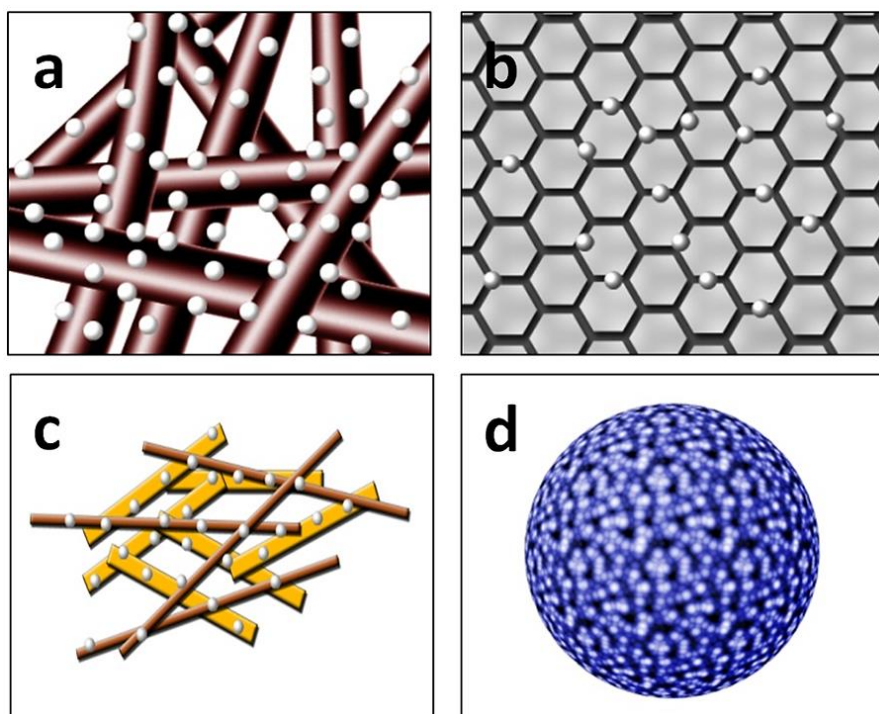


Figure 2. Schematic representation of different substrates used to disperse TiO₂ nanoparticles: a) Fibers, b) Mesoporous materials, c) Clays and d) Microporous nanoparticles.

The use of organic fibers to disperse TiO₂ was reported by K. Lang et al.⁷¹ By using the nanospider electrospinning industrial technology, composites of TiO₂/organic nanofiber surfaces (polyamide 6, polystyrene and polyurethane; 460 nm) can be obtained. The titanium dioxide is deposited on the nanofiber network from an acidified supersaturated TiOSO₄ solution, in similar way to the method described by Yamabi and Imai.⁷² The entirely TiO₂ coated nanofibers exhibit high surface area values. A good photocatalytic performance in removing NO_x gases is obtained with this composite (16% NO conversion). The MCM-41, a mesoporous siliceous material with a large specific surface, has also been used as efficient support to disperse nano-TiO₂.⁷³ This support is impregnated with Ti(iOPr)₄ as a precursor of nano-TiO₂ and, subsequently, calcined at 500 °C in air flow. The Ti/Si ratio can be changed in the composite. For the best cases, samples with specific surface values up to 1000 m²·g⁻¹ are obtained, having photocatalytic performance for the removal of NO_x near to 60%. In an alternative way, TiO₂/Al₂O₃ composites with a large surface area (up to 290 m²·g⁻¹) were prepared by using the sol-gel method.⁷⁴ The TiO₂ results dispersed well onto an Al₂O₃ matrix, thus improving its photocatalytic activity in 20% and 40% compared to P25 after 30 min of irradiation.

Conversely, several research groups have used clay-based composites in order to improve the photocatalytic activity of TiO₂. In this sense the halloysite (Al₄Si₄OH₈O₁₀·8H₂O) is one of the substrates selected.⁷⁵ The hydrothermal synthesis of an aqueous

dispersion of halloysite and titanium tetraisopropoxide leads to the preparation of Hal/TiO₂ composites (TiO₂ diameter = 10-30 nm) with a high surface area of 180 m²·g⁻¹. The photocatalytic properties are improved up to 45% compared to P25 based. An interesting way to achieve a better dispersion of TiO₂ nanoparticles (about 25 nm) consists of the use of two different nanoclays, thereby synthesising a nanocomposite of three phases.⁷⁶ The joint use of palygorskite ((Mg,Al)₂Si₄O₁₀(OH)·4(H₂O)) and halloysite decreases the agglomeration of the clay particles, thus leaving more free space for the deposition of TiO₂. The composite is prepared by hydrothermal synthesis using a dispersion of clays and Ti(OC₃H₇)₄ as a precursor of TiO₂. The clay samples were size fractionated to obtain particles < 2.0 μm by gravity separation. Separation of clay fraction was carried out by using centrifugation methods. Different mixtures were studied: Hal20:Pal10, Hal15:Pal15, Hal10:Pal20. The 2-clays/TiO₂ composite exhibits a SSA of around 200 m²·g⁻¹ being superior to that of P25, 50 m²·g⁻¹. In correlation with this high SSA, the photocatalytic capacity is increased (57% more efficiency than P25), even using visible light (30% more efficiency than P25), because the TiO₂, anatase polymorph, is well dispersed on the surfaces of the clay minerals. Alternatively, using the solvothermal technique, flake-shaped saponite nanoparticles coated with TiO₂ are obtained from a suspension of saponite ((Si_{7.74}Al_{0.26})(Al_{0.51}Fe³⁺_{1.47}Mg_{2.65})_{4.64}Ca_{0.13}Mg_{0.37}Na_{0.01}O₂₀(OH)₄) and TiCl₃ — dispersed in ethanol — as the TiO₂ precursor.⁷⁷ The specific morphology afforded by the composite provides a large specific

surface of 250-300 m²·g⁻¹. Again, an increase of photocatalytic activity with respect to P25 is obtained due to the good dispersion of TiO₂ through a material with very high SSA.

The aerosol assisted co-assembly of nanoparticles (AACA) technique emerges also as an efficient way to get composites with increased surface area.⁷⁸ The AACA is a very fast procedure achieving the preparation of nanoporous microparticles (6.1 μm of particle size and 10-100 nm of pore size) from sprayed droplets of a colloidal solution as aerosol prepared by dispersing P25 and SiO₂ nanoparticles (Aerosil 200, Degussa) The large surface area measured for this composite, up to 150 m²·g⁻¹, together with the pore structure increase considerably the contact with the reactant molecules. Thus, the photocatalytic performance for the degradation of NO_x gases increases by 10% in comparison with that exhibited by the P25 nanoparticles. A different approach is followed by Lee et al. searching for a substrate that serves to disperse TiO₂ nanoparticles but also to facilitate the NO molecules adsorption.^{22,}
⁷⁹ Thus, activated carbon (AC) is used as a highly crystalline absorbent with high internal porosity. These properties can be used to form compounds with greater specific surface area than pristine TiO₂. Using the AC-TiO₂ composites, an enhanced photocatalytic efficiency of TiO₂, reaching 97% in the case of NO and 95% for total NO_x, is obtained in comparison with the values measured for AC, 83% and 70% respectively. These good results can be explained by considering that the presence of carbon facilitates the adsorption of NO molecules, which are then transferred to TiO₂ and transformed

into NO₂ by the just produced h⁺ holes prior to hole/electron recombination.

On the other hand, high photocatalytic De-NO_x performances for TiO₂ were obtained by tuning the morphology and size of the nanoparticles. Titania nanotubes (TNTs) were obtained by hydrothermal synthesis using TiO₂ as a precursor and a posterior calcination process at different temperatures.⁸⁰ The most active sample obtained exhibited 106.3 m²·g⁻¹ of SSA and 12.4 nm of diameter. The enhanced photocatalytic behaviour in De-NO_x reaction was ascribed to the unidimensional morphology — facilitating the electron transfer —, the large surface area as well as the high crystallinity. Thus, a photocatalytic efficiency of 46% more in comparison to P25 after 4 hours of irradiation is obtained. Moreover, there are other forms for the use of nanotubes. Self-ordered nano-tubular TiO₂ films⁸¹ were grown by electrochemical anodisation of titanium foils. These nanotubes, between 110–140 nm of outer tube diameter, perform a 22.6 % of NO_x oxidation at best. As a simple way to obtain nanoparticles, J. Jurng et al. propose the use of a thermal decomposition process applied to a specific titanium precursor.⁸² With this simple technique they can obtain TiO₂ particles of around 10 nm with SSA values greater than 130 m²·g⁻¹. For comparison purposes we must note that the known corresponding values for the standard P25 are 21 nm and 50 m²·g⁻¹, respectively. Furthermore, the nanoparticles synthesised by this method have a main polyhedral structure. With these features it is possible to obtain up to 10% more efficiency than P25 in the NO_x

removal test. Finally, the technique of thermohydrolysis is presented as an environmentally friendly method of synthesis for TiO_2 nanoparticles, using in this case TiOSO_4 as precursor.⁸³ Once obtained, the nanoparticles' crystallinity can be increased by calcination. The performance obtained in the removal of NO_x gases was better for the prior to calcination samples than for P25, and the latter better than that obtained for the calcined ones. The results were explained based on the high SSA values obtained for the pristine samples ($167 \text{ m}^2\cdot\text{g}^{-1}$) and its decrease after the calcining process (until $27 \text{ m}^2\cdot\text{g}^{-1}$) because crystallinity increased.

A comparison of the exhibited De- NO_x ability for some of the above commented TiO_2 based systems and that of P25 is shown in Figure 3.

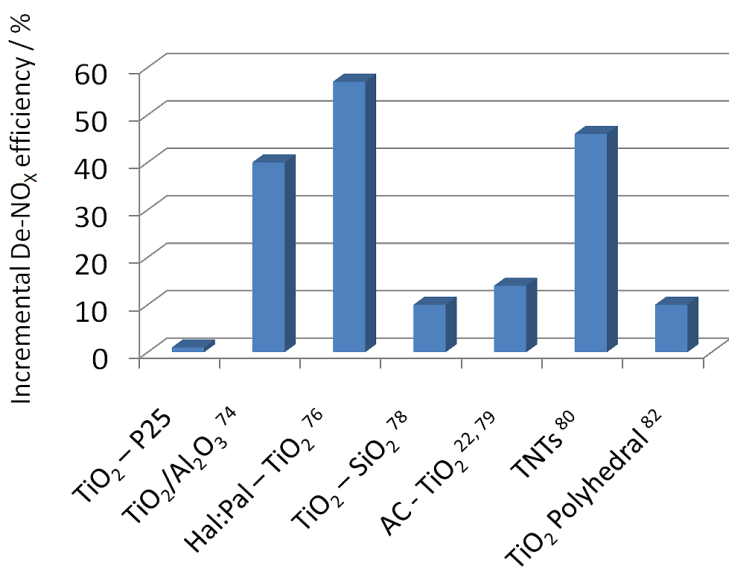


Figure 3. De- NO_x ability values of supported TiO_2 materials in comparison with that corresponding to TiO_2 -P25. As a reference, the zero value was assigned to TiO_2 -P25.

Chemically modified nano-TiO₂

One of the main drawbacks for TiO₂ in photocatalysis applications is that the photogeneration of charge carriers can only be produced by the absorption of UV light. Fourteen years ago, Asahi et al.⁸⁴ reported that nitrogen-doped TiO₂ showed photocatalytic activity under visible light. Since then, doping or modifying of TiO₂ to change the band gap has attracted much attention.⁸⁵⁻⁸⁷ The ions, in the anionic or cationic sublattices, could be replaced by the dopant or could be placed in interstitial sites of the crystal lattice. The incorporation of dopant causes distortion of the crystal lattice originating changes in the structure of electronic bands by creating excited interstates or deforming its electronic bands.⁸⁸ These changes in the electronic band structure, induced by doping, could be translated in changes in the reflection spectra, due to absorption of visible light and improving its activity towards De-NO_x reactions.

An impurity energy level in the band gap of TiO₂ is formed when a metal ion is incorporated into the TiO₂ lattice. The substitution of metal ions introduces an intraband state close to CB or VB edge, inducing visible light absorption at sub-band gap energies. In addition, metal ions alter the charge carrier equilibrium concentration by serving as electron–hole trap and enhance the degradation rate.⁸⁹ Zhang et al. prepared N-TiO₂ co-doped with Fe using one step hydrothermal method.⁹⁰ With a two-step hydrothermal method the authors obtained N-TiO₂/Fe₂O₃

composites, indicating that synthesis method showed great influence on the iron status in the final products. In both cases, the morphology is a rod-like nanoparticle (10 nm in diameter; 20–60 nm in length) that is more homogeneous in the case of N-TiO₂/Fe₂O₃ samples. The Fe co-doping did not show any influence on the morphology. The SSA decreases significantly in the case of N-TiO₂/Fe₂O₃ (120 m²·g⁻¹) in comparison with Fe-N-TiO₂ samples (180 m²·g⁻¹). According to the authors, using iron as dopant, the photocatalytic activity decreases even with small amounts of iron because of the formation of lattice anion vacancy. In the case of N-TiO₂/Fe₂O₃ the photocatalytic activity is enhanced, despite the drastic decrease of specific surface area. This find was ascribed to an effective separation of photo-induced electrons and holes by the heterogeneous electron transfer from N-TiO₂ to Fe₂O₃. In both cases, good photocatalytic activity under visible light is observed in consequence with the presence of N atoms and oxygen vacancies.⁹¹

The presence of an iron dopant in TiO₂ structure provides a recombination pathway for the photogenerated electrons and holes suppressing the formation of NO₂ during the photocatalytic decomposition of nitric oxide. In the same way, to improve the activity of photocatalyst, Bajnoczi et al.⁹² indicated that there is a clear correspondence between the local structure of the Fe(III) and the photocatalytic activity of TiO₂. Also, the beneficial effect of silver ions in doped titania was studied. In a similar way, Konami et al.⁹³ prepared modified titania with metal chloride (Pt, Rh, Pd, Fe y Cu). The doped-TiO₂ exhibited lower SSA values than undoped TiO₂

(280, 335, 196, 263 y 275 m²·g⁻¹, respectively). The levels of removal of NO_x greatly depended on the type of metal under visible light irradiation. The NO_x removal capability order for these metals is Rh < Pt < Pd < Fe < Cu. Alternatively, Kocí et al.⁹⁴ evaluated the N₂O decomposition by Ag doped TiO₂, with different content of Ag. The results obtained were better than others reported in the literature. The reason for these results could be due to the decrease of the recombination rate by the spatial separation of electrons and holes in surrounding the Ag cluster.

With the same philosophy, another strategy could be doping with non-metal ion, which is referred to doping with N, C, B and S, especially the first two. For these doped materials the visible light response arises from the presence of localized energy levels of the dopant lying above the valence band or oxygen vacancies.⁹¹ Nitrogen can be easily introduced in the TiO₂ structure because of its comparable atomic size with oxygen, small ionization energy and high stability.⁹⁵ Many methods, dry and wet, have been used to incorporate N into TiO₂ either in the bulk or as a surface dopant.⁹⁶ Of the different synthesis methods found in the literature, the most frequently used is the sol-gel method.⁹⁶⁻⁹⁷ The success of this method lies in the relatively simple equipment required and the possibility to control the material's nanostructure, morphology and porosity in a fine way. Amadelli et al. found good De-NO_x visible light photoactivity for N-doped TiO₂, with ≈60% of NO removal under λ > 450 nm light irradiation.⁹⁸ On the one hand, it is known that carbon doping improves the adsorption of organic pollutant

molecules on a catalyst surface. The carbon assists the phase transformation of the amorphous phase TiO₂ directly to rutile phase, and creates interface between the anatase and carbon covering rutile phase. The band gap was lowered due to the interface states in the mixed phase, and the photoactivities were enhanced due to carbon covering, which may effectively serve as traps for the created electron and hole pairs and result in optimal photoactivities.⁹⁹ Tseng et al.¹⁰⁰ successfully prepared C-TiO₂ by an impregnation process using ethanol as the carbon source. The visible light activity and absorption of prepared TiO₂ is sharply decreased by calcinations at temperatures higher than 250 °C. This compound is also able to reduce the probability of electron-hole recombination.

The use of two different ions in the preparation of doped TiO₂ was also reported. Using a mechanochemical method Yin et al.¹⁰¹ prepared N-C co-doped titania. They found that when the pure TiO₂ sample is milled, the NO conversion decreases by 10-20%, ascribing this behaviour to the introduction of crystal defects or a phase transformation anatase-rutile. However, when the milled sample is the N and C co-doped, the activity was six to seven times higher than that of milled TiO₂. In this case, the behaviour is related to the presence of an oxygen rich surface formed during the milling process. TiO₂ photocatalyst co-doped with B and N is prepared by the sol-gel method and exhibited a higher photocatalytic activity than pure TiO₂, N-TiO₂ and B-TiO₂ under UV and visible light irradiation.¹⁰² The higher UV-light photocatalytic activity of B-N-TiO₂

was attributed to the narrowed band gap of TiO₂ induced by interstitial N and NOB species in the TiO₂ crystal lattice. The enhancement in the visible light photocatalytic activity of B-N-TiO₂ was ascribed to photoelectron transitions from the energy levels of interstitial N and NOB species and the surface state energy levels of NO_x species to conduction band of TiO₂. Todorova et al.¹⁰³ studied the N and N-S co-doped titanium dioxide. Upon UV illumination the pure TiO₂ exhibited the highest activity in NO_x removal from the gas phase. Under visible light illumination, the N doped samples exhibited enhanced NO_x oxidation activity, while the N-S co-doped samples were inactive. The outcome was ascribed to the high electron-hole recombination and the inhibiting effect of S on the formation of OH• species.

A different strategy to modify the band structure of TiO₂ and enhance its photocatalytic activity under visible light results from the deposition of metals on the surface of TiO₂. Many noble metals have shown improvements in the process of photocatalysis with TiO₂. As the Fermi levels of these noble metals are lower than that of TiO₂, photo-excited electrons can be transferred from CB to metal particles deposited on the surface of TiO₂, while photo-generated VB holes remain on the TiO₂. Thus, the recombination process of electron-hole is minimized, improving charge separation and reaction rate and helping the electron transfer to improve the photocatalytic activity.¹⁰⁴ In this sense, the synthesis process followed to obtain the modified material must be taken into account. Inturi et al.¹⁰⁵ use the method of flame aerosol pyrolysis to

prepare the modified materials with V (% 80, d_A 35, d_R 138), Cr (% 56, d_A 31, d_R 97), Fe (% 35, d_A 26, d_R 74), Co (% 16, d_A 35, d_R 85), Mn (% 25, d_A 27, d_R 90), Mo (% 74, d_A 24, d_R 127), Ni (% 12, d_A 54, d_R 74), Cu (% 29, d_A 42, d_R 122), Y (% 64, d_A 26, d_R 130), Ce (% 48, d_A 22, d_R 138) and Zr (% 71, d_A 24, d_R 118), % being the amount of anatase phase, d_A and d_R the particle size of the anatase and rutile phases, respectively. Takeuchi et al.¹⁰⁶ also found good results when Cr modified TiO₂. In this case, the improvement of the photocatalytic activity is related to the increase in oxygen vacancies causing doping with Cr.

The chemical coprecipitation-peptisation method was used to prepare Pd modified titania films.¹⁰⁷ No significant differences were found between TiO₂ samples when a small amount of Pd salt (0.25 y 1%) was added. The chemical states of elements were elucidated by the XPS technique. Small amounts of Pd were found at surface of TiO₂ film with the existence of Pd(0) and Pd(II). The photocatalytic activity for these samples, towards the NO conversion, decreased in the order Pd(0.25%)/TiO₂ > TiO₂ > Pd(1%)/TiO₂. The Pd²⁺ ion on the TiO₂ surface acts as a trapping site to capture photogenerated electrons from TiO₂ conduction band, separating the photogenerated electron-holes pairs.¹⁰⁸ This would explain the observed enhanced photoactivity of Pd(0.25%)/TiO₂ versus TiO₂. However, the excess Pd content hinders reaction rate because of enhancement in the reduction of deposited NO₃⁻ to NO₂. As the authors comments, because the Pd(II) would be reduced to Pd(0) by the photogenerated electrons – playing the metallic Pd the

role of a hole trapper –, the reversible reaction conducting to the reduction of NO₃⁻ to NO₂ is increased in samples with higher Pd content. The same results were found by Wu et al.¹⁰⁹ They found that a small amount of Pd (0.05%) could improve the NO conversion reaction by up to 70%. On the other hand, platinum modified TiO₂ was synthesised by the sol-gel process followed by impregnation of Pt precursor.¹¹⁰ No significant differences relative to particle size (doped was around 3–10 nm lower), crystal structure and surface area (between 225 y 260 m²·g⁻¹) were found for TiO₂ and Pt-TiO₂. The coexistence of platinum oxides, PtO and PtO₂, on the surface of TiO₂ was evidenced. In this modified titania photocatalyst the chemical state of platinum species seems to act, facilitating the oxidation of NO₂ to NO₃⁻ because the Pt functioned also as adsorption center of O₂.

The last strategy to modify the TiO₂ is preparing composites with other metal and non-metals oxides. The aim is to prepare a mixture of compounds with enhanced activity towards the De-NO_x process. Bellardita et al.¹¹¹ prepared the SiO₂-TiO₂ composite depositing TiO₂ onto different silica by a wet method under mild conditions. The good photocatalytic activity of the sample obtained by supporting TiO₂ on pure Cabot silica seems interesting for a possible employment of this material as an additive for photocatalytic cements with the aim to abate noxious volatile compounds. In the case of NO_x degradation, they found that about 90% of NO_x was abated after 15 min of light irradiation. The authors

point out that other less expensive silicas (Axim and Fly Ash) were not suitable for photocatalytic applications because the presence of other species, working as centers of recombination of the hole-electron pairs. Alternatively, Yang et al.¹¹² prepared the composite V₂O₅/TiO₂ with carbon nanotubes. The samples were prepared by a sol-gel method. The addition of carbon nanotubes could increase the specific surface area and pore volume of the samples and improve the NO conversion efficiency. N-doped TiO₂/ZrO₂ samples were prepared for Kim et al.¹¹³ using a polymer complex solution method. The addition of ZrO₂ avoids the phase transformation from anatase to rutile, promotes the thermal stability of the photocatalyst and induces more surface OH groups, which inhibited the electron-hole recombination. These composite materials improve the efficiency because the photocatalytic activity is retained for a longer time.

Even though there are no doubts about the De-NO_x efficiency showed by the above commented materials, it is our opinion that deeper knowledge must be gained about the intrinsic PCO mechanism accounted for each photocatalyst. By way of example, while NO_x oxidation reactions are mediated mainly by the •OH and less by •O₂⁻ species,²⁸ it has been suggested that for N-doped TiO₂ the photogenerated holes formed under visible light irradiation do not possess suitable reduction to generate •OH radical by the oxidation of H₂O.⁹¹ This conflict in the interpretation of the research results is probably originated by the unknown about whether or not the band edges of TiO₂ are changed by the dopant,⁹⁶ the nitrogen

on this example. Also, structural defects in TiO₂ surface can affect to the photocatalytic reactivity. One of the most important types of defects is oxygen vacancies affecting electronic and geometric structure, optical properties, etc.¹¹⁴ Therefore, additional efforts are required to the scientific community on these important issues.

As a brief summary of the above commented strategies, Figure 4 shows the modified TiO₂ band structures in the cases of chemical ion-doping, metal deposition and composites.

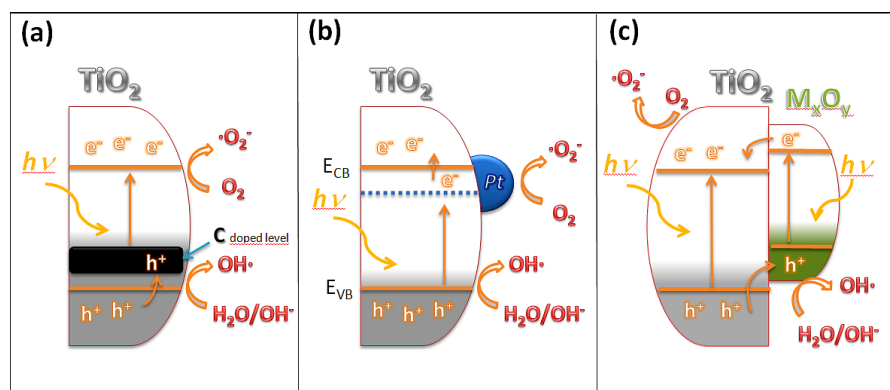


Figure 4. Scheme of TiO₂ band structures: a) chemical ion-doping, b) metal deposition and c) composites.

3.1.4. Alternative nano-particulated systems

There is no doubt about the excellent performance of TiO₂ as a photocatalyst, but its photocatalytic activity only occurs with UV light ($\lambda < 387$ nm). As a consequence, the photocatalytic performance of De-NO_x materials using TiO₂ dramatically decreases in certain circumstances: in dark areas of the cities — shadows of

buildings or narrow streets where there is no direct sunlight — ; in the cities of Central/Northern Europe or North America where, owing to geography and gloomy weather conditions, only low levels of UV radiation reach the surface.⁴⁹ Moreover, we have commented that the future implementation of De-NO_x materials in our cities will be a large-scale operation, therefore, the lowest cost materials must be considered. These issues have raised the interest of researchers to study new alternative photocatalytic nanomaterials to combat the NO_x pollution.

The ZnO based systems were evaluated for the photodegradation of NO_x. S. Komarneni et al. prepared several multi-cationic layered double hydroxides (Zn/Ni/La/Ti-LDH) by the hydrothermal method.¹¹⁵ The corresponding calcined products, at higher temperatures, were nickel zinc titanium oxide phases. For these, the photocatalytic activity of NO_x decomposition decreased with increasing calcination temperature, being the activation of the De-NO_x due to the formation of ZnO during calcination. Following with zinc oxide, fabrication of highly oriented ZnO nanorod/nanotube arrays over a large area of nitrogen doped titania (TiO_{2-x}N_y) nanoparticles, as visible-light-responsive photocatalyst, was reported.¹¹⁶ This nano-scale superstructure showed excellent photocatalytic activity for the decomposition of NO (under $\lambda > 290$ nm, $\lambda > 400$ nm and $\lambda > 510$ nm light irradiation) when compared with the performance of pure ZnO nanorods, nanotube, P25 and TiO_{2-x}N_y. This superior activity was explained on the basis of the unique surface features of the well-aligned

structure and the promotion and increase in the charge separation of the pair h^+/e^- done by the ZnO/TiO_{2-x}N_y heterojunction structure.

In this sense, some research groups pay attention to the preparation of visible-light nanostructured photocatalysts. Thus, a first report studied the use of bismuth oxybromide nanoplate microspheres to remove NO_x under visible light.⁷⁰ The BiOBr microspheres were synthesised with a nonaqueous sol-gel method by using bismuth (III) nitrate, cetyltrimethyl ammonium bromide and ethylene glycol. The mixture was poured into a Teflon-lined stainless and heated at 180 °C for 12 h under autogenously pressure. The surfaces of the microspheres were rough being composed of numerous radially grown nanoplates interweaving together to form a flower-like hierarchical spheres. For the purpose of comparison, the authors also prepared BiOBr bulk powders by a chemical precipitation on which a bismuth (III) acidic solution was added into an aqueous NaBr solution. The photocatalytic study was devoted to the conversion of NO, with $\lambda > 420$ nm light irradiation, at 400 parts-per-billion level, which is considered the typical concentration for indoor air quality. The microspheres exhibited superior photocatalytic activity (30% of NO removal rate in 10 minutes of irradiation) to the counterpart BiOBr bulk powder (8%), P25 and the C-doped TiO₂. The excellent catalytic activity observed is explained on the basis that the diffusion of intermediates and final products of NO oxidation was favoured with the peculiar structure of the microspheres. Following this work, the bismuth oxyhalides (BiOX; X = Cl, Br, I) are presented as promising

photocatalysts towards the De-NO_x reaction because of their interesting physical and chemical properties. Dong et al. prepared porous BiOI/BiOCl composite nanoplate microflowers with high activity for the removal of NO.¹¹⁷ Moreover, the influence of the halide type in the composition was studied in layered 2D BiOX (X = Cl, Br, I) structures.¹¹⁸ The layered structures were composed of a large quantity of smooth nanoplates stacked together. The thickness of a single nanoplate changed between compounds: 72-108 nm for Cl, 58 nm for Br and 158-216 nm for I. It was found that band gap and thermal stability of the BiOX compound decrease with increasing X atomic number. The BiOCl and BiOBr compounds exhibited more remarkable photoactivity than BiOI. Between them, the BiOBr nanoplates exhibited the highest photocatalytic activity, this being ascribed to their own physical properties (ultrathin nanoplates, layered structures, relatively high surface area) and more suitable band structure.

L. Zhang et al. reported on the use of hollow In(OH)_xS_y nanocubes to remove NO.¹¹⁹ The samples were prepared based on a solution route at low temperature of 80 °C. These exhibited porous structures, a large surface area and new valence band features explaining the best photocatalytic performance observed in comparison with the counterpart In(OH)_xS_y hydrothermally synthesised at 180 °C. UV light below 420 nm was used in the photocatalytic tests. The highest NO removal efficiency was found in the sample with S/In ratio of 1.0. Conversely, the high-activity of

Fe-loaded SrTiO₃ photocatalyst (SrTiO₃/Fe₂O₃), consisting of small particles around 50 nm in diameter, was reported.¹²⁰ Moreover, these samples were coupled with CaAl₂O₄:(Eu, Nd). The visible light responsive photocatalytic ability of SrTiO₃ was generated by Fe₂O₃. The excellent photocatalytic performance of the CaAl₂O₄:(Eu, Nd)/(SrTiO₃/Fe₂O₃) composite was tentatively ascribed to the promotion of the photogenerated electron-hole pairs. The continuously flowing NO was efficiently degraded by this composite not only under UV-Vis irradiation but also in the dark with the assistance of CaAl₂O₄:(Eu, Nd). Thus, after turning off the light, the NO destruction ability was retained for more than 160 min because SrTiO₃/Fe₂O₃ sample can absorb the fluorescence from the CaAl₂O₄:(Eu, Nd), indicating the fluorescence light-assisted photocatalytic activity of SrTiO₃/Fe₂O₃ composite. The De-NO_x ability was found maximal for the compound with 0.5 % Fe content by mol of SrTiO₃, being of around 70, 45 and 18 % under $\lambda > 290$ nm, $\lambda > 400$ nm and $\lambda > 510$ nm light irradiation, respectively.

In similar way, evidences of the photochemical ability of Fe₂O₃ towards De-NO_x reactions were previously pointed out³⁴ and afterwards corroborated in two works devoted to nanostructured iron oxide. By using the chemical vapor deposition CVD method, the selective preparation of nanostructured α - and β -Fe₂O₃ materials was done.¹²¹ The deposition temperature played a key role in tailoring the nano-organisation. Upon going from 400 to 500°C, the metastable β -Fe₂O₃ phase was converted into the most

thermodynamically stable α -Fe₂O₃ polymorph. For the β -Fe₂O₃ film the nano-organisation was characterised by the presence of interconnected pyramidal nanostructures (230 ± 30 nm), resulting from the aggregation of triangular faceted nanoparticles. In a different way, the α -Fe₂O₃ film presented rounded-like structures with an average diameter of 200 ± 50 nm, with a significantly high roughness, suggesting a correspondingly high surface area. The performances of both CVD-derived nanostructures were investigated in the NO photo-oxidation. In line with its own physical features, the photo-catalytic performance was higher for the α -Fe₂O₃ specimen. More recently, hematite (α -Fe₂O₃) was proposed as an efficient De-NO_x photocatalyst.¹²² The mechanism and capture of NO_x gases was validated for α -Fe₂O₃ nanopowders (particle size < 100 nm). The mechanism proposed follows the NO→NO₂→NO₃⁻ photo-oxidation process, from which NO and NO₂ toxic gases are retained as HNO₂/NO₃⁻ on hematite particles surface. The adsorbed product (NO₃⁻) was identified by IR spectroscopy. The nano-hematite showed a low performance for the photocatalytic process (12.5% decreases in NO concentration). However, the efficiency of hematite towards the PCO De-NO_x process was clearly enhanced by preparing C-hematite compounds (18%). More interestingly, on the C-Fe₂O₃ samples the release of NO₂ gas, produced during the PCO process, was mitigated and the total NO_x removal efficiency was as high as 17% (only 6.5% in the case of pure nano-hematite). The presence of C probably assists in the PCO process, owing to its NO-

adsorption ability and by reducing the probability of hole/electron recombination.

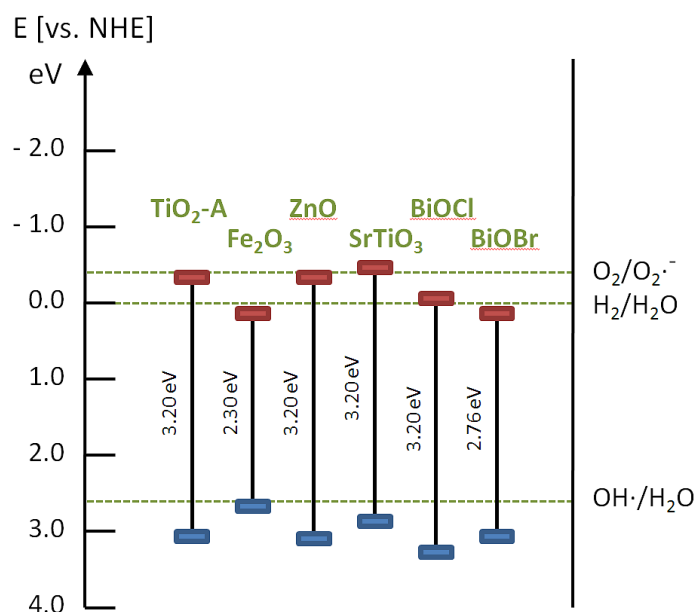


Figure 5. Band gap energy and band gap edge positions of different semiconductor oxides and oxyhalides, along with selected redox potentials.

In order to have a more fundamental view of the above commented semiconductor oxides, Figure 5 depicts their equivalent band structure diagram.

3.1.5. Conclusions

Because the presence of NO_x gases in the atmosphere cause different adverse and harmful effects, decreasing their concentration has become an obligatory and necessary task today. Some methods have been developed and implemented in order to control NO_x emissions. Between them, the photocatalysis is an innovative and promising technique, and very interesting because it is applicable to directly remove the NO_x breathable by the residents that are located in the urban centres. In this way, new de-polluting building materials capable to develop the photocatalytic oxidation (PCO) of NO_x gases are being implemented in our cities. Through the PCO mechanism, NO and NO₂ gases are oxidised to NO₃⁻ form and thus removed from the air.

Under the perspective of nanoscience new materials are developed by the researchers with the aim to enhance their photocatalytic activity towards De-NO_x processes. The main focus is devoted to TiO₂, because this oxide is the most promising photocatalyst due to its non-toxicity, strong oxidation power and chemical inertness. New advanced TiO₂ materials are prepared with higher specific surface area (SSA), different morphology and chemical modifications.

In order to increase the SSA, with the resulting enhancement of the photocatalytic activity towards De-NO_x reactions, different substrates were used to disperse the TiO₂ nanoparticles: organic and carbon fibers, mesoporous materials, clays composites, and

nanoporous microparticles. Between them, the use of activated carbon (AC)/TiO₂ composites seems to be the most promising because AC not only enhances the photocatalytic process but also facilitates the adsorption of NO molecules. On the other hand, high photocatalytic De-NO_x performances for TiO₂ were obtained by tuning the morphology and size of the nanoparticles, through the preparation of TiO₂ nanotube, self-orderer nano-tubular films and nanoparticles with the lowest size.

Conversely, various strategies such as surface deposition of metals, doping with ions or the formation of composites accounts for the chemical modification of TiO₂ with the aim to surpass its main drawback concerning the charge carrier recombination and large band gap. There is no direct relationship between the deposition of metals on the surface of TiO₂ and the photocatalytic efficiency. However, it can be said that the behaviour is accepted when the amount deposited is moderate, because of the increased oxygen vacancies arising on the surface of TiO₂. In the case of doping with ions, the compounds exhibited a better photocatalytic performance under visible light, which is related to the creation of intermediate energy states between the conduction band and the valence band. In general, the best performance against NO_x removal is due to the slower rate of the recombination reaction.

In the other hand, alternative visible light photocatalysts are reported as alternative systems to TiO₂. The ZnO/TiO_{2-x}N_y composites and bismuth oxyhalides are among the best photocatalysts working under $\lambda > 400$ nm visible light irradiation.

However, in all the cases, the performance for the NO_x removal is very low for visible light with wavelength higher than 510 nm.

Finally, it must be commented the potential use of these nanomaterials for the intended application: the preparation of urban infrastructure materials with De-NO_x ability. A first interesting issue is related to their compatibility with the hardened cement and concrete compounds. From a physic-chemical point of view, no disadvantages are expected in the use of TiO₂, ZnO and Fe₂O₃ oxides because photocatalytic cement based materials incorporating these additives have been previously reported.^{34, 123-124} Also, the substrates mentioned on this work are compatible in use with cement based materials.¹²⁵⁻¹²⁸ However, deeper research would be desired to know about the chemical interaction between cement and bismuth oxyhalides, compounds exhibiting a very attractive photocatalytic behaviour. In the other hand, the nanometric scale of the photocatalytic additives does not damage the mechanical properties.¹²⁹ Other important matter is the related to the scalability in the production of new advanced nano-photocatalyst. Thus, for their practical implementation, the new additives must be produced in large quantities at the lowest cost before entering to the built environment.

In summary, there are an interesting range of nano-materials with high potential interest for their practical application in the preparation of commercial De-NO_x products. The new challenges must be addressed to a better understanding about the PCO mechanism, the enhancing of the photochemical visible-light

activity, the development of new formulations of cement based materials including these advanced photocatalytic additives, and the scalability in their production.

Acknowledgements

This work was funded by Junta de Andalucía (Group FQM-175 and P09-FQM-4764 Project from Consejería de Innovación, Ciencia y Empresa), the European Union (P09-FQM-4764; Programa Operativo FEDER de Andalucía 2007-13) and Instituto Universitario de Química Fina y Nanoquímica (Universidad de Córdoba).

References

1. Manahan, S. E., *Environmental Chemistry, Ninth Edition*. Taylor & Francis: 2009.
2. Colls, J., *Air pollution*. 2nd ed.; Spon Press Taylor & Francis Group: London, 2002.
3. Nevers, N. d., *Air Pollution Control Engineering*. Second Edition ed.; McGraw-Hill: Illinois, 2000; p 586.
4. Newman, M. C.; Clement, W. H., Ecotoxicology. In *Ecotoxicology*, Raton, B., Ed. CRC Press: Florida, 2008.
5. Chen, B.; Hong, C.; Kan, H., Exposures and health outcomes from outdoor air pollutants in China. *Toxicology* **2004**, *198* (1–3), 291-300.
6. Morrow, P. E., Toxicological data on NO_x : An overview. *J. Toxicol. Environ. Health* **1984**, *13* (2-3), 205-227.
7. Last, J. A.; Sun, W. M.; Witschi, H., Ozone, NO, and NO₂: oxidant air pollutants and more. *Environ. Health Perspect.* **1994**, *102* (Suppl 10), 179-184.
8. Cormier, S. A.; Lomnicki, S.; Backes, W.; Dellinger, B., Origin and Health Impacts of Emissions of Toxic By-Products and Fine Particles from Combustion and Thermal Treatment of Hazardous Wastes and Materials. *Environ. Health Perspect.* **2006**, *114* (6), 810-817.
9. Frampton, M. W.; Greaves, I. A., NO_x - NO_x: Who's There? *Am. J. Respir. Crit. Care. Med.* **2009**, *179* (12), 1077-1078.

10. Williams, M. L.; Carslaw, D. C., New Directions: Science and policy – Out of step on NO_x and NO₂? *Atmos. Environ.* **2011**, *45* (23), 3911-3912.
11. Baukal, C., Everything you need to know about NO_x: Controlling and minimizing pollutant emissions is critical for meeting air quality regulations. *Met. Finishing* **2005**, *103* (11), 18-24.
12. Chen, M.; Chu, J.-W., NO_x photocatalytic degradation on active concrete road surface — from experiment to real-scale application. *Journal of Cleaner Production* **2011**, *19* (11), 1266-1272.
13. Lasek, J.; Yu, Y.-H.; Wu, J. C. S., Removal of NO_x by photocatalytic processes. *J. Photochem. Photobiol. C* **2013**, *14*, 29-52.
14. Normann, F.; Andersson, K.; Leckner, B.; Johnsson, F., Emission control of nitrogen oxides in the oxy-fuel process. *Progr. Energy Combust. Sci.* **2009**, *35* (5), 385-397.
15. Roy, S.; Hegde, M. S.; Madras, G., Catalysis for NO_x abatement. *Appl. Energy* **2009**, *86* (11), 2283-2297.
16. Pârvulescu, V. I.; Grange, P.; Delmon, B., Catalytic removal of NO. *Catal. Today* **1998**, *46* (4), 233-316.
17. Cassar, L.; Baglioni, P., *International RILEM Symposium on Photocatalysis, Environment and Construction Materials: October 8-9, 2007, Florence, Italy - Istituto degli Innocenti*. RILEM Publications: 2007.

18. Dalton, J. S.; Janes, P. A.; Jones, N. G.; Nicholson, J. A.; Hallam, K. R.; Allen, G. C., Photocatalytic oxidation of NO_x gases using TiO₂: a surface spectroscopic approach. *Environ. Pollut.* **2002**, *120* (2), 415-422.
19. Devahasdin, S.; Fan Jr, C.; Li, K.; Chen, D. H., TiO₂ photocatalytic oxidation of nitric oxide: transient behavior and reaction kinetics. *J. Photochem. Photobiol. A* **2003**, *156* (1–3), 161-170.
20. Poon, C. S.; Cheung, E., NO removal efficiency of photocatalytic paving blocks prepared with recycled materials. *Constr. Build. Mater.* **2007**, *21* (8), 1746-1753.
21. Zhao, J.; Yang, X., Photocatalytic oxidation for indoor air purification: a literature review. *Build. Environ.* **2003**, *38* (5), 645-654.
22. Ao, C. H.; Lee, S. C., Enhancement effect of TiO₂ immobilized on activated carbon filter for the photodegradation of pollutants at typical indoor air level. *Appl. Catal. B: Environ.* **2003**, *44* (3), 191-205.
23. Folli, A.; Campbell, S. B.; Anderson, J. A.; Macphee, D. E., Role of TiO₂ surface hydration on NO oxidation photo-activity. *J. Photochem. Photobiol. A* **2011**, *220* (2–3), 85-93.
24. Ballari, M. M.; Hunger, M.; Hüsken, G.; Brouwers, H. J. H., NO_x photocatalytic degradation employing concrete pavement containing titanium dioxide. *Appl. Catal. B: Environ.* **2010**, *95* (3–4), 245-254.

25. Lackhoff, M.; Prieto, X.; Nestle, N.; Dehn, F.; Niessner, R., Photocatalytic activity of semiconductor-modified cement— influence of semiconductor type and cement ageing. *Appl. Catal. B: Environ.* **2003**, *43* (3), 205-216.
26. Folli, A.; Pochard, I.; Nonat, A.; Jakobsen, U. H.; Shepherd, A. M.; Macphee, D. E., Engineering photocatalytic cements: Understanding TiO₂ surface chemistry to control and modulate photocatalytic performances. *J. Am. Ceram. Soc.* **2010**, *93* (10), 3360-3369.
27. Chen, J.; Poon, C.-S., Photocatalytic activity of titanium dioxide modified concrete materials— influence of utilizing recycled glass cullets as aggregates. *J. Environ. Manag.* **2009**, *90* (11), 3436-3442.
28. Ballari, M. M.; Hunger, M.; Hüsken, G.; Brouwers, H. J. H., Modelling and experimental study of the NO_x photocatalytic degradation employing concrete pavement with titanium dioxide. *Catal. Today* **2010**, *151* (1–2), 71-76.
29. Chen, J.; Kou, S.-c.; Poon, C.-s., Hydration and properties of nano-TiO₂ blended cement composites. *Cement and Concrete Composites* **2012**, *34* (5), 642-649.
30. Laufs, S.; Burgeth, G.; Duttlinger, W.; Kurtenbach, R.; Maban, M.; Thomas, C.; Wiesen, P.; Kleffmann, J., Conversion of nitrogen oxides on commercial photocatalytic dispersion paints. *Atmos. Environ.* **2010**, *44* (19), 2341-2349.

31. Martínez, T.; Bertron, A.; Ringot, E.; Escadeillas, G., Degradation of NO using photocatalytic coatings applied to different substrates. *Build. Environ.* **2011**, *46* (9), 1808-1816.
32. de Melo, J. V. S.; Trichês, G., Evaluation of the influence of environmental conditions on the efficiency of photocatalytic coatings in the degradation of nitrogen oxides (NO_x). *Build. Environ.* **2012**, *49*, 117-123.
33. Dillert, R.; Stötzner, J.; Engel, A.; Bahnemann, D. W., Influence of inlet concentration and light intensity on the photocatalytic oxidation of nitrogen(II) oxide at the surface of Aeroxide® TiO₂ P25. *J. Hazard. Mater.* **2012**, *211–212*, 240-246.
34. Sugrañez, R.; Cruz-Yusta, M.; Mármol, I.; Morales, J.; Sánchez, L., Preparation of Sustainable Photocatalytic Materials through the Valorization of Industrial Wastes. *ChemSusChem* **2013**, *6* (12), 2340-2347.
35. Hassan, M. M.; Dylla, H.; Mohammad, L. N.; Rupnow, T., Evaluation of the durability of titanium dioxide photocatalyst coating for concrete pavement. *Constr. Build. Mater.* **2010**, *24* (8), 1456-1461.
36. Sugrañez, R.; Álvarez, J. I.; Cruz-Yusta, M.; Mármol, I.; Morales, J.; Vila, J.; Sánchez, L., Enhanced photocatalytic degradation of NO_x gases by regulating the microstructure of mortar cement modified with titanium dioxide. *Build. Environ.* **2013**, *69*, 55-63.

37. Hunger, M.; Hüsken, G.; Brouwers, H. J. H., Photocatalytic degradation of air pollutants — From modeling to large scale application. *Cem. Concr. Res.* **2010**, *40* (2), 313-320.
38. Guerrini, G. L., Photocatalytic performances in a city tunnel in Rome: NO_x monitoring results. *Constr. Build. Mater.* **2012**, *27* (1), 165-175.
39. Kalidindi, S. B.; Jagirdar, B. R., Nanocatalysis and Prospects of Green Chemistry. *ChemSusChem* **2012**, *5* (1), 65-75.
40. Haruta, M.; Yamada, N.; Kobayashi, T.; Iijima, S., Gold catalysts prepared by coprecipitation for low-temperature oxidation of hydrogen and of carbon monoxide. *J. Catal.* **1989**, *115* (2), 301-309.
41. Tayyeb Javed, M.; Irfan, N.; Gibbs, B. M., Control of combustion-generated nitrogen oxides by selective non-catalytic reduction. *J. Environ. Manag.* **2007**, *83* (3), 251-289.
42. Liu, Z.; Ihl Woo, S., Recent advances in catalytic De-NO_x science and technology. *Catal. Rev. Sci. Eng.* **2006**, *48* (1), 43-89.
43. Muzio, L. J.; Quartucy, G. C., Implementing NO_x control: Research to application. *Progr. Energy Combust. Sci.* **1997**, *23* (3), 233-266.
44. Roy, S.; Baiker, A., NO_x storage–reduction catalysis: from mechanism and materials properties to storage–reduction performance. *Chem. Rev.* **2009**, *109* (9), 4054-4091.
45. Roy, S.; Hedge, M. S.; Madras, G., Catalysis for NO_x abatement *J. Appl. Energy* **2009**, *86* (11), 2283.

46. Skalska, K.; Miller, J. S.; Ledakowicz, S., Trends in NO_x abatement: A review. *Sci. Total Environ.* **2010**, *408* (19), 3976-3989.
47. Ângelo, J.; Andrade, L.; Madeira, L. M.; Mendes, A., An overview of photocatalysis phenomena applied to NO_x abatement. *J. Environ. Manag.* **2013**, *129*, 522-539.
48. Augustynski, J., The role of the surface intermediates in the photoelectrochemical behaviour of anatase and rutile TiO₂. *Electrochim. Acta* **1993**, *38* (1), 43-46.
49. Folli, A.; Bloh, J. Z.; Strøm, M.; Pilegaard Madsen, T.; Henriksen, T.; Macphee, D. E., Efficiency of solar-light-driven TiO₂ photocatalysis at different latitudes and seasons. Where and when does TiO₂ really work? *J. Phys. Chem. Lett.* **2014**, *5* (5), 830-832.
50. Wan, L.; Gao, Y.; Xia, X.-H.; Deng, Q.-R.; Shao, G., Phase selection and visible light photo-catalytic activity of Fe-doped TiO₂ prepared by the hydrothermal method. *Mater. Res. Bull.* **2011**, *46* (3), 442-446.
51. Chen, H.; Nanayakkara, C. E.; Grassian, V. H., Titanium dioxide photocatalysis in atmospheric chemistry. *Chem. Rev.* **2012**, *112* (11), 5919-5948.
52. Ibusuki, T., Science & Technology. In *Photocatalysis: Science & Technology*, 2003 ed.; Kaneko, M.; Okura, I., Eds. Springer: Japan, 2003; pp 143 - 155.

53. Cassar, L.; Pepe, C., Hydraulic binder and cement compositions containing photocatalyst particles. USA Patents: 2002.
54. Su, R.; Bechstein, R.; Sjø, L.; Vang, R. T.; Sillassen, M.; Esbjörnsson, B.; Palmqvist, A.; Besenbacher, F., How the anatase-to-rutile ratio influences the photoreactivity of TiO₂. *J. Phys. Chem. C* **2011**, *115* (49), 24287-24292.
55. Linsebigler, A.; Liu, G.; Yates, J., Photocatalytic degradation of the dye sulforhodamine-B: A comparative study of different light sources. *Chem. Rev* **1995**, *95*, 735-758.
56. Wade, R. S.; Castro, C. E., Reactions of oxymyoglobin with NO, NO₂, and NO₂⁻ under argon and in air. *Chem. Res. Toxicol.* **1996**, *9* (8), 1382-1390.
57. Bloh, J. Z.; Folli, A.; Macphee, D. E., Photocatalytic NO_x abatement: why the selectivity matters. *RSC Adv.* **2014**, *4* (86), 45726-45734.
58. Hashimoto, K.; Wasada, K.; Toukai, N.; Kominami, H.; Kera, Y., Photocatalytic oxidation of nitrogen monoxide over titanium(IV) oxide nanocrystals large size areas. *J. Photochem. Photobiol. A* **2000**, *136* (1-2), 103-109.
59. Hadjiivanov, K.; Knozinger, H., Species formed after NO adsorption and NO+O₂ co-adsorption on TiO₂: an FTIR spectroscopic study. *Phys. Chem. Chem. Phys.* **2000**, *2* (12), 2803-2806.

60. Haubrich, J.; Quiller, R. G.; Benz, L.; Liu, Z.; Friend, C. M., In situ ambient pressure studies of the chemistry of NO_2 and water on rutile $\text{TiO}_2(110)$. *Langmuir* **2010**, *26* (4), 2445-2451.
61. Bedjanian, Y.; El Zein, A., Interaction of NO_2 with TiO_2 surface under UV irradiation: products study. *J. Phys. Chem. A* **2012**, *116* (7), 1758-1764.
62. Goodman, A. L.; Underwood, G. M.; Grassian, V. H., Heterogeneous reaction of NO_2 : characterization of gas-phase and adsorbed products from the reaction, $2\text{NO}_{2(g)} + \text{H}_2\text{O}_{(a)} \rightarrow \text{HONO}_{(g)} + \text{HNO}_{3(a)}$ on hydrated silica particles. *J. Phys. Chem. A* **1999**, *103* (36), 7217-7223.
63. Ramazan, K. A.; Syomin, D.; Finlayson-Pitts, B. J., The photochemical production of HONO during the heterogeneous hydrolysis of NO_2 . *Phys. Chem. Chem. Phys.* **2004**, *6* (14), 3836-3843.
64. Finlayson-Pitts, B. J., Reactions at surfaces in the atmosphere: integration of experiments and theory as necessary (but not necessarily sufficient) for predicting the physical chemistry of aerosols. *Phys. Chem. Chem. Phys.* **2009**, *11* (36), 7760-7779.
65. Hüsken, G.; Hunger, M.; Brouwers, H. J. H., Experimental study of photocatalytic concrete products for air purification. *Build. Environ.* **2009**, *44* (12), 2463-2474.
66. Gustafsson, R. J.; Orlov, A.; Griffiths, P. T.; Cox, R. A.; Lambert, R. M., Reduction of NO_2 to nitrous acid on illuminated titanium dioxide aerosol surfaces: implications for

- photocatalysis and atmospheric chemistry. *Chem. Commun. (Cambridge, U. K.)* **2006**, (37), 3936-3938.
67. Yu, Q. L.; Brouwers, H. J. H., Indoor air purification using heterogeneous photocatalytic oxidation. Part I: Experimental study. *Appl. Catal. B: Environ.* **2009**, 92 (3–4), 454-461.
68. Rosseler, O.; Sleiman, M.; Montesinos, V. N.; Shavorskiy, A.; Keller, V.; Keller, N.; Litter, M. I.; Bluhm, H.; Salmeron, M.; Destailhats, H., Chemistry of NO_x on TiO₂ surfaces studied by ambient pressure XPS: products, effect of UV irradiation, water, and coadsorbed K⁺. *J. Phys. Chem. Let.* **2013**, 4 (3), 536-541.
69. Li, S.-C.; Jacobson, P.; Zhao, S.-L.; Gong, X.-Q.; Diebold, U., Trapping nitric oxide by surface hydroxyls on rutile TiO₂(110). *J. Phys. Chem. C* **2012**, 116 (2), 1887-1891.
70. Ai, Z.; Ho, W.; Lee, S.; Zhang, L., Efficient Photocatalytic Removal of NO in indoor air with hierarchical bismuth oxybromide nanoplate microspheres under visible light. *Environ. Sci. Technol.* **2009**, 43 (11), 4143-4150.
71. Szatmáry, L.; Šubrt, J.; Kalousek, V.; Mosinger, J.; Lang, K., Low-temperature deposition of anatase on nanofiber materials for photocatalytic NO_x removal. *Catal. Today* **2014**, 230, 74-78.
72. Yamabi, S.; Imai, H., Growth conditions for wurtzite zinc oxide films in aqueous solutions. *J. Mater. Chem.* **2002**, 12 (12), 3773-3778.

73. Signoretto, M.; Ghedini, E.; Trevisan, V.; Bianchi, C. L.; Ongaro, M.; Cruciani, G., TiO₂-MCM-41 for the photocatalytic abatement of NO_x in gas phase. *Appl. Catal. B: Environ.* **2010**, *95* (1–2), 130-136.
74. Shelimov, B. N.; Tolkachev, N. N.; Tkachenko, O. P.; Baeva, G. N.; Klementiev, K. V.; Stakheev, A. Y.; Kazansky, V. B., Enhancement effect of TiO₂ dispersion over alumina on the photocatalytic removal of NO_x admixtures from O₂-N₂ flow. *J. Photochem. Photobiol. A* **2008**, *195* (1), 81-88.
75. Papoulis, D.; Komarneni, S.; Panagiotaras, D.; Stathatos, E.; Toli, D.; Christoforidis, K. C.; Fernández-García, M.; Li, H.; Yin, S.; Sato, T.; Katsuki, H., Halloysite-TiO₂ nanocomposites: Synthesis, characterization and photocatalytic activity. *Appl. Catal. B: Environ.* **2013**, *132–133*, 416-422.
76. Papoulis, D.; Komarneni, S.; Panagiotaras, D.; Stathatos, E.; Christoforidis, K. C.; Fernández-García, M.; Li, H.; Shu, Y.; Sato, T.; Katsuki, H., Three-phase nanocomposites of two nanoclays and TiO₂: Synthesis, characterization and photocatalytic activities. *Appl. Catal. B: Environ.* **2014**, *147*, 526-533.
77. Nikolopoulou, A.; Papoulis, D.; Komarneni, S.; Tsohis-Katagas, P.; Panagiotaras, D.; Kacandes, G. H.; Zhang, P.; Yin, S.; Sato, T., Solvothermal preparation of TiO₂/saponite nanocomposites and photocatalytic activity. *Appl. Clay Sci.* **2009**, *46* (4), 363-368.
78. Kim, S. K.; Chang, H.; Cho, K.; Kil, D. S.; Cho, S. W.; Jang, H. D.; Choi, J.-W.; Choi, J., Enhanced photocatalytic property of

- nanoporous TiO₂/SiO₂ micro-particles prepared by aerosol assisted co-assembly of nanoparticles. *Mater. Lett.* **2011**, *65* (21–22), 3330-3332.
79. Ao, C.; Lee, S., Indoor air purification by photocatalyst TiO₂ immobilized on an activated carbon filter installed in an air cleaner. *Chem. Eng. Sci.* **2005**, *60* (1), 103-109.
80. Nguyen, N. H.; Bai, H., Photocatalytic removal of NO and NO₂ using titania nanotubes synthesized by hydrothermal method. *J. Environ. Sci.* **2014**, *26* (5), 1180-1187.
81. Kontos, A. G.; Katsanaki, A.; Likodimos, V.; Maggos, T.; Kim, D.; Vasilakos, C.; Dionysiou, D. D.; Schmuki, P.; Falaras, P., Continuous flow photocatalytic oxidation of nitrogen oxides over anodized nanotubular titania films. *Chem. Eng. J.* **2012**, *179*, 151-157.
82. Chin, S.; Park, E.; Kim, M.; Jeong, J.; Bae, G.-N.; Jurng, J., Preparation of TiO₂ ultrafine nanopowder with large surface area and its photocatalytic activity for gaseous nitrogen oxides. *Powder Technol.* **2011**, *206* (3), 306-311.
83. Di Paola, A.; Bellardita, M.; Palmisano, L.; Amadelli, R.; Samiolo, L., Preparation and photoactivity of nanocrystalline TiO₂ powders obtained by thermohydrolysis of TiOSO₄. *Catal. Lett.* **2013**, *143* (8), 844-852.
84. Asahi, R.; Morikawa, T.; Ohwaki, T.; Aoki, K.; Taga, Y., Visible-Light Photocatalysis in Nitrogen-Doped Titanium Oxides. *Science* **2001**, *293* (5528), 269.

85. Huang, Y.; Ho, W.; Lee, S.; Zhang, L.; Li, G.; Yu, J. C., Effect of carbon doping on the mesoporous structure of nanocrystalline titanium dioxide and its solar-light-driven photocatalytic degradation of NO_x. *Langmuir* **2008**, *24* (7), 3510-3516.
86. Lee, S.-H.; Yamasue, E.; Okumura, H.; Ishihara, K. N., Effect of oxygen and nitrogen concentration of nitrogen doped TiO_x film as photocatalyst prepared by reactive sputtering. *Appl. Catal. A: Gen.* **2009**, *371* (1–2), 179-190.
87. Wang, Y.; Huang, Y.; Ho, W.; Zhang, L.; Zou, Z.; Lee, S., Biomolecule-controlled hydrothermal synthesis of C–N–S-tridoped TiO₂ nanocrystalline photocatalysts for NO removal under simulated solar light irradiation. *J. Hazard. Mater.* **2009**, *169* (1–3), 77-87.
88. P. Blöß, S.; Elfenthal, L., Doped titanium dioxide as a photocatalyst for UV and visible light. In *International RILEM Symposium on Photocatalysis, Environment and Construction Materials - TDP 2007*, Cassar, P. B. a. L., Ed. RILEM Publications SARL: 2007; pp 31 - 38.
89. Devi, L. G.; Kavitha, R., A review on non metal ion doped titania for the photocatalytic degradation of organic pollutants under UV/solar light: Role of photogenerated charge carrier dynamics in enhancing the activity. *Appl. Catal. B: Environ.* **2013**, *140–141*, 559-587.
90. Zhang, P.; Yin, S.; Sato, T., The influence of synthesis method on the properties of iron contained N doped TiO₂

- photocatalysts. *Appl. Catal. B: Environ.* **2011**, *103* (3–4), 462–469.
91. Banerjee, S.; Pillai, S. C.; Falaras, P.; O’Shea, K. E.; Byrne, J. A.; Dionysiou, D. D., New Insights into the Mechanism of Visible Light Photocatalysis. *J. Phys. Chem. Lett.* **2014**, *5* (15), 2543–2554.
92. Bajnóczi, É. G.; Balázs, N.; Mogyorósi, K.; Srankó, D. F.; Pap, Z.; Ambrus, Z.; Canton, S. E.; Norén, K.; Kuzmann, E.; Vértes, A.; Homonnay, Z.; Oszkó, A.; Pálincó, I.; Sipos, P., The influence of the local structure of Fe(III) on the photocatalytic activity of doped TiO₂ photocatalysts—An EXAFS, XPS and Mössbauer spectroscopic study. *Appl. Catal. B: Environ.* **2011**, *103* (1–2), 232–239.
93. Kominami, H.; Sumida, K.; Yamamoto, K.; Kondo, N.; Hashimoto, K.; Kera, Y., Visible-light-induced oxidative removal of nitrogen oxides in air by metal chloride-modified titanium (IV) oxide nanoparticles. *Res. Chem. Intermed.* **2008**, *34* (5), 587–601.
94. Kočí, K.; Krejčíková, S.; Šolcová, O.; Obalová, L., Photocatalytic decomposition of N₂O on Ag-TiO₂. *Catal. Today* **2012**, *191* (1), 134–137.
95. Fujishima, A.; Zhang, X.; Tryk, D. A., TiO₂ photocatalysis and related surface phenomena. *Surf. Sci. Rep.* **2008**, *63* (12), 515–582.
96. Bloh, J. Z.; Folli, A.; Macphee, D. E., Adjusting nitrogen doping level in titanium dioxide by codoping with tungsten:

- properties and band structure of the resulting materials. *J. Phys. Chem. C* **2014**, *118* (36), 21281-21292.
97. Pelaez, M.; Nolan, N. T.; Pillai, S. C.; Seery, M. K.; Falaras, P.; Kontos, A. G.; Dunlop, P. S. M.; Hamilton, J. W. J.; Byrne, J. A.; O'Shea, K.; Entezari, M. H.; Dionysiou, D. D., A review on the visible light active titanium dioxide photocatalysts for environmental applications. *Appl. Catal. B: Environ.* **2012**, *125*, 331-349.
98. Amadelli, R.; Samiolo, L.; Borsa, M.; Bellardita, M.; Palmisano, L., N-TiO₂ Photocatalysts highly active under visible irradiation for NO_x abatement and 2-propanol oxidation. *Catal. Today* **2013**, *206*, 19-25.
99. Treschev, S. Y.; Chou, P.-W.; Tseng, Y.-H.; Wang, J.-B.; Perevedentseva, E. V.; Cheng, C.-L., Photoactivities of the visible-light-activated mixed-phase carbon-containing titanium dioxide: The effect of carbon incorporation. *Appl. Catal. B: Environ.* **2008**, *79* (1), 8-16.
100. Tseng, Y.-H.; Kuo, C.-H., Photocatalytic degradation of dye and NO_x using visible-light-responsive carbon-containing TiO₂. *Catal. Today* **2011**, *174* (1), 114-120.
101. Yin, S.; Komatsu, M.; Zhang, Q.; Saito, F.; Sato, T., Synthesis of visible-light responsive nitrogen/carbon doped titania photocatalyst by mechanochemical doping. *J. Mater. Sci.* **2007**, *42* (7), 2399-2404.

102. Yuan, J.; Wang, E.; Chen, Y.; Yang, W.; Yao, J.; Cao, Y., Doping mode, band structure and photocatalytic mechanism of B–N-codoped TiO₂. *Appl. Surf. Sci.* **2011**, *257* (16), 7335-7342.
103. Todorova, N.; Vaimakis, T.; Petrakis, D.; Hishita, S.; Boukos, N.; Giannakopoulou, T.; Giannouri, M.; Antiohos, S.; Papageorgiou, D.; Chaniotakis, E.; Trapalis, C., N and N,S-doped TiO₂ photocatalysts and their activity in NO_x oxidation. *Catal. Today* **2013**, *209*, 41-46.
104. Ni, M.; Leung, M. K. H.; Leung, D. Y. C.; Sumathy, K., A review and recent developments in photocatalytic water-splitting using for hydrogen production. *Renew. Sust. Energ. Rev.* **2007**, *11* (3), 401-425.
105. Inturi, S. N. R.; Boningari, T.; Suidan, M.; Smirniotis, P. G., Visible-light-induced photodegradation of gas phase acetonitrile using aerosol-made transition metal (V, Cr, Fe, Co, Mn, Mo, Ni, Cu, Y, Ce, and Zr) doped TiO₂. *Appl. Catal. B: Environ.* **2014**, *144*, 333-342.
106. Takeuchi, M.; Matsuoka, M.; Anpo, M., Ion engineering techniques for the preparation of the highly effective TiO₂ photocatalysts operating under visible light irradiation. *Res. Chem. Intermed.* **2012**, *38* (6), 1261-1277.
107. Hsiao, Y.-C.; Tseng, Y.-H. Preparation of Pd-containing TiO₂ film and its photocatalytic properties *Micro Nano Lett.* 2010, p. 317-320.
108. Roy, S.; Hegde, M. S.; Ravishankar, N.; Madras, G., Creation of redox adsorption sites by Pd²⁺ ion substitution in nano TiO₂

- for high photocatalytic activity of CO oxidation, NO reduction, and NO decomposition. *J. Phys. Chem. C* **2007**, *111* (23), 8153-8160.
109. Wu, Z.; Sheng, Z.; Liu, Y.; Wang, H.; Tang, N.; Wang, J., Characterization and activity of Pd-modified TiO₂ catalysts for photocatalytic oxidation of NO in gas phase. *J. Hazard. Mater.* **2009**, *164* (2–3), 542-548.
110. Huang, C.-H.; Wang, I. K.; Lin, Y.-M.; Tseng, Y.-H.; Lu, C.-M., Visible light photocatalytic degradation of nitric oxides on PtO_x-modified TiO₂ via sol–gel and impregnation method. *J. Mol. Catal. A: Chem.* **2010**, *316* (1–2), 163-170.
111. Bellardita, M.; Addamo, M.; Di Paola, A.; Marci, G.; Palmisano, L.; Cassar, L.; Borsa, M., Photocatalytic activity of TiO₂/SiO₂ systems. *J. Hazard. Mater.* **2010**, *174* (1–3), 707-713.
112. Li, Q.; Yang, H.; Qiu, F.; Zhang, X., Promotional effects of carbon nanotubes on V₂O₅/TiO₂ for NO_x removal. *J. Hazard. Mater.* **2011**, *192* (2), 915-921.
113. Kim, J. Y.; Kim, C. S.; Chang, H. K.; Kim, T. O., Synthesis and characterization of N-doped TiO₂/ZrO₂ visible light photocatalysts. *Adv. Powder Technol.* **2011**, *22* (3), 443-448.
114. Pan, X.; Yang, M.-Q.; Fu, X.; Zhang, N.; Xu, Y.-J., Defective TiO₂ with oxygen vacancies: synthesis, properties and photocatalytic applications. *Nanoscale* **2013**, *5* (9), 3601-3614.
115. Sarkarat, M.; Komarneni, S.; Rezvani, Z.; Wu, X.; Yin, S.; TsugioSato; Yan, Z.-F., Multi-cationic layered double

- hydroxides: Calcined products as photocatalysts for decomposition of NO_x. *Appl. Clay Sci.* **2013**, *80–81*, 390-397.
116. Huang, Y.; Wei, Y.; Wu, J.; Guo, C.; Wang, M.; Yin, S.; Sato, T., Low temperature synthesis and photocatalytic properties of highly oriented ZnO/TiO₂-xNy coupled photocatalysts. *Appl. Catal. B: Environ.* **2012**, *123–124*, 9-17.
117. Dong, F.; Sun, Y.; Fu, M.; Wu, Z.; Lee, S. C., Room temperature synthesis and highly enhanced visible light photocatalytic activity of porous BiOI/BiOCl composites nanoplates microflowers. *J. Hazard. Mater.* **2012**, *219–220*, 26-34.
118. Zhang, W.; Zhang, Q.; Dong, F., Visible-light photocatalytic removal of NO in air over BiOX (X = Cl, Br, I) single-crystal nanoplates prepared at room temperature. *Ind. Eng. Chem. Res.* **2013**, *52* (20), 6740-6746.
119. Ge, S.; Zhang, L., Efficient visible light driven photocatalytic removal of RhB and NO with low temperature synthesized In(OH)_xSy hollow nanocubes: a comparative study. *Environ. Sci. Technol.* **2011**, *45* (7), 3027-3033.
120. Li, H.; Yin, S.; Wang, Y.; Sato, T., Microwave-assisted hydrothermal synthesis of Fe₂O₃-sensitized SrTiO₃ and its luminescent photocatalytic De-NO_x activity with CaAl₂O₄:(Eu, Nd) Assistance. *J. Am. Ceram. Soc.* **2013**, *96* (4), 1258-1262.
121. Carraro, G.; Sugrañez, R.; Maccato, C.; Gasparotto, A.; Barreca, D.; Sada, C.; Cruz-Yusta, M.; Sánchez, L., Nanostructured iron(III) oxides: From design to gas- and

- liquid-phase photo-catalytic applications. *Thin Solid Films* **2014**, *564*, 121-127.
122. Sugrañez, R.; Balbuena, J.; Cruz-Yusta, M.; Martín, F.; Morales, J.; Sánchez, L., Efficient behaviour of hematite towards the photocatalytic degradation of NO_x gases. *Appl. Catal. B: Environ.* **2015**, *165*, 529-536.
123. Chen, J.; Poon, C.-s., Photocatalytic construction and building materials: From fundamentals to applications. *Build. Environ.* **2009**, *44* (9), 1899-1906.
124. Senff, L.; Tobaldi, D. M.; Lemes-Rachadel, P.; Labrincha, J. A.; Hotza, D., The influence of TiO₂ and ZnO powder mixtures on photocatalytic activity and rheological behavior of cement pastes. *Constr. Build. Mat.* **2014**, *65*, 191-200.
125. Badanoiu, A.; Holmgren, J., Cementitious composites reinforced with continuous carbon fibres for strengthening of concrete structures. *Cement Concrete Comp.* **2003**, *25* (3), 387-394.
126. Zhao, S.; Li, G. Z.; Cao, Y.; Tian, Y., Effect of polypropylene fiber and polymer emulsion on the performance of cement mortar. *J. Build. Mat.* **2007**, *6*, 004.
127. Barbhuiya, S.; Mukherjee, S.; Nikraz, H., Effects of nano-Al₂O₃ on early-age microstructural properties of cement paste. *Constr. Build. Mat.* **2014**, *52*, 189-193.
128. Tregger, N. A.; Pakula, M. E.; Shah, S. P., Influence of clays on the rheology of cement pastes. *Cem. Concr. Res.* **2010**, *40* (3), 384-391.

129. Meng, T.; Yu, Y.; Qian, X.; Zhan, S.; Qian, K., Effect of nano-TiO₂ on the mechanical properties of cement mortar. *Constr. Build. Mat.* **2012**, *29*, 241-245.

3.2. Enhanced activity of α -Fe₂O₃ for the photocatalytic NO removal



RSC Advances

PAPER

Enhanced activity of α -Fe₂O₃ for photocatalytic NO removal†

J. Balbuena,^a M. Cruz-Yusta,^a A. L. Cuevas,^b M. C. López-Escalante,^c F. Martín,^c A. Pastor^a and L. Sánchez^{*a}

A unique electrospun α -Fe₂O₃ nanofiber catalyst was obtained. The fibers are hollow and built by flat nanocrystals with {001} and {012} facets. The nanocrystals are assembled as a mosaic with all of the facets mainly constituting the total surface area, with a value of 22.1 m² g⁻¹. These peculiar fibers exhibited outstanding photocatalytic efficiency towards the NO gas oxidation compared to nanometric hematite powders.



Cite this: *RSC Adv.*, 2016, 6, 92917

Received 28th July 2016
Accepted 23rd September 2016

DOI: 10.1039/c6ra19167c

www.rsc.org/advances

3.2.1. Introduction

Atmospheric pollution has been recognised as one of the most serious environmental problems. Even though intense regulations have been declared by the USA and Europe in order to limit the presence of NO_x in the atmosphere, the recommended maximum amount of breathable NO_x is usually surpassed in the centre of large cities.¹⁻² Thus, decreasing the atmospheric concentration of nitrogen oxides ($\text{NO}_x = \text{NO} + \text{NO}_2$), De- NO_x action, has become an obligatory and necessary task. Over the past ten years, the photocatalytic oxidation (PCO) of NO_x emissions has proven to be an available technology.³⁻⁷ By using TiO_2 as an efficient photocatalyst, NO_x oxidation is promoted by using atmospheric oxygen, water, and UV-A radiation.⁸ This is the basis for the preparation of de-polluting building materials such as photocatalytic pavements, cement, mortars, and paints, a strategy which is used to combat NO_x .⁹ Therefore, in order to reach De- NO_x materials with competitive costs for their commercialisation, the search for low-cost catalysts with improved photocatalytic efficiency is desired.

The present work is devoted to the preparation of a unique 1D nanoarchitecture of iron oxide (III), hematite phase ($\alpha\text{-Fe}_2\text{O}_3$), as an efficient alternative choice for De- NO_x photocatalyst. $\alpha\text{-Fe}_2\text{O}_3$ is eligible for practical photochemical applications because its abundance and environmentally

benign nature, being the most stable iron oxide with n-type semiconducting properties under ambient conditions, exhibiting a 1.9–2.2 eV band gap to absorb visible light – in contrast to TiO₂ which only absorbs UV light –, and outstanding photocatalytic performances were found through the preparation of nanoarchitectures.¹⁰⁻¹⁵ Recently, our research group has reported the ability of hematite as a De-NO_x photocatalyst, but the efficiency was not as high as desired.¹⁶ As a way to increase its efficiency as a photocatalyst¹⁷, this study pays attention to the preparation of α -Fe₂O₃ nanofibers through the use of the electrospinning technique. Ceramic nanofibers generated by electrospinning, including α -Fe₂O₃, have found a wide variety of applications in catalysis, the environment and energy.¹⁸⁻²⁰ However, to the best of our knowledge, only a very few works in the recent literature have reported on the preparation of pure electrospun α -Fe₂O₃ fibers or nanotubes for photocatalysis.²⁰⁻²⁴ With regard to morphology, three types of Hematite Electrospun Fibers (HEF) can be distinguished: solid, hollow and porous.²⁵⁻³⁵ With relation to the synthetic procedure employed, the nanometric scale is not usually reached and fibers with a diameter lower than 100 nm are scarcely obtained.^{25, 27, 31-32, 34} The HEF presented in this work combine two peculiar features for the first time: nanometric diameter (< 55 nm) and the presence of well-defined nanocrystals constituting the fibers walls. These

features are important for photocatalysis. By promoting the 1D shape – with a lower diameter – the electron transport is enhanced.³⁶ This will help to decrease the electron/hole recombination, which results enough fast for α -Fe₂O₃.¹⁰ Conversely, the surface of the photocatalyst is constituted of flat nanocrystals with well-defined facets all of them exposed to contact with the reactant gas molecule.³⁷

3.2.2. Materials and methods

Preparation of samples

The α -Fe₂O₃ nanofibers were obtained by electrospinning at 15 kV using a BERTAN power source 225-30R model with negative polarity in the active electrode. The solution was 10% in weight of Iron II nitrate nona-hydrate in PVP (Polyvinylpyrrolidone, average mol. wt. 10.000), and dissolved in 40 mL of ethanol and 10 mL H₂O. A fast thermal treatment was performed by introducing the as-obtained electrospun PVP fibres in a preheated oven at 350 °C in order to avoid melting creep and sticking, followed by a heating ramp of 15 °C min⁻¹ to 650 °C and kept at this temperature for 3 h. For comparison purposes, standard hematite nanopowders (HNP) were obtained through calcination of nano-Fe₂O₃ maghemite phase [<50 nm, iron(III) oxide, Aldrich] at 600 °C for 4 h.

Instrumentation

The identification of crystalline phases was achieved using X-ray diffraction (XRD) on a PANalytical X'Pert PRO MPD with CuK_{α1,2} radiation. Scanning electron microscopy (SEM) images were obtained with a FEI Helios Nanolab 650 FESEM. Nitrogen absorption isotherms were obtained at 77.4 K on an ASAP 2020 instrument from Micromeritics. Specific surface areas were calculated from N₂ sorption isotherms, using the multipoint Brunauer-Emmett-Teller (BET) method; microporosity and size distributions were estimated using the t-plot, Barret-Joyner-Halenda (BJH) method. Infrared spectra (IR) were obtained by Attenuated Total Reflectance (ATR) using a ATR System Vertex-70 of BRUKER. Raman spectra were recorded by Raman Spectrometer (SENTERRA) with confocal microscope (Olympus BX series) using 785 nm to avoid fluorescence.

X-ray photoelectron spectra, XPS, were recorded using non-monochromated MgK_α radiation ($h\nu = 1253.6$ eV) and a hemispherical analyser operating at a constant pass energy of 29.35 eV (Physical Electronics PHI 5700 spectrometer). Binding energies were corrected against that for C1s peak of adventitious carbon fixed at 284.8 eV, before etching with 4 KeV Ar⁺ ions, and for O 1s at 530 eV.³⁸ Survey spectra over the range 0–1100 eV were recorded at a 187.85 pass energy. Spectra were recorded after each minute of Ar etching.

Spectral data were processed by PHI-ESCA V8.0c and Multipack V9.3 software (Physical Electronics). The deconvolution of the Fe 3p XPS region was carried out considering the Fe 3p_{3/2} peak at 55.6 eV.³⁹

Photocatalysis

The photocatalytic activity of the materials towards the oxidation of NO was studied by using a 50 x 50 mm sample holder placed in a laminar flow reactor. A 10 mg sample was used in each photocatalytic test. Artificial sunlight from a Solarbox 3000e RH – 25 and 580 W m⁻² for UV and Visible irradiances, respectively – was used as irradiation. The accurate measurement of the concentration of NO was carried out using a chemiluminescence analyser (model Environnement AC32M). A mixture of air/NO was sent to the photoreactor. Air and NO gas streams were mixed to obtain the desired NO concentration: 150 ppb.^{13, 16, 40-41} This NO content is representative of NO concentrations found during intense photochemical pollution events in urban environments.⁴² Previously, air was conveyed by a gas-washing bottle, filled with demineralised water in order to keep the relative humidity of the supplied gas fixed at 50 ± 5 %. A flow rate, Q, of 0.30 L min⁻¹ was employed. For each test, the air/NO gas stream ran over the sample in the dark for a period of 10 min without changes in the NO concentration profiles were observed, discarding the NO adsorption on the sample surface or its direct photolysis. Subsequently, the

photoreactor was irradiated for 30 min. The tests were repeated three times to obtain average concentration values. The calculated standard deviation is ± 0.3 ppb conversion, NO₂ Released and NO_x concentration.

3.2.3. Results and discussion

The electrospun Fe(NO₃)₃-PVP (Polyvinylpyrrolidone) precursor fibers resulted in an average diameter of about 120 nm, Fig. S1 (Supplementary Information). After calcination at 650 °C, Fig. 1, the HEF were hollow with an external diameter in the range from 35-55 nm and an internal diameter as an increasing percentage of the external diameter when the latter is increased (Fig. S2). The fibers are constituted of a mosaic of plate-like nanocrystals of 30–70 nm in size sintered around the longitudinal axis.

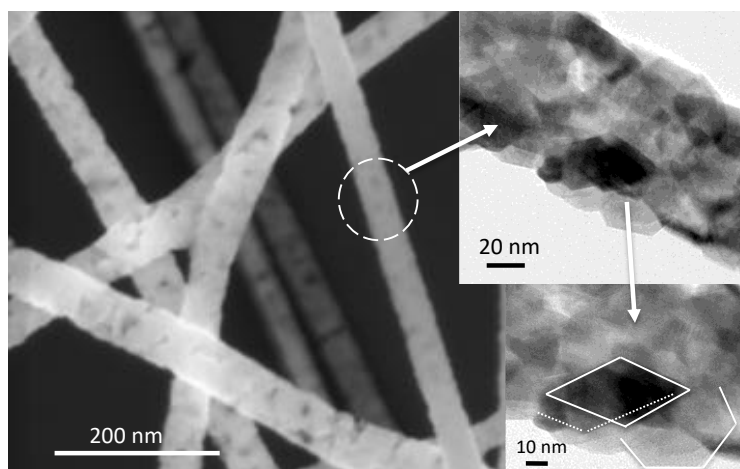
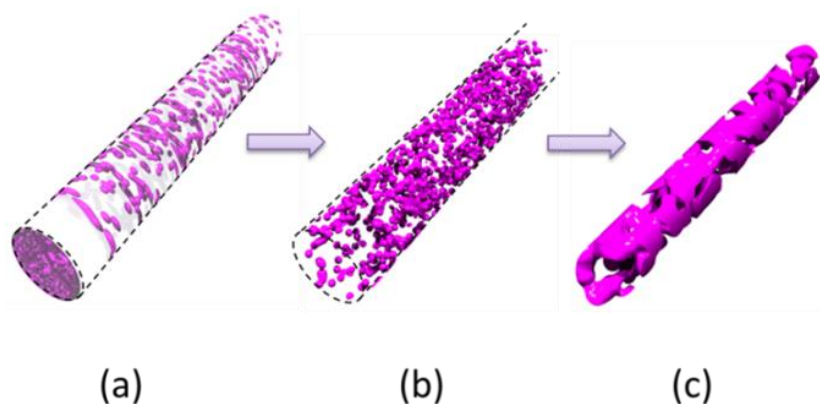


Figure 1. SEM/HRTEM images of the HEF sample. Detail of the rhombohedral and hexagonal nanocrystals.

The fast removal of PVP occurs according to the very high heating rate programmed. Following the loss of solvent, the fiber shrinks, causing precipitation of the Fe_2O_3 on the surface of the fiber. When the rate of the gas released from PVP decomposition is larger than that of gas diffusion through the fiber surface, the pressure inside the fibers increases to become larger than that outside the composite fibers; consequently, hollow fibers are obtained.²⁶ A probable growth route is illustrated in Scheme 1.



Scheme 1. Schematic diagram of the morphological evolution of the porous HEF nanofibers. (a) Particles of Fe_2O_3 precursor inside of the PVP nanofiber as obtained by electrospinning. (b) The Fe_2O_3 precipitate near of the surface when the nanofiber is shrinking due to drying and calcination processes. (c) The nanocrystals particles of Fe_2O_3 fused together to form a hollow cylindrical shell.

The nanocrystals were hexagonal in shape – {001} facet –, but in some cases, rhombohedral – {012} facet –, Fig. 1. It was reported that the exposed facets of nanocrystals are thermodynamically determined by the supersaturation of monomers during crystal growth. The facets with high surface energy are favoured in a high supersaturation solution, and stable facets with low surface energy are usually dominated in nanocrystals formed at a state of equilibrium with relatively low supersaturation solution.⁴³ By considering that, for α -Fe₂O₃, the surface energy of {001} is lower than that of {012}^{37, 44}, low supersaturation solution conditions would be reached with the synthetic route employed. On the other hand, surfactants are often applied to restrict crystal growth in some directions through preferential absorption, thereby promoting relative growth on other crystal faces. Conversely, through interactions between surface hydroxyl groups on oxides and the hydroxyl groups/lactim groups of PVP, the α -Fe₂O₃ nanocrystals can be stabilised.⁴⁵ On this basis, and following our experimental procedure, the formation of monodispersed crystals forming a mosaic and avoiding the agglomeration of nanocrystals observed in other previously reported α -Fe₂O₃ fibers could be explained³¹.

Fig. 2a shows the XRD patterns of HEF corresponding to rhombohedral α -Fe₂O₃ [PDF card No. 00-33-0664]. Hematite can also be easily distinguished from other iron oxides or

hydroxides using Raman spectroscopy. Seven optical modes of even symmetry ($2A_{1g} + 5E_g$) are expected in the Raman spectrum of $\alpha\text{-Fe}_2\text{O}_3$, all of which are shown in the Raman spectra of the HEF nanofibers (Fig. 2b); A_{1g} at 226, 496 cm^{-1} , and E_g at 245, 293, 299, 411 and 612 cm^{-1} .⁴⁶⁻⁴⁷ No other peaks were detected, indicating that the sample is free from other iron oxides and iron oxyhydroxides.

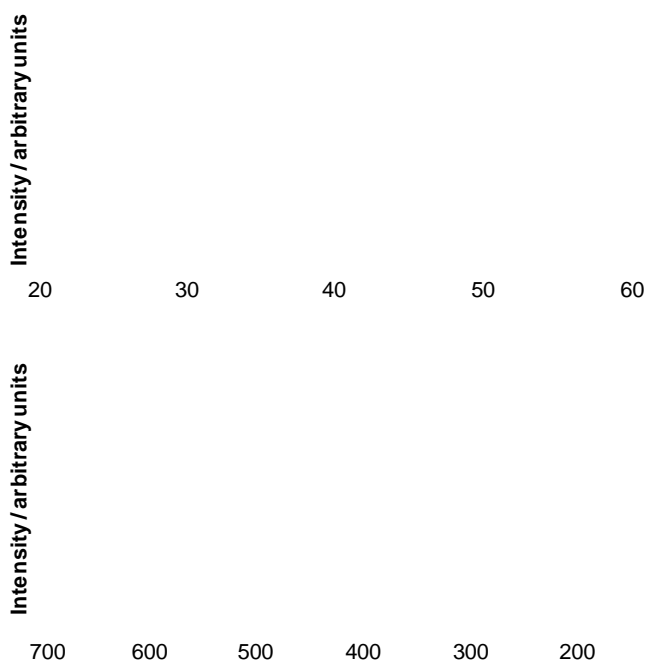


Figure 2. (a) XRD pattern and (b) Raman spectra obtained for the HEF sample.

The chemical composition was also confirmed by XPS. The spectrum of the Fe 2p region exhibits broad $2p_{1/2}$ and $2p_{3/2}$ signals, (Fig. 3a). The observed positions were at 725.4 and

711.3 eV, which correspond to that reported for 2p_{1/2} and 2p_{3/2} signals, respectively, of Fe³⁺ in Fe₂O₃.^{38, 48} The presence and position of the shake-up satellite pattern of the Fe 2p region is also sensitive to the oxidation state. As expected for Fe₂O₃, the satellite signal appeared to be 8 eV higher than the main Fe 2p_{3/2} peak (719.2 eV), whereas a signal at around 715 eV would be expected for the existence of Fe²⁺.⁴⁸

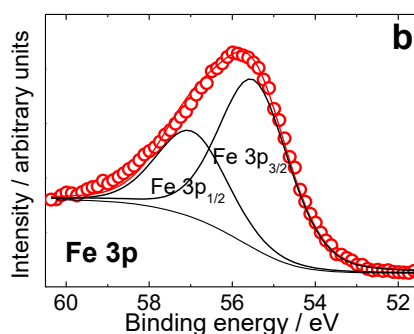


Figure 3. XPS spectra - (a) Fe 2p and (b) Fe 3p signals - obtained for the HEF sample.

The Fe 3p XPS region (Fig. 3b) shows only one peak because the XPS spectrometer does not have the resolution to resolve the 3p_{1/2} and 3p_{3/2} signals. By deconvolution, the binding-energy value for Fe³⁺ 3p_{3/2} of 55.6 eV was obtained. With regard to the optical properties of HEF samples, the acquired diffuse reflectance spectra was converted to the Kubelka-Munk transformation – $F(R) = (1 - R)^2 / (2R) = F(R_\infty) -$; $F(R_\infty)$ is the so-called Kubelka-Munk function, and R the reflectance. For a direct band semiconductor $[F(R_\infty) h\nu]^2 = C$

$(h\nu - E_g)$, and plotting $[F(R_\infty) h\nu]^2$ against $h\nu$, the band gap E_g of the HEF was calculated as 2.15 eV (Fig. S3), with this value being very close to the expected 2.2 eV for bulk $\alpha\text{-Fe}_2\text{O}_3$.¹⁶

Subsequently, we applied the HEF sample in the framework of photocatalytic processes for atmospheric remediation, specifically the NO removal. To this aim, it is of interest to achieve the complete oxidation of NO to nitrate or nitric acid ($\text{NO}_3^-/\text{HNO}_3$), a complex process that involves several intermediate species.^{3, 13, 16, 49-50} Basically, the mechanism entails several one-electron transfer steps, *via* nitrous acid (HNO_2) and nitrogen dioxide (NO_2) as intermediate species.⁵ As the $\alpha\text{-Fe}_2\text{O}_3$ nanocrystals are irradiated by UV–vis light, an electron in the valence band (VB) acquires the energy of a photon to become a photogenerated electron (e^-), which migrates to the conduction band (CB) and simultaneously leaves behind a photogenerated hole (h^+), as it is shown in reaction (1).⁵¹ The pair of mobile charges produced can reach the surface of the semiconductor particle and, in contact with oxygen and water molecules – reactions (2) and (3) –, assist in the formation of reactive oxygen species (ROS) which initiate the progressive oxidation of NO gas.⁵²⁻⁵³ The hydroxyl radicals ($\text{OH}\bullet$) lead to the oxidation of NO to NO_2 which, in turns, produce nitrite and nitrate ions, reactions (4) to (7). On the other hand, the superoxide radical can participate in the final

oxidation of nitrogen oxide gases to nitrate ions, reactions (8) and (9).¹⁶

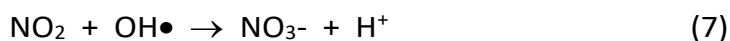
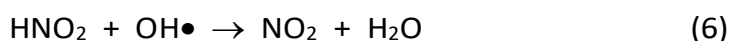
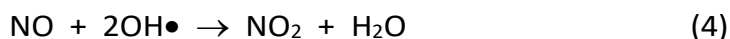
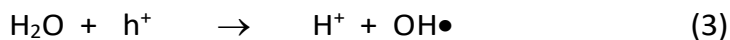


Fig. 4a shows the nitric oxide (NO) concentration profile obtained during the NO oxidation test under UV–vis light irradiation. In the absence of UV–vis light irradiation, the concentration of NO was kept constant. Under irradiation, because activation of the $\alpha\text{-Fe}_2\text{O}_3$ sites occurred, the heterogeneous photocatalytic reaction took place and the oxidation of the pollutant began. When the irradiation was off, the NO concentration slowly returned to its initial value.

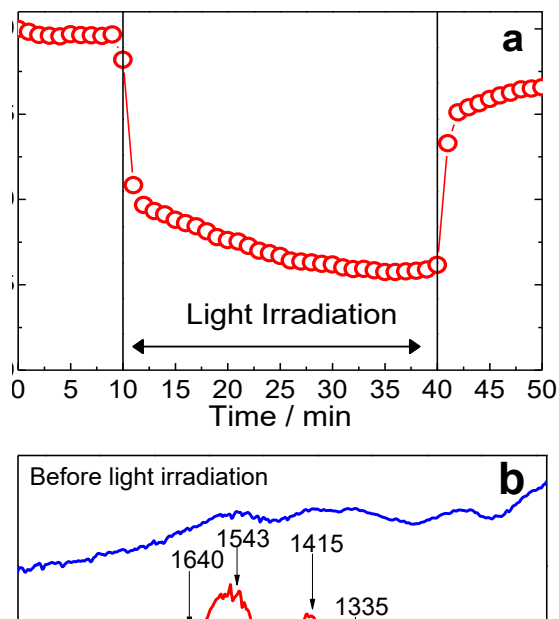


Figure 4. (a) Concentration profile evolution obtained during the photochemical degradation of NO gas over the HEF sample. (b) IR spectra obtained for HEF sample before and after light irradiation.

To gain more of an insight into the photocatalytic reaction mechanism, IR spectra of the HEF sample, before and after irradiation, were measured to investigate the presence of adsorbed products (Fig. 4b). Before irradiation (in the dark), no bands concerning N–O vibration modes were detected. New bands in the $1000\text{--}1600\text{ cm}^{-1}$ range appear in the spectra

obtained after irradiation. The band located at 1543 cm⁻¹ corresponds to vibrations of nitrate species, while those at 1415 and 1335 cm⁻¹ are assigned to the presence of nitrite anions. The lowest bands at 1150 and 1041 cm⁻¹ must be tentatively assigned to bridging ions⁵⁴⁻⁵⁶.

The low intensity band at 1640 cm⁻¹ corresponds to the existence of large numbers of residual hydroxyl groups, which imply the O–H vibrating mode of traces of adsorbed water. Finally, the identification of NO₂⁻/NO₃⁻ species occurred, confirming that the photocatalytic oxidation of NO and removal of NO_x gases took place.

Even though the accumulation of nitrite/nitrate compounds on HEF surface would deactivate the photocatalyst during the photocatalytic process, this kind of slight deactivation is easily regenerated by washing the photocatalyst with water.^{16, 57-59}

On this sense, we have preliminarily evaluated the stability/reusability of HEF sample, Fig. S4. No obvious loss of the photocatalytic activity was observed during the first few cycles of reutilization indicating the good regeneration of HEF photocatalyst. Between experiments, the photocatalyst was washed in order to eliminate the nitrite/nitrate species.

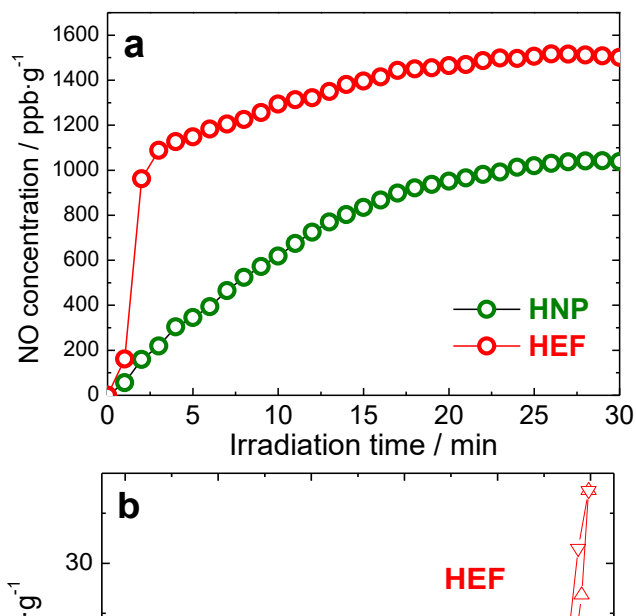


Figure 5. (a) Specific NO gas removal measured for HEF and HNP samples. (b) Nitrogen adsorption-desorption isotherm of HEF and HNP samples.

Fig. 5a shows the specific amount of NO oxidised by the mass of photocatalyst, which progressively increased, reaching an almost constant level of 1500 ppb g^{-1} for irradiation times >20 min. For comparison purposes, the NO photo-oxidation efficiency of $\alpha\text{-Fe}_2\text{O}_3$ nano-powders – HNP sample – was

studied. The SEM/TEM images (Fig. S5) show that the HNP sample is constituted of agglomerates of round nanoparticles with a size of 40–100 nm. Even though the particle size was similar to that of HEF sample, the efficiency of NO removal (Fig. 5a) significantly decreased.

Thus, the amount of NO gas removed after 30 minutes of light irradiation was only 1050 ppb g⁻¹, 30% lower than that found for HEF samples. This difference could be mainly ascribed to the highest surface area of the HEF system (Fig. 5b). A value of 22.1 m² g⁻¹ was measured (similarly to other iron oxide electrospun fibers) in comparison to that of 5.1 m² g⁻¹ for the NH sample.^{20, 23} Therefore, it should be highlighted that the effective surface area plays a key role in determining the system reactivity.

It is known that photocatalytic degradation of NO molecules on metal oxides follows first-order kinetics.¹⁶ This behaviour is also confirmed by the present data, evidencing a linear plot of ln(C/C₀) vs. irradiation time (Fig. 6). The initial rate constants of NO degradation over hematite oxide were estimated to be 9.0 10⁻³ and 7.6 10⁻⁴ min⁻¹ for HEF and HNP samples, respectively, showing the highest activity for the HEF sample.

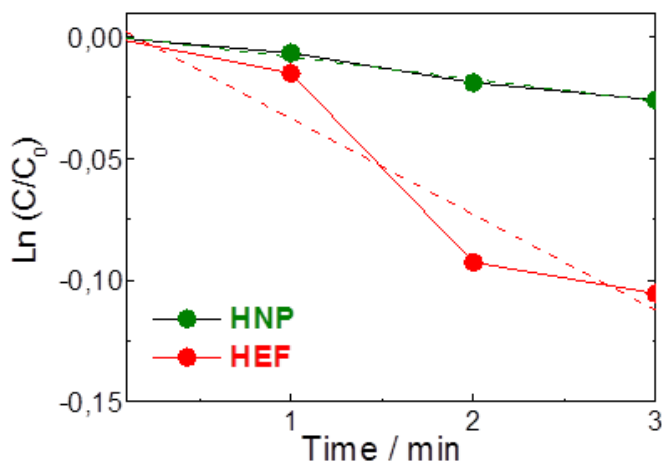


Figure 6. Dependence of $\text{Ln}(C/C_0)$ on irradiation time.

Moreover, the micropore and external area values measured for HEF were 2.2 and 19.9 $\text{m}^2 \text{g}^{-1}$, respectively (Table 1 in Supplementary Information). This means that the external area, which is constituted by the nanocrystal facets, is the mainly exposed to the gas reactant molecules increasing the photocatalytic efficiency. In this sense, it's known that exposed crystal facets favour the catalytic performance of $\alpha\text{-Fe}_2\text{O}_3$.⁶⁰ The results of this study suggest strongly that designing electrospun $\alpha\text{-Fe}_2\text{O}_3$ fibers the photocatalytic removal of NO is highly enhanced, opening new perspectives to convert hematite in a valuable "real-world" De- NO_x material.

3.2.4. Conclusions

α -Fe₂O₃ fibers were obtained through using the electrospinning technique. As a novel finding to that previously reported, HEFs are nanometric in diameter, hollow and they are comprised of a mosaic of nanocrystals with {001} and {012} facets. The singular nano-architecture led to the majority of nanocrystals being accessible for reactant molecules, specifically NO gas. Under UV–vis light irradiation, the photocatalytic NO removal happens over HEF being the photocatalyst easily regenerated by simple washing. Moreover, the large surface-to-volume ratio of HEF sample favours a highly efficient photochemical activity when compared with standard powder nanoparticles.

Acknowledgements

This work was funded by Junta de Andalucía (Group FQM-175), Córdoba University (XX PP. Modalidad 4.1) and Ministerio de Economía y Competitividad (TEC2014-53906-R).

References

1. Frampton, M. W.; Greaves, I. A., NO_x - NO_x: Who's There? *Am. J. Respir. Crit. Care. Med.* **2009**, *179* (12), 1077-1078.
2. Williams, M. L.; Carslaw, D. C., New Directions: Science and policy – Out of step on NO_x and NO₂? *Atmos. Environ.* **2011**, *45* (23), 3911-3912.
3. Devahasdin, S.; Fan Jr, C.; Li, K.; Chen, D. H., TiO₂ photocatalytic oxidation of nitric oxide: transient behavior and reaction kinetics. *J. Photochem. Photobiol. A* **2003**, *156* (1–3), 161-170.
4. Ao, C. H.; Lee, S. C., Enhancement effect of TiO₂ immobilized on activated carbon filter for the photodegradation of pollutants at typical indoor air level. *Appl. Catal. B: Environ.* **2003**, *44* (3), 191-205.
5. Bloh, J. Z.; Folli, A.; Macphee, D. E., Photocatalytic NO_x abatement: why the selectivity matters. *RSC Adv.* **2014**, *4* (86), 45726-45734.
6. Li, H.; Liu, B.; Wang, Y.; Yin, S.; Ma, X.; Wang, X.; Wu, Q.; shen, R.; Chen, H., A facile one-step hydrothermal synthesis of a B-doped graphene/rod-shaped TiO₂ nanocomposite. *RSC Adv.* **2014**, *4* (72), 37992-37997.
7. Tobaldi, D. M.; Seabra, M. P.; Otero-Irurueta, G.; de Miguel, Y. R.; Ball, R. J.; Singh, M. K.; Pullar, R. C.; Labrincha, J. A., Quantitative XRD characterisation and gas-phase photocatalytic activity testing for visible-light (indoor

- applications) of KRONOClean 7000[registered sign]. *RSC Adv.* **2015**, 5 (124), 102911-102918.
8. Folli, A.; Campbell, S. B.; Anderson, J. A.; Macphee, D. E., Role of TiO₂ surface hydration on NO oxidation photo-activity. *J. Photochem. Photobiol. A* **2011**, 220 (2–3), 85-93.
 9. Folli, A.; Pade, C.; Hansen, T. B.; De Marco, T.; Macphee, D. E., TiO₂ photocatalysis in cementitious systems: Insights into self-cleaning and depollution chemistry. *Cem. Concr. Res.* **2012**, 42 (3), 539-548.
 10. Wheeler, D. A.; Wang, G.; Ling, Y.; Li, Y.; Zhang, J. Z., Nanostructured hematite: synthesis, characterization, charge carrier dynamics, and photoelectrochemical properties. *Energy Environ. Sci.* **2012**, 5 (5), 6682-6702.
 11. Shi, Y.; Li, H.; Wang, L.; Shen, W.; Chen, H., Novel α -Fe₂O₃/CdS Cornlike nanorods with enhanced photocatalytic performance. *ACS Appl. Mater. Interfaces* **2012**, 4 (9), 4800-4806.
 12. Barreca, D.; Carraro, G.; Gasparotto, A.; Maccato, C.; Rossi, F.; Salviati, G.; Tallarida, M.; Das, C.; Fresno, F.; Korte, D.; Štangar, U. L.; Franko, M.; Schmeisser, D., Surface functionalization of nanostructured Fe₂O₃ polymorphs: from design to light-activated applications. *ACS Appl. Mater. Interfaces* **2013**, 5 (15), 7130-7138.
 13. Carraro, G.; Sugrañez, R.; Maccato, C.; Gasparotto, A.; Barreca, D.; Sada, C.; Cruz-Yusta, M.; Sánchez, L., Nanostructured iron(III) oxides: From design to gas- and

- liquid-phase photo-catalytic applications. *Thin Solid Films* **2014**, *564*, 121-127.
14. Liu, Y.; Yu, C.; Dai, W.; Gao, X.; Qian, H.; Hu, Y.; Hu, X., One-pot solvothermal synthesis of multi-shelled α -Fe₂O₃ hollow spheres with enhanced visible-light photocatalytic activity. *J. Alloys Compd.* **2013**, *551*, 440-443.
 15. Liu, Y.; Yu, L.; Hu, Y.; Guo, C.; Zhang, F.; Wen Lou, X., A magnetically separable photocatalyst based on nest-like γ -Fe₂O₃/ZnO double-shelled hollow structures with enhanced photocatalytic activity. *Nanoscale* **2012**, *4* (1), 183-187.
 16. Sugrañez, R.; Balbuena, J.; Cruz-Yusta, M.; Martín, F.; Morales, J.; Sánchez, L., Efficient behaviour of hematite towards the photocatalytic degradation of NO_x gases. *Appl. Catal. B: Environ.* **2015**, *165*, 529-536.
 17. Pei, C. C.; Leung, W. W.-F., Enhanced photocatalytic activity of electrospun TiO₂/ZnO nanofibers with optimal anatase/rutile ratio. *Catal. Commun.* **2013**, *37*, 100-104.
 18. Ren, P.; Fan, H.; Wang, X., Electrospun nanofibers of ZnO/BaTiO₃ heterostructures with enhanced photocatalytic activity. *Catal. Commun.* **2012**, *25*, 32-35.
 19. Lu, X.; Wang, C.; Wei, Y., One-Dimensional Composite Nanomaterials: Synthesis by Electrospinning and Their Applications. *Small* **2009**, *5* (21), 2349-2370.
 20. Thavasi, V.; Singh, G.; Ramakrishna, S., Electrospun nanofibers in energy and environmental applications. *Energy Environ. Sci.* **2008**, *1* (2), 205-221.

21. Mishra, M.; Chun, D.-M., α -Fe₂O₃ as a photocatalytic material: A review. *Appl. Catal. A: Gen.* **2015**, *498*, 126-141.
22. Sundaramurthy, J.; Li, N.; Kumar, P. S.; Ramakrishna, S., Perspective of electrospun nanofibers in energy and environment. *Biofuel Res. J.* **2014**, *1* (2), 44-54.
23. Dai, Y.; Liu, W.; Formo, E.; Sun, Y.; Xia, Y., Ceramic nanofibers fabricated by electrospinning and their applications in catalysis, environmental science, and energy technology. *Polym. Adv. Technol.* **2011**, *22* (3), 326-338.
24. Shao, H.; Zhang, X.; Chen, F.; Liu, S.; Ji, Y.; Zhu, Y.; Feng, Y., Preparation of α -Fe₂O₃ nanotubes via electrospinning and research on their catalytic properties. *Appl. Phys. A: Mater. Sci. Process.* **2012**, *108* (4), 961-965.
25. Liu, Y.; Yu, H.; Zhan, S.; Li, Y.; Lv, Z.; Yang, X.; Yu, Y., Fast degradation of methylene blue with electrospun hierarchical α -Fe₂O₃ nanostructured fibers. *J. Sol-Gel Sci. Technol.* **2011**, *58* (3), 716-723.
26. Cheng, Y.; Zou, B.; Wang, C.; Liu, Y.; Fan, X.; Zhu, L.; Wang, Y.; Ma, H.; Cao, X., Formation mechanism of Fe₂O₃ hollow fibers by direct annealing of the electrospun composite fibers and their magnetic, electrochemical properties. *CrystEngComm* **2011**, *13* (8), 2863-2870.
27. Zhu, Y.; Zhang, J. C.; Zhai, J.; Jiang, L., Preparation of superhydrophilic α -Fe₂O₃ nanofibers with tunable magnetic properties. *Thin Solid Films* **2006**, *510* (1-2), 271-274.

28. Sundaramurthy, J.; Kumar, P. S.; Kalaivani, M.; Thavasi, V.; Mhaisalkar, S. G.; Ramakrishna, S., Superior photocatalytic behaviour of novel 1D nanobraid and nanoporous $\alpha\text{-Fe}_2\text{O}_3$ structures. *RSC Adv.* **2012**, 2 (21), 8201-8208.
29. Zhan, S.; Qiu, M.; Yang, S.; Zhu, D.; Yu, H.; Li, Y., Facile preparation of MnO_2 doped Fe_2O_3 hollow nanofibers for low temperature SCR of NO with NH_3 . *J. Mater. Chem. A* **2014**, 2 (48), 20486-20493.
30. Nie, G.; Lu, X.; Lei, J.; Jiang, Z.; Wang, C., Electrospun V_2O_5 -doped $\alpha\text{-Fe}_2\text{O}_3$ composite nanotubes with tunable ferromagnetism for high-performance supercapacitor electrodes. *J. Mater. Chem. A* **2014**, 2 (37), 15495-15501.
31. Chen, X.; Unruh, K. M.; Ni, C.; Ali, B.; Sun, Z.; Lu, Q.; Deitzel, J.; Xiao, J. Q., Fabrication, formation mechanism, and magnetic properties of metal oxide nanotubes via electrospinning and thermal treatment. *J. Phys. Chem. C* **2011**, 115 (2), 373-378.
32. Zhan, S.; Chen, D.; Jiao, X.; Liu, S., Facile fabrication of long $\alpha\text{-Fe}_2\text{O}_3$, $\alpha\text{-Fe}$ and $\gamma\text{-Fe}_2\text{O}_3$ hollow fibers using sol-gel combined co-electrospinning technology. *J. Colloid Interface Sci.* **2007**, 308 (1), 265-270.
33. Lang, L.; Xu, Z., Controllable Synthesis of Porous $\alpha\text{-Fe}_2\text{O}_3$ Microtube and tube-in-tube by non-coaxial electrospinning. *Chem. Lett.* **2013**, 42 (7), 750-752.
34. Zhao, C.; Hu, W.; Zhang, Z.; Zhou, J.; Pan, X.; Xie, E., Effects of SnO_2 additives on nanostructure and gas-sensing properties of $\alpha\text{-Fe}_2\text{O}_3$ nanotubes. *Sens. Actuators, B* **2014**, 195, 486-493.

35. Binitha, G.; Soumya, M. S.; Madhavan, A. A.; Praveen, P.; Balakrishnan, A.; Subramanian, K. R. V.; Reddy, M. V.; Nair, S. V.; Nair, A. S.; Sivakumar, N., Electrospun α -Fe₂O₃ nanostructures for supercapacitor applications. *J. Mater. Chem. A* **2013**, *1* (38), 11698-11704.
36. Xiao, F.-X.; Miao, J.; Tao, H. B.; Hung, S.-F.; Wang, H.-Y.; Yang, H. B.; Chen, J.; Chen, R.; Liu, B., One-dimensional hybrid nanostructures for heterogeneous photocatalysis and photoelectrocatalysis. *Small* **2015**, *11* (18), 2115-2131.
37. Zhou, X.; Xu, Q.; Lei, W.; Zhang, T.; Qi, X.; Liu, G.; Deng, K.; Yu, J., Origin of tunable photocatalytic selectivity of well-defined α -Fe₂O₃ nanocrystals. *Small* **2014**, *10* (4), 674-679.
38. Yamashita, T.; Hayes, P., Analysis of XPS spectra of Fe²⁺ and Fe³⁺ ions in oxide materials. *Appl. Surf. Sci.* **2008**, *254* (8), 2441-2449.
39. Riveros, G.; Ramírez, D.; Dalchiele, E. A.; Marotti, R.; Grez, P.; Martín, F.; Ramos-Barrado, J. R., Electrodeposition and characterization of hematite films obtained from DMSO Solution. *J. Electrochem. Soc.* **2014**, *161* (6), D353-D361.
40. Monge, M. E.; D'Anna, B.; George, C., Nitrogen dioxide removal and nitrous acid formation on titanium oxide surfaces-an air quality remediation process? *Phys. Chem. Chem. Phys.* **2010**, *12* (31), 8991-8998.
41. Signoretto, M.; Ghedini, E.; Trevisan, V.; Bianchi, C. L.; Ongaro, M.; Cruciani, G., TiO₂-MCM-41 for the photocatalytic

- abatement of NO_x in gas phase. *Appl. Catal. B: Environ.* **2010**, *95* (1–2), 130-136.
42. Pandey, S. K.; Kim, K.-H.; Chung, S.-Y.; Cho, S. J.; Kim, M. Y.; Shon, Z.-H., Long-term study of NO_x behavior at urban roadside and background locations in Seoul, Korea. *Atmos. Environ.* **2008**, *42* (4), 607-622.
43. Ouyang, J.; Pei, J.; Kuang, Q.; Xie, Z.; Zheng, L., Supersaturation-controlled shape evolution of $\alpha\text{-Fe}_2\text{O}_3$ nanocrystals and their facet-dependent catalytic and sensing properties. *ACS Appl. Mater. Interfaces* **2014**, *6* (15), 12505-12514.
44. Guo, H.; Barnard, A. S., Thermodynamic modelling of nanomorphologies of hematite and goethite. *J. Mater. Chem.* **2011**, *21* (31), 11566-11577.
45. Lin, M.; Tan, H. R.; Tan, J. P. Y.; Bai, S., Understanding the growth mechanism of $\alpha\text{-Fe}_2\text{O}_3$ nanoparticles through a controlled shape transformation. *J. Phys. Chem. C* **2013**, *117* (21), 11242-11250.
46. Bersani, D.; Lottici, P. P.; Montenero, A., Micro-Raman investigation of iron oxide films and powders produced by sol-gel syntheses. *J. Raman Spectrosc.* **1999**, *30* (5), 355-360.
47. Tahir, A. A.; Wijayantha, K. G. U.; Saremi-Yarahmadi, S.; Mazhar, M.; McKee, V., Nanostructured $\alpha\text{-Fe}_2\text{O}_3$ thin films for photoelectrochemical hydrogen generation. *Chem. Mater.* **2009**, *21* (16), 3763-3772.

48. Morales, J.; Sánchez, L.; Martín, F.; Berry, F.; Ren, X., Synthesis and characterization of nanometric iron and iron-titanium oxides by mechanical milling:: electrochemical properties as anodic materials in lithium cells. *J. Electrochem. Soc.* **2005**, *152* (9), A1748-A1754.
49. Balbuena, J.; Cruz-Yusta, M.; Sánchez, L., Nanomaterials to combat NO_x pollution. *J. Nanosci. Nanotechnol.* **2015**, *15* (9), 6373-6385.
50. Lasek, J.; Yu, Y.-H.; Wu, J. C. S., Removal of NO_x by photocatalytic processes. *J. Photochem. Photobiol. C* **2013**, *14*, 29-52.
51. Yu, J.; Yu, X.; Huang, B.; Zhang, X.; Dai, Y., Hydrothermal Synthesis and Visible-light Photocatalytic Activity of Novel Cage-like Ferric Oxide Hollow Spheres. *Cryst. Growth Des.* **2009**, *9* (3), 1474-1480.
52. Niu, M.; Huang, F.; Cui, L.; Huang, P.; Yu, Y.; Wang, Y., Hydrothermal synthesis, structural characteristics, and enhanced photocatalysis of SnO₂/α-Fe₂O₃ semiconductor nanoheterostructures. *ACS Nano* **2010**, *4* (2), 681-688.
53. Yu, B. Y.; Kwak, S.-Y., Carbon quantum dots embedded with mesoporous hematite nanospheres as efficient visible light-active photocatalysts. *J. Mater. Chem.* **2012**, *22* (17), 8345-8353.
54. Hadjiivanov, K. I., Identification of neutral and charged Surface NO_x species by IR spectroscopy. *Catal. Rev. Sci. Eng.* **2000**, *42* (1-2), 71-144.

55. Sá, J.; Anderson, J. A., FTIR study of aqueous nitrate reduction over Pd/TiO₂. *Appl. Catal. B: Environ.* **2008**, *77* (3–4), 409-417.
56. Zhao, B.; Ran, R.; Wu, X.; Weng, D.; Wu, X.; Huang, C., Comparative study of Mn/TiO₂ and Mn/ZrO₂ catalysts for NO oxidation. *Catal. Commun.* **2014**, *56*, 36-40.
57. Ai, Z.; Ho, W.; Lee, S.; Zhang, L., Efficient photocatalytic removal of NO in indoor air with hierarchical bismuth oxybromide nanoplate microspheres under visible light. *Environ. Sci. Technol.* **2009**, *43* (11), 4143-4150.
58. Ibusuki, T., Science & Technology. In *Photocatalysis: Science & Technology*, 2003 ed.; Kaneko, M.; Okura, I., Eds. Springer: Japan, 2003; pp 143 - 155.
59. Balbuena, J.; Carraro, G.; Cruz, M.; Gasparotto, A.; Maccato, C.; Pastor, A.; Sada, C.; Barreca, D.; Sanchez, L., Advances in photocatalytic NO_x abatement through the use of Fe₂O₃/TiO₂ nanocomposites. *RSC Adv.* **2016**, *6* (78), 74878-74885.
60. Zhao, Y.; Pan, F.; Li, H.; Niu, T.; Xu, G.; Chen, W., Facile synthesis of uniform α-Fe₂O₃ crystals and their facet-dependent catalytic performance in the photo-Fenton reaction. *J. Mater. Chem. A* **2013**, *1* (24), 7242-7246.

Electronic Supplementary Information

Enhanced activity of α -Fe₂O₃ for the photocatalytic

NO removal

J. Balbuena,^a M. Cruz-Yusta,^a A. L. Cuevas,^b M. Cruz López-Escalante,^c F. Martín,

A. Pastor^a and L. Sánchez^{a,}*

^aInorganic Chemistry Department, Campus de Rabanales, Universidad de Córdoba, Córdoba, 14071, Spain. luis-sanchez@uco.es

^bUnidad de Nanotecnología. Edificio de Bioinnovación. Universidad de Málaga - Málaga, 29071, Spain. analaura.cuevas@uma.es

^cChemical Engineering Department, Campus de Teatinos, Universidad de Málaga, Málaga, 29071, Spain. marjim@uma.es

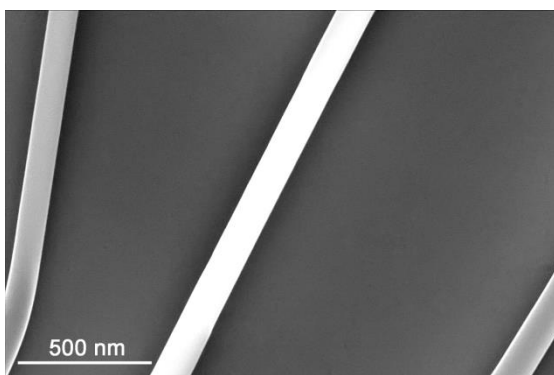
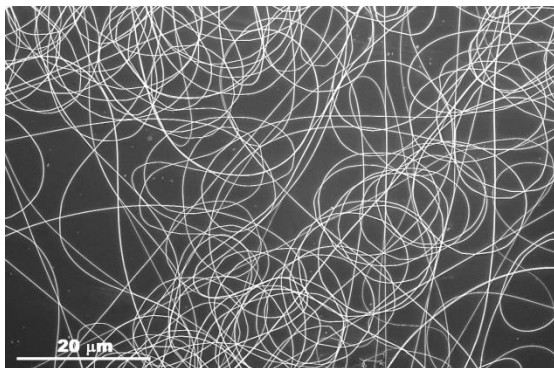


Figure S1. SEM images of as-spun Fe(III)/PVP nanofibers

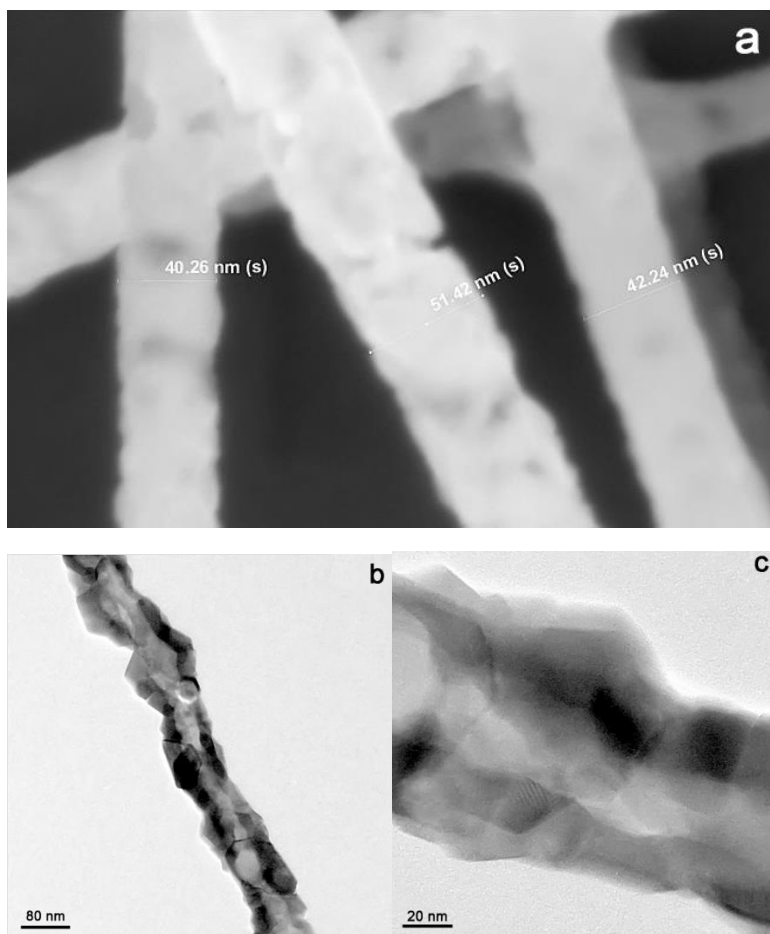


Figure S2. SEM (a) and HR-TEM (b, c) images obtained for HEF sample.

Figure S3. *Kubelka-Munk transformed reflectance spectra of HEF.*

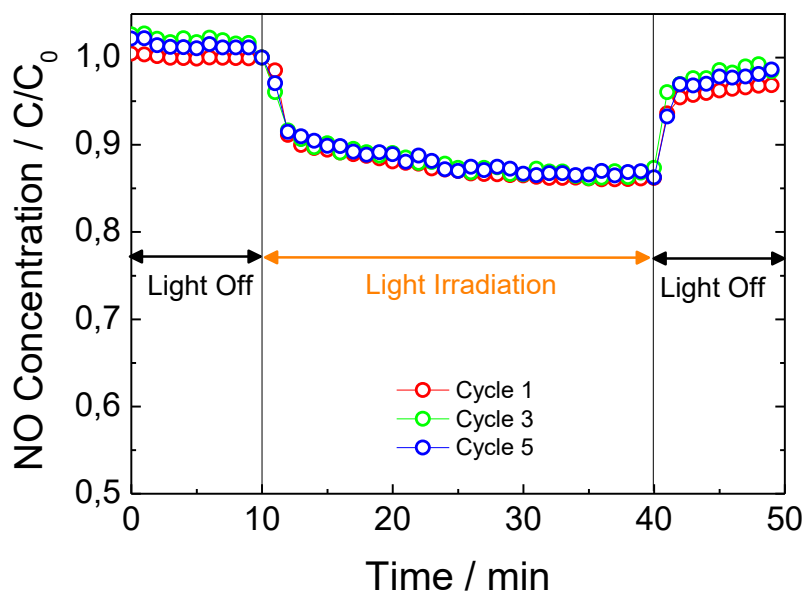


Figure S4. Concentration profiles obtained for HEF sample during successive experiments of photochemical degradation of NO gas under UV-vis light irradiation.

Successive additional cycling reactions were performed as preliminar evaluation of photocatalyst reuse. Between experiments, with the aim to eliminate the nitrite/nitrate compounds accumulated on surface, the photocatalyst was washed with distilled water, filtered and dried at 60 °C for 24 h.

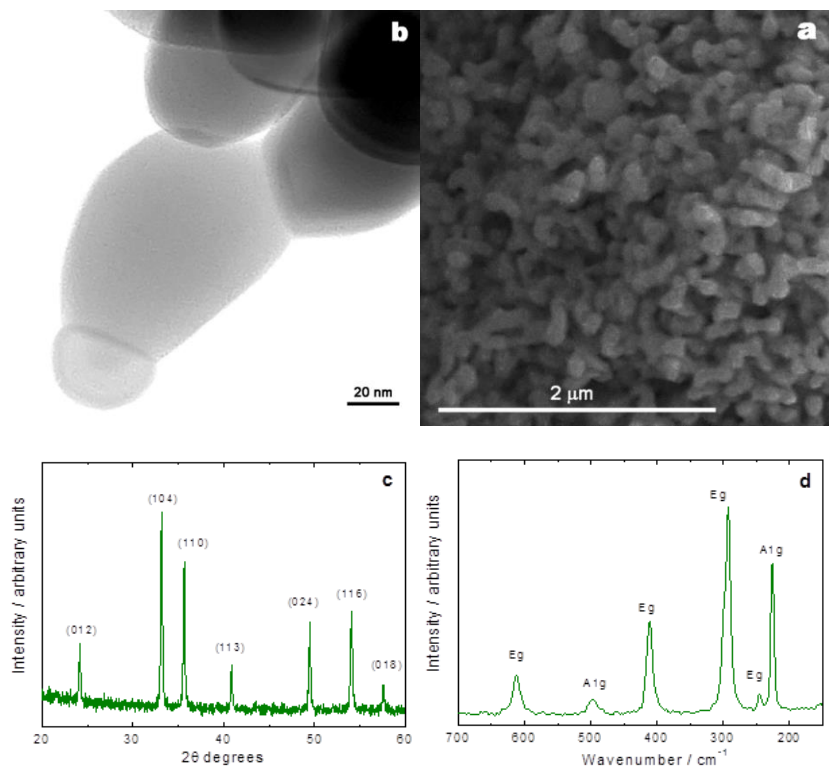


Figure S5. (a) SEM and (b) TEM images, (c) XRD and (d) Raman spectra of $\alpha\text{-Fe}_2\text{O}_3$ nano-powders (HNP sample).

Table 1. Surface area and porosity parameters for α -Fe₂O₃ samples.

Samples	HEF	HNP
Surface area / m²·g⁻¹		
^a A _{BET}	22.13	9.14
^b A _{micropore}	2.19	2.63
^b A _{External}	19.93	6.51
Pore Volume / cm³·g⁻¹		
^c V _{Total}	0.0577	0.0172
^b V _{Micropore}	0.0007	0.0013
^d V _{Mesopore}	0.0570	0.0159
Pore Size / Å		
^e Pore Width	104.23	75.35

^a Determined by adsorption of N₂ at 77 K (BET eq. with Am = 0.162 nm²).

^b Determined from the N₂ adsorption isotherm by t-plot method (Harkins and Jura eq.).

^c Determined from the N₂ adsorption isotherm by taking volume adsorbed at P/Po = 0.995.

^d Determined by V_{Total}-V_{Micropore}.

^e Adsorption average pore width (4V/A by BET).

3.3. Advances in photocatalytic NO_x abatement through the use of Fe₂O₃/TiO₂ nanocomposites



RSC Advances

PAPER

[View Article Online](#)
[View Journal](#) | [View Issue](#)

Advances in photocatalytic NO_x abatement through the use of Fe₂O₃/TiO₂ nanocomposites†

José Balbuena,^a Giorgio Carraro,^{*b} Manuel Cruz,^a Alberto Gasparotto,^b Chiara Maccato,^b Adrián Pastor,^a Cinzia Sada,^c Davide Barreca^d and Luis Sánchez^{*a}

Supported Fe₂O₃/TiO₂ nanocomposites were prepared for the first time by a plasma-assisted route and successfully tested in photocatalytic NO_x abatement driven by solar illumination. In particular, a sequential low-temperature (<100 °C) plasma enhanced-chemical vapor deposition (PE-CVD)/radio frequency (RF) sputtering approach was used to fabricate Fe₂O₃/TiO₂ nanocomposites with controlled composition and morphology. The preparation process was accompanied by a thorough multi-technique investigation carried out by complementary techniques, including X-ray photoelectron spectroscopy (XPS), secondary ion mass spectrometry (SIMS), field emission-scanning electron microscopy (FE-SEM), X-ray diffraction (XRD), and atomic force microscopy (AFM). The results evidenced the formation of high purity nanocomposites, in which TiO₂ content could be tailored by controlled variations of the sole sputtering time, and characterized by an intimate Fe₂O₃/TiO₂ contact, of key importance to exploit the chemical and electronic coupling between the two oxides. The obtained nanomaterials were tested in NO photo-oxidation activated by sunlight, showing a remarkable activity in NO_x (NO + NO₂) removal and a high selectivity (>60%) in their conversion to nitrate species. Overall, the present performances candidate the present photocatalysts as valuable materials for next-generation technologies aimed at the abatement of harmful gaseous pollutants.



Cite this: *RSC Adv.*, 2016, 6, 74878

Received 20th June 2016
Accepted 1st August 2016

DOI: 10.1039/c6ra15958c

www.rsc.org/advances

3.3.1. Introduction

In the modern society, atmospheric pollution has been recognized as one of the most severe threats for both the environment and human health. Among the most important primary pollutants, NO_x (NO and NO₂) trigger the production of tropospheric ozone and acid rains, and, in addition, severely affect respiratory and immune systems.¹⁻⁴ As a consequence, the control of NO_x emissions has been largely regulated by environmental legislation, which limit their allowed hourly concentration below 0.2 ppm.^{1,5} In spite of these requirements, the above value is still often exceeded especially in big cities,⁶⁻⁷ rendering the efficient NO_x removal (De-NO_x) a main open challenge for environmental remediation purposes.⁸⁻¹¹

In this regard, photocatalysis has emerged as a viable technology, as testified by the growing number of commercial products available on the market and the increasing scientific interest on related processes.^{1,3,5} In fact, the possibility of carrying out photocatalytic air remediation in the presence of sunlight, atmospheric oxygen and water - abundant and largely available natural resources - opens attractive perspectives for the development of “green” daylight-driven processes.^{1,5} This possibility has paved the way to the integration of depolluting materials in advanced building components, ranging from photocatalytic pavements and mortars to windows and paints, in an attempt to achieve an effective NO_x de-pollution in urban areas.¹²⁻¹³

In particular, TiO₂-based photocatalysts (PCs) have been widely exploited thanks to titania favorable properties, including chemical inertness, long-term stability and low cost.^{5, 14-18} Nevertheless, the relatively large band gap of TiO₂ ($E_G \approx 3.2$ eV) enables the harvesting of the sole UV light, accounting for only $\approx 5\%$ of the incoming solar energy.^{3, 19} Therefore, the development of alternative sunlight-activated photocatalysts with high efficiency and stability is highly demanded. Among the various strategies proposed to extend radiation absorption into the visible (Vis) range, such as doping and dye photosensitization,^{11, 14, 17, 20} a proficient way concerns the fabrication of nanocomposite systems, such as Fe₂O₃-TiO₂.²¹⁻²⁴ Fe₂O₃, a non-toxic and largely available semiconducting oxide ($E_G = 2.2$ eV), can in fact enable to extent light absorption into the Vis range, but is characterized by a fast electron-hole recombination, resulting in poor photocatalytic performances.²⁵⁻²⁸ Attempts to circumvent these problems have included the control of Fe₂O₃ nano-organization, as well as its chemical modification by doping, surface passivation or functionalization with suitable systems.^{19, 23, 28-29} In particular, the design of Fe₂O₃/TiO₂ nanocomposites is expected to provide an improved efficiency in solar-driven De-NO_x processes, synergistically exploiting the favorable properties of single-phase components and reducing, at the same time, their disadvantages.^{21, 28} Indeed, as also reported for other composite systems, TiO₂ coupling with other materials can enhance visible light absorption, and results in an effective separation of photogenerated electron-hole pairs and fast interfacial charge

transfer.³⁰⁻³² Up to date, $\text{Fe}_2\text{O}_3/\text{TiO}_2$ nanosystems in powdered form have been obtained by means of various routes and used for many photo-assisted dye degradation processes in the liquid phase,^{21, 24, 33-36} whereas only a few TiO_2 -based composites (*i.e.* $\text{N-TiO}_2/\text{Fe}_2\text{O}_3$ ³⁷ and $\text{N-TiO}_2/\text{ZrO}_2$ ³⁸) were studied for gas phase De- NO_x photocatalytic processes. In addition, only a few reports have so far been dedicated to Fe-Ti-O photocatalysts prepared as thin films/supported nanocomposites.³⁹⁻⁴² Indeed, the latter are a preferred choice for final end-uses, since they present a lower tendency to sintering/deactivation than powdered PCs and enable to avoid filtration processes required for their recovery.^{21, 43} Nevertheless, to the best of our knowledge, no reports on the use of supported $\text{Fe}_2\text{O}_3/\text{TiO}_2$ composite materials for De- NO_x processes are available in the literature.

Herein, we propose the preparation of supported $\text{Fe}_2\text{O}_3/\text{TiO}_2$ composite materials by an original low-temperature plasma-assisted strategy, based on the initial PE-CVD of Fe_2O_3 followed by RF-sputtering of moderate TiO_2 amounts. Under controlled conditions, PE-CVD yields highly porous Fe_2O_3 systems with tailored nano-organization,^{25, 44} whereas RF-sputtering, thanks to its infiltration power, enables an efficient in-depth dispersion of Ti-based species into the Fe_2O_3 matrix,⁴⁵⁻⁴⁶ resulting in an intimate $\text{Fe}_2\text{O}_3/\text{TiO}_2$ contact. As already demonstrated, this approach is a highly versatile tool for the fabrication of supported nanomaterials with tunable structure and composition, thanks to the unique activation mechanisms characterizing the adopted non-equilibrium

plasmas.⁴⁵⁻⁴⁶ The utility and flexibility of the latter are indeed due to their high chemical reactivity even in the absence of external thermal supplies, enabling material processing at temperatures lower than conventional vapor-phase routes.⁴⁷ As a consequence, PE-CVD processes can be considered more cost-effective than the homologous thermal CVD ones, paving the way to a possible industrial scale-up. Similar observations hold even for RF-sputtering processes, used in the present work for the Fe₂O₃ functionalization with TiO₂.⁴⁵

In this work, beyond the structural, compositional and morphological characterization, the photocatalytic NO_x abatement performances of Fe₂O₃/TiO₂ nanocomposites are presented, with particular attention to the release of toxic intermediates into the outer atmosphere.⁴⁸ Remarkably, the obtained systems display a high NO_x removal efficiency, superior to that evaluated for Degussa P25 and other modified TiO₂-based materials.^{1, 3, 49}

3.3.2. Experimental

Synthesis

Fe₂O₃ depositions were carried out by means of a two-electrode custom-built PE-CVD apparatus ($\nu = 13.56$ MHz).⁵⁰ Depositions were performed on *p*-type Si(100) substrates (MEMC®, Merano, Italy, 30 mm × 30 mm × 1 mm), subjected to an established cleaning procedure prior to each deposition.²⁵ Electronic grade argon and oxygen were used as plasma sources. The iron precursor,

Fe(dpm)₃ (dpm = 2,2,6,6-tetramethyl-3,5-heptanedionate), synthesized as recently reported,⁴⁴ was placed in an external glass vaporizer heated at 130°C with an oil bath, and transported into the reaction chamber by an Ar flow [rate = 60 standard cubic centimeters per minute (sccm)]. Two further auxiliary gas-lines were used to separately introduce Ar and O₂ (flow rates = 15 and 20 sccm, respectively) directly into the reaction chamber. To prevent detrimental condensation phenomena, the delivery gas lines were maintained at 160°C by means of external heating tapes. After preliminary optimization experiments aimed at ensuring the reproducibility of sample characteristics, the growth parameters were set as follows: inter-electrode distance = 6 cm; deposition time = 60 min; RF-power = 20 W; substrate temperature = 100°C; total pressure = 1.0 mbar. In the following, the bare iron oxide reference sample is labeled as Fe₂O₃.

Subsequently, functionalization with TiO₂ was performed by RF-sputtering, using the above-described apparatus, and Ar as plasma source. A Ti target (Alfa Aesar®; thickness = 0.3 mm; purity = 99.95%) was fixed on the RF-electrode. The TiO₂ sputtering parameters were optimized basing on preliminary deposition experiments aimed at avoiding a too thick TiO₂ layer, that would have negatively affected the porosity of the underlying Fe₂O₃ matrix. Sputtering processes were carried out under the following conditions: substrate temperature = 60°C; RF power = 20 W; total pressure = 0.3 mbar; Ar flow rate = 10 sccm; duration = 2 h (sample FeTi2) or 4 h (sample FeTi4). In addition, to obtain a comparison for

the nanocomposite functional performances, pure TiO₂ specimens were fabricated by sputtering for 4 h on Si(100) (sample TiO₂). Under the adopted conditions, the thickness of the TiO₂ deposit was estimated to be lower than 5 nm.

For comparison purposes, commercially available TiO₂ P25 was used as a reference photocatalyst (10 mg of powders in a sample holder of 30 mm × 30 mm).

Characterization

The deposit mass was measured by using a Mettler Toledo XS105DU Microbalance (average weight = 0.55 ± 0.05 mg).

XRD measurements were run at a fixed incidence angle of 1.0° by means of a Bruker D8 Advance instrument equipped with a Göbel mirror, using a CuKα X-ray source ($\lambda = 1.54056 \text{ \AA}$).

FE-SEM micrographs were collected by a Zeiss SUPRA 40VP instrument, using primary beam acceleration voltages of 10 kV.

AFM analyses were carried out by using a Bruker Dimension Icon AFM (Digital Instruments) operated in tapping mode and in air. Images were recorded on different sample areas in order to check surface homogeneity. Root-mean-square (RMS) roughness values were calculated from the height profile of 2.0 × 2.0 μm² micrographs.

XPS measurements were performed by using a Perkin-Elmer Φ5600ci spectrometer with a non-monochromatized AlKα source ($h\nu = 1486.6 \text{ eV}$). Charging effects were corrected by assigning a binding energy (BE) of 284.8 eV to the adventitious C1s signal. The

estimated uncertainty on BE values was ± 0.2 eV. After a Shirley-type background subtraction, raw spectra were fitted by adopting Gaussian–Lorentzian peak shapes.⁵¹ The surface titanium molar fraction was calculated basing on Ti and Fe atomic percentages (at.%), according to the following relation:

$$X_{\text{Ti}} = \text{Ti at.\%} / (\text{Ti at.\%} + \text{Fe at.\%}) \times 100 \quad (1)$$

In-depth SIMS analyses were carried out by means of a IMS 4f mass spectrometer (Cameca) using a 14.5 keV Cs⁺ primary beam (current = 25 nA, stability = 0.3%) and by negative secondary ion detection, using an electron gun for charge compensation. Beam blanking mode and high mass resolution configuration were adopted. The target signals were recorded by rastering over a $175 \times 175 \mu\text{m}^2$ area and detecting secondary ions from a sub-region of $7 \times 7 \mu\text{m}^2$, in order to avoid the occurrence of crater effects.

Infrared (IR) spectra were recorded by means of a Perkin Elmer FTIR System Spectrum BX, operating in transmittance mode at normal incidence.

Photocatalytic tests

Photocatalytic De-NO_x experiments were performed at room temperature using a protocol similar to the standardized one developed for the characterization of air-purification performances.⁵² In particular, taking into account the sample geometric area (9.0 cm^2) and the low average deposit mass ($0.55 \pm 0.05 \text{ mg}$), a small-sized reactor (volume = 50 cm^3) and an NO

concentration of 100 ppb (obtained by mixing synthetic air and pure NO) were deliberately chosen, in order to achieve an optimal sensitivity. To this aim, it is worthwhile noticing that a similar NO content, representative of NO concentrations found during intense photochemical pollution events in urban environments,⁵³ was already successfully adopted not only in our previous research works,^{29, 54} but also in the studies carried out by other investigators.^{16, 55}

In each experiment, the NO flow was passed over the sample, placed inside the reaction chamber and irradiated from the top through a quartz window. The reactor was placed inside a light sealed irradiation box (Solarbox 3000e RH) equipped with a Xe lamp and illuminated with artificial sunlight. UV and Vis irradiance (25 and 580 W m⁻², respectively) were adjusted by a Delta Ohm HD 232.0 photo-radiometer provided with LP 471 UV ($\lambda = 315\text{-}400$ nm) and LP 471 RAD ($\lambda = 400\text{-}1050$ nm) irradiance probes. Synthetic air (flow rate = 0.30 L min⁻¹) was passed through a gas-washing bottle, filled with demineralized water in order to maintain a constant relative humidity level 50 ± 5 %. Prior to each test, the air/NO mixture was pre-fluxed over the sample in the dark for 10 min, in order to ensure a proper system stabilization. Under these conditions, no variation in the NO and NO₂ concentration profiles was observed, enabling thus to discard any relevant NO_x adsorption/degradation phenomenon on the sample surface. Subsequently, irradiation for 60 min was performed. Nitrogen oxides concentrations as a function of illumination time were

measured using a chemiluminescence analyzer (Environment AC32M). The tests were repeated three times to obtain average concentration values. The calculated standard deviation is ± 0.3 ppb for NO concentration, and ± 1.0 ppb for NO₂ and NO_x concentration. NO conversion, NO₂ released and NO_x conversion were defined as follows:

$$\text{NO conversion (\%)} = \{ ([\text{NO}]_{\text{in}} - [\text{NO}]_{\text{out}}) / [\text{NO}]_{\text{in}} \} \times 100 \quad (2)$$

$$\text{NO}_2 \text{ released (\%)} = ([\text{NO}_2]_{\text{out}} / [\text{NO}]_{\text{in}}) \times 100 \quad (3)$$

$$\text{NO}_x \text{ conversion (\%)} = \{ ([\text{NO}_x]_{\text{in}} - [\text{NO}_x]_{\text{out}}) / [\text{NO}_x]_{\text{in}} \} \times 100 \quad (4)$$

where [NO]_{in}, [NO_x]_{in} and [NO]_{out}, [NO₂]_{out}, [NO_x]_{out} denote the measured inlet and outlet concentrations, respectively, while [NO_x] = [NO] + [NO₂]. The used values were the average of the measured one under steady state period (irradiation time: 40-70 minutes).

The system selectivity, *S*, is determined according to equation (5):⁵⁶

$$S (\%) = \frac{([\text{NO}_x]_{\text{in}} - [\text{NO}_x]_{\text{out}}) / [\text{NO}_x]_{\text{in}}}{([\text{NO}]_{\text{in}} - [\text{NO}]_{\text{out}}) / [\text{NO}]_{\text{in}}} \times 100 \quad (5)$$

3.3.3. Results and discussion

The Fe₂O₃/TiO₂ specimens synthesized in the present work were fabricated using two different Ti sputtering times [2 h (FeTi2), and 4 h (FeTi4)], in order to obtain two different loadings and spatial distribution of TiO₂ into the iron oxide matrix.

The system structure and phase composition were preliminarily investigated by XRD analyses. XRD patterns of Fe₂O₃-

containing systems (ESI, Fig. S1) evidenced Bragg reflections of the rhombohedral *hematite* (α -Fe₂O₃) phase.⁵⁷ In addition, the higher intensity of the (110) signal with respect to the (104) one may suggest a preferential alignment of the [110] axis perpendicularly to the substrate (*i.e.*, *c*-oriented growth).⁵⁸ Irrespective of the adopted sputtering time, no diffraction peaks corresponding to TiO₂ polymorphs or to ternary Fe-Ti-O phases were detected, likely due to the low TiO₂ amount.^{22, 28, 46, 59}

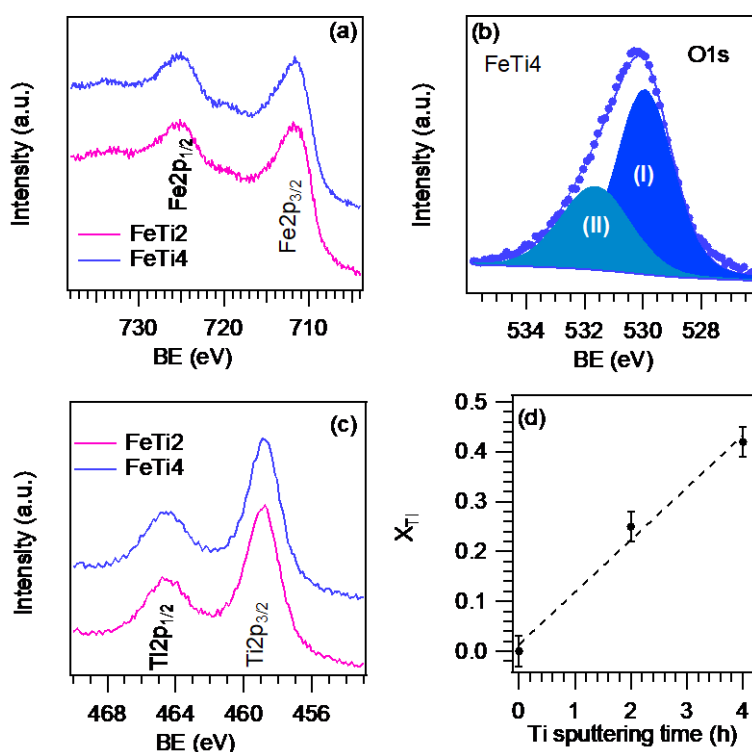


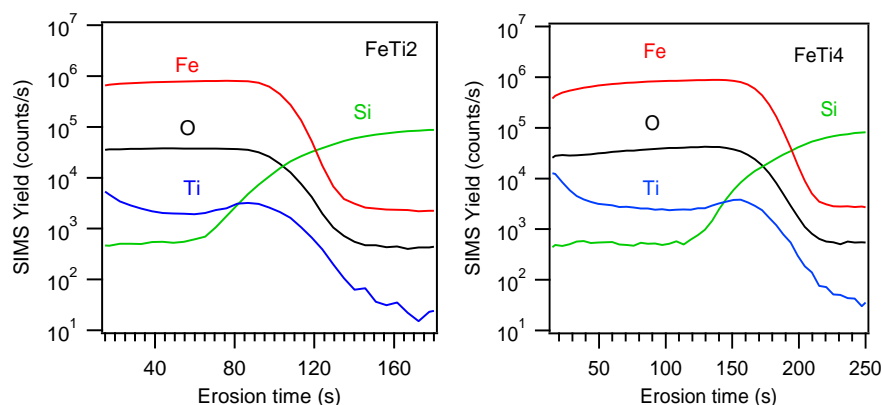
Figure 1. Surface XPS photoelectron peaks for: (a) Fe2p, (b) O1s and (c) Ti2p. (d) Surface titanium molar fraction as a function of the used sputtering time.

For the same reason, no appreciable titania reflections could

be detected for the bare TiO_2 specimen. The presence of TiO_2 was however confirmed by compositional analyses (see below).

In order to investigate the surface and in-depth chemical composition, XPS and SIMS analyses were performed, focusing in particular on iron and titanium chemical states and on their mutual distribution throughout the deposit thickness. For all systems, the presence of Fe, Ti and O XPS surface peaks was detected, along with a minor contribution from adventitious carbon arising from atmospheric exposure (ESI, Fig. S2). In line with XRD results, the spectral features of the Fe2p signal [BE ($\text{Fe}2p_{3/2}$) = 711.2 eV, Fig. 1a] were similar for all specimens and confirmed Fe_2O_3 presence.^{25, 28, 44-46, 60} As a matter of fact, surface iron signals could be detected even for the higher titanium loadings (≈ 11 at. % after 4 h of sputtering, sample FeTi4).

Two different components contributed to the O1s surface signal (Fig. 1b). Beside a major band at 530.0 eV [(I), 67% of the overall O content], related to M–O–M bonds (M = Fe, Ti), a second component (II) at higher BE (531.6 eV) was attributed to hydroxyl/carbonate species arising from exposure to the outer atmosphere.^{21, 25, 46} Irrespective of the sputtering time, Ti2p_{3/2} BE values (458.8 eV, Fig. 1c) were in line with TiO_2 presence and enabled to exclude the formation of Fe-Ti-O ternary phases.^{21, 28, 59-60} The surface titanium molar fraction (Fig. 1d) displayed a linear increase with sputtering time, indicating thus the possibility of exerting a fine control over the system surface properties by tuning the preparative conditions.



¹ⁿ⁷
Figure 2. SIMS in-depth profiles for Fe₂O₃/TiO₂ specimens.

Since the mutual distribution of Fe₂O₃ and TiO₂ is a key issue for an optimal nanocomposite engineering, a further insight into the system composition was achieved by in-depth SIMS analyses (Fig. 2). In both nanocomposites, Ti ionic yield underwent a progressive decrease within the first seconds of erosion, and subsequently reached an almost constant value. These phenomena, particularly evident for the specimen characterized by the highest TiO₂ loading (FeTi4), indicated a titania accumulation in the near-surface system layers. Nevertheless, the presence of Ti signal up to the interface with the Si substrate suggested that TiO₂ was present even in the inner *hematite* regions. This finding, attributed to the synergistic coupling of the Fe₂O₃ porosity (see below) and the sputtering infiltration power, resulted in an intimate TiO₂/Fe₂O₃ coupling, a key issue to exploit their mutual interplay for the target functional applications.

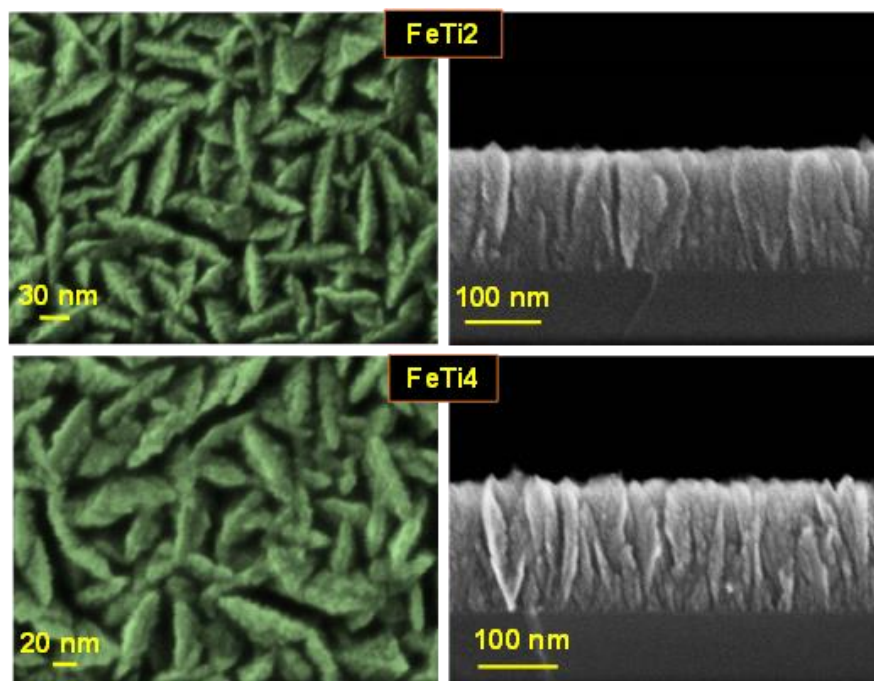


Figure 3. Plane view (left) and cross sectional (right) FE-SEM micrographs for FeTi2 and FeTi4 samples.

The system morphological organization was investigated by FE-SEM analyses. As can be appreciated in ESI, Fig. S3, bare iron oxide presented interconnected leaf-like nanostructures (mean lateral size = 20 nm; mean deposit thickness = 150 nm), characterized by a cross-section columnar habit. The arrangement of such structures resulted in the obtainment of highly porous systems, amenable candidates for solar-driven applications, as well as for the subsequent functionalization with phases, like TiO_2 .^{21, 45-46} In fact, the reduced lateral size of Fe_2O_3 nanostructures is a key tool to improve charge carrier transport and light harvesting properties, since they have a long axis enabling an efficient sunlight absorption

and a short radial distance for the diffusion of photogenerated carriers to the material surface.⁴⁶

Upon TiO₂ introduction (Fig. 3), Fe₂O₃ morphology did not undergo dramatic modifications, thanks to the use of relatively mild processing conditions.⁴⁵⁻⁴⁶ A detailed comparison of FE-SEM micrographs in Figs. 3 and S3 revealed indeed that the systems morphology become slightly more rounded upon TiO₂ deposition. This effect directly depended on Ti sputtering time (and loading), since it was more evident for the FeTi4 specimen. In any case, the TiO₂ overlayer thickness could not be clearly measured.

The present results, in line with those recently reported for Fe₂O₃-Co₃O₄ composites fabricated by a similar route,⁴⁶ were further supported by AFM Analyses, that did not reveal appreciable differences between the bare Fe₂O₃ and FeTi4 sample with the highest Ti loading (compare ESI, Fig. S4). Taking into account also the above discussed XRD and XPS results, these findings suggest either a high dispersion of Ti-containing species, or the formation of a very thin/porous titania overlayer.²⁸ As already observed, the intimate contact between the two oxides, that was achieved without any detrimental alteration of the pristine Fe₂O₃ porosity, is a key feature to synergistically exploit Fe₂O₃/TiO₂ heterojunction and cooperative effects in photocatalytic applications. To this regard, the present materials were tested in NO_x photocatalytic abatement. The complete oxidation of NO to nitrate or nitric acid (NO₃⁻/HNO₃) is a complex process, that involves several

intermediate species.^{48, 61-62} Basically, the mechanism entails several one-electron transfer steps, *via* nitrous acid (HNO₂) and nitrogen dioxide (NO₂) as intermediate species. The *in-situ* generated reactive oxygen species (mainly hydroxyl radicals but also superoxides; see also below and ESI, Fig. S7) assist as strong oxidants the process, whose steps can be sketched as follows:^{56, 63-64}

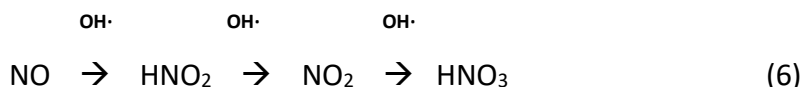


Fig. 4 displays the NO, NO₂ and total nitrogen oxide (NO_x) concentration profiles recorded for different specimens as a function of irradiation time. It is worth recalling that photocatalytic experiments were carried out by flowing 100 ppb of NO into a flow-through reactor. As can be observed from Fig. 4a, during the first 10 min in the dark the concentration of NO remained constant, highlighting the crucial role of sunlight exposure to activate the process. Subsequently, under irradiation from 10 to 70 min, a significant NO signal decrease was observed, evidencing the occurrence of a light-induced chemical reaction on Fe₂O₃/TiO₂ surfaces.^{3, 16} The constant NO values achieved after 40 min indicated that a steady state condition of maximum activity was reached. Finally, upon illumination shutdown, the NO concentration returned almost to its initial value.

The difference in values measured between dark and light conditions is related to the amount of removed NO.

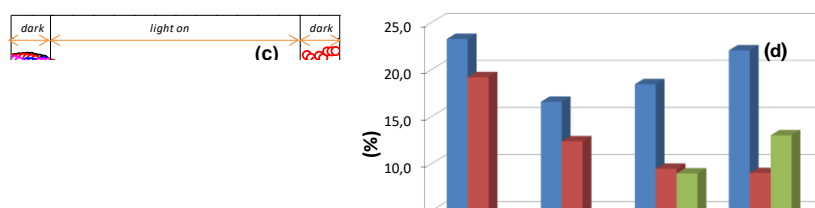


Figure 4. (a-c) Nitrogen oxides concentration profiles obtained during the photo-degradation of gaseous NO under sunlight irradiation on Fe₂O₃/TiO₂ composite systems. The curves pertaining to bare TiO₂ and bare Fe₂O₃ are also shown for comparison. (d) NO conversion (%), NO₂ released (%), and NO_x conversion (%) for Fe₂O₃, FeTi2, FeTi4 and TiO₂ samples.

As can be observed from Fig. 4a, NO conversion values were higher than 15% for all samples, and reached a maximum value close to 25% for base Fe₂O₃, corresponding to an almost doubled efficiency if compared to that previously reported for powdered *hematite*.⁵⁴ However, an effective air quality improvement does not rely on the sole NO removal, but also on suppression of undesired intermediates (in particular NO₂).⁵⁶ Hence, the photocatalyst performances should be evaluated also in terms of NO₂ formation

and total NO_x removal. To this aim, Fig. 4b evidences that non-negligible NO_2 amounts are released during the irradiation of bare Fe_2O_3 samples, suggesting that, in this case, NO is mainly oxidized to NO_2 . As observed in Fig. 4c, the NO_x removal results very poor (3%) for bare Fe_2O_3 . This phenomenon was attributed to the inherent *hematite* drawbacks, and, in particular, to its short excited-state lifetime, which, in turn, promotes a fast recombination²⁶ and prevent the formation of OH^\bullet in sufficient amount to complete photo-oxidation processes (6).⁵⁴ In a different way, the use of composite $\text{Fe}_2\text{O}_3/\text{TiO}_2$ systems resulted in an appreciable decrease of the released NO_2 amount (Fig. 4b). Furthermore, as displayed in Fig. 4c, the overall NO_x removal increased, yielding nearly twofold (FeTi2) and threefold (FeTi4) performances compared to bare Fe_2O_3 (see also Fig. 4d). In addition, the De- NO_x action exhibited by composite samples was higher than that tested for the bare TiO_2 sample prepared for comparison purposes (Fig. 4d). Another important benefit of the $\text{Fe}_2\text{O}_3\text{-TiO}_2$ interaction is evidenced by their PC activity under the sole Vis light illumination. As can be noticed from Fig. S5 in the ESI, that compares the PC performances of representative samples under Vis irradiation, the reactivity order was $\text{TiO}_2 \ll \text{Fe}_2\text{O}_3 < \text{FeTi4}$. In particular, the activity of bare TiO_2 was almost negligible, due to the large *titania* band-gap preventing visible light absorption. In a different way, NO abatement was clearly evident on bare Fe_2O_3 , as a consequence of its lower band-gap. Remarkably, upon going from bare Fe_2O_3 to FeTi4, a further activity improvement was detected. This effect can not be due to

TiO₂ light absorption properties but, rather, to the formation of Fe₂O₃/TiO₂ junctions, enhancing hole lifetime and promoting charge carrier separation. Furthermore, thanks to titania favourable properties, the latter effect can also boost the formation of OH[•] species in sufficient amount to complete NO photo-oxidation.

The possibility of photocatalyst reuse has been preliminarily investigated for FeTi4, the most active specimen. The obtained results (ESI, Fig. S6) displayed a modest activity loss ($\approx 14\%$) in the first few cycles of reutilization, and a subsequent activity stabilization from the fifth cycle. In order to properly interpret this result, it is worth noticing that the sample was rinsed with water between consecutive cycles in order to eliminate nitrite/nitrate species. Even though the identification of an appropriate cleaning procedure for the target specimens is not a straightforward task and will require additional efforts, the data collected so far suggest that no significant photocatalyst degradation took place under the adopted experimental conditions. Taken together, these results clearly highlight the beneficial synergy between Fe₂O₃ and TiO₂, resulting in improved photocatalytic performances. As reported also for other composite systems, the main advantages of Fe₂O₃ and TiO₂ coupling can be traced back not only to the improved solar light harvesting in the Vis range with respect to bare TiO₂, but also to the minimized electron-hole recombination and faster photogenerated charge transfer at the Fe₂O₃/TiO₂ interface (ESI, Fig. S7).^{30-31, 65-67} In this way, the holes accumulated in the valence band assist the formation of OH[•] radicals that can further contribute to

the progressive NO oxidation (6), whereas electron accumulated in the conduction band can favor the generation of O_2^- species, directly involved in the process (see above).²¹

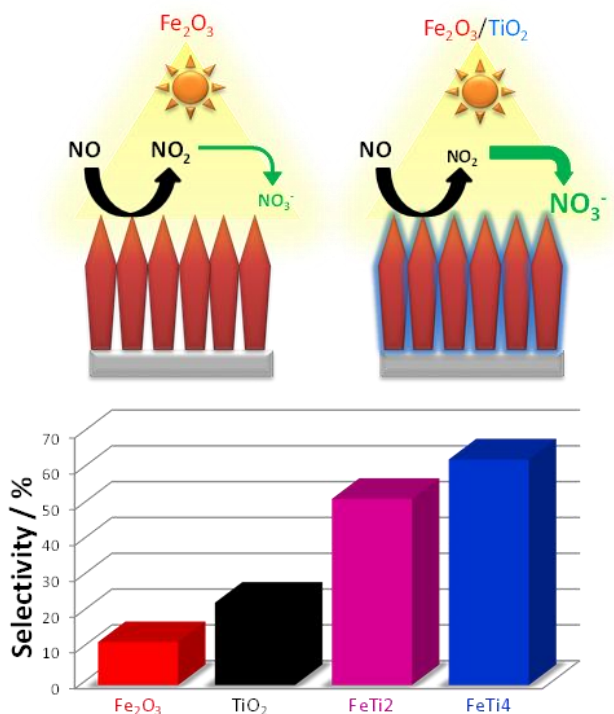


Figure 5. NO abatement selectivity values for the target specimens investigated in the present work.

Fig. 5 shows a comparison of the photocatalytic NO_x abatement selectivity (S) for bare Fe_2O_3 and $\text{Fe}_2\text{O}_3\text{-TiO}_2$ composites. This parameter expresses the ratio of degraded NO that is ultimately converted into harmless nitrate, rather than into toxic nitrogen dioxide. As can be appreciated, the selectivity underwent a remarkable enhancement upon increasing TiO_2 loading and, in particular, the sample with the highest TiO_2 content (FeTi_4)

displayed a value as high as 63%. Interestingly, this value exceeded that reported for the standard TiO₂ P25 ($S = 25\%$), used as benchmark in similar processes, and of other modified TiO₂-based materials investigated in previous works ($45\% < S < 53\%$),^{1, 3, 49} validating thus the significance of the present results in eventual practical applications. The highest S values obtained herein indicate the occurrence of good performances for the $\text{NO} \rightarrow \text{NO}_2 \rightarrow \text{NO}_3^-$ oxidation process (6).

In order to further support this conclusion, and validate the selectivity values measured from the NO_x concentration profiles, IR spectra of the most efficient photocatalyst (FeTi4) and bare Fe₂O₃ (ESI, Fig. S8) were collected before and after irradiation, to investigate the presence of possible adsorbed products.

Considering that during PC experiments only a few ppbs of nitrite/nitrate species were formed, a detailed observation in the IR region characteristic for nitrite/nitrate vibration modes ($1800\text{-}1200\text{ cm}^{-1}$) is requested to evidence their possible presence. In the case of bare Fe₂O₃ (ESI, Fig. S8a), a low intensity band at 1640 cm^{-1} was observed, corresponding to the absorption of water molecules from the reaction environment onto the surface, whereas no N–O bands were detected. This finding reveals that *hematite* capacity to remove NO_x molecules is negligible, in line with the above results. In a different way, it is worth noting that for the FeTi4 specimen, the most performing one (ESI, Fig. S8b), bands related to NO₂⁻/NO₃⁻ species could be observed in the spectra.

3.3.4. Conclusions

Supported Fe_2O_3 nanosystems have been functionalized with tailored TiO_2 amounts by means of a versatile, low temperature plasma-assisted strategy. The adopted synthetic protocol, adopted for the first time in the present investigation, enabled to prevent solid state reactions between Fe_2O_3 and TiO_2 and to fabricate pure and large-area nanocomposites. The target systems were characterized by a tailored morphology and an intimate $\text{Fe}_2\text{O}_3/\text{TiO}_2$ contact, of strategic importance in view of solar-driven NO oxidation. In particular, an improved De- NO_x efficiency with respect to bare Fe_2O_3 was obtained, highlighting the occurrence of a photocatalytic synergy between the two oxides. In fact, the efficient $\text{NO} \rightarrow \text{NO}_2^-/\text{NO}_3^-$ conversion could be driven only by $\text{Fe}_2\text{O}_3/\text{TiO}_2$ nanomaterials, but not by the single components. In contrast to the negligible NO_x amount removed by Fe_2O_3 sample, a selectivity as high as 63 % was achieved by $\text{Fe}_2\text{O}_3/\text{TiO}_2$ nanocomposites. Such values, among the best ever reported in the literature for similar systems, demonstrate the importance of their morphological/compositional control in the obtainment of advanced functional performances.

On the basis of the above results, future perspectives for the developments of the present research will concern the detailed analysis of band gap values, VB and CB positions, as well as a deeper understanding of the photocatalytic mechanism by photoluminescence and photoelectrochemical measurements. In

addition, further efforts will be devoted to a careful modulation of Fe₂O₃ morphology, to fabricate nanosystems endowed with a higher active area, as well as to the investigation of higher TiO₂ loadings and of their effects on the ultimate functional behavior. In this way, the high potential of the proposed approach for De-NO_x process triggered not only by solar light, but even by the sole Vis illumination, will be fully exploited in real-world end-uses for environmental remediation.

Acknowledgements

The research leading to these results has received funding from the FP7 project “SOLAROGENIX” (NMP4-SL-2012-310333). Padova University ex-60% 2012-2015, SOLLEONE (CPDR132937/13) and ACTION projects, are also gratefully acknowledged. In addition, this work was partially funded by Junta de Andalucía (Group FQM-175) and Córdoba University (XX PP. Modalidad 4.1).

References

1. Ângelo, J.; Andrade, L.; Mendes, A., Highly active photocatalytic paint for NO_x abatement under real-outdoor conditions. *Appl. Catal., A* **2014**, *484*, 17-25.
2. Colls, J., *Air Pollution*. Spon Press: London-New York, 2002.
3. Ma, J.; Wu, H.; Liu, Y.; He, H., Photocatalytic removal of NO_x over visible light responsive oxygen-deficient TiO₂. *J. Phys. Chem. C* **2014**, *118* (14), 7434-7441.
4. Habib, H. A.; Basner, R.; Brandenburg, R.; Armbruster, U.; Martin, A., Selective catalytic reduction of NO_x of ship diesel engine exhaust gas with C₃H₆ over Cu/Y zeolite. *ACS Catal.* **2014**, *4* (8), 2479-2491.
5. Folli, A.; Campbell, S. B.; Anderson, J. A.; Macphee, D. E., Role of TiO₂ surface hydration on NO oxidation photo-activity. *J. Photochem. Photobiol., A* **2011**, *220* (2-3), 85-93.
6. Frampton, M. W.; Greaves, I. A., NO_x - NO_x: Who's There? *Am. J. Respir. Crit. Care Med.* **2009**, *179* (12), 1077-1078.
7. Williams, M. L.; Carslaw, D. C., New Directions: Science and policy - Out of step on NO_x and NO₂? *Atmos. Environ.* **2011**, *45* (23), 3911-3912.
8. Newman, M. C.; Clement, W. H., *Ecotoxicology: A Comprehensive Treatment*. CRC Press: Boca Raton, Florida, 2008.

9. Chen, B.; Hong, C.; Kan, H., Exposures and health outcomes from outdoor air pollutants in China. *Toxicol.* **2004**, *198* (1–3), 291-300.
10. Cormier, S. A.; Lomnicki, S.; Backes, W.; Dellinger, B., Origin and health impacts of emissions of toxic by-products and fine particles from combustion and thermal treatment of hazardous wastes and materials. *Environ. Health Perspect.* **2006**, *114* (6), 810-817.
11. Yamamoto, A.; Mizuno, Y.; Teramura, K.; Hosokawa, S.; Tanaka, T., Noble-metal-free NO_x storage over Ba-modified TiO₂ photocatalysts under UV-light irradiation at low temperatures. *ACS Catal.* **2015**, *5* (5), 2939-2943.
12. Poon, C. S.; Cheung, E., NO removal efficiency of photocatalytic paving blocks prepared with recycled materials. *Constr. Build. Mater.* **2007**, *21* (8), 1746-1753.
13. Sugrañez, R.; Álvarez, J. I.; Cruz-Yusta, M.; Mármol, I.; Morales, J.; Vila, J.; Sánchez, L., Enhanced photocatalytic degradation of NO_x gases by regulating the microstructure of mortar cement modified with titanium dioxide. *Build. Environ.* **2013**, *69*, 55-63.
14. Karapati, S.; Giannakopoulou, T.; Todorova, N.; Boukos, N.; Dimotikali, D.; Trapalis, C., Eco-efficient TiO₂ modification for air pollutants oxidation. *Appl. Catal., B* **2015**, *176–177*, 578-585.

15. Chen, H.; Nanayakkara, C. E.; Grassian, V. H., Titanium dioxide photocatalysis in atmospheric chemistry. *Chem. Rev.* **2012**, *112* (11), 5919-5948.
16. Monge, M. E.; D'Anna, B.; George, C., Nitrogen dioxide removal and nitrous acid formation on titanium oxide surfaces-an air quality remediation process? *Phys. Chem. Chem. Phys.* **2010**, *12* (31), 8991-8998.
17. Pelaez, M.; Nolan, N. T.; Pillai, S. C.; Seery, M. K.; Falaras, P.; Kontos, A. G.; Dunlop, P. S. M.; Hamilton, J. W. J.; Byrne, J. A.; O'Shea, K.; Entezari, M. H.; Dionysiou, D. D., A review on the visible light active titanium dioxide photocatalysts for environmental applications. *Appl. Catal., B* **2012**, *125*, 331-349.
18. Petala, A.; Ioannidou, E.; Georgaka, A.; Bourikas, K.; Kondarides, D. I., Hysteresis phenomena and rate fluctuations under conditions of glycerol photo-reforming reaction over CuOx/TiO₂ catalysts. *Appl. Catal., B* **2015**, *178*, 201-209.
19. He, L.; Jing, L.; Luan, Y.; Wang, L.; Fu, H., Enhanced visible activities of α -Fe₂O₃ by coupling N-doped graphene and mechanism insight. *ACS Catal.* **2014**, *4* (3), 990-998.
20. Trapalis, A.; Todorova, N.; Giannakopoulou, T.; Boukos, N.; Speliotis, T.; Dimotikali, D.; Yu, J., TiO₂/graphene composite photocatalysts for NO_x removal: A comparison of surfactant-stabilized graphene and reduced graphene oxide. *Appl. Catal., B* **2016**, *180*, 637-647.

21. Barreca, D.; Carraro, G.; Warwick, M. E. A.; Kaunisto, K.; Gasparotto, A.; Gombac, V.; Sada, C.; Turner, S.; Van Tendeloo, G.; Maccato, C.; Fornasiero, P., Fe₂O₃-TiO₂ nanosystems by a hybrid PE-CVD/ALD approach: controllable synthesis, growth mechanism, and photocatalytic properties. *CrystEngComm* **2015**, *17* (32), 6219-6226.
22. Zhu, S.; Yao, F.; Yin, C.; Li, Y.; Peng, W.; Ma, J.; Zhang, D., Fe₂O₃/TiO₂ photocatalyst of hierarchical structure for H₂ production from water under visible light irradiation. *Microporous Mesoporous Mater.* **2014**, *190*, 10-16.
23. Barreca, D.; Carraro, G.; Gasparotto, A.; Maccato, C.; Rossi, F.; Salviati, G.; Tallarida, M.; Das, C.; Fresno, F.; Korte, D.; Stangar, U. L.; Franko, M.; Schmeisser, D., Surface functionalization of nanostructured Fe₂O₃ polymorphs: from design to light-activated applications. *ACS Appl. Mater. Interfaces* **2013**, *5* (15), 7130-7138.
24. Tang, H.; Zhang, D.; Tang, G.; Ji, X.; Li, W.; Li, C.; Yang, X., Hydrothermal synthesis and visible-light photocatalytic activity of α-Fe₂O₃/TiO₂ composite hollow microspheres. *Ceram. Int.* **2013**, *39* (8), 8633-8640.
25. Carraro, G.; Gasparotto, A.; Maccato, C.; Bontempi, E.; Barreca, D., PECVD of Hematite nanoblades and nanocolumns: synthesis, characterization, and growth model *Chem. Vap. Deposition* **2015**, *21*, 294-299.
26. Wheeler, D. A.; Wang, G.; Ling, Y.; Li, Y.; Zhang, J. Z., Nanostructured hematite: synthesis, characterization, charge

- carrier dynamics, and photoelectrochemical properties. *Energy Environ. Sci.* **2012**, 5 (5), 6682-6702.
27. Mishra, M.; Chun, D.-M., α -Fe₂O₃ as a photocatalytic material: A review. *Appl. Catal., A* **2015**, 498, 126-141.
28. Ahmed, M. G.; Kretschmer, I. E.; Kandiel, T. A.; Ahmed, A. Y.; Rashwan, F. A.; Bahnemann, D. W., A facile surface passivation of hematite photoanodes with TiO₂ overlayers for efficient solar water splitting. *ACS Appl. Mater. Interfaces* **2015**, 7 (43), 24053-24062.
29. Carraro, G.; Sugrañez, R.; Maccato, C.; Gasparotto, A.; Barreca, D.; Sada, C.; Cruz-Yusta, M.; Sánchez, L., Nanostructured iron(III) oxides: From design to gas- and liquid-phase photo-catalytic applications. *Thin Solid Films* **2014**, 564, 121-127.
30. Yang, X.; Qin, J.; Jiang, Y.; Chen, K.; Yan, X.; Zhang, D.; Li, R.; Tang, H., Fabrication of P25/Ag₃PO₄/graphene oxide heterostructures for enhanced solar photocatalytic degradation of organic pollutants and bacteria. *Appl. Catal., B* **2015**, 166–167, 231-240.
31. Yang, X.; Qin, J.; Jiang, Y.; Li, R.; Li, Y.; Tang, H., Bifunctional TiO₂/Ag₃PO₄/graphene composites with superior visible light photocatalytic performance and synergistic inactivation of bacteria. *RSC Adv.* **2014**, 4 (36), 18627-18636.
32. Yang, X.; Qin, J.; Li, Y.; Zhang, R.; Tang, H., Graphene-spindle shaped TiO₂ mesocrystal composites: Facile synthesis and

- enhanced visible light photocatalytic performance. *J. Hazard. Mater.* **2013**, *261*, 342-350.
33. Jo, W.-K.; Selvam, N. C. S., Synthesis of GO supported Fe₂O₃-TiO₂ nanocomposites for enhanced visible-light photocatalytic applications. *Dalton Trans.* **2015**, *44* (36), 16024-16035.
34. Moniz, S. J. A.; Shevlin, S. A.; An, X.; Guo, Z.-X.; Tang, J., Fe₂O₃-TiO₂ Nanocomposites for enhanced Charge Separation and Photocatalytic Activity. *Chem. Eur. J.* **2014**, *20* (47), 15571-15579.
35. Zhang, X.; Xie, Y.; Chen, H.; Guo, J.; Meng, A.; Li, C., One-dimensional mesoporous Fe₂O₃@TiO₂ core-shell nanocomposites: Rational design, synthesis and application as high-performance photocatalyst in visible and UV light region. *Appl. Surf. Sci.* **2014**, *317* (0), 43-48.
36. Xia, Y.; Yin, L., Core-shell structured α-Fe₂O₃@TiO₂ nanocomposites with improved photocatalytic activity in the visible light region. *Phys. Chem. Chem. Phys.* **2013**, *15* (42), 18627-18634.
37. Zhang, P.; Yin, S.; Sato, T., The influence of synthesis method on the properties of iron contained N doped TiO₂ photocatalysts. *Appl. Catal., B* **2011**, *103* (3-4), 462-469.
38. Kim, J. Y.; Kim, C. S.; Chang, H. K.; Kim, T. O., Synthesis and characterization of N-doped TiO₂/ZrO₂ visible light photocatalysts. *Adv. Powder Technol.* **2011**, *22* (3), 443-448.
39. Mahadik, M. A.; Shinde, S. S.; Mohite, V. S.; Kumbhar, S. S.; Moholkar, A. V.; Rajpure, K. Y.; Ganesan, V.; Nayak, J.;

- Barman, S. R.; Bhosale, C. H., Visible light catalysis of rhodamine B using nanostructured Fe_2O_3 , TiO_2 and $\text{TiO}_2/\text{Fe}_2\text{O}_3$ thin films. *J. Photochem. Photobiol. B* **2014**, *133* (0), 90-98.
40. Ctibor, P.; Pala, Z.; Stengl, V.; Musalek, R., Photocatalytic activity of visible-light-active iron-doped coatings prepared by plasma spraying. *Ceram. Int.* **2014**, *40* (1, Part B), 2365-2372.
41. Zhang, X.; Lei, L., Preparation of photocatalytic Fe_2O_3 - TiO_2 coatings in one step by metal organic chemical vapor deposition. *Appl. Surf. Sci.* **2008**, *254* (8), 2406-2412.
42. Sathasivam, S.; Bhachu, D. S.; Lu, Y.; Bawaked, S. M.; Obaid, A. Y.; Al-Thabaiti, S.; Basahel, S. N.; Carmalt, C. J.; Parkin, I. P., Highly Photocatalytically active iron(III) titanium oxide thin films via aerosol-assisted CVD. *Chem. Vap. Deposition* **2015**, *21*, 21-25.
43. Barreca, D.; Carraro, G.; Gombac, V.; Gasparotto, A.; Maccato, C.; Fornasiero, P.; Tondello, E., Supported metal oxide nanosystems for hydrogen photogeneration: quo vadis? *Adv. Funct. Mater.* **2011**, *21* (14), 2611-2623.
44. Carraro, G.; Maccato, C.; Gasparotto, A.; Barreca, D.; Walter, M.; Mayrhofer, L.; Moseler, M.; Venzo, A.; Seraglia, R.; Marega, C., An old workhorse for new applications: $\text{Fe}(\text{dpm})_3$ as a precursor for low-temperature PECVD of iron(III) oxide. *Phys. Chem. Chem. Phys.* **2015**, *17* (17), 11174-11181.
45. Carraro, G.; Gasparotto, A.; Maccato, C.; Bontempi, E.; Bilo, F.; Peeters, D.; Sada, C.; Barreca, D., A plasma-assisted approach

- for the controlled dispersion of CuO aggregates into β -iron(iii) oxide matrices. *CrystEngComm* **2014**, *16* (37), 8710-8716.
46. Carraro, G.; Maccato, C.; Gasparotto, A.; Kaunisto, K.; Sada, C.; Barreca, D., Plasma-assisted fabrication of Fe₂O₃/Co₃O₄ nanomaterials as anodes for photoelectrochemical water splitting. *Plasma Processes Polym.* **2016**, *13*, 191-200.
 47. Gasparotto, A.; Barreca, D.; Bekermann, D.; Devi, A.; Fischer, R. A.; Maccato, C.; Tondello, E., Plasma processing of nanomaterials: Emerging technologies for sensing and energy applications. *J. Nanosci. Nanotechnol.* **2011**, *11* (9), 8206-8213.
 48. Balbuena, J.; Cruz-Yusta, M.; Sánchez, L., Nanomaterials to combat NO_x pollution. *J. Nanosci. Nanotechnol.* **2015**, *15* (9), 6373-6385.
 49. Polat, M.; Soylyu, A. M.; Erdogan, D. A.; Erguven, H.; Vovk, E. I.; Ozensoy, E., Influence of the sol-gel preparation method on the photocatalytic NO oxidation performance of TiO₂/Al₂O₃ binary oxides. *Catal. Today* **2015**, *241*, 25-32.
 50. Barreca, D.; Gasparotto, A.; Tondello, E.; Sada, C.; Polizzi, S.; Benedetti, A., Nucleation and Growth of Nanophasic CeO₂ Thin Films by Plasma-Enhanced CVD. *Chem. Vap. Deposition* **2003**, *9* (4), 199-206.
 51. Briggs, D.; Seah, M. P., *Practical Surface Analysis: Auger and X-ray Photoelectron Spectroscopy*, 2nd ed. John Wiley & Sons: New York: 1990.

52. ISO 22197-1. Fine ceramics (advanced ceramics, advanced technical ceramics); test method for air purification performance of semiconducting photocatalytic materials. Part 1: removal of nitric oxide; 2007.
53. Pandey, S. K.; Kim, K.-H.; Chung, S.-Y.; Cho, S. J.; Kim, M. Y.; Shon, Z.-H., Long-term study of NO_x behavior at urban roadside and background locations in Seoul, Korea. *Atmospheric Environ.* **2008**, *42* (4), 607-622.
54. Sugrañez, R.; Balbuena, J.; Cruz-Yusta, M.; Martín, F.; Morales, J.; Sánchez, L., Efficient behaviour of hematite towards the photocatalytic degradation of NO_x gases. *Appl. Catal., B* **2015**, *165*, 529-536.
55. Signoretto, M.; Ghedini, E.; Trevisan, V.; Bianchi, C. L.; Ongaro, M.; Cruciani, G., TiO₂-MCM-41 for the photocatalytic abatement of NO_x in gas phase. *Appl. Catal., B* **2010**, *95* (1-2), 130-136.
56. Bloh, J. Z.; Folli, A.; Macphee, D. E., Photocatalytic NO_x abatement: why the selectivity matters. *RSC Adv.* **2014**, *4* (86), 45726-45734.
57. Binitha, G.; Soumya, M. S.; Madhavan, A. A.; Praveen, P.; Balakrishnan, A.; Subramanian, K. R. V.; Reddy, M. V.; Nair, S. V.; Nair, A. S.; Sivakumar, N., Electrospun α -Fe₂O₃ nanostructures for supercapacitor applications. *J. Mater. Chem. A* **2013**, *1* (38), 11698-11704.
58. Warwick, M. E. A.; Kaunisto, K.; Barreca, D.; Carraro, G.; Gasparotto, A.; Maccato, C.; Bontempi, E.; Sada, C.; Ruoko, T.-

- P.; Turner, S.; Van Tendeloo, G., Vapor Phase Processing of α -Fe₂O₃ Photoelectrodes for Water Splitting: An Insight into the Structure/Property Interplay. *ACS Appl. Mater. Interfaces* **2015**, 7 (16), 8667-8676.
59. Barreca, D.; Carraro, G.; Gasparotto, A.; Maccato, C.; Lebedev, O. I.; Parfenova, A.; Turner, S.; Tondello, E.; Van Tendeloo, G., Tailored vapor-phase growth of Cu_xO–TiO₂ (x = 1, 2) nanomaterials decorated with Au particles. *Langmuir* **2011**, 27 (10), 6409-6417.
60. Moulder, J. F.; Stickle, W. F.; Sobol, P. E.; Bomben, K. D., *Handbook of X-ray Photoelectron Spectroscopy*. Perkin Elmer Corporation, Eden Prairie, MN, USA: 1992.
61. Lasek, J.; Yu, Y.-H.; Wu, J. C. S., Removal of NO_x by photocatalytic processes. *J. Photochem. Photobiol., C* **2013**, 14, 29-52.
62. Laufs, S.; Burgeth, G.; Duttlinger, W.; Kurtenbach, R.; Maban, M.; Thomas, C.; Wiesen, P.; Kleffmann, J., Conversion of nitrogen oxides on commercial photocatalytic dispersion paints. *Atmos. Environ.* **2010**, 44 (19), 2341-2349.
63. Devahasdin, S.; Fan Jr, C.; Li, K.; Chen, D. H., TiO₂ photocatalytic oxidation of nitric oxide: transient behavior and reaction kinetics. *J. Photochem. Photobiol., A* **2003**, 156 (1–3), 161-170.
64. Kaneko, M.; Okura, I., *Photocatalysis: Science and Technology*. Springer, Berlin Heidelberg: 2002.

65. Li, H.; Yin, S.; Wang, Y.; Sato, T., Efficient persistent photocatalytic decomposition of nitrogen monoxide over a fluorescence-assisted $\text{CaAl}_2\text{O}_4:(\text{Eu}, \text{Nd})/(\text{Ta}, \text{N})$ -codoped $\text{TiO}_2/\text{Fe}_2\text{O}_3$. *Appl. Catal., B* **2013**, 132–133, 487-492.
66. Liu, H.; Shon, H. K.; Sun, X.; Vigneswaran, S.; Nan, H., Preparation and characterization of visible light responsive $\text{Fe}_2\text{O}_3\text{--TiO}_2$ composites. *Appl. Surf. Sci.* **2011**, 257 (13), 5813-5819.
67. Wade, R. S.; Castro, C. E., Reactions of Oxymyoglobin with NO , NO_2 , and NO_2^- under Argon and in Air. *Chem. Res. Toxicol.* **1996**, 9 (8), 1382-1390.
68. Mikhaylov, R. V.; Lisachenko, A. A.; Shelimov, B. N.; Kazansky, V. B.; Martra, G.; Coluccia, S., FTIR and TPD study of the room temperature interaction of a NO –Oxygen mixture and of NO_2 with titanium dioxide. *J. Phys. Chem. C* **2013**, 117 (20), 10345-10352.
69. Sá, J.; Anderson, J. A., FTIR study of aqueous nitrate reduction over Pd/TiO_2 . *Appl. Catal. B* **2008**, 77 (3–4), 409-417.
70. Zhao, B.; Ran, R.; Wu, X.; Weng, D.; Wu, X.; Huang, C., Comparative study of Mn/TiO_2 and Mn/ZrO_2 catalysts for NO oxidation. *Catal. Commun.* **2014**, 56, 36-40.
71. Hadjiivanov, K. I., Identification of neutral and charged N_xO_y surface species by IR spectroscopy. *Catal. Rev.* **2000**, 42 (1-2), 71-144.

Electronic Supplementary Information

Advances in photocatalytic NO_x abatement through the use of Fe₂O₃/TiO₂ nanocomposites

José Balbuena,^a Giorgio Carraro,^{b,} Manuel Cruz,^a Alberto Gasparotto,^b*

Chiara Maccato,^b Adrián Pastor,^a Cinzia Sada,^c Davide Barreca,^d and Luis

Sánchez^{a,}*

^a Department of Inorganic Chemistry and Engineering Chemistry, Córdoba University, 14071 Córdoba, Spain.

^b Department of Chemistry, Padova University and INSTM, 35131 Padova, Italy.

^c Department of Physics and Astronomy, Padova University and INSTM, 35131 Padova, Italy.

^d ICMATE-CNR and INSTM, Department of Chemistry, Padova University and INSTM, 35131 Padova, Italy.

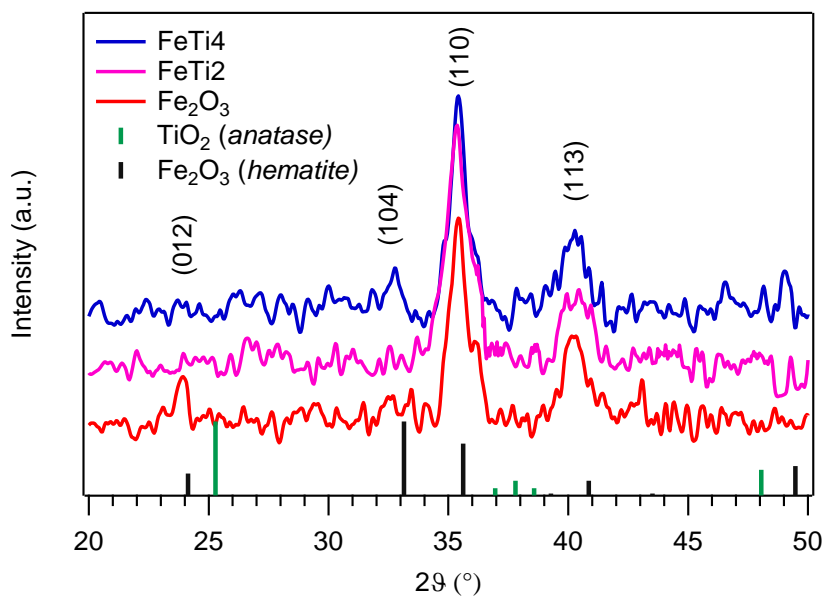


Figure S1. XRD diffraction patterns for bare Fe_2O_3 and for $\text{Fe}_2\text{O}_3\text{-TiO}_2$ nanocomposites. Peak positions for hematite [Pattern N° 33-0664, JCPDS (2000)] and anatase [Pattern N° 021-1272, JCPDS (2000)] are marked by vertical bars.

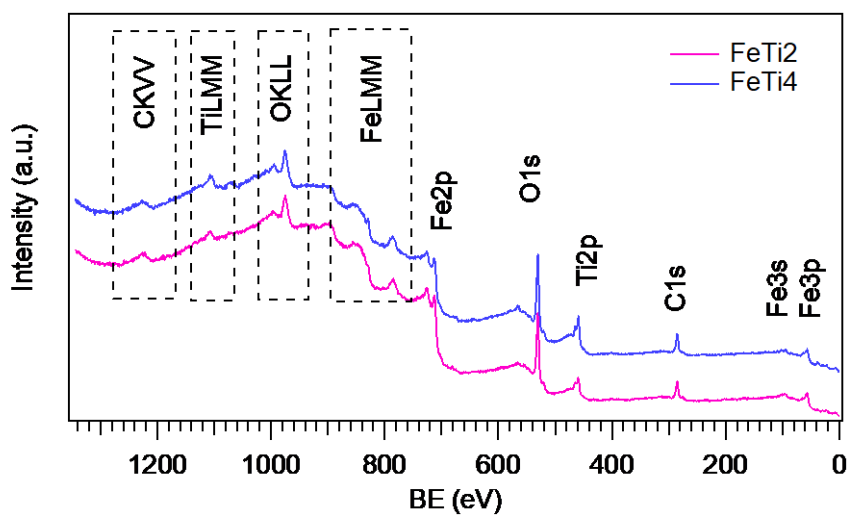


Figure S2. Surface XPS survey spectra of Fe₂O₃-TiO₂ nanocomposites.

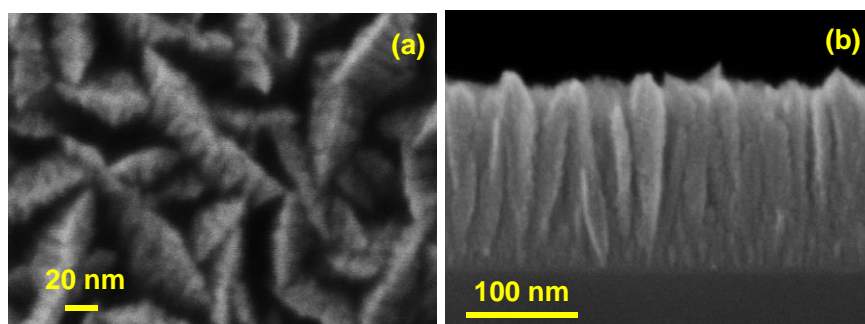


Figure S3. Plane view (a) and cross sectional (b) FE-SEM micrographs for a bare Fe₂O₃ deposit.

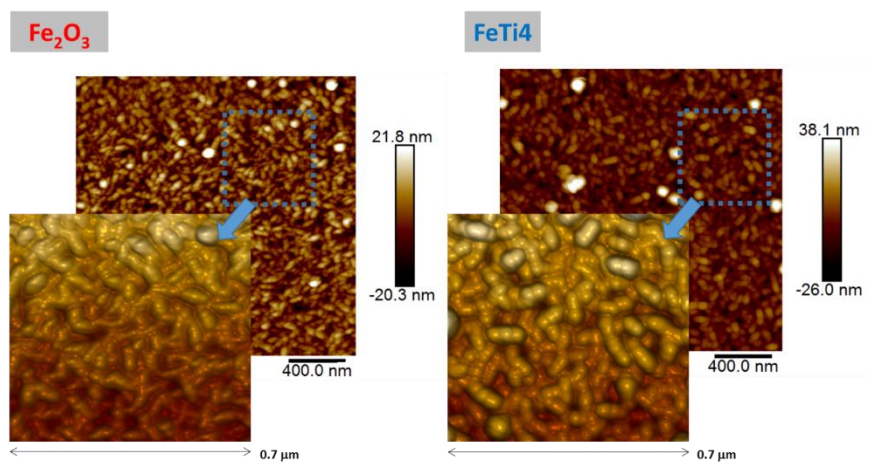


Figure S4. Representative AFM micrographs for bare Fe_2O_3 and FeTi4 specimens. Calculated root-mean-square (RMS) roughness values for Fe_2O_3 and FeTi4 samples are 74 and 84 nm, respectively.

Figure S5. *Concentration profiles obtained for P25, TiO₂, Fe₂O₃ and FeTi4 samples during the photochemical degradation of gaseous NO under Vis light irradiation.*

Figure S6. *Nitrogen oxide concentration profiles obtained for FeTi4 specimen under different utilization cycles.*

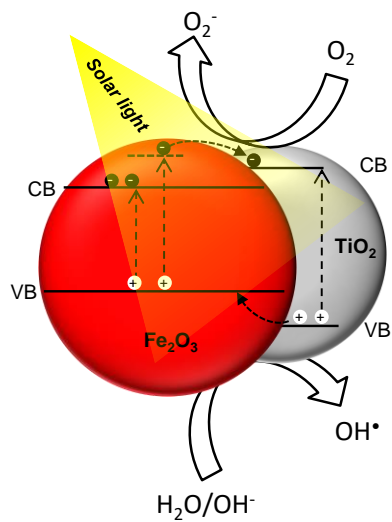


Figure S7. Simplified representation of the mechanism for PC activity enhancement occurring in $\text{Fe}_2\text{O}_3/\text{TiO}_2$ nanocomposites.

IR analysis

Infrared (IR) spectra were recorded by means of a Perkin Elmer FTIR System Spectrum BX, operating in transmittance mode at normal incidence.

The assignment of IR bands pertaining to Fig. S8 spectra is the following.

The band around 1640 cm^{-1} corresponds to O–H bending vibrations, implying the presence of adsorbed water (Fig. S8a). The bands marked in Fig. S8b were assigned basing on to the previously reported information on the interaction of nitrogen oxides with TiO_2 .⁶⁸⁻⁷⁰ The bands located at 1529 , 1506 and 1487 cm^{-1} correspond to stretching vibrations of nitrate species^{68-69, 71} whereas those at 1417 and 1261 cm^{-1} are ascribed to nitrite ones.^{69, 71} The band at 1710 cm^{-1} can be tentatively assigned to adsorbed NO_2 .⁷⁰ A more detailed attribution of IR bands attributed to N–O stretching vibrations of surface nitrate (NO_3^-) and nitrite (NO_2^-) species is a difficult task, since $\nu(\text{N-O})$ of different NO_3^- and NO_2^- species fall in the same $1700\text{--}1000\text{ cm}^{-1}$ interval and their IR bands are strongly overlapped.⁶⁸

Figure S8. IR spectra in the 1800 – 1200 cm⁻¹ range of (a) Fe₂O₃ and (b) FeTi4 samples before and after NO_x degradation tests.

3.4 Mesoporous and visible light active anatase: a high selectivity De-NO_x photocatalyst.

Mesoporous and visible light active anatase: a high selectivity De-NO_x photocatalyst

*J. Balbuena,^a J.M. Calatayud,^b M. Cruz-Yusta,^a P. Pardo,^b F. Martín,^c J. Alarcón,^{*b} and L. Sánchez^{*a}*

(a) Inorganic Chemistry Department, Campus de Rabanales, Universidad de Córdoba, Córdoba, 14071, Spain.

E-mail: luis-sanchez@uco.es

(b) Inorganic Chemistry Department, University of Valencia, Calle Dr. Moliner 50, Burjasot (Valencia), 46100, Spain.

E-mail: javier.alarcon@uv.es

(c) Chemical Engineering Department, Campus de Teatinos, Universidad de Málaga, Málaga, 29071, Spain.

E-mail: marjim@uma.es

* Corresponding Authors:

Abstract

The combined high effectiveness and selectivity on the NO_x abatement of a new photocatalyst with anatase structure is reported. The material was synthesized by a hydrothermal approach as nanoparticles sized around 20 nm and with surface area and pore volume of 63.5 m²·g⁻¹ and 0.22 cm³·g⁻¹, respectively. The reached maximized selectivity can be associated with the mesocrystalline nature of the anatase photocatalyst.

Keywords

Titanium oxide, Photocatalytic oxidation, Nitrogen oxides, Selectivity

STATUS: Submitted to Chemical Engineering Journal.

3.4.1. Introduction

Nitrogen oxides, commonly referred as NO_x – the nitric oxide (NO) and nitrogen dioxide (NO_2) –, are a group of different compounds that play a major role in atmospheric chemistry and air pollution. Several procedures have been developed to reduce the NO_x emission of combustion processes. Even though the selective catalytic or non-catalytic reduction processes are well-known, they aren't applicable to directly remove the NO_x gases in the urban atmosphere (De- NO_x action), which inlets are mostly coming from the road traffic.

The NO_x breathable by local residents is a major concern in the modern Society, because the human health is affected when the amount of NO_x interacting with lung tissues increases. As consequence, several diseases such as emphysemas, bronchitis, etc.¹, can be developed. In this sense, the environmental agencies in the USA and Europe communities limit the hourly NO_x air concentration at 0.1 ppm and 0.2 ppm, respectively. However, these limits are difficult to be attained because the NO_x emissions rates from vehicles worsen with their lifetime. In fact, nowadays higher NO_x levels are measured worldwide in very populated cities².

It has been recently evidenced that semiconductor photocatalysis could be a suitable alternative of removing NO_x and other air pollutants from the air once it has been already

released and dispersed³. It could be, therefore, applicable to directly remove large amounts of NO_x gases from the urban centers in our cities. In fact, at present, depolluting construction materials, using TiO₂ as photocatalytic additive, are integrated in some advanced buildings in an attempt to achieve an effective NO_x de-pollution in urban areas⁴⁻⁵. In the last few years, a great interest arise in the preparation of modified titania with enhanced De-NO_x photocatalytic performance⁶, being the advanced studies paying attention to: i) the semiconductor band gap modification, with the aim to take advantage of Visible light (Vis), because TiO₂ is a wide gap semiconductor with values over the range 3.0-3.2 eV and it is known that the UV light account for less than 5 % of the total solar irradiation⁷⁻⁸; ii) the increase of surface area to improve the contact between reactants in the heterogeneous catalysis process⁹; and iii) the preparation of new TiO₂ composites¹⁰⁻¹⁴.

However, when and how these advanced titania compounds could be considered as true De-NO_x photocatalyst in a commercial product? In order to answer this question it results of interest the MacPhee's work about the selectivity matter in the photocatalytic NO_x abatement¹⁵. The complete photocatalytic NO_x removal from air proceeds through the complete oxidation of NO (the main nitrogen gas emitted by vehicles) to nitrate or nitric acid (NO₃⁻/HNO₃), being this a complex process, that involves several intermediate species⁶.¹⁶. The nitrogen dioxide (NO₂) appears as intermediate specie,

which is undesired because is 8 to 25 times more dangerous than NO¹⁷. Therefore, the excellence for a titania De-NO_x photocatalyst won't be only focused into obtaining the highest NO conversion values but also the highest De-NO_x selectivity. This means that no photo-oxidized NO molecules was released again to the atmosphere as the highly toxic NO₂. However, it is to remark that in the recent literature, the reported modified titania photocatalysts do not fully inhibit the emission of NO₂ gas. According to the literature, these emissions reach low levels but only for either a very short period of light irradiation^{8, 18-19} or when negligible NO photochemical oxidation accounts^{15, 20} (Supporting Information, Table S1). Likewise, the excellent selectivity measured for different benchmark TiO₂ samples during the first hour of De-NO_x test decays to very low values in the subsequent few hours, because the emission of NO₂ increases continuously under light irradiation²¹.

In our viewpoint, the selectivity of the De-NO_x photocatalytic reaction deserves much attention, being the main target of this work. As a novelty, here is presented a very high selective De-NO_x titania photocatalyst combining high NO conversion values also, being both characteristics maintained for a large irradiation period. To achieve this successfully we have improved the photochemical performance of titania by expanding its activity towards Vis light and developing a mesocrystalline structure. It has been recently proposed that the ordering of nanocrystalline structures in self-

assembled nanomaterials considerably influences charge transport and recombination, which are directly related to the performance of photocatalysts. Moreover, the presence of mesoporous on these structures increases the surface area of the samples and its accessibility towards the reactant molecules, given rise to high degradation efficiency in solid-liquid²²⁻²⁴ and in air-liquid processes²⁵. As far as we know the use of mesocrystalline anatase as De-NO_x photocatalyst was not previously studied.

3.4.2. Materials and methods

Preparation of mesoporous anatase

Samples were prepared by a modified hydrothermal approach already reported in the literature²⁶. The starting materials were tetraisopropyl orthotitanate (C₁₂H₂₈O₄Ti) and triethanolamine (TEOA) was used as complexing agent. The nominal concentration of TiO₂ in the PTFE stainless steel autoclave was 0.25 M. The synthetic procedure can be described as follows. First, an amount of TEOA was solved in doubly distilled water to reach a titanium alkoxide/TEOA molar ratio of 1/2. This solution was hydrothermally aged in two steps. Through the first a gel was formed after heating at 100 °C for 24 h followed by the heating at 140 °C for 72 h. After the hydrothermal aging the sample was centrifuged and washed three times with water. The product was finally dried overnight in a drying oven at 100 °C and labeled as A. In order to remove TEOA, the as-prepared sample A was annealed at 350 °C for 30 min and

named as A350.

Instrumentation

Chemical, structural and microstructural characteristics of nanoparticles were monitored by different experimental techniques.

Elemental analysis was carried out in a CE Instruments EA1110 Elemental Analyzer, set for the detection of Nitrogen, Carbon and Hydrogen, using atropine as standard.

X-ray diffraction (XRD) analysis (model D-8 Advance, Bruker) was performed using CuK α radiation. The diffractometer had 1 and 3 mm divergence and antiscattering slits respectively, and a 3° 2 θ range Lynxeye linear detector. For the phase identification, the diffractogram was run with a step size of 0.02 2 θ ° and a counting time of 0.2 s. Raman spectra of samples were obtained by means of a Raman spectrometer (Model XploRA, Horiba) with 785 nm laser. X-ray photoelectron spectra (XPS) were recorded using non-monochromated MgK radiation (hv= 1253.6 eV) and a hemispherical analyser operating at a constant pass energy of 29.35 eV (Physical Electronics PHI 5700 spectrometer) with the X-ray generator operating at 15 kV and 300 W.

The microstructure of samples was examined by field emission scanning electron microscopy (FESEM) at 20 kV (Model S-4800, Hitachi Ltd., Tokyo, Japan). The samples were prepared by dropping a dispersion of the powders in water

directly onto the holder sample. Before the examination all specimens were coated with gold/palladium in an ion beam coater. The morphology of A and A350 titania particles was also examined using transmission electron microscopy (TEM; Model 1010, Jeol Ltd., Tokyo, Japan) at an accelerating voltage of 100 kV. Samples were dispersed in doubly distilled water and drops of the dispersion were transferred to a specimen copper grid carrying a lacey carbon film. High resolution transmission electron microscopy (HRTEM) images and Selected Area Diffraction (SAED) were collected using a Tecnai G2 F20 field emission electron microscope equipped with a Gatan CCD camera. Data treatment was performed with Digital Micrograph software. The samples were prepared in a similar way to the ones for TEM.

Nitrogen absorption isotherms were obtained at 77.4 K on an ASAP 2020 instrument from Micromeritics. Specific surface areas were calculated from N₂ sorption isotherms, using the multipoint Brunauer–Emmett–Teller (BET) method and microporosity and size distributions were estimated using the t-plot, Barret-Joyner-Halenda (BJH).

UV-Vis diffuse reflectance (DR) spectra of the specimens (Model V-670, Jasco) were obtained using the diffuse reflectance technique in the range of 200 to 2500 nm.

Probe NO (>99.9%, from Abello Linde S.A.) was carried out in an IR cell connected with a conventional outgassing/gas

manipulation apparatus and spectra were recorded in a Nicolet Nexus 6700 spectrometer with MCT detector.

Additional information is provided in Supporting Information (SI).

Photocatalysis

The photocatalytic activity of the materials towards the oxidation of NO was studied by using a 50 x 50 mm sampler holder placed in a laminar flow reactor. The reactor was placed inside a light sealed irradiation box (Solarbox 3000e RH) equipped with a Xe lamp with controlled irradiance. A 200 mg sample was used in each photocatalytic test. Artificial sunlight (25 and 550 $\text{W}\cdot\text{m}^{-2}$ for UV and visible irradiances, respectively) was used as irradiation. A mixture of air/NO was sent to the photoreactor. Air and NO gas streams were mixed to obtain the desired NO concentration: 500 ppb. Previously, air was conveyed by a gas-washing bottle, filled with demineralised water in order to keep the relative humidity of the supplied gas fixed at 50 ± 5 %. A flow rate, Q , of $0.75 \text{ L}\cdot\text{min}^{-1}$ was employed. The accurate measurement of the concentration of NO, NO_x and NO_2 was carried out using a chemiluminescence analyser (model Environnement AC32M). For each test, the air/NO gas stream ran over the sample in the dark for a period of 10 min without changes in the NO_x concentration profiles were observed, discarding the NO_x adsorption on the sample surface or its direct photolysis. Subsequently, the photoreactor was irradiated for 300 min. The tests were repeated three times to obtain average

concentration values. The calculated standard deviation is ± 0.3 ppb for NO concentration, and ± 1.0 ppb for NO₂ and NO_x concentration.

NO conversion, NO₂ released and NO_x conversion were defined as follows:

$$\text{NO removal rate (\%)} = \{ ([\text{NO}]_{\text{in}} - [\text{NO}]_{\text{out}}) / [\text{NO}]_{\text{in}} \} \times 100 \quad (1)$$

$$\text{NO}_2 \text{ released (\%)} = ([\text{NO}_2]_{\text{out}} / [\text{NO}]_{\text{in}}) \times 100 \quad (2)$$

$$\text{NO}_x \text{ conversion (\%)} = \{ ([\text{NO}_x]_{\text{in}} - [\text{NO}_x]_{\text{out}}) / [\text{NO}_x]_{\text{in}} \} \times 100 \quad (3)$$

where [NO]_{in}, [NO_x]_{in} and [NO]_{out}, [NO₂]_{out}, [NO_x]_{out} denote the measured inlet and outlet concentrations, respectively, while [NO_x] = [NO] + [NO₂]. The used values were the average of the measured one under steady state period.

Conversely, the selectivity towards the removal of efficient removal of NO_x gas molecules, *S*, here is derived according to equation (4):

$$S (\%) = \frac{([\text{NO}_x]_{\text{in}} - [\text{NO}_x]_{\text{out}}) / [\text{NO}_x]_{\text{in}}}{([\text{NO}]_{\text{in}} - [\text{NO}]_{\text{out}}) / [\text{NO}]_{\text{in}}} \times 100 \quad (4)$$

3.4.3. Results and discussion

Samples characterization

Anatase was prepared by a hydrothermal approach, which allowed obtaining discrete, size-controlled and well-defined

morphologically mesocrystalline nanoparticles. The titanium source was tetraisopropyl orthotitanate ($\text{C}_{12}\text{H}_{28}\text{O}_4\text{Ti}$), and triethanolamine (TEOA) was used as complexing agent. The XRD pattern of the as-prepared sample after hydrothermal aging at $140\text{ }^\circ\text{C}$ for 72 h, named sample A, is shown in Fig. 1(a). All detected peaks can be attributed to a crystalline phase with anatase structure (ICDD 00-021-1272). The lattice parameters of sample A obtained by refinement of the XRD pattern by the Rietveld method (Table S2) and the corresponding Rietveld plot (Fig. S1) confirmed anatase as the only crystalline phase formed through the hydrothermal aging.

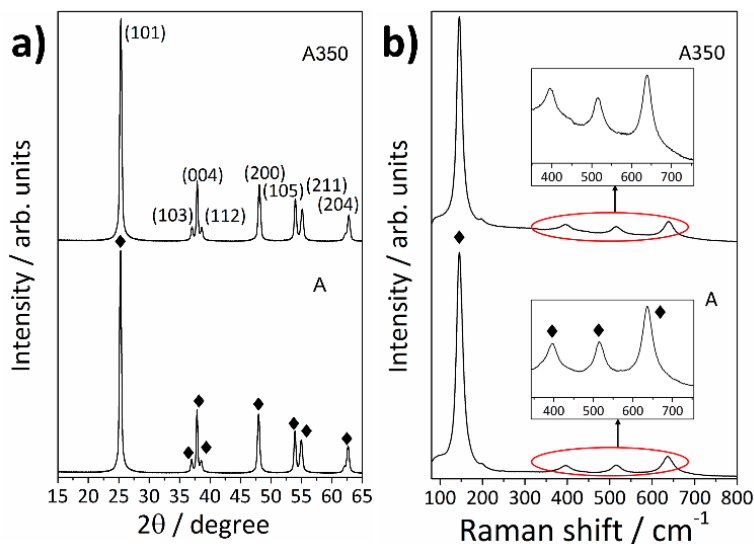


Figure 1. (a) XRD patterns and (b) Raman spectra of samples: A (as-prepared by hydrothermal aging) and A350 (after further annealing at $350\text{ }^\circ\text{C}$ for 0.5 h). [◆ = anatase phase].

The Raman spectrum of the as-prepared sample A is shown in Fig. 1b, Bands at around 142, 195, 389, 510 and 635 cm^{-1} are detected, confirming the presence of a phase with anatase structure²⁷.

The amount of carbon and nitrogen determined by elemental analysis in the as-prepared sample A is shown in Table S3. The C/N ratio near to the theoretical one, 6.0, reveals the presence of TEOA attached to anatase nanoparticles, being estimated in 3.4 TEOA wt % content. Through the calcination of sample A a rapid decreases of C/N ratio and C and N content is found (Table S3). Therefore, TEOA is easily eliminated at relatively low annealing temperatures. For sample A350 (obtained after annealing the pristine sample A at 350 °C during 30 min) can be assumed that no TEOA amine remains attached to the surface so it can be considered to be pure anatase. Thus, as it could be expected for that sample A350 no structural changes were detected (Fig 1; Fig S2; Table S2).

The valence states of titanium cations were investigated by XPS measurements on the surface. Fig. S3 (left) shows comparatively the Ti 2p XPS regions of the samples A and A350. The binding energies at 458.8 eV and 464 eV are attributed to Ti^{4+} 2p_{3/2} and Ti 2p_{1/2}²⁸. No nitrogen signal was found in the region of N 1s for both samples. This could be attributed to the fact that the adsorbed residual amine could have been desorbed during the overnight high vacuum treatment carried out before XPS measurement. This fact

indicates that no substitutional and/or interstitial nitrogen is inside the anatase nanoparticles. The XPS spectra for the O 1s region for samples A and A350 are also displayed in Fig. S3 (right). The O 1s peak can be de-convoluted in two peaks for both samples, one main peak appearing at 530 eV which is associated with lattice oxygen (Ti–O–Ti) in TiO_2 ²⁸, being the signal at 531 eV attributed to Ti–OH hydroxyl groups²⁹.

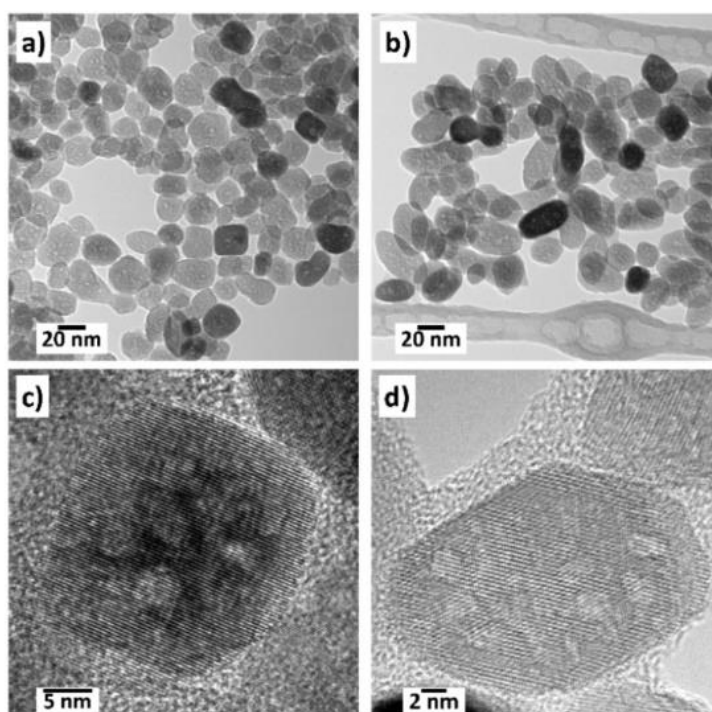


Figure 2. TEM micrograph of samples: (a) A; (b) A350. HRTEM micrographs of samples: (c) A; (d) A350. These micrographs show that the particles are formed by an assembly of anatase nanocrystals sized around 2 nm which grow all oriented in the same direction, dominated by the (101) surface.

TEM micrographs of samples A and A350 are displayed in Figs 2a and 2b, respectively. As can be seen, both samples contain non-aggregated particles with sizes around 20 nm. It is to note that the equidimensional cross-section of nanoparticles in sample A become more elongated after annealing at 350 °C (sample A350). TEM images display porous structure in both samples, indicating that voids exist in the discrete nanoparticles. SEM micrographs of samples A and A350 shown in Fig. S4 confirm that both prepared anatase samples contain discrete particles.

HRTEM images of anatase samples A and A350 could provide further structural and microstructural information. Figs. 3a and 3d show ordered fringes with 0.35 nm of spacing in samples A and A350. Those fringes can be assigned to the (101) planes of anatase with the lattice parameters shown in Table S2. SAED of both samples, Figs. 3c and 3f, confirm the high crystallinity of the nanoparticles. All rings in the patterns can be unambiguously attributed to a crystalline phase with the structure of anatase. Further features related with their mesocrystallinity can also be found in the HRTEM images of these nanoparticles. Thus, in Figs. 2c and 2d can be clearly distinguished the presence of very small nanocrystals, being dominated in both samples by the (101) surfaces. It is to note also that the porosity of these spherical assemblies (nanoparticles) is disordered.

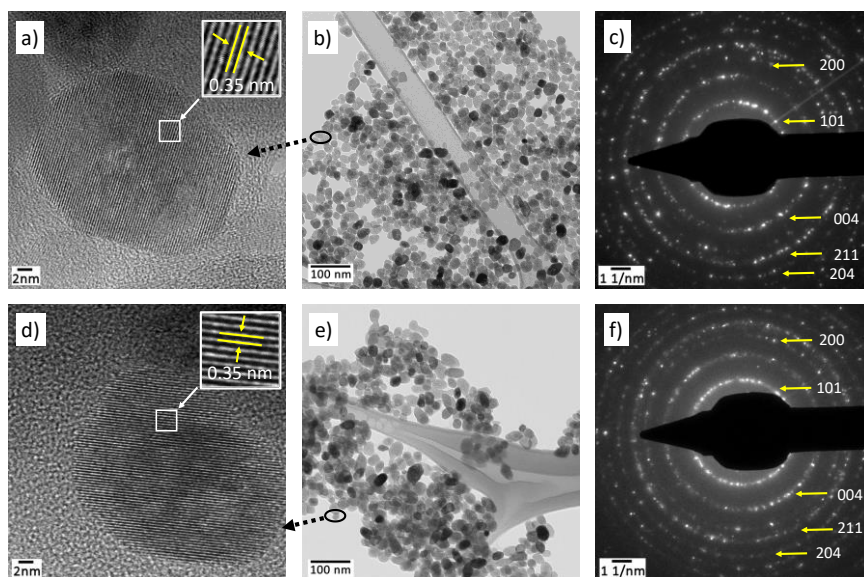


Figure 3. HRTEM micrographs of samples A and A350: a) and d) lattice fringes of samples A and A350 associated with planes (101); b) and e) set of nanoparticles of sample A and A350; c) and f) SAED of the previous set of nanoparticles showing the indexed rings to anatase phase.

These results clearly indicate the formation of mesocrystalline anatase built by anatase nanocrystals sized around 2 nm which aggregate all oriented in the same direction giving rise to uniform assemblies (nanoparticles) with spherical shape and mesoporosity.

Following the aim of this work, additional characterization concerning to their light activation and the surface area exposed to the reactant molecules was performed. The surface area and porous structure were elucidated from the corresponding N_2 adsorption-desorption isotherm of samples A and A350, Fig. 4a. As

can be seen the isotherms of both prepared samples exhibit hysteresis loop at high relative pressure between around 0.08 and 1.0, which indicates the presence of mesopores. Table S4 summarizes the main microstructural characteristics of the prepared samples A and A350. The pore size distribution for both prepared anatase samples is similar with maximum pore size around 13 nm (Fig 4a inset), being the surface area 74.9 and 63.6 m² g⁻¹ for the samples A and A350, respectively. The set of structural characteristics together with the results of XRD, SEM and TEM indicate that the annealing at low temperature of the as-prepared sample A has only small effects on the morphology and crystal structure (sample A350). The corresponding UV-Vis DR spectra of the samples are shown in Fig. 4b. As expected, a strong absorption extended over the UV radiation up to around 400 nm for the both samples. Sample A exhibits also a strong absorption on 400 – 800 nm Vis range, which could be associated with the presence of TEOA attached to the anatase nanoparticle surface³⁰. Interestingly, even though the TEOA is removed, a weak absorption tail remains at wavelengths higher than 400 nm even for the sample A350. A similar behavior was reported by Elbanna et al.²² on preparing anatase mesocrystals, being the absorption associated to both interstitial and molecularly chemisorbed N in N-doped TiO₂ or oxygen vacancies. Since our results from XPS did not indicate the presence of structural or interstitial nitrogen it could be associated with some chemisorbed nitrogen and/or even oxygen vacancies in the lattice of mesocrystalline anatase. For comparison purposes the

commercial Aeroxide[®] TiO_2 P25 (Evonik) was also studied, a material broadly used worldwide as reference in photocatalysis. The corresponding physical characterization is provided in SI, Fig. S5.

Figure 4. (a) N_2 adsorption-desorption isotherm and (b) UV-Vis DR spectra for samples A (black) and A350 (red). The spectra of the reference P25 is also included (blue).

NO_x photocatalytic oxidation test

The photocatalytic De-NO_x behavior is evaluated from the evolution of nitrogen oxides concentration profiles recorded for the titania samples as a function of UV-Vis irradiation time, Fig. 5. The NO concentration only decreases under irradiation, evidencing the occurrence of a light-induced chemical reaction. Previously, during the first 10 min the gas concentration remains constant avoiding the existence of adsorption phenomena. When illumination is shutdown, the gas concentration returned almost to its initial value. The NO conversion values recorded for sample A350 were quite similar to that of reference P25; (59 and 70 % NO conversion, respectively). In both cases, the constant values achieved after five hours indicated that a steady state condition of maximum activity was reached^{21, 31}. As can be seen in Fig. 5a the photocatalytic behavior of sample A resulted radically different and NO concentration increases continuously under light irradiation. This is consequence of the presence of TEOA molecules anchored to the surface of the titania particles, being this organic compound degraded by photocatalysis. Therefore the pristine sample is not suitable as De-NO_x photocatalyst, being necessary to work with calcined samples on which TEOA was previously eliminated. Anyway, the effective air quality improvement reached by photocatalyst must take into account the presence of NO₂ undesired intermediates.³² It is to remark in this sense the excellent De-NO_x activity of the A350 prepared titania. As shown in Fig. 5b,

very low NO₂ concentrations were measured for sample A350. Therefore, the annealed at very low temperature titania sample A350 is able to photo-chemically oxidize the NO molecules minimizing as maximum the release of harmful nitrogen oxide gases to the atmosphere, with a very high selectivity value of 89 %. As far as we know this is the first time that this significant feature is reported for long time irradiated samples.

With regard to this, it is to note that some of the samples listed on Table S1 exhibited high selectivity values (low emission of NO₂). However, it must be noted that those studies were performed at short time of irradiation (30 to 120 min), gives rise to uncertainty about those values because the NO_x removal capability of many TiO₂ based phototacalysts diminishes as the illumination proceeds in a large period^{21, 31}. This feature has been related to the photochemical renoxitification pathway leading to the release of NO and NO₂ from surface NO₃⁻ molecules^{31, 33}.

This is corroborated for the P25 titania, as previously reported²¹. From its NO_x concentration profiles, Fig 5c, it is observed that the theoretical full oxidation of NO towards nitrites/nitrates lowers with the irradiation time and very high amounts of NO₂ molecules are increasingly released during the experiment. In fact, after five hours of irradiation, the P25 oxidized around 70 % of molecules, but one third of them are converted in the highly toxic NO₂.

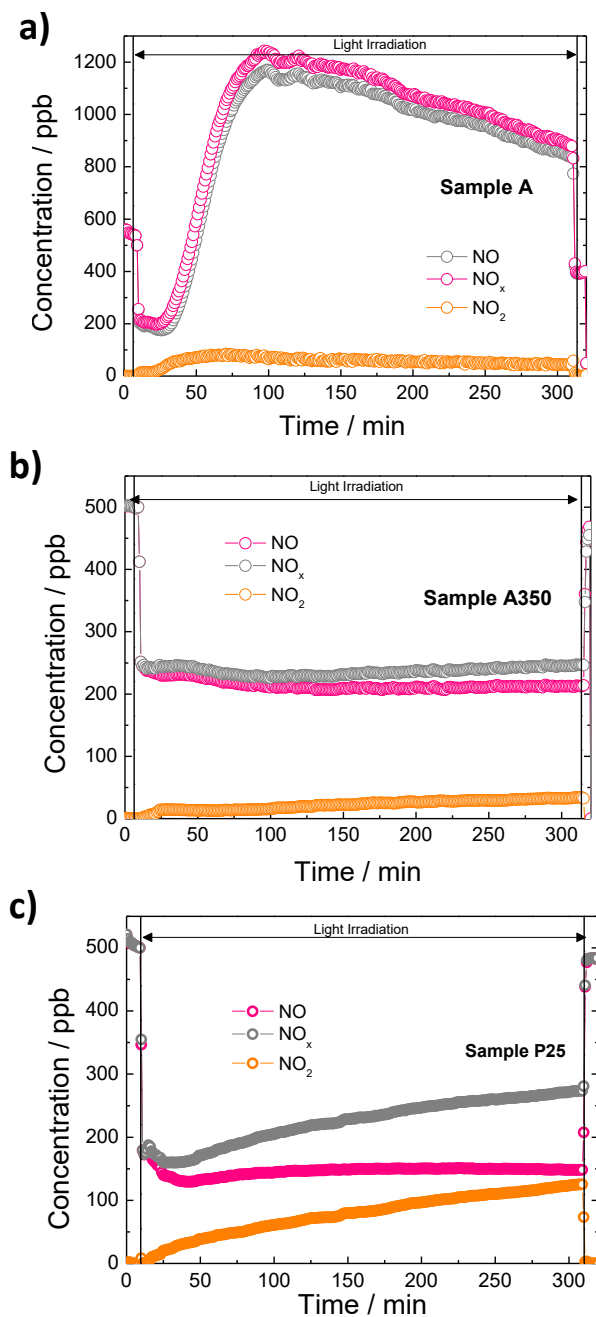


Figure 5. Nitrogen oxides concentration profiles obtained during the photo-degradation of gaseous NO under UV-Vis irradiation on Samples (a) A, (b) A350 and (c) P25.

Consequently, in terms of NO_x removal capability the prepared titania appear as a desired photocatalyst, as summarized in Fig 6. Thus, it combines the high efficiency on the photochemical NO conversion (grey bar) and selectivity (green bar), resulting the highest NO_x conversion (orange bar). Moreover, the stability of sample A350 was investigated. After the photocatalytic reaction, the sample was subjected to a washing process with 5 mL of MilliQ water for 1.0 h, subsequently the product was collected by centrifugation and dried. Similar NO nitrogen oxides concentration profiles were recorded (Fig. S6) over the course of a new 5 hours photocatalytic cycle, supporting the good reusability of this catalyst.

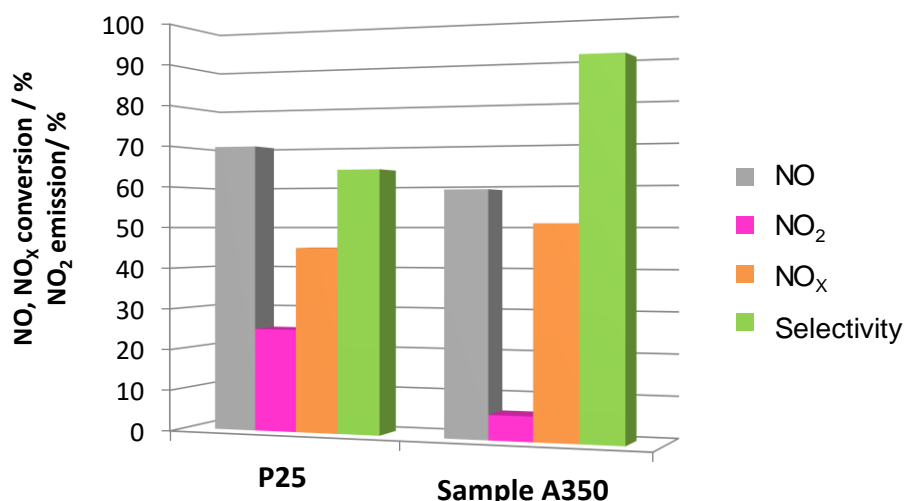


Figure 6. NO conversion (%), NO_2 released (%), NO_x conversion (%) and selectivity values (%) for A350 and P25 TiO_2 samples after five hours of light irradiation.

It is worthwhile to note that the sample A350 also exhibits De- NO_x activity under Vis light. This functionality is of high interest

for practical applications because the 4-5% of UV energy incoming from sunlight rapidly decreases to 0-2% in the cities of Central/Northern Europe or North America, owing to geography and gloomy weather condition³⁴. Fig. S7 shows the NO concentration profile recorded for the A350 and P25 samples under Vis light ($\lambda > 510$ nm), obtained as a short demonstrative test. The NO conversion efficiency is proportional to the Vis absorption ability showed by each sample, Fig 4b³⁰. It is outstanding that the conversion efficiency for sample A350 is 2.5 times greater than that of P25.

It must be highlighted that other advanced De-NO_x titania photocatalysts and P25 also, with similar or lower particle size or higher surface active area did not shown such high selectivity (Table 1S). Therefore, the singular mesopore structure seems to play an important role in the photochemical NO oxidation process inhibiting the NO₂ emission. During the photochemical oxidation of NO towards nitrites/nitrates, following the already proposed mechanisms⁶, NO₂ molecules could be released to the atmosphere because: i) their weak adsorption on the TiO₂ surface³³; ii) or the existence of a renoxification pathway involving the photochemistry of the NO₃• radical³⁵⁻³⁶. In order to gain a deeper knowledge, two additional experiences were performed. Firstly, NO adsorption studies were carried out onto sample A350 surface (experimental details are provided in SI). Prior to the NO admission into the IR cell, the sample was outgassed during 8 h at 50 °C in vacuum, Fig 7a.

Subsequently, a pulse of NO (5 Torr) was introduced at the cell. The IR spectrum was recorded after gas phase evacuation at 50 °C during 10 min, Fig. 7b. For comparison, the IR spectrum for P25 sample was also obtained, Fig 7c. The spectrum of samples A350 and P25 were rather different indicating a remarkably difference for the reactive NO adsorption. For sample A350, two main IR bands located at 1.351 and 1375 cm^{-1} , characteristic of nitro/nitrite compounds ($\text{M}-\text{NO}_2$; $\text{M}-\text{ONO}$;) were found³⁷⁻³⁸.

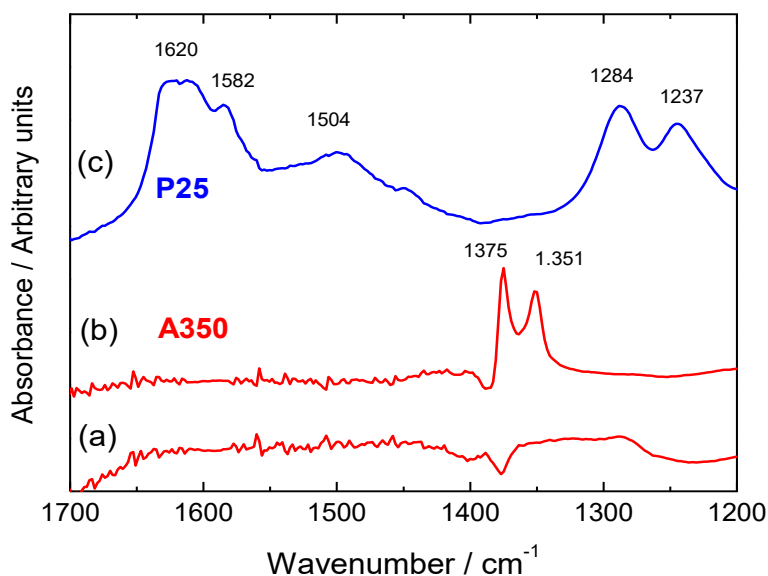


Figure 7. (a) IR spectra of Sample A350 after 8 hours of outgassing at 50 °C in vacuum. IR spectra of samples (b) A350 and (c) P25 after exposure to 5.0 Torr NO and evacuation at 50 °C for 10 min.

Conversely, a set of bands at 1620, 1582, 1504, 1284 and 1237 cm^{-1} are identified on the P25 IR spectrum. According with similar experiences of NO adsorption on P25, these bands are assigned to bidentate and bridged nitrate ($\text{M}-\text{NO}_3$)³⁹. The

elucidation of the specific mechanism for the reactive NO adsorption in both samples is beyond to this study. However it is interesting to point out that, in contrast for sample A350, the presence of NO₃⁻ molecules on P25 after NO adsorption let to suggest that a renoxification mechanism would be easily initiated when the surface is irradiated with UV light³⁵⁻³⁶, in agreement with the NO_x concentration profiles of Fig 5c.

On the other hand, it is known that mesoporous networks make easy the accessibility of active reactive sites to the reactant molecules²³⁻²⁴. These pores would be a sink on which the nitrogen oxide gases and water vapour molecules are trapped, which serve to restrain the in situ formed NO₂ molecules. With the aim to obtain indirect evidence about the influence of the mesoporous network onto the photochemical activity, the NO_x removal capability of A600 sample (Table S3) was preliminary studied. The microstructure of this titania A600 was slightly different to that of sample A350. Even though mesopores still exist, the volume of pores and surface area are reduced more than half (Fig S8 a), this had a direct drastic influence on its photochemical activity also for a short irradiation period as shown in Fig S8 b, mainly concerning to the selectivity. The NO conversion efficiency wasn't highly affected by the decrease of surface area. However, the loss of mesopore volume seems to be crucial because most of the NO converted molecules are now released as NO₂ and the selectivity value decays to 71 %. Therefore, the adsorption of NO₂ molecules seems to be

favoured on mesostructured sample A350, facilitating the completion of the $\text{NO} \rightarrow \text{NO}_2 \rightarrow \text{NO}_3^-$ photo-oxidation process to reach the highest selective De-NO_x values.

3.4.4. Conclusions

In summary, discrete, size-controlled and well-defined morphologically mesocrystalline anatase nanoparticles were synthesized by a hydrothermal approach. The titania samples exhibited mesoporosity and photoactivity towards Vis light. Both singular characteristics allow obtaining not only high NO conversion values but also a more selective De-NO_x process, being this reported by the first time. The high reproducibility of this facile method of preparation of nanoparticles, its easy scaled up to industrial level, and the high efficiency for the abatement of NO_x gases provide optimism in the preparation of new advanced applications to remove the NO_x breathable by the residents that are located in the polluted urban centers.

Acknowledgements

This work was financially supported by the Spanish Government (CSD2010-00065 and TEC2014-53906-R projects), Generalitat Valenciana (Prometeo II/2015/002), Junta de Andalucía (Group FQM-175) and Córdoba University (XX PP. Modalidad 4.1). We thank to Marina Cortes Reyes for her collaboration in the NO adsorption measurements.

Supporting Information Paragraph

Supporting Information accompanying this paper includes more information about: the characterization of the samples; reported De-NO_x values of different titanium based photocatalysts; crystallographic data, chemical analysis and textural properties; X-ray diffraction; XPS spectroscopy; SEM-TEM micrographs; P25 characterization; photocatalytic activity. This material is available free of charge via the Internet at <http://pubs.acs.org>.

References

1. Chen, B.; Hong, C.; Kan, H., Exposures and health outcomes from outdoor air pollutants in China. *Toxicology* **2004**, *198* (1–3), 291-300.
2. Chen, Y.; Borcken-Kleefeld, J., NO_x Emissions from diesel passenger cars worsen with age. *Environ. Sci. Technol.* **2016**, *50* (7), 3327-3332.
3. de_Richter, R.; Caillol, S., Fighting global warming: The potential of photocatalysis against CO₂, CH₄, N₂O, CFCs, tropospheric O₃, BC and other major contributors to climate change. *J. Photochem. Photobiol. C* **2011**, *12* (1), 1-19.
4. Sugrañez, R.; Álvarez, J. I.; Cruz-Yusta, M.; Mármol, I.; Morales, J.; Vila, J.; Sánchez, L., Enhanced photocatalytic degradation of NO_x gases by regulating the microstructure of mortar cement modified with titanium dioxide. *Build. Environ.* **2013**, *69*, 55-63.
5. Folli, A.; Pochard, I.; Nonat, A.; Jakobsen, U. H.; Shepherd, A. M.; Macphee, D. E., Engineering photocatalytic cements: understanding TiO₂ surface chemistry to control and modulate photocatalytic performances. *J. Am. Ceram. Soc.* **2010**, *93* (10), 3360-3369.
6. Balbuena, J.; Cruz-Yusta, M.; Sánchez, L., Nanomaterials to Combat NO_x Pollution. *J. Nanosci. Nanotechnol.* **2015**, *15* (9), 6373-6385.
7. Pan, J. H.; Wang, X. Z.; Huang, Q.; Shen, C.; Koh, Z. Y.; Wang, Q.; Engel, A.; Bahnemann, D. W., Large-scale synthesis of urchin-

- like mesoporous TiO₂ hollow spheres by targeted etching and their photoelectrochemical properties. *Adv. Funct. Mater.* **2014**, *24* (1), 95-104.
8. Trapalis, A.; Todorova, N.; Giannakopoulou, T.; Boukos, N.; Speliotis, T.; Dimotikali, D.; Yu, J., TiO₂/graphene composite photocatalysts for NO_x removal: A comparison of surfactant-stabilized graphene and reduced graphene oxide. *Appl. Catal. B: Environ.* **2016**, *180*, 637-647.
 9. Chin, S.; Park, E.; Kim, M.; Jeong, J.; Bae, G.-N.; Jurng, J., Preparation of TiO₂ ultrafine nanopowder with large surface area and its photocatalytic activity for gaseous nitrogen oxides. *Powder Technol.* **2011**, *206* (3), 306-311.
 10. Martins, N. C. T.; Ângelo, J.; Girão, A. V.; Trindade, T.; Andrade, L.; Mendes, A., N-doped carbon quantum dots/TiO₂ composite with improved photocatalytic activity. *Appl. Catal. B: Environ.* **2016**, *193*, 67-74.
 11. Nguyen, N. H.; Bai, H., Effect of washing pH on the properties of titanate nanotubes and its activity for photocatalytic oxidation of NO and NO₂. *Appl. Surf. Sci.* **2015**, *355*, 672-680.
 12. Ângelo, J.; Andrade, L.; Mendes, A., Highly active photocatalytic paint for NO_x abatement under real-outdoor conditions. *Appl. Catal. A: Gen.* **2014**, *484*, 17-25.
 13. Neupane, M. P.; Lee, S. J.; Kang, J. Y.; Park, I. S.; Bae, T. S.; Lee, M. H., Surface characterization and corrosion behavior of silanized magnesium coated with graphene for biomedical application. *Mater. Chem. Phys.* **2015**, *163*, 229-235.

14. Xiao, S.; Zhu, W.; Liu, P.; Liu, F.; Dai, W.; Zhang, D.; Chen, W.; Li, H., CNTs threaded (001) exposed TiO₂ with high activity in photocatalytic NO oxidation. *Nanoscale* **2016**, *8* (5), 2899-2907.
15. Bloh, J. Z.; Folli, A.; Macphee, D. E., Photocatalytic NO_x abatement: why the selectivity matters. *RSC Adv.* **2014**, *4* (86), 45726-45734.
16. Yamamoto, A.; Mizuno, Y.; Teramura, K.; Hosokawa, S.; Tanaka, T., Noble-metal-free NO_x storage over Ba-modified TiO₂ photocatalysts under UV-light irradiation at low temperatures. *ACS Catalysis* **2015**, *5* (5), 2939-2943.
17. Lewis, R. J.; Sax, N. I., *Sax's dangerous properties of industrial materials*. 12th ed.; Van Nostrand Reinhold: New York, 2012; Vol. 5, p 5862.
18. Ma, J.; Wu, H.; Liu, Y.; He, H., Photocatalytic removal of NO_x over visible light responsive oxygen-deficient TiO₂. *J. Phys. Chem. C* **2014**, *118* (14), 7434-7441.
19. Todorova, N.; Giannakopoulou, T.; Karapati, S.; Petridis, D.; Vaimakis, T.; Trapalis, C., Composite TiO₂/clays materials for photocatalytic NO_x oxidation. *Appl. Surf. Sci.* **2014**, *319*, 113-120.
20. Katsanaki, A. V.; Kontos, A. G.; Maggos, T.; Pelaez, M.; Likodimos, V.; Pavlatou, E. A.; Dionysiou, D. D.; Falaras, P., Photocatalytic oxidation of nitrogen oxides on N-F-doped titania thin films. *Appl. Catal. B: Environ.* **2013**, *140-141*, 619-625.

21. Hernández Rodríguez, M. J.; Pulido Melián, E.; González Díaz, O.; Araña, J.; Macías, M.; González Orive, A.; Doña Rodríguez, J. M., Comparison of supported TiO₂ catalysts in the photocatalytic degradation of NO_x. *J. Mol. Catal. A: Chem.* **2016**, *413*, 56-66.
22. Elbanna, O.; Zhang, P.; Fujitsuka, M.; Majima, T., Facile preparation of nitrogen and fluorine codoped TiO₂ mesocrystal with visible light photocatalytic activity. *Appl. Catal. B: Environ.* **2016**, *192*, 80-87.
23. Wang, Y.; Huang, H.; Gao, J.; Lu, G.; Zhao, Y.; Xu, Y.; Jiang, L., TiO₂-SiO₂ composite fibers with tunable interconnected porous hierarchy fabricated by single-spinneret electrospinning toward enhanced photocatalytic activity. *J. Mater. Chem. A* **2014**, *2* (31), 12442-12448.
24. Chattopadhyay, S.; Saha, J.; De, G., Electrospun anatase TiO₂ nanofibers with ordered mesoporosity. *J. Mater. Chem. A* **2014**, *2* (44), 19029-19035.
25. Zhao, J.; He, Y.; Zhang, L.; Lu, K., Preparation of porous TiO₂ powder with mesoporous structure by freeze-drying method. *J. Alloys Compd.* **2016**, *678*, 36-41.
26. Sugimoto, T.; Okada, K.; Itoh, H., Synthetic of Uniform Spindle-Type Titania Particles by the Gel-Sol Method. *J. Colloid Interface Sci.* **1997**, *193* (1), 140-143.
27. Zhang, W. F.; He, Y. L.; Zhang, M. S.; Yin, Z.; Chen, Q., Raman scattering study on anatase TiO₂ nanocrystals. *J. Phys. D: Appl. Phys.* **2000**, *33* (8), 912.

28. Moulder, J. F.; Chastain, J., *Handbook of X-ray Photoelectron Spectroscopy: A Reference Book of Standard Spectra for Identification and Interpretation of XPS Data*. Physical Electronics Division, Perkin-Elmer Corporation: 1992.
29. Simonsen, M. E.; Li, Z.; Søggaard, E. G., Influence of the OH groups on the photocatalytic activity and photoinduced hydrophilicity of microwave assisted sol-gel TiO₂ film. *Appl. Surf. Sci.* **2009**, *255* (18), 8054-8062.
30. Mills, A.; Lee, S.-K.; Sheridan, M., Development of a novel UV indicator and dosimeter film. *Analyst* **2005**, *130* (7), 1046-1051.
31. Mills, A.; Elouali, S., The nitric oxide ISO photocatalytic reactor system: Measurement of NO_x removal activity and capacity. *J. Photochem. Photobiol. A* **2015**, *305*, 29-36.
32. Zhang, Q.; Huang, Y.; Xu, L.; Cao, J.-j.; Ho, W.; Lee, S. C., Visible-light-active plasmonic Ag-SrTiO₃ nanocomposites for the degradation of NO in air with high selectivity. *ACS Appl. Mater. Interfaces* **2016**, *8* (6), 4165-4174.
33. Monge, M. E.; D'Anna, B.; George, C., Nitrogen dioxide removal and nitrous acid formation on titanium oxide surfaces-an air quality remediation process? *Phys. Chem. Chem. Phys.* **2010**, *12* (31), 8991-8998.
34. Folli, A.; Bloh, J. Z.; Strøm, M.; Pilegaard Madsen, T.; Henriksen, T.; Macphee, D. E., Efficiency of solar-light-driven TiO₂ photocatalysis at different latitudes and seasons. Where and when does TiO₂ really work? *J. Phys. Chem. Lett.* **2014**, *5* (5), 830-832.

35. Rosseler, O.; Sleiman, M.; Montesinos, V. N.; Shavorskiy, A.; Keller, V.; Keller, N.; Litter, M. I.; Bluhm, H.; Salmeron, M.; Destailats, H., Chemistry of NO_x on TiO₂ surfaces studied by ambient pressure XPS: products, effect of UV irradiation, water, and coadsorbed K⁺. *J. Phys. Chem. Lett.* **2013**, *4* (3), 536-541.
36. Mikhaylov, R. V.; Lisachenko, A. A.; Shelimov, B. N.; Kazansky, V. B.; Martra, G.; Coluccia, S., FTIR and TPD study of the room temperature interaction of a NO–Oxygen mixture and of NO₂ with titanium dioxide. *J. Phys. Chem. C* **2013**, *117* (20), 10345-10352.
37. Hadjiivanov, K. I., Identification of neutral and charged surface NO_x species by IR spectroscopy. *Catal. Rev. Sci. Eng.* **2000**, *42* (1-2), 71-144.
38. Hadjiivanov, K.; Knozinger, H., Species formed after NO adsorption and NO+O₂ co-adsorption on TiO₂: an FTIR spectroscopic study. *Phys. Chem. Chem. Phys.* **2000**, *2* (12), 2803-2806.
39. Tang, N.; Liu, Y.; Wang, H.; Wu, Z., Mechanism study of NO catalytic oxidation over MnO_x/TiO₂ catalysts. *J. Phys. Chem. C* **2011**, *115* (16), 8214-8220.

Supporting Information

Mesoporous and visible light active anatase: a high selectivity De-NO_x photocatalyst

*J. Balbuena,^a J.M. Calatayud,^b M. Cruz-Yusta,^a P. Pardo,^b F. Martín,^c J. Alarcón,^{*b} and L. Sánchez^{*a}*

(a) Inorganic Chemistry Department, Campus de Rabanales, Universidad de Córdoba, Córdoba, 14071, Spain. E-mail: luis-sanchez@uco.es

(b) Inorganic Chemistry Department, University of Valencia, Calle Dr. Moliner 50, Burjasot (Valencia), 46100, Spain. E-mail: javier.alarcon@uv.es

(c) Chemical Engineering Department, Campus de Teatinos, Universidad de Málaga, Málaga, 29071, Spain. E-mail: marjim@uma.es

* Corresponding Authors:

- Prof. Luis Sánchez

Inorganic Chemistry Department, Campus de Rabanales, Universidad de Córdoba, Córdoba, 14071, Spain.

E-mail: luis-sanchez@uco.es

Tel: +00-34-957-218634

- Prof. Javier Alarcón

Inorganic Chemistry Department, University of Valencia, Calle Dr. Moliner 50, Burjasot (Valencia), 46100, Spain.

E-mail: javier.alarcon@uv.es

Tel: +00-34-96-354-4584

Materials and methods

Techniques of characterization

X-ray diffraction (XRD) analysis (model D-8 Advance, Bruker) was performed using CuK α radiation. Crystalline structure was refined with the Rietveld technique, by using FulProf software, on diffractograms acquired from 5 to 120° 2 θ with a step size of 0.02° 2 θ and an accumulated counting time of 2s. The refinement of anatase phase was started using the *I4₁/amd* space group and structure parameters derived by Li et al¹.

Raman spectra of samples were obtained by means of a Raman spectrometer (Model XploRA, Horiba) with 785 nm laser. The samples were measured in backscattering geometry at room temperature. A 100x microscope objective was used to focus the excitation laser on the sample and collect the scattered light to the spectrometer. More than 3 different areas were analyzed per sample, to obtain representative results. Exposure time was 10 s and number of acquisitions was 5. Data acquisition was carried out with the LabSpec 6 software packages from Horiba Scientific.

X-ray photoelectron spectra (XPS) were recorded using non-monochromated MgK radiation ($h\nu= 1253.6$ eV) and a hemi-spherical analyser operating at a constant pass energy of 29.35 eV (Physical Electronics PHI 5700 spectrometer) with the X-ray generator operating at 15 kV and 300 W. The pressure in

the analysis chamber was about 10^{-7} Pa. Binding energies were corrected against that for C 1s peak of adventitious carbon fixed at 284.8 eV. The 1s peaks O and 2p of Ti were curve-fitted by the software MultiPak version 9.3 using a convolution of independent Gaussian and Lorentzian contributions (the so-called Voigt profile).

Probe NO (>99.9%, from Abello Linde S.A.) was carried out in an IR cell connected with a conventional outgassing/gas manipulation apparatus and spectra were recorded in a Nicolet Nexus 6700 spectrometer with MCT detector. For the study, 100 scans were registered in the range between 4000 and 400 cm^{-1} with a resolution of 4 cm^{-1} and KBr beam splitters. The system was also composed of a vertical furnace that allowed the thermal treatment of the samples. The samples were pressed into 13 mm disks using a hydraulic press and placed in the sample holder of a quartz cell with KBr windows, permanently connected to a conventional vacuum line ($\approx 1 \cdot 10^{-4}$ torr).

References

1. Li, J.; Song, G.B.; Wang, M. L.; Zhang, B.S., Preparation and structure characters of nano-powder of $\text{Ti}_{1-x}\text{Ce}_x\text{O}_2$ system. *Chin. J. High Press. Phys.* **2006**, *20*, 211-216.

Tables

Table S1. Particle size, surface area and photocatalytic efficiency for the removal of NO_x gases of different titania compounds.

Sample	Particle size (nm)	Surface Area (m ² ·g ⁻¹)	NO conversión (%)	NO _x conversion (%)	* Selectivity (%)
TiO ₂ ^a	9	--	35	20	57
N-TiO ₂ ^a	15	--	30	15	50
TiO ₂ ^b	8	282.7	65	55	84
TiO ₂ /HT ^c	--	--	45	38	85
Fe-TiO ₂ ^d	--	105.4	58	38	65
TiO ₂ /graphene ^e	10	142.7	53	45	85
Pt-TiO ₂ ^f	9	112.7	25	--	66
WN-TiO ₂ ^g	--	--	--	< 1.0	97
NF-TiO ₂ film ^h		136	6.7	--	93

* Selectivity values were calculated from the cited articles by following the definition of MacPhee et al.^g and using the equation (4).

^a Todorova, N.; Vaimakis, T.; Petrakis, D.; Hishita, S.; Boukos, N.; Giannakopoulou, T.; Giannouri, M.; Antiohos, S.; Papageorgiou, D.; Chaniotakis, E.; Trapalis, C., *Catal. Today*, **2013**, *209*, 41-46.

^b Ma, J.; Wu, H.; Liu Y.; He, H., *J. Phys. Chem. C*, **2014**, *118*, 7434-7441.

^c Todorova, N.; Giannakopoulou, T.; Karapati, S.; Petridis, D.; Vaimakis, T.; Trapalis, C., *Appl. Surf. Sci.*, **2014**, *319*, 113-120.

^d Ma, J.; He, H.; Liu, F., *Appl. Catal. B: Environ.*, **2015**, *179*, 21-28.

^e Trapalis, A.; Todorova, N.; Giannakopoulou, T.; Boukos, N.; Speliotis, T.; Dimotikali, D.; Yu, J., *Appl. Catal. B: Environ.*, **2016**, *180*, 637-647.

^f Hu, Y.; Song, X.; Jiang S.; Wei, C., *Chem. Eng. J.*, **2015**, *274*, 102-112.

^g Bloh, J. Z.; Folli, A.; Macphee, D. E., *RSC Adv.*, **2014**, *4*, 45726-45734.

^h Katsanaki, A.V.; Kontos, A.G.; Magos, T.; Peláez, M.; Likodimos, V.; Pavlatou, E.A.; Dionysiou, D.D.; Falaras, P., *Appl. Catal. B: Environ.*, **2013**, *140-141*, 619-625.

Table S2. Crystallographic data and details of the Rietveld refinement of samples A and A350.

Samples	a=b / Å	c / Å	R _{wp}	R _{exp}	Chi2
A	3.7934 (1)	9.5071 (2)	8.77	5.41	2.62
A350	3.7844 (1)	9.5001 (2)	8.82	5.78	2.33

Table S3. N and C chemical analysis for TiO₂ samples obtained at different temperatures and time of calcination

Samples	Temperature / °C	Time / h	N content / %	C content / %	C/N ratio
A *	140	72	0.32	1.9	5.93
A350	350	30	0.14	0.51	3.64
A400	400	4	0.20	0.16	0.82
A600	600	4	0.23	0.16	0.70
A800	800	1	0.06	0.007	0.11
P25	---	----	0.07	---	---

* Sample A was obtained by hydrothermal method. The series of samples correspond to that obtained after a specific calcination procedure.

Table S4. Surface area and pore volume for TiO₂ samples.

Samples	A	A350	P25
BET Surface Area / m ² ·g ⁻¹	74.9	63.6	52.4
Pore Volume / cm ³ ·g ⁻¹	0.23	0.22	0.18

Figures

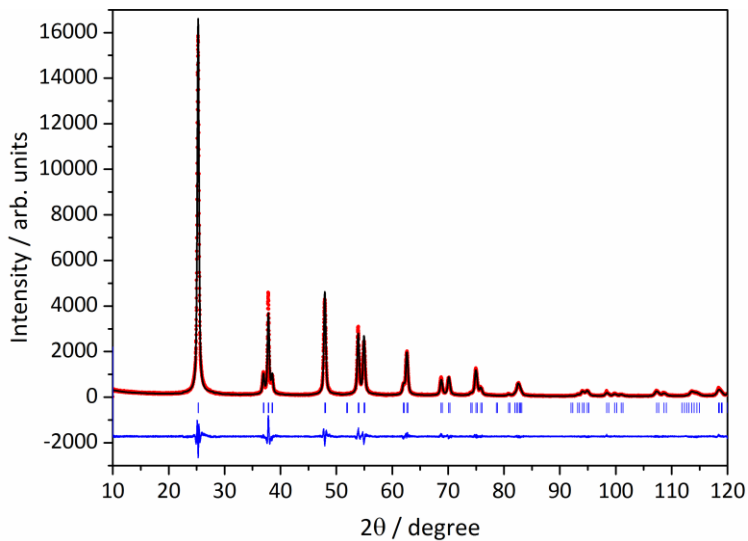


Figure S1. Rietveld plot of sample A showing the difference between the experimental and calculated diffracted intensities.

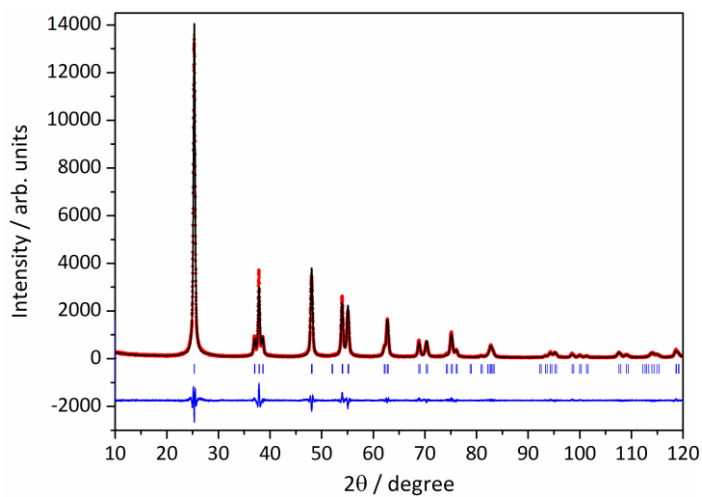


Figure S2. Rietveld plot of sample A350 showing the difference between the experimental and calculated diffracted intensities.

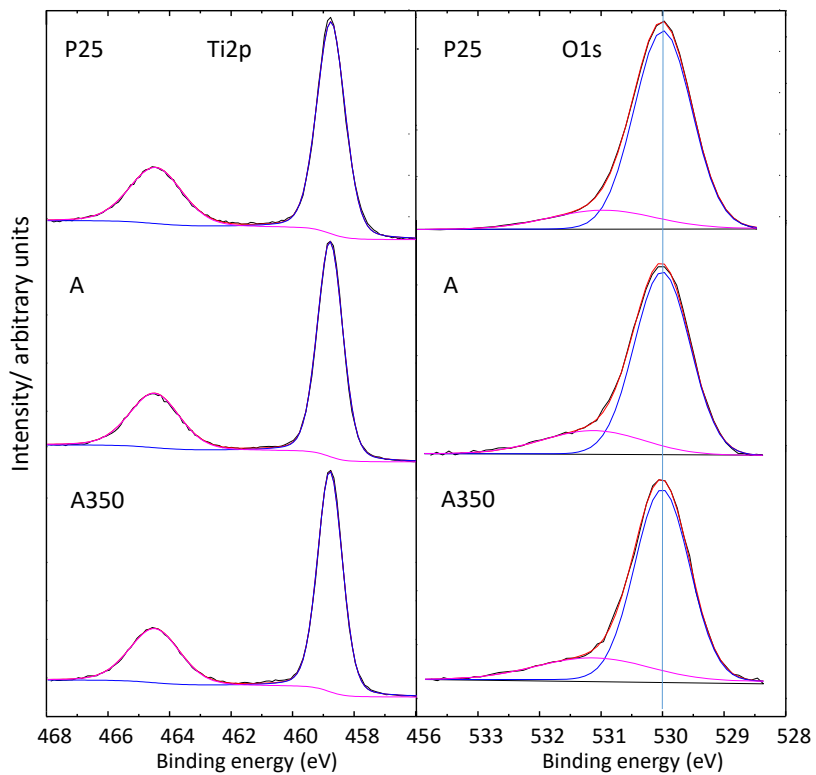


Figure S3. Ti 2p (left) and O 1s (right) XPS regions of the samples A, A350 and the reference P25.

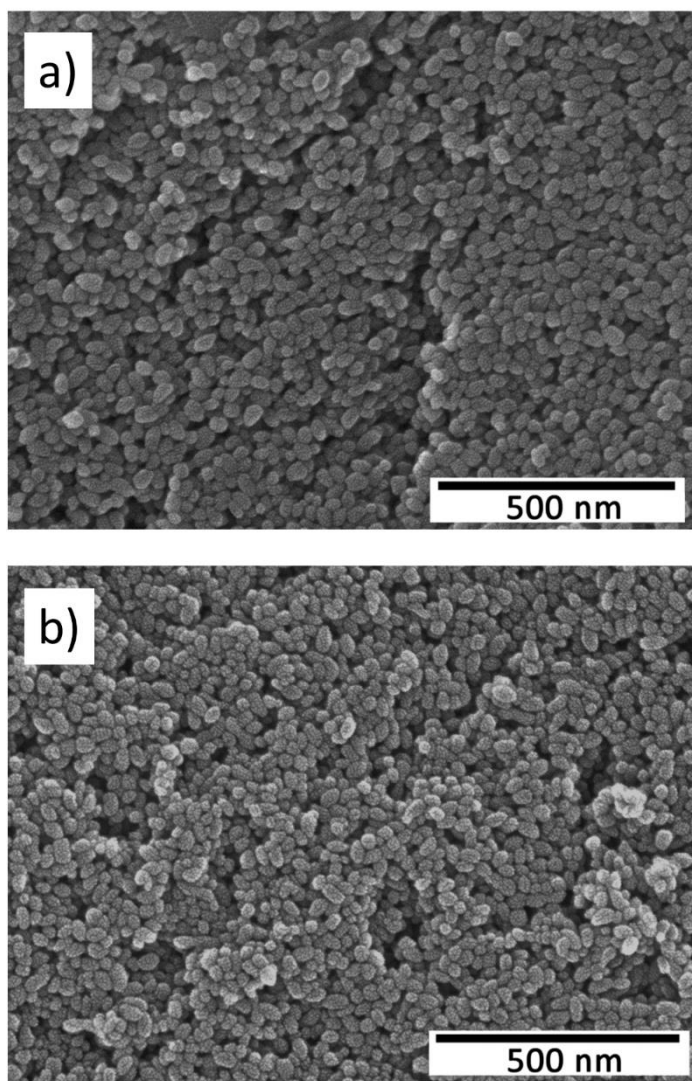


Figure S4. SEM micrographs of samples (a) A and (b) A350.

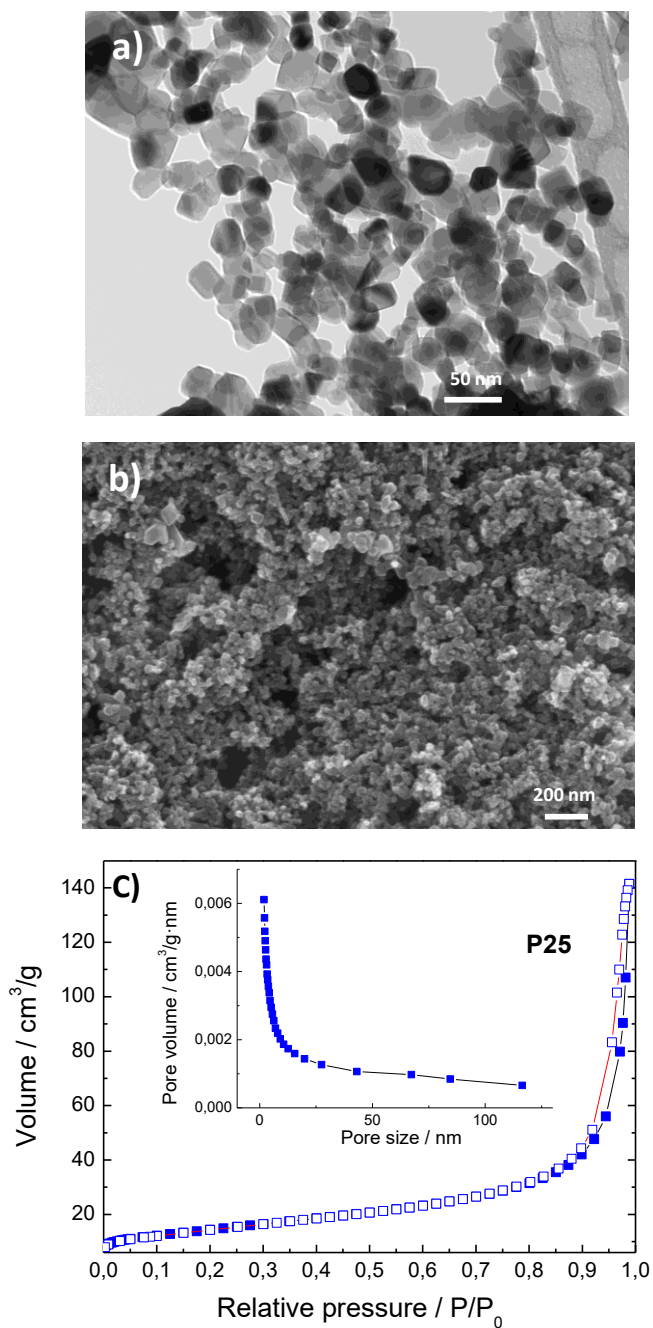


Figure S5: (a) TEM, (b) SEM micrographs and (c) N₂ adsorption-desorption isotherm of TiO₂ P25 sample.

The P25 nanoparticles, around 20-50 nm in size, are flat in surface and do not show any kind of voids, Fig S5 a. Moreover, a very narrow hysteresis loop at relative pressure higher than 0.9 is observed in the corresponding N₂ isotherm shown in Fig. S5c. It is to note the surface area of 52.4 m² g⁻¹ measured for the reference P25 which is significantly lower to that of prepared titania samples, and being the pore size nanometric (< 5 nm): Table S4. As can be seen in Fig. 3b, the UV-Vis DR spectrum of the reference P25 displays a rather weak absorption over the range between 400 and 450 nm. As it is known this P25 contains around 25 % of rutile.

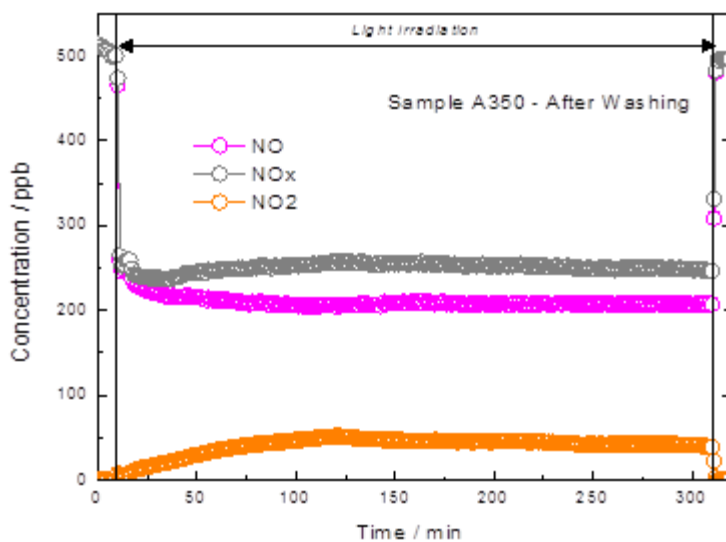


Figure S6. Nitrogen oxides concentration profiles obtained during the photo-degradation of gaseous NO under UV-Vis irradiation on washed Sample A350 in a second photocatalytic cycle.

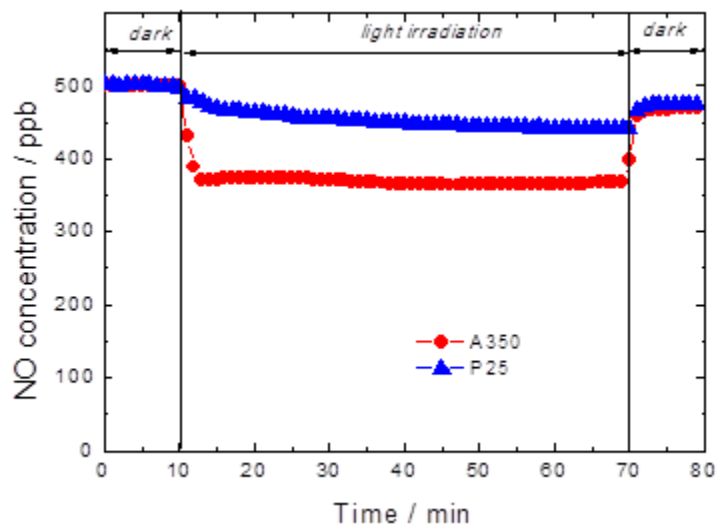


Figure S7. NO concentration profile recorded for A350 and P25 samples under Vis light irradiation ($\lambda > 510 \text{ nm}$).

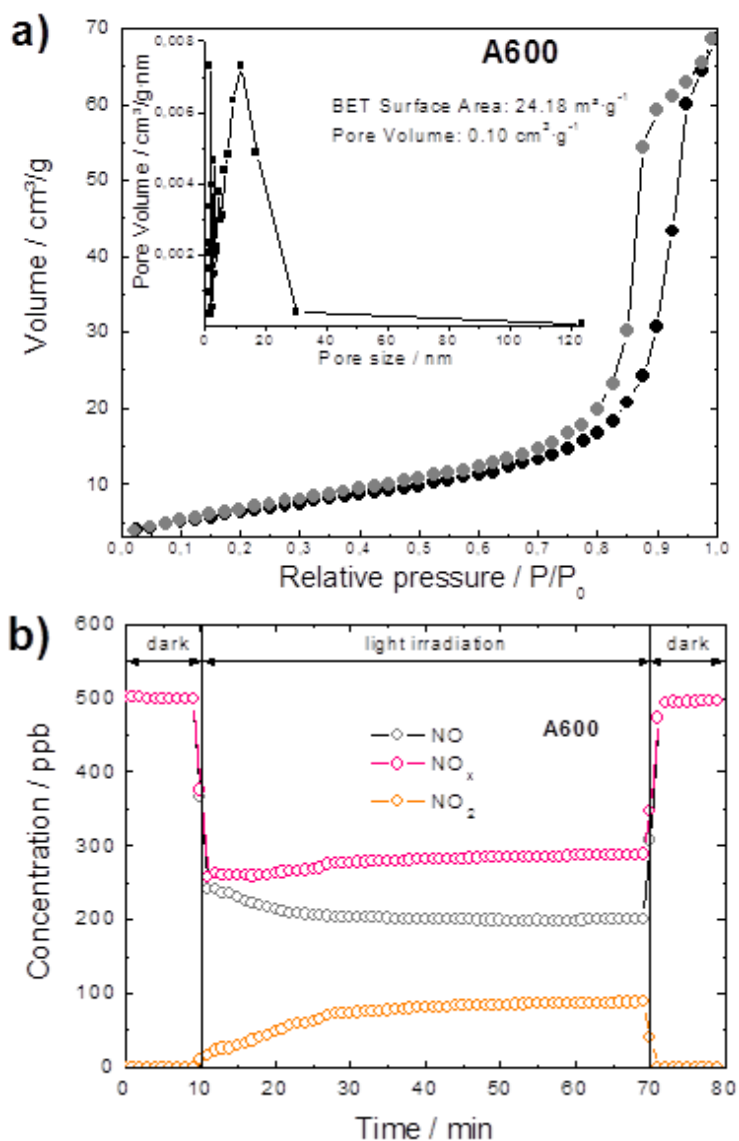


Figure S8. (a) N_2 adsorption-desorption isotherm for sample A600. (b) Nitrogen oxides concentration profiles obtained during the photo-degradation of gaseous NO under UV-Vis irradiation on Sample A600.

4. Preparation of new De-NO_x photocatalysts through the valorisation of industrial waste

4.1. Introduction

The Chemical Industry is one of the sectors that contribute to guarantee the continuous improvement in the three areas of Sustainable Development. It concerns social, environmental and economic aspects. Currently, sustainable development is translated into four basic dimensions: resources, residues, risks and costs, and the proper waste management is one of the requirements.¹

Until a few years ago, in the most occasions, the wastes generated by industrial activities were released to the environment causing important modifications in the landscape, contamination of soils and aquifers and generating a big loss of potential resources, because a large quantity of materials susceptible to be recovered were rejected as waste. The non-reuse of these materials forces to consume a greater amount of natural resources, highlighting more the negative effect on the environment and in this way, acting against the principles of sustainable development.

On this basis, companies have developed recycling strategies for waste and co-products, generally adding them to final products and giving them some commercial value. The reuse of this waste can, on the one hand, help to diversify production and reduce final costs, and on the other, provide a range of alternative materials for use as raw materials in different industrial sectors. Nevertheless, sustainable production of materials should not only be restricted to recycling products but also they could be transformed into

materials that provide new benefits to society, for example in the field of the environment.

The constitutional right to enjoy a satisfactory environment for the growth of the person, requires that the public authorities establish effective mechanisms to protect it and preserve it. This purpose can only be achieved by seeking the compatibility of human activity with the preservation of the environment. For that, environmental legislation is clear and provide legal certainty. EU environmental policies and legislation protect natural habitats, keep air and water clean, ensure proper waste disposal, improve knowledge about toxic chemicals and help businesses move toward a sustainable economy.²

Recycling and recovery are nowadays, the routes with the most real potential, from a technical, ecological and economic point of view. The construction industry is one of the best targets of solid-waste reconversion by the large amounts of raw materials it consumes and the large volume of final products. A variety of waste materials, including construction rubble³, tyre rubber ash⁴, blast furnace slag⁵, silica fume, fly ash⁶⁻⁷, or biological limestone⁸, have been successfully tested in the preparation of mortars with proven advantages and beneficial effects over existing alternatives. Recently, the ability of building materials to act as self-cleaning and self-depolluting materials, with very interesting applications in the fields of cultural heritage and environment, has been reported.⁹⁻¹² Thus, building materials treated with a photocatalyst eliminate NO_x particles that are produced by vehicles, industry and energy

production, the main objective of this research Project. On this scenary, the use of waste as raw material can be done in several ways, briefly summarised here as way of example:

- a) Use of the residues as pozzolanic material in the construction sector (Pozzolans are materials with a high content of amorphous silica capable of reacting in aqueous medium with calcium hydroxide giving rise to hydrated phases like those obtained in the setting of the cement). If the residue has pozzolanic activity can substitute part of the cement or the binder material, providing additional economic and environmental advantages. As a way of example, A. R. G. Azevedo et al.¹³ studied the use of residues from the paper industry. The paper and cellulose industry is responsible for generating large amounts of solid wastes, which are produced during various stages of the production process. Currently this material is stored in landfills and generating costs for the company. This study aimed to determine the pozzolanic activity index in the residue studied to verify its viability in the incorporation of the same as cementitious material. The data found show that the material has the possibility of being incorporated in the mortar due to its pozzolanic activity index. F. Pelisser et al. studied the pozzolanic effect of porcelain polishing residue in portland cement. Ceramic tiling is used on a large scale by the construction industry. The production process of tiles produces porcelain polishing residues (PPR),

one of the main residues in the sludge, with loss rates above 1%. Since it is a residue that is impure, for reuse again on this industrial process, it ends up being discarded in landfills. However, considering its characteristics, its fineness and chemical composition, its potential as a pozzolanic material was evaluated for use in the manufacture of cement-based construction materials to improve their yield. The results of compressive strength (at 84 days) determined for the mortars showed an increase of 18%, with reduced cement consumption for mortar at 20% residue content. Thermogravimetric analysis revealed that the portlandite formed during the cement hydration was consumed by the silica present in the residue, forming calcium silicate hydrate (C-S-H), which characterizes a pozzolanic reaction. This effect contributed to the study and to the applications of supplementary cementitious materials, while optimizing the use of Portland cement and reducing the environmental impact of carbon dioxide emissions originating from its production.¹⁴ And as a final example, L. Sánchez et al. were studying the use of olive biomass fly ash in the preparation of environmentally friendly mortars. The incorporation of fly ash from olive biomass (FAOB) combustion in cogeneration plants into cement based mortars was explored by analyzing the chemical composition, mineralogical phases, particle size, morphology, and IR spectra of the resulting material. Pozzolanic activity was detected and found to be related with the presence of calcium aluminum silicates phases.

The preparation of new olive biomass fly ash content mortars is effective by replacing either CaCO₃ filler or cement with FAOB. This can provide an alternative way to manage the olive biomass fly ash as waste produced in thermal plants and reduce cement consumption in the building industry, and hence an economically and environmentally attractive choice.⁷

- b) Use of waste as a secondary raw material. In this case the advantages of the use of the residues lie in avoiding their disposal in landfills, as well as their associated impacts, reduction in the exploitation of quarries, reduction of the final cost of the product, etc. Some examples may be ashes of pyrite (Fe), paper sludge (CaCO₃), smelting sands (SiO₂), etc. By substituting part of the raw materials for waste that has similar characteristics in its composition, the exploitation of natural resources equivalent to more than 1.3 years of a typical excavation is avoided. As a way of example, it could be mentioned the work of L. Sánchez et al. which use the mussel shell as a source of natural CaCO₃. In this work, various types of cement–SiO₂–CaCO₃ mortar were prepared by replacing quarry limestone aggregate with limestone obtained as a by-product from waste of the mussel cannery industry. The CaCO₃ aggregate consists mainly of elongated prismatic particles less than 4 µm long rather than of the rounded particles of smaller size (2–6 µm) obtained with quarry limestone. The mechanical and structural properties of the mortars were found to be

influenced by aggregate morphology. Mortars with a high content in mussel shell limestone exhibited a more packed microstructure, which helps setting of cement and results in improved mortar strength. The enhanced mechanical properties of this new mortars allow the cement content in the final mortar composition to be decreased and thus production costs can be reduced.⁸ Another example for the use of wastes as a secondary raw material may be the work of N. M. Al-Akhras et al. who studied the effect of tire rubber ash as filler. The test results showed that tire rubber ash (TRA) could be used as a partial replacement of sand in mortar mixtures to produce workable mortar. The mortar containing different TRA replacement levels showed higher compressive strength, flexural strength, higher resistance to freezing and thawing damage and chloride-ion penetration than that of control mortar.⁴

- c) Use of waste for create new functionalities in materials. Some waste, due to their characteristics or with a suitable thermal or chemical treatment, can be used to give a new functionality to the material in which they are included. An example of this type of new functionalities can be the transformation of a residue into pigment to impart colour to a given product studied by L. Sánchez et al. in “Use of granite sludge wastes for the production of coloured cement-based mortars”.¹⁵ The value of granite sludge wastes (GS) in cement-based mortar formulations was examined by assessing their potential as

structural components and pigments. GS were easily converted into a reddish pigment by calcination at low temperatures (700–900 °C) for a short time obtaining the presence of α -Fe₂O₃ which act as pigment. Therefore, the preparation of coloured mortar with good compressive strength can be an attractive, environmentally friendly method of managing granite sludge wastes. Another example of new functionalities is the depollution of NO_x gases. M. Sampiña et al. studied the re-use of hazardous waste of difficult management, electric arc furnace dust (EAFD), as photocatalytic material. Direct tests on EAFD and mortar containing this waste have been performed to evaluate its potential as photocatalyst itself and within a cementitious material. The photocatalytic properties were studied by two different methods: NO_x degradation and Rhodamine B (RhB) degradation. Thus, it can be said that EAFD exhibited photocatalytic activity for both configurations with UV and visible light, having the mortar enhanced photocatalytic activity for NO_x with respect to the EAFD itself. Furthermore, in direct tests on the EAFD, it has could degrade RhB even in the dark, which has been attributed to transfer of electrons between the adsorbed RhB and the conduction band of some oxides in the dust.¹⁶

In this chapter, we will focus on the last section. Following this topic, given its experience in wastes valorization in building sector^{7-8, 15}, FQM-175 research group has been pioneer in the re-use of

wastes to obtain new self-cleaning and de-polluting materials through the use of photocatalysis. Thus, two very important works were published. In these papers focused on the valorization of granite waste (GW) and sandblasting operation wastes (SOW) through incorporation, as a filler-functional admixture, into cement-based mortar formulations. The preparation of advanced photocatalytic materials that exhibit self-cleaning and depolluting properties was possible by the inclusion of GW-TiO₂ and SOW- TiO₂ in a cement-based mortar. The synergy observed between both materials and TiO₂ enhanced their photocatalytic action.¹⁷⁻¹⁸

Following this philosophy, and with the aim to prepare new materials for the photocatalytic NO abatement, these two articles are based on the reuse of industrial waste to:

- 1) Give new characteristics to a pavement mortar using the residue generated in the process of cleaning the hulls of ships in the shipyards. After the proper mechanical and thermal treatment, the waste is transformed in a photocatalytic material with the suitable properties to be introduced in the mentioned mortar.
- 2) The use of rice husks as support and template for the synthesis of a new photocatalyst with De-NO_x effect.

References

1. Lange, J.-P., Sustainable Chemical Manufacturing: A Matter of Resources, Wastes, Hazards, and Costs. *ChemSusChem* **2009**, *2* (6), 587-592.
2. Environment and climate change. http://eur-lex.europa.eu/summary/chapter/environment.html?root_default=SUM_1_CODED%3D20&locale=en (accessed March, 2017).
3. Alvarez Cabrera, J.; Urrutia, F.; Lecusay, D.; Fernandez, A., Masonry mortars demolition. *Mater. Constr* **1997**, *47*, 43-48.
4. Al-Akhras, N. M.; Smadi, M. M., Properties of tire rubber ash mortar. *Cement Concrete Comp.* **2004**, *26* (7), 821-826.
5. Cerulli, T.; Pistolesi, C.; Maltese, C.; Salvioni, D., Durability of traditional plasters with respect to blast furnace slag-based plaster. *Cem. Concr. Res.* **2003**, *33* (9), 1375-1383.
6. Li, G.; Wu, X., Influence of fly ash and its mean particle size on certain engineering properties of cement composite mortars. *Cem. Concr. Res.* **2005**, *35* (6), 1128-1134.
7. Cruz-Yusta, M.; Mármol, I.; Morales, J.; Sánchez, L., Use of Olive Biomass Fly Ash in the Preparation of Environmentally Friendly Mortars. *Environ. Sci. Technol.* **2011**, *45* (16), 6991-6996.
8. Ballester, P.; Mármol, I.; Morales, J.; Sánchez, L., Use of limestone obtained from waste of the mussel cannery industry for the production of mortars. *Cem. Concr. Res.* **2007**, *37* (4), 559-564.

9. Chen, J.; Poon, C.-s., Photocatalytic construction and building materials: From fundamentals to applications. *Build. Environ.* **2009**, *44* (9), 1899-1906.
10. Strini, A.; Cassese, S.; Schiavi, L., Measurement of benzene, toluene, ethylbenzene and o-xylene gas phase photodegradation by titanium dioxide dispersed in cementitious materials using a mixed flow reactor. *Appl. Catal. B: Environ.* **2005**, *61* (1), 90-97.
11. Hüsken, G.; Hunger, M.; Brouwers, H. J. H., Experimental study of photocatalytic concrete products for air purification. *Build. Environ.* **2009**, *44* (12), 2463-2474.
12. Sugrañez, R.; Álvarez, J. I.; Cruz-Yusta, M.; Mármol, I.; Morales, J.; Vila, J.; Sánchez, L., Enhanced photocatalytic degradation of NO_x gases by regulating the microstructure of mortar cement modified with titanium dioxide. *Build. Environ.* **2013**, *69*, 55-63.
13. Azevedo, A. R. G.; Alexandre, J.; Petrucci, L. J. T.; Zanelato, E. B.; Oliveira, T. F., Evaluation of the pozzolanic activity of residue from the paper industry. In *Characterization of Minerals, Metals, and Materials 2017*, Ikhmayies, S.; Li, B.; Carpenter, J. S.; Li, J.; Hwang, J.-Y.; Monteiro, S. N.; Firrao, D.; Zhang, M.; Peng, Z.; Escobedo-Diaz, J. P.; Bai, C.; Kalay, Y. E.; Goswami, R.; Kim, J., Eds. Springer International Publishing: Cham, 2017; pp 657-662.
14. Jacoby, P. C.; Pelisser, F., Pozzolanic effect of porcelain polishing residue in Portland cement. *Journal of Cleaner Production* **2015**, *100*, 84-88.

15. Mármol, I.; Ballester, P.; Cerro, S.; Monrós, G.; Morales, J.; Sánchez, L., Use of granite sludge wastes for the production of coloured cement-based mortars. *Cement and Concrete Composites* **2010**, *32* (8), 617-622.
16. Sapiña, M.; Jimenez-Relinque, E.; Castellote, M., Turning waste into valuable resource: potential of electric arc furnace dust as photocatalytic material. *Environmental Science and Pollution Research* **2014**, *21* (20), 12091-12098.
17. Sugrañez, R.; Cruz-Yusta, M.; Mármol, I.; Martín, F.; Morales, J.; Sánchez, L., Use of industrial waste for the manufacturing of sustainable building materials. *ChemSusChem* **2012**, *5* (4), 694-699.
18. Sugrañez, R.; Cruz-Yusta, M.; Mármol, I.; Morales, J.; Sánchez, L., Preparation of sustainable photocatalytic materials through the valorization of industrial wastes. *ChemSusChem* **2013**, *6* (12), 2340-2347.

4.2. Preparation of self-cleaning and de-polluting building materials through the valorization of industrial wastes.

2-3 September 2013
University of Portsmouth

Preparation of self-cleaning and de-polluting building materials through the valorization of industrial wastes

J. Balbuena¹, R. Segráñez¹, M. Cruz-Yusta¹, I. Mármo², J. Morales¹, D. Kovandzic³, L. Sánchez*¹

¹ Departamento de Química Inorgánica, Facultad de Ciencias – Universidad de Córdoba, Córdoba, Spain.

* luis-sanchez@uco.es

² Grupo Puma S.L., Avda. Agrupación Córdoba nº 17, Córdoba, Spain

³ Agencia de Obra Pública de la Junta de Andalucía, c/ Diego Martínez Barrio, Sevilla, Spain

ABSTRACT

Appropriate waste management is one of the main requisites for sustainable development at present. This task is nowadays tackled by the material construction industry. The present work is focused on the proper valorization of industrial sandblasting operation wastes (SOW) for the production of new self-cleaning and de-polluting materials cementitious materials.

The studied wastes are generated on shipyard works during the cleaning of boat/ship's hull. The SOW is constituted by Fe₂O₃ (60.7 %), SiO₂ (29.1 %) and Al₂O₃ (3.9 %) as main components. The high content in iron oxide is used to prepare a photocatalytic raw material. Thermal transformation of SOW, at temperatures of 600, 750 and 900 °C, is performed with the aim to enrich the sample on α-Fe₂O₃, as semiconductor photocatalyst.

Mortar specimens containing SOW as photocatalyst admixture let the preparation of self-cleaning and de-polluting materials. It is evaluated the degradation of rhodamine-B (RhB) dye as organic compound on the surface of mortar specimens. Moreover, it is presented the use of wastes for the preparation of materials enhancing the photocatalytic oxidation of NO_x gases. Conversely, building materials with good photocatalytic properties were prepared using the synergistic effect of TiO₂ and SOW photocatalysts. Finally, the preparation of sustainable building materials is demonstrated through an adequate reuse of industrial sandblasting operation wastes.

Book ISBN: 978 1 86137 642

Pages: 189 - 194

4.2.1. Introduction

The chemical industry is one of the sectors that contribute most to ensure continuous improvement in all three areas (social, environmental and economic) that make up the Sustainable Development. Currently, there are a variety of co-products and wastes which could provide – through the proper treatment – a range of materials with new features, including photocatalysis. The construction industry is one of the best targets for solid waste reconversion due to the consumption of large amounts of raw materials and the large volume of the final products. Recently, considerable interest has been aroused in the implementation of photocatalysts in building materials, like TiO_2 , because it involves additional benefits such as the self-cleaning of pollutants attached on surface or the de-polluting action over the environmental air pollutants.¹⁻³

In that concerning to air purification, the presence of nitrogen oxides ($\text{NO}_x = \text{NO} + \text{NO}_2$) in the atmosphere is a great concern for modern society, due to the several adverse and harmful effects of these compounds on human health. TiO_2 -containing materials are interesting thanks to their ability to promote photocatalytic oxidation (PCO) of these gases. Thus, by using TiO_2 as an efficient photocatalyst, NO_x oxidation is easily promoted using only atmospheric oxygen, water and UV-A solar radiation.⁴ This simple mechanism is the basis for the preparation of de-polluting building materials. An intense effort has been devoted to

understanding and enhancing the PCO of NO_x gases by using TiO₂-containing cementitious materials in recent years.⁵⁻⁶ Nevertheless, the cost of TiO₂ is higher than that of cement, sands or fillers, the raw materials used in construction. This precludes its widespread use, and therefore, promising applications of this type of material will be limited in our cities.

An interesting option to TiO₂ is iron oxide. Hematite (α -Fe₂O₃) is the most stable iron oxide with n-type semiconducting properties under ambient conditions. Even though its photocatalytic activity is lower than that of the TiO₂ anatase phase, this oxide can absorb visible light (1.9–2.2 eV band gap). This absorption ability has attracted a strong interest in its potential applications for the photocatalytic degradation of pollutants in water and air.⁷ On the other hand, iron oxides can also be obtained as by-products in several industrial processes, such as steelworks, the granite cutting industry, etc.

An interesting waste is that produced in the cleaning operations performed in shipyards. Fayalite, Fe₂SiO₄, is a common material used as a sandblaster to clean the outer surface of boats and ships, which explains the high iron content present in this waste. This type of industrial activity produces large amounts of solid wastes for which the management is rather problematic for the producers, who must find appropriate places for storage and deposition. This waste can be used to prepare a raw material with potential photocatalytic properties.

The present work focused on the valorization of industrial

sandblasting operation wastes (SOW) for the production of new self-cleaning and de-polluting materials, more specifically cementitious materials.

4.2.2. Experimental

The as-received SOW samples were dried at 110 °C to a constant weight. In order to homogenize the particle size, the samples were grinded using a planetary mill (300 rpm). The chemical composition of each SOW sample was determined by X-ray fluorescence analysis (XRF). The mineralogical characterization and identification of crystalline phases was performed using X-ray diffraction (XRD). Diffuse reflectance spectra were recorded using a CM-5 from Konica Minolta.

A pavement mortar (UNE-EN-1015-11 y UNE-EN-12808-2) was studied to evaluate the use of SOW samples as additives for the preparation of self-cleaning and de-polluting materials. Mortar specimens were prepared using cement (Portland BL I 52.5 R), silica sand, calcite as a filler, and organic additives. The different formulations were adjusted to obtain an appropriate consistency (UNE-EN 1015-3) and acceptable workability. All samples were cured at 25 °C and 50–90 % relative humidity (RH).

To evaluate the self-cleaning property of mortar with the SOW or TiO₂ additives, the specimens were stained on the surface with rhodamine-B (RhB, red dye).⁸ The specimens were irradiated

for 26 h (3 and 40 W·m⁻², UV and visible irradiance, respectively). The variations in color during light exposure were measured with CM-5 from Konica Minolta. The results were expressed using the CIE L^* , a^* and b^* color parameters. L^* is the lightness axis (black (0) → white (100)), a^* is the green (–) → red (+) axis and b^* is the blue (–) → yellow (+) axis. As RhB applied to the materials gave an initial pink coloration, only the color parameter a^* was, in fact, considered, its initial value being a_0^* . The degradability of RhB is represented by the R_{26} index: $R_{26} = [a^*(0h) - a^*(26 h) / a^*(0h)] \times 100$, where $a^*(0h)$ and $a^*(26 h)$ denote the value of a^* before and after 26 h of irradiation.

Concerning the de-polluting action of the photocatalytic oxidation of nitrogen oxide, NO was studied. The NO oxidation tests were carried following the methodology described in to ISO 22197-1 which is applicable to photocatalytic materials produced for air purification. However, some of the specifications described on this standard were modified in order to obtain the better performance with the samples object of this study. Thus, the tests were carried out on 50 x 50 mm mortar samples placed in a laminar flow reactor and irradiated with artificial sunlight (25 and 580 W·m⁻², UV and visible irradiance, respectively). Air was supplied with a relative humidity of 50 ± 10%. Air and NO gas streams were mixed to obtain the desired concentration (500 ppb NO) and sent to the photoreactor. The accurate measurement of the concentration of NO_x was carried out using a chemiluminescence analyzer; a flow

rate, Q, of 0.75 L·min⁻¹ was employed. The removal rate (%) of NO_x was defined according to the following equation:

$$\text{NO}_x \text{ removal rate (\%)} = \frac{[\text{NO}_x]_{\text{inlet}} - [\text{NO}_x]_{\text{outlet}}}{[\text{NO}_x]_{\text{inlet}}} \times 100$$

where $[\text{NO}_x]_{\text{inlet}}$ represents the concentration of NO_x in the feed stream and $[\text{NO}_x]_{\text{outlet}}$ is the concentration of NO_x in the outlet stream. The photochemical experiments were performed through the use of a Solarbox 3000e RH testing instrument equipped with a xenon lamp with controlled irradiance.

4.2.3. Results and discussion

Waste characterization and transformation

The studied wastes were generated from shipyard works during the cleaning of boat/ship hulls. With the aim of effectively removing scale and rust and minimizing the production of mineral dust, the fayalite mineral is the preferred abrasive in sandblasting operations. A large number of SOW samples were studied, the common feature being a uniform composition. The SOW was composed of Fe₂O₃ (60.7 %), SiO₂ (29.1 %) and Al₂O₃ (3.9 %) as the main components. Other minor components included CaO (1.64 %), MgO (1.28 %), K₂O (1.23 %) and Na₂O (0.80 %). The Fe/Si ratio of 2.08 was bigger than expected for fayalite stoichiometry, indicating that a certain amount of iron came from sandblasted steel. The chemical analysis was in agreement with the XRD pattern recorded

for the SOW waste (Figure 1). Thus, Fe₂SiO₄ and iron oxides (Fe₃O₄/γ-Fe₂O₃) were present as the main crystalline phases.

In order to obtain an enrichment in hematite (α-Fe₂O₃), the SOW was subjected to a mechanical and thermal treatment. Through grinding, a decrease in the particle size is desired in order to favor the iron oxide transformation towards α-Fe₂O₃ during the thermal treatment. Thus, the SOW was grinded during periods of 12, 16, 20 and 24 h and the resulting particle size distribution measured by using the laser diffraction technique. The particle size decreased from 0.6-110 μm to 0.2-20 μm after milling (Figure 2). The milling wastes were heated at 600 °C (4h). A clear enrichment in hematite only occurs in samples milled at periods higher than 12 h. The grinding period of 16h results to be the best choice. This sample is hereafter designated as SOW16-T.

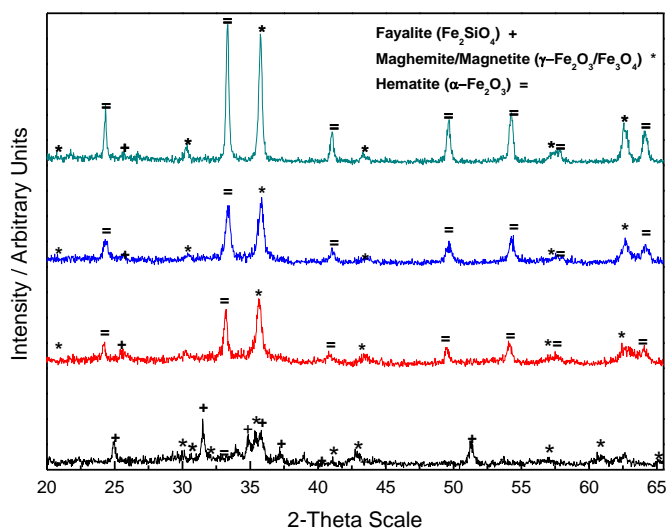


Figure 1. XRD patterns for original and heated waste: SOW16 (black), SOW16-T600 (red), SOW16-T750 (blue) and SOW16-T900 (green).

In order to study the decomposition of the fayalite in $\alpha\text{-Fe}_2\text{O}_3$, the SOW16-T waste was thermally treated at temperatures of 600 y 750 for 4 h and 900 °C for 1 h (samples: SOW16-T600, SOW16-T750 and SOW16-T900, respectively). Under these conditions, Fe_2SiO_4 is transformed into SiO_2 and iron oxides as revealed by the XRD patterns shown Figure 1. In an air atmosphere, Fe^{3+} is stabilized at temperatures around 600 °C with the subsequent formation of $\alpha\text{-}$ and $\gamma\text{-}$ Fe_2O_3 phases. At higher temperatures (900 °C), the enrichment of hematite ($\alpha\text{-Fe}_2\text{O}_3$) is evident.

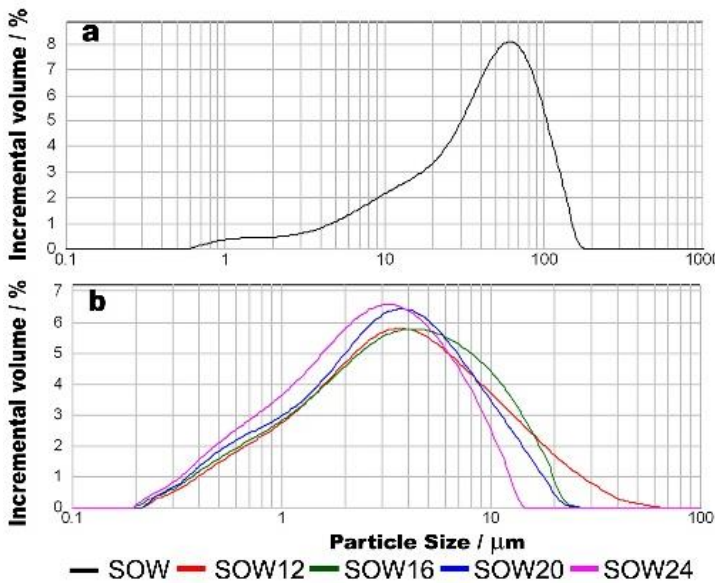


Figure 2. Particle size distributions of SOW and the resulting waste after grinding periods of 12, 16, 20 and 24 h.

Figure 3 shows the visible spectra of the SOW16-T samples. No absorption bands were observed in the case of SOW waste. However, the spectra of SOW16-T samples were similar to the

spectrum registered for standard hematite powder, with bands located at 525 (stronger band) and 660 nm. Moreover, a small increase in the absorbance observed for the SOW16-T900 sample corroborates the enrichment in α -Fe₂O₃, in good agreement with the XRD data and with the photocatalytic properties, as shown below.

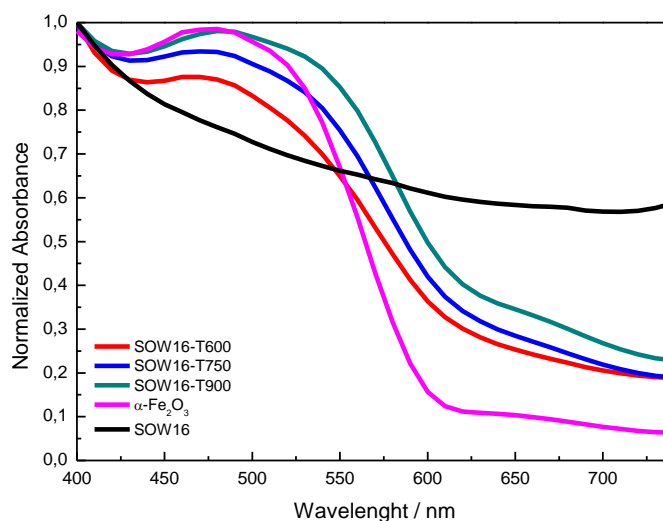


Figure 3. Diffuse reflectance spectra for SOW and SOW16-T samples. The spectrum of pure α -Fe₂O₃ has been included for comparison.

Self-cleaning and de-polluting materials

We examined the potential applications of these functional wastes as admixtures for new cement-based mortars with self-cleaning and de-pollution properties.

Table 1 shows the percent composition of the mortars studied. The mortar M was used as a reference. In the case of mortars M5SOW and M10SOW, the CaCO₃ filler and dolomite sands

were partially replacing by SOW16-T900. In some cases, 0.25 or 0.5 % wt of TiO_2 Evonik-P25 was also added to the M formulation (mortars M-0.25T and M-0.5T, respectively).

The mechanical properties of mortars were also. As way of example, in Table 2 is reported the values obtained for some of them. After 28 days of curing all samples have a flexural strength after 28 days rather than $7 \text{ N}\cdot\text{mm}^{-2}$, compressive strength considerably higher than $\text{N}\cdot\text{mm}^{-2}$ and abrasion strength lowest to 400 mm^3 , fulfilling the requirements of UNE-EN 1015-11 and UNE-EN 12808-2 standars. Therefore, the inclusion of the SOW and TiO_2 photocatalysts in the formulation of these mortars does not preclude their practical application.

Table 1. Composition of the studied mortars (wt%)

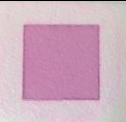
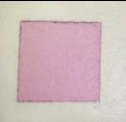
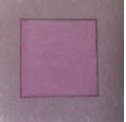
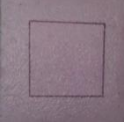
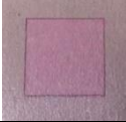
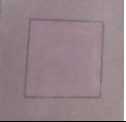
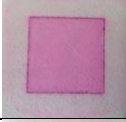
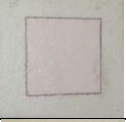

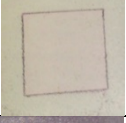
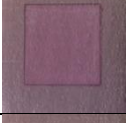
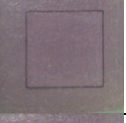
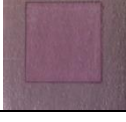
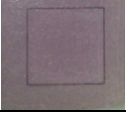
<i>Mortar</i>	<i>SiO₂</i>	<i>Cement</i>	<i>CaCO₃</i>	<i>Additives</i>	<i>SOW-T</i>	<i>TiO₂</i>
M	55.7	33	10	1.3	--	--
M5SOW	55.7	33	5	1.3	5.0	--
M10SOW	55.7	33	0	1.3	10.0	--
M0.25T	55.7	33	10	1.3	--	0.25
M0.5T	55.7	33	10	1.3	--	0.5
M10SOW-0.25T	55.7	33	0	1.3	10.0	0.25
M10SOW-0.5T	55.7	33	0	1.3	10.0	0.5

Table 2. Mechanical strengths of the studied mortars after 28 days of curing.

Mortar	Flexural Strength / N·mm⁻²	Compressive Strength / N·mm⁻²	Abrasion Strength / mm³
M	9,618	76,404	89
M10SOW	11,178	71,117	95
M-0.25T	9,223	69,988	95
M-0.5T	8,101	67,977	102

Rhodamine-B (RhB) degradation was used as a test reaction to check the ability of these building materials as self-cleaning pollutants based on their photocatalytic properties. In the series of mortars prepared, the photocatalytic ability of SOW16-T900 was compared with that of TiO₂ Evonik-P25, the standard additive used in photocatalytic building materials.² The red stain was reduced down after irradiation (Figure 4). In order to know quantitative evaluation of RhB dye photodegradation on each mortar the final a^* color parameter of the stain was measured. Figure 4 shows the R₂₆ index measured for each mortar, which denotes the decrease in red color after 26 h of sunlight irradiation and, by consequence, dye degradation (see experimental section). From these values, we can observe that a fast photocatalytic process is achieved by increasing the amount of the TiO₂ photocatalyst.

Figure 4. RhB Photodegradation in studied mortars

Mortar	0h Irradiation	26h Irradiation	R26[%]
M			--
M-5SOW			21.0
M-10SOW			29.4
M-0.25T			18.5
M-0.5T			27.8
M-10SOW-0.25T			30.3
M-10SOW-0.5T			36.3

It must be highlighted that similar values were obtained with mortars containing SOW16-T, the main difference being the need for a higher waste content in the mortar formulation to compensate for the weaker photocatalytic properties of hematite. Finally, the best dye photodegradation efficiency was obtained by combining the TiO₂ and SOW16-T as photocatalytic additives. The best performing mortar was M10SOW-0.5T, being able to degrade RhB up to 36.3%

The use of a photocatalytic pavement mortar is of interest in order to reduce the urban pollution through the photocatalysis. On this sense, Ai et al. reported that the removal of NO accounts for its photocatalytic oxidation to NO₂⁻/NO₃⁻.⁹ The model proposed for the photoactivity of TiO₂ was also valid to explain the PCO mechanism for NO_x gas conversion. When the semiconductor material is activated by irradiation with high energy photons – $h\nu$; 315-400 nm for TiO₂ – the electrons in the valence band are transferred to the conduction band, leaving electron holes – h^{+} –. The pair of mobile charges produced can reach the surface of the semiconductor particle and initiate the redox process. Moreover, reactive oxygen species are created from the water and oxygen molecules adsorbed on the particle surface, which act as strong oxidants. Subsequently, hydroxyl radicals – OH•– lead to the oxidation of NO to NO₂ which, in turn, produces nitrite and nitrate ions.⁹

The mortars here studied were used to promote the photocatalytic oxidation of NO and demonstrating their potential air purification application. TiO₂ containing mortars were studied too. Figure 5 shows the nitrogen oxide concentration profiles obtained during the NO oxidation test under illumination, with NO_x as the total sum of oxides: NO + NO₂. These profiles were characterized by the following common stages. i) In the absence of solar light (UV-A/Vis) radiation, neither the activation of the SOW16-T/TiO₂ sites on the surface of the photocatalytic mortars nor NO_x oxidation took place. The concentration of NO was kept constant at around 500 ppb during the first 10 minutes. ii) Under solar light radiation during thirty minutes, a heterogeneous photocatalysis reaction took place soon afterwards and the oxidation of the pollutant, NO, began. The decrease in NO_x concentrations became maximum and constant in this period of time, indicating the complete activation of photocatalyst sites. iii) During the ten last minutes of the test, when the solar light radiation was turned off, the NO_x concentrations slowly tended to return to the initial values.

The PCO efficiency increases with the amount of photocatalyst additive, SOW or TiO₂ (Figure 5). Moreover, the best efficiency is observed with the joint use of SOW16-T and TiO₂ in the mortar formulation. In this sense, good NO_x de-pollutant materials can be obtained, concurrently reducing the use of TiO₂. Figure 5c shows that similar PCO efficiency is obtained decreasing the amount of

TiO₂ by half and adding the valorized waste material under study. The photochemical assays for the degradation of RhB and NO_x showed synergistic photocatalytic activity between TiO₂ and the waste material, which is ascribed to the optical absorption ability of TiO₂ and α-Fe₂O₃ oxides in the longer wavelength region.¹

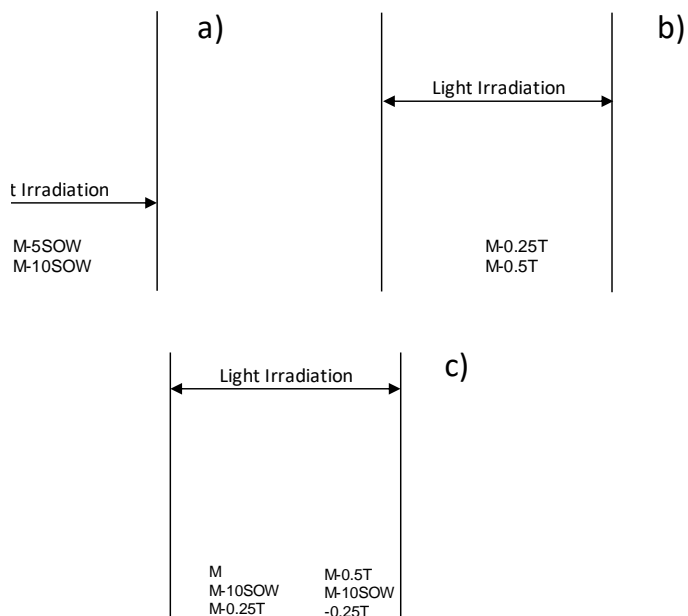


Figure 5. NO_x concentration profiles obtained during the photocatalytic degradation of NO gas over (a) M-SOW, (b) M-TiO₂ and (c) M-SOW-TiO₂ mortars, under artificial solar light.

Moreover, when both oxides are in contact, the separation efficiency of photo-generated electrons and holes is enhanced, thus resulting in better photochemical performance.¹⁰

4.2.4. Conclusions

The high amount of iron oxide present in the composition of industrial sandblasting operation wastes (SOW) makes them useful in potential applications based photocatalysis. The mechanical and thermal treatment of this waste gave rise to its enrichment in α - Fe_2O_3 , an iron oxide with photocatalytic properties under ambient conditions.

The product obtained after the waste transformation, SOW16-T, was used as admixture in a pavement mortar. The inclusion of SOW16-T in the mortar formulation does not alter significantly the mechanical properties. However, this mortar exhibits interesting self-cleaning and self-depolluting properties.

Moreover, the observed photocatalytic activity increased with the joint use of SOW-T and TiO_2 . The synergy observed for the mutual TiO_2 and α - Fe_2O_3 photocatalytic action allows for a reduction in the amounts of TiO_2 , a very expensive additive, used in new generation building materials.

Acknowledgements

The authors would like to thank the FEDER of European Union for financial support via project *“Preparación de materiales de construcción de última generación para la mejora de la sostenibilidad ambiental en entornos urbanos: disminución de gases contaminantes (NO_x) emitidos por los sistemas de transporte”* of de

“Programa Operativo FEDER de Andalucía 2007-2013”. We also thank all Agency of Public Works of Andalusia Regional Government staff and researchers for their dedication and professionalism.

References

1. Sugrañez, R.; Cruz-Yusta, M.; Mármol, I.; Martín, F.; Morales, J.; Sánchez, L., Use of industrial waste for the manufacturing of sustainable building materials. *ChemSusChem* **2012**, 5 (4), 694-699.
2. Chen, J.; Poon, C.-s., Photocatalytic construction and building materials: From fundamentals to applications. *Build. Environ.* **2009**, 44 (9), 1899-1906.
3. Hüsken, G.; Hunger, M.; Brouwers, H. J. H., Experimental study of photocatalytic concrete products for air purification. *Build. Environ.* **2009**, 44 (12), 2463-2474.
4. Folli, A.; Campbell, S. B.; Anderson, J. A.; Macphee, D. E., Role of TiO₂ surface hydration on NO oxidation photo-activity. *J. Photochem. Photobiol. A* **2011**, 220 (2-3), 85-93.
5. Ballari, M. M.; Hunger, M.; Hüsken, G.; Brouwers, H. J. H., NO_x photocatalytic degradation employing concrete pavement containing titanium dioxide. *Appl. Catal. B: Environ.* **2010**, 95 (3-4), 245-254.
6. Martinez, T.; Bertron, A.; Ringot, E.; Escadeillas, G., Degradation of NO using photocatalytic coatings applied to different substrates. *Build. Environ.* **2011**, 46 (9), 1808-1816.
7. Hahn, N. T.; Ye, H.; Flaherty, D. W.; Bard, A. J.; Mullins, C. B., Reactive ballistic deposition of α -Fe₂O₃ thin films for photoelectrochemical water oxidation. *ACS Nano* **2010**, 4 (4), 1977-1986.
8. Determinazione dell'attività fotocatalitica di leganti idraulici - Metodo della rodamina. 2008; Vol. UNI 11259:2008.
9. Ai, Z.; Ho, W.; Lee, S.; Zhang, L., Efficient photocatalytic removal of NO in indoor air with hierarchical bismuth oxybromide nanoplate

microspheres under visible light. *Environ. Sci. Technol.* **2009**, *43* (11), 4143-4150.

10. Ghorai, T. K.; Chakraborty, M.; Pramanik, P., Photocatalytic performance of nano-photocatalyst from TiO₂ and Fe₂O₃ by mechanochemical synthesis. *J. Alloys Compd.* **2011**, *509* (32), 8158-8164.

4.3. Synthesis of α -Fe₂O₃ on rice husk as efficient De-NO_x photocatalyst.

Synthesis of α -Fe₂O₃ on rice husk as efficient De-NO_x photocatalyst

*José Balbuena, Manuel Cruz-Yusta, Adrián Pastor and Luis Sánchez**

Departamento de Química Inorgánica, Instituto Universitario de Investigación en Química Fina y Nanoquímica IUIQFN, Universidad de Córdoba, Campus de Rabanales, E-14071 Córdoba, España.

* Corresponding Author:

- Prof. Luis Sánchez

ORCID ID: 0000-0002-0194-1908

Departamento de Química Inorgánica, Instituto Universitario de Investigación en Química Fina y Nanoquímica IUIQFN, Universidad de Córdoba, Campus de Rabanales, E-14071 Córdoba, España.

E-mail: luis-sanchez@uco.es

Tel: +00-34-957-218634

Abstract

α -Fe₂O₃ catalyst supported on rice husk ash (RHA) with enhanced photochemical NO_x abatement is reported. The Fe₂O₃/SiO₂ composites are prepared through the calcination of a mixture composed of RH and FeCl₃ at temperatures of 600 and 900 °C, for periods of 1 and 4 h. Fe₂O₃ crystallises, covering the cob-shaped silica skeleton. The thermal procedure determines the mineralogical composition, crystalline growth and surface area of samples. Samples obtained at 600 °C are α -Fe₂O₃ (hematite) with low levels of Fe₂SiO₄ and exhibit a microstructure constituted of meso- and macropores, with surface area values of 19.6 and 16.1 m² g⁻¹. At 900 °C only pure hematite is obtained but the microstructure is denser with very small surface area. Increasing the time of calcination to 4 h, apart the nano- and microparticles aggregates, hexagonal plates and truncated pseudocubes large crystals appear at temperatures of 600 and 900 °C, respectively. All the samples exhibit light absorption in the 300 to 900 nm UV-vis range. The photocatalytic abatement of NO gas is related to the surface area of the samples. In the best case an NO conversion value of 24% is found, the highest reported for hematite De-NO_x photocatalysts. Moreover, the selectivity of NO → NO₂ → NO₃⁻ oxidation process reaches values as high as 72% with the presence of large hexagonal plate hematite crystals.

Keywords

Iron oxide, Rice husk ash, Photocatalytic oxidation, Nitrogen oxides

STATUS: Submitted to Journal of Hazardous Materials.

4.3.1. Introduction

Nowadays, the air pollution by nitrogen oxide gases (NO_x = NO + NO₂) has become a major environmental problem that is accelerating due to extensive combustion of biomass and fossil fuels. Unfortunately, the 0.1 to 0.2 ppm hourly NO_x air concentration limits established by the international environmental agencies¹⁻² is usually surpassed in urban atmospheres of big cities. NO_x pollution provokes adverse effects on human health because of its toxicity, but also in the environment, by formation of ozone and acid rain³⁻⁶. This concern has raised the interest of the research community to study new actions effectively to remove NO_x gases from air (De-NO_x action).

Semiconductor photocatalysis is proposed as a 'green' and suitable technology as a De-NO_x approach in urban environments⁷⁻⁹. The photocatalytic De-NO_x process only requires sunlight, molecular oxygen and water as reagents, both being already present in outdoor conditions¹⁰⁻¹¹. Because of its exceptional optical, electronic and chemical properties, TiO₂ is the preferred semiconductor for the preparation of building materials, such as photocatalytic pavements, cement, mortars, and paints, as tools to combat NO_x pollution in our cities¹²⁻¹⁴. However, the practical application of photocatalysis for this air purification process lags behind the theoretical expectations¹⁵. In this connection, important challenges have to be addressed to overcome the main drawbacks found with TiO₂:

- i) Full solar light activity. The photocatalytic activity of TiO₂ only occurs with UV light of wavelengths shorter than 387 nm, owing to its band-gap of 3.2 eV, which allows it to take advantage of just 4–5% of the energy from sunlight¹⁰. This limits its use in dark areas of cities in which there is no direct sunlight, or in northern latitudes where only low levels of UV radiation reach to the surface¹⁶
- ii) Selective photocatalysis. The complete photocatalytic removal of NO_x from air proceeds when a complete oxidation of the nitrogen gases to NO₃⁻/HNO₃ species occurs. This a complex process involving several intermediate species⁹, an intermediate being the highly toxic NO₂ gas¹⁷. Thus, a selective process inhibiting the emission of NO₂ to the atmosphere is essential. However, the De-NO_x selectivity of TiO₂ (e.g. commercial Aeroxide® TiO₂ P25) is commonly lower than 65%, and
- iii) Sustainable production. The production of pure titanium dioxide involves several stages and is demanding in terms of chemical reagents and energy¹⁸, the production costs and environmental impact being relatively high for extended and massive use in our cities.

From the above, the researchers in the field have devoted their efforts to the preparation of modified titanium dioxide with enhanced De-NO_x effect, or the preparation of alternative materials^{17, 19-23}. Among different metal oxide materials, hematite (α -Fe₂O₃) appears to be an interesting De-NO_x photocatalyst due to its

favourable optical band gap (1.9–2.2 eV), extraordinary chemical stability in an oxidative environment, abundance and low cost²⁴. This was recently reported by our research group, for the first time²⁵⁻²⁶. However the observed De-NO_x efficiency is poor, probably as a consequence of inherent hematite semiconductor characteristics: relatively poor absorptivity, very short excited-state lifetime, poor oxygen evolution reaction kinetics, and a short hole diffusion length²⁴⁻²⁷. To solve these limitations and improve the De-NO_x efficiency, carbon-doped and nanostructure architectures were prepared^{25, 28-29}. However, more efficient hematite photocatalysts obtained through environmentally rational methods are desired.

SiO₂ was investigated as a suitable catalyst support due to its high surface area, porous structure and stability. Thus, some TiO₂/SiO₂ composites have been presented as enhanced De-NO_x photocatalysts³⁰⁻³¹. Rice husk (RH) is an agricultural waste, the ash of which contains about 92–95% silica (SiO₂)³². Compared to the conventional silicon alkoxides routes, the route to synthesise silica nanoparticles from RHs offers additional advantages, including greener raw materials, lower cost, and higher sustainability³³. Previous studies of RH ash (RHA) have revealed not only amorphous SiO₂ particles having a size in the nanoscale range, but also the typical characteristics of the particles; specifically, that a high surface area could be generated by the final process of heat treatment³⁴⁻³⁶. In this way, the use of rice husk ash as catalyst support for metals and metal oxides has previously been reported^{32-33, 37-43}.

In this work, beyond the structural and morphological characterisation, the photocatalytic NO_x abatement performances of Fe₂O₃/SiO₂ nanocomposites prepared using RH are presented. Remarkably, the synthetic procedure influences on the Fe₂O₃ crystal growth and the mesoporous structure, both parameters having an influence on the De-NO_x activity. The obtained systems display a high NO_x removal efficiency in comparison to prior-reported Fe₂O₃ De-NO_x photocatalysts, the selectivity being conditioned by the particle shape. Moreover, the composites are obtained by a simple and low-cost method, which helps to minimise the environmental issues associated with the current undesirable disposal of RHs ³³.

4.3.2. Experimental

Preparation of Fe₂O₃/SiO₂ composites

Prior to the preparation of Fe₂O₃/SiO₂ composites, RH (Herba Ricemills, S.L.U.) was washed to remove dirt by boiling in deionised water for 2 h under continuous stirring, then filtered and dried in an oven at 70 °C for 24 h. Following previously reported RHA/catalyst precursor ratios, 20 g of dry RH was mixed with 22.7 g of FeCl₃·6H₂O from Panreac, as iron precursor. In order to homogenise the RH particle size and to enhance the contact between components, the mixture was milled using a planetary mill (45 min, 300 rpm). Finally, mixtures were calcined at 600 (sample A) and 900 °C (sample B) in air for periods of 1 h (samples A1 and B1) and 4 h (samples A2 and B2).

Characterization

Crystalline phases were identified by using X-ray diffraction (XRD) on a Siemens D5000 X-ray diffractometer with CuK_α radiation. The diffractogram was run with a step size of 0.02 2θ° and a counting time of 0.2 s. The morphology of samples was examined by scanning electron microscopy (SEM) with a Jeol JMS-6400 microscope. Nitrogen absorption isotherms were obtained at 77.4 K on an ASAP 2020 instrument from Micromeritics. Samples were degassed at 105 °C for 3 h. Specific surface areas were calculated from N₂ sorption isotherms, using the multipoint Brunauer–Emmett–Teller (BET) method, and microporosity and size distributions were estimated using the t-plot, Barrett-Joyner-Halenda (BJH) method. Diffuse reflectance (DR) spectra were recorded at a scan rate of 30 nm min⁻¹ from 300 to 900 nm in 0.5 nm steps, using a Varian Cary 1E spectrophotometer. The modified DR absorption spectra were obtained by using the Kubelka–Munk function, $F(R) = (1 - R)^2 / (2R)$.

Photocatalytic activity measurement

The ability of samples for photochemical NO abatement was studied by using a 50 x 50 mm sampler holder placed in a laminar flow reactor. The reactor was placed inside a Solarbox 3000e RH light irradiation box equipped with an Xe lamp with controlled irradiance (25 and 580 W m⁻² for UV and visible). A 500 mg sample

was used in each photocatalytic test. As pollutant, a mixture of air/NO was sent to the photoreactor with a NO concentration of 150 ppb (obtained by mixing synthetic air and pure NO). This NO concentration was deliberately chosen in order to achieve an optimal sensitivity, being representative of NO concentrations found during intense photochemical pollution events in urban environments⁴⁴. Previously, the air was first passed through a gas-washing bottle, filled with demineralised water in order to keep the relative humidity of the supplied gas fixed at $50 \pm 5\%$. A flow rate, Q , of 0.30 L min^{-1} was employed. The accurate measurement of the concentration of NO, NO_x and NO₂ was carried out using a chemiluminescence analyser (model Environnement AC32M). For each test, the air/NO gas stream was passed over the sample in the dark for a period of 10 min in order to discard the NO_x adsorption on the sample surface or its direct photolysis, and, the photoreactor subsequently irradiated. Each test was repeated three times to obtain average concentration values. The calculated standard deviations were $\pm 0.3 \text{ ppb}$ for NO concentration and $\pm 1.0 \text{ ppb}$ for NO₂ and NO_x concentrations. The photocatalytic efficiency was discussed by evaluation of the following parameters:

$$\text{NO conversion (\%)} = \{ ([\text{NO}]_{\text{in}} - [\text{NO}]_{\text{out}}) / [\text{NO}]_{\text{in}} \} \times 100 \quad (1)$$

$$\text{NO}_2 \text{ released (\%)} = ([\text{NO}_2]_{\text{out}} / [\text{NO}]_{\text{in}}) \times 100 \quad (2)$$

$$\text{NO}_x \text{ conversion (\%)} = \{ ([\text{NO}_x]_{\text{in}} - [\text{NO}_x]_{\text{out}}) / [\text{NO}_x]_{\text{in}} \} \times 100 \quad (3)$$

where [NO]_{in}, [NO_x]_{in} and [NO]_{out}, [NO_x]_{out} denote the measured inlet and outlet concentrations, respectively, while [NO_x] = [NO] + [NO₂].

The system selectivity ¹⁷, *S*, is determined according to the equation:

$$S (\%) = \frac{([NO_x]_{in} - [NO_x]_{out})/[NO_x]_{in}}{([NO]_{in} - [NO]_{out})/[NO]_{in}} \times 100 \quad (4)$$

4.3.3. Results and discussion

Photocatalyst characterisation

Firstly, the expected SiO₂ support obtained after the calcination process was characterised. Once the RH was heated at temperatures ≥600 °C in air, the carbon content was removed and the product obtained consisted mainly of silica (>92%) and minor metallic impurities, as previously reported ⁴⁵. The pristine RH particles (Fig. 1a) adopted a cob-shaped cellulose skeleton when calcined (Fig. 1b). The X-ray diffraction pattern exhibits a broad peak centred at 22° (Fig. 1c) corresponding to amorphous SiO₂ ⁴².

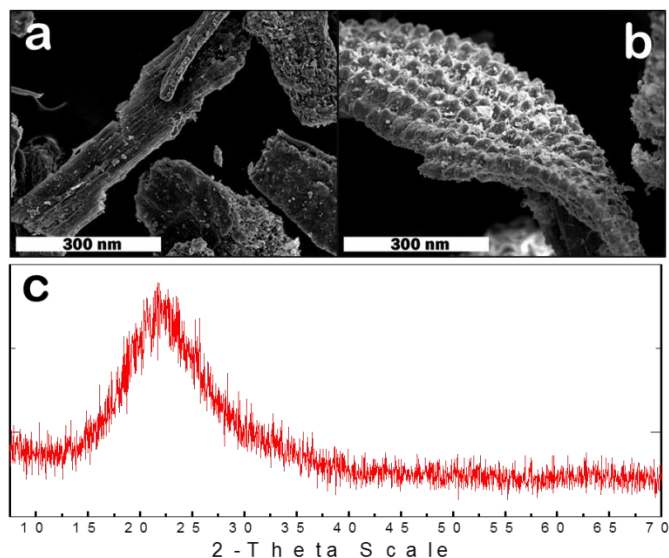


Figure 1. (a) SEM image of RH sample. (b) SEM image and (c) XRD pattern of RHA sample.

$\text{Fe}_2\text{O}_3/\text{SiO}_2$ composites were obtained after the calcination of the RH- FeCl_3 precursor mixture. The XRD patterns obtained for the four samples are shown in Fig. 2. For samples obtained at high temperature, samples B1 and B2, all detected peaks were ascribable to the hkl reflections of rhombohedral $\alpha\text{-Fe}_2\text{O}_3$ (hematite). Thus, the diffraction peaks at 24.1° , 33.1° , 35.6° , 40.8° , 49.4° , 54.1° and 57.6° can be attributed to (012), (104), (110), (113), (024), (116) and (018) crystal planes of $\alpha\text{-Fe}_2\text{O}_3$, respectively [PDF card No. 00-33-0664]. However, in the case of samples A1 and A2 (obtained at 600°C) minor impurities tentatively ascribed to amorphous Fe_2SiO_4 oxide were found^{26, 46}. On the other hand, the peaks became larger and narrower in samples A2 and B2, associated

with a higher crystallinity. Apart from its amorphous character, the negligible presence of the silica halo expected at 22° would be indicative of a good iron oxide covering on the silica support.

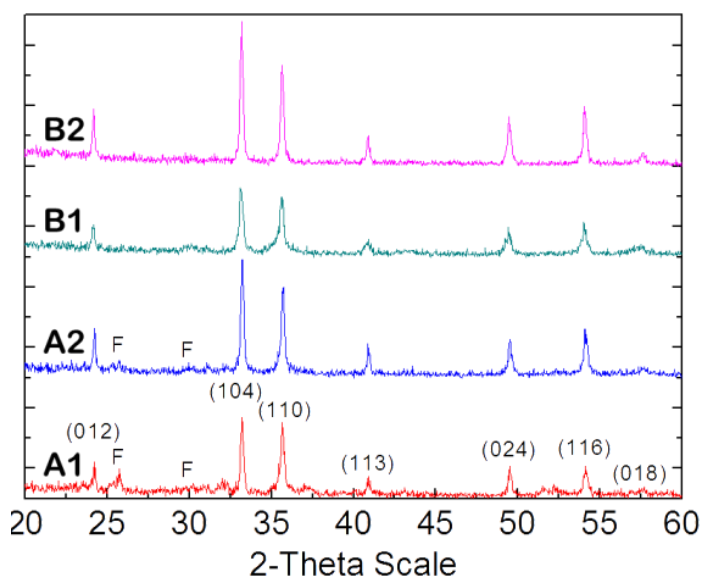


Figure 2. XRD patterns of $\text{Fe}_2\text{O}_3/\text{SiO}_2$ composites (F = Fayalite; Fe_2SiO_4)

As observed from SEM images (Fig. 3), the hematite crystals grew dispersed on the cob-shaped skeleton. Interestingly, different particle shapes were obtained for each heating procedure. For sample A1, obtained after 1 h at 600°C , the silica substrate was covered by a dense film consisting of aggregates of irregular nanoparticles (Fig. 3a and b).

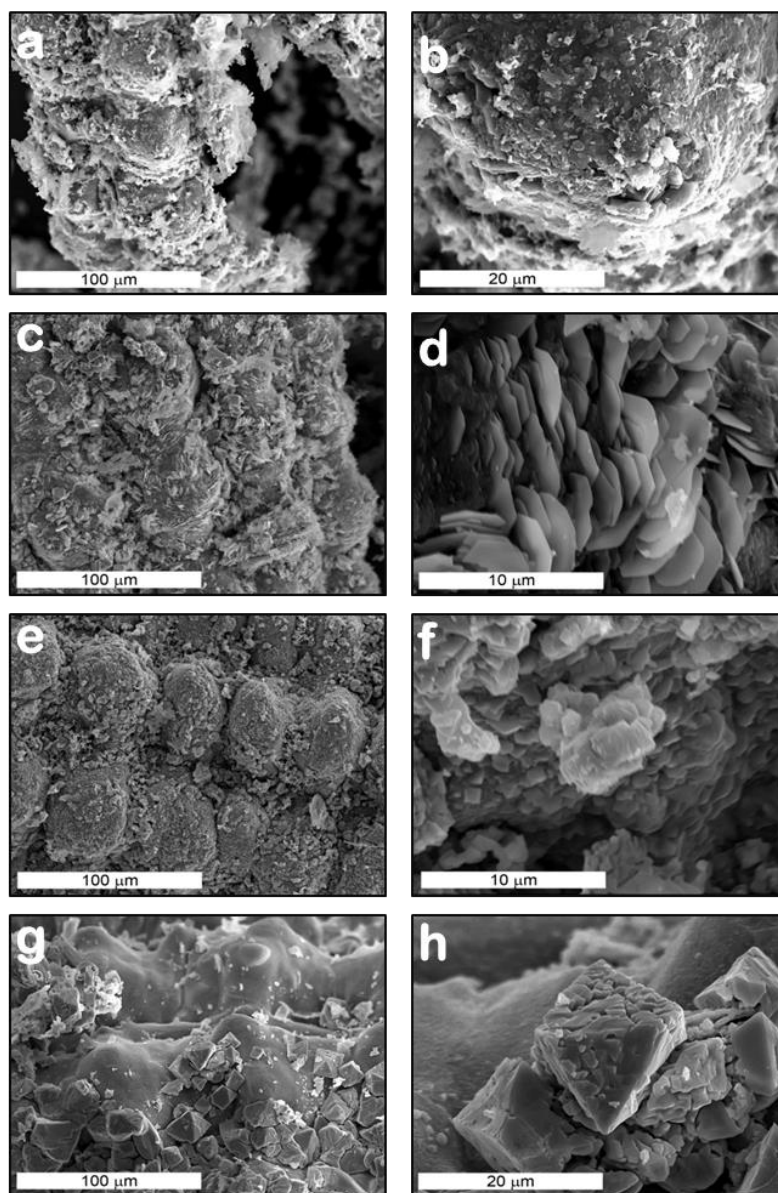


Figure 3. SEM images of samples A1 (a,b), A2 (c,d), B1 (e,f) and B2 (g,h).

Extending the heating period to 4 hours (sample A2), embryonic hexagonal plates of hematite emerged from the film (Fig. SI-1), and also more perfect hexagonal plates of width

$\approx 4 \mu\text{m}$ and height $\approx 80 \text{ nm}$ were observed (Fig. 3c and d). At higher temperature, $900 \text{ }^\circ\text{C}$, the covering hematite film appeared denser and the particles larger and more crystallised than their counterparts obtained at $600 \text{ }^\circ\text{C}$ (Fig. 3e and f). Again, after 4 h calcination, large crystals of hematite emerged from the film in different forms of truncated pseudocube embryos (Fig. 3g and Fig SI-2). In most cases, these crystals exhibited many imperfections on their facets (Fig 3h), indicating that the period of calcination was too short to complete the crystallisation. In order to understand the mechanism of crystallisation of hematite on $\text{Fe}_2\text{O}_3/\text{SiO}_2$ composites, a similar thermal procedure was used for the preparation of pure $\alpha\text{-Fe}_2\text{O}_3$ from FeCl_3 precursor. The corresponding SEM images (Fig. SI-3) did not reveal significant changes in morphology with heating procedure. The four hematite samples were now comprised of unshaped pseudo-polyhedral micronic particles, and a significant increase in size was observed only after heating at $900 \text{ }^\circ\text{C}$ for 4 hours. Therefore, in the case of the $\text{Fe}_2\text{O}_3/\text{SiO}_2$ composite study objects, the silica skeleton acts as support, but also as a template influencing the growth of the hematite crystals.

The following crystal growth mechanism is proposed. Because the RH skeleton disperses the FeCl_3 molecules on its surface, during calcination the iron oxide crystallises as nanometric ($600 \text{ }^\circ\text{C}$) and submicronic particles ($900 \text{ }^\circ\text{C}$),

constituting a denser film on the silica skeleton at the higher temperature. Extending the time of calcination accounts for the formation of hexagonal plates and imperfect truncated pseudocubes. Hematite twins on the {001} and {102} planes⁴⁷. For the hexagonal prisms the side facets can be {001} or {110}, while truncated pseudocubes are enclosed by the family of {100}, {101} and {012} facets⁴⁸. Because the surface energy of {012} is lower than that of {001} the formation of a pseudocube is thermodynamically preferred to a hexagonal prism. However, the difference between the relative free energies of crystals and the surface energy values of the index planes are determined by several parameters: crystal size, atmospheric conditions, solvent concentration, inorganic-organic additives and metallic ions⁴⁷⁻⁵². In our case, the chemical composition of the support matrix, the iron precursor and the thermal procedure favour the formation of hexagonal prisms at the lower temperature.

It is generally accepted that the reactivity of a photocatalyst is determined by its surface area and electronic structure. The surface area and porous structure were elucidated from the corresponding N₂ adsorption-desorption isotherm of both RHA and Fe₂O₃/SiO₂ samples. The isotherm of bare RHA support (Fig. SI-4) is identified as a type (IV) isotherm according to BET classification and with a type H1 hysteresis loop according to IUPAC classification⁴²⁻⁴³. The step increase in

N_2 adsorption with increasing relative pressure, P/P_0 , with an amount of $50 \text{ cm}^3 \cdot \text{g}^{-1}$ of N_2 adsorbed at $P/P_0 = 0.1$ suggests the presence of an appreciable number of micropores ⁴². The presence of mesopores is revealed by the slightly slope of the isotherm in the 0.1–0.92 P/P_0 range. The curve of the pore size distribution evaluated from desorption data using the BJH model (Fig. SI-4 inset) exhibits a narrower pore size distribution, ranging from 1–6 nm.

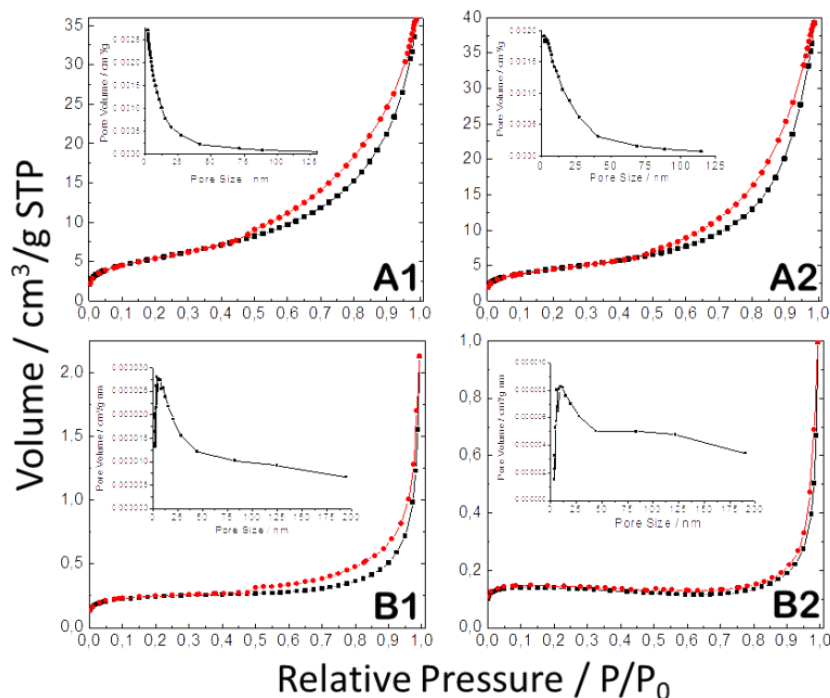


Figure 4. N_2 adsorption-desorption isotherm and pore size distribution for $\text{Fe}_2\text{O}_3/\text{SiO}_2$ composites

A considerable change in pore structure is evident when the RHA supports the hematite film on its surface. The

isotherms of Fe₂O₃/SiO₂ composites (Fig. 4) exhibited almost the same shape, and are similar to BET classification type II, except in the case of sample B2. These porous materials combine the existence of meso- and macropores in a wide range of sizes (Fig. 4 insets), the proportion of macropores increasing with the temperature of calcination (sample B1). Table 1 summarises the main surface properties of the Fe₂O₃/SiO₂ samples, including that of RHA for comparison purposes. As α -Fe₂O₃ forms onto the silica skeleton, the pores of RHA are completely covered by the hematite crystals, forming a new porous structure whose surface area, around 19.6 m²·g⁻¹, is one order of magnitude lower than that of RHA. According to observations by XRD and SEM, the film texture changes with the temperature and time of calcination, becoming denser as both parameters increase. In fact, the sample B2 could not be catalogued as a porous material, because N₂ adsorption was clearly negligible. Therefore, because of its lack of an appropriate surface area, this sample was not used as photocatalyst in later studies. In spite of the drastic loss of surface area found from RHA to Fe₂O₃/SiO₂ samples, the use of a silica skeleton as support is of interest. Thus, samples A1 and A2 exhibit surface area values around three times higher than pure hematite nanopowder previously reported as a De-NO_x photocatalyst ²⁵.

Additional characterisation concerning the light activation of composites was performed. The absorption spectra converted to the Kubelka–Munk function (Fig. 5) shows that all $\text{Fe}_2\text{O}_3/\text{SiO}_2$ samples shared a comparable absorption edge.

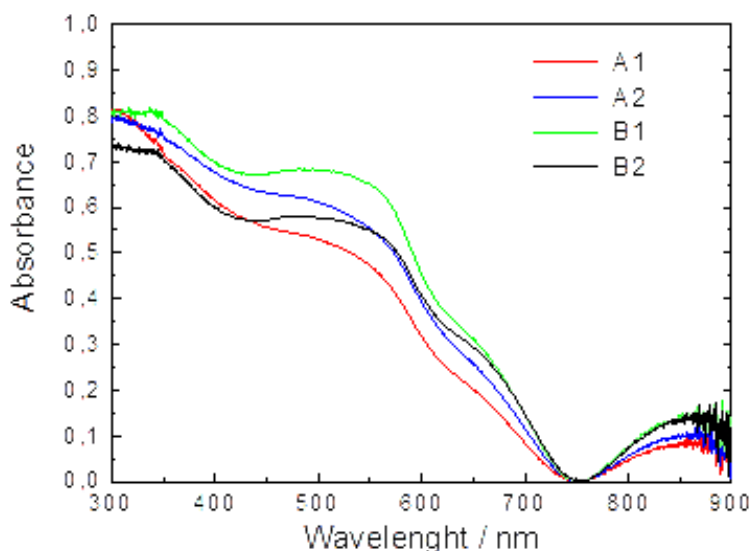
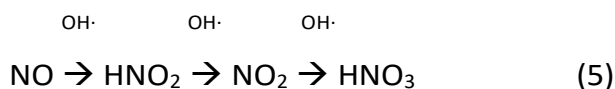


Figure 5. UV-Vis DR spectra for $\text{Fe}_2\text{O}_3/\text{SiO}_2$ composites

As in the case of standard hematite⁵³, they exhibited a strong band at 320 nm corresponding to the Fe-ligand charge exchange interaction. The broad signals at 540, 660 and 856 nm can be assigned to the ${}^6\text{A}_{1g} \rightarrow {}^4\text{A}_{1g}$, ${}^6\text{A}_{1g} \rightarrow {}^4\text{T}_{2g}$ and ${}^6\text{A}_{1g} \rightarrow {}^4\text{T}_{1g}$ transitions typical of the octahedral Fe^{3+} ion in hematite⁵⁴. The light absorption differed between samples because of the crystallinity and surface texture of each. The band gap for all samples was determined to be 1.94 eV (Fig. SI-5), as expected for hematite⁵⁵.

De-NO_x photocatalytic tests

Following the main goal of this work, the photochemical ability of Fe₂O₃/SiO₂ samples to abate the atmospheric concentration of NO was studied. The photochemical process removes NO gas from air through its complete oxidation to nitrate or nitric acid (NO₃⁻/HNO₃) species, a complex process involving several intermediate species ^{7, 9, 56}. As in the case of TiO₂, the ability of hematite to achieve the complete photochemical process has recently been reported ^{25, 29}. Basically, the mechanism consists of several one-electron transfer steps, via nitrous acid (HNO₂) and nitrogen dioxide (NO₂) as intermediate species ⁷. When the α-Fe₂O₃ nanocrystals are irradiated by UV–vis, because an electron in the valence band (VB) acquires the necessary energy to migrate to the conduction band (CB), pairs of mobile charges (e⁻ and h⁺) reach the surface of the semiconductor particles. In the presence of adsorbed water molecules, reactive oxygen species (ROS) such as hydroxyl radicals (OH•) are formed, which initiate the progressive oxidation of NO gas:



Figs. 6a and SI-6 show the concentration profiles of nitrogen oxide evolution recorded for the Fe₂O₃/SiO₂ samples as a function of UV-Vis irradiation time. In the absence of light

irradiation for the first 10 min, the concentration of NO was constant. This confirms that NO gas adsorption on the Fe_2O_3 particle surface does not occur.

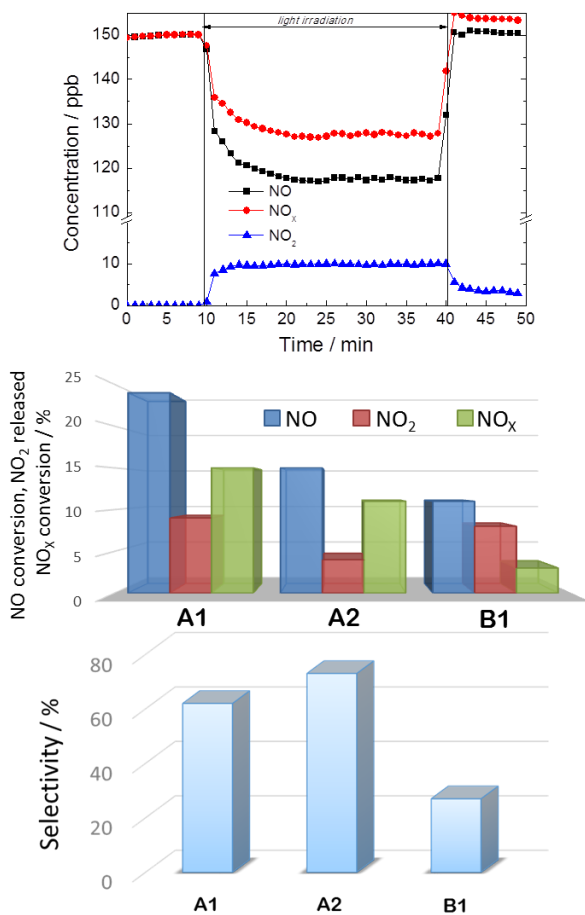


Figure 6. (a) Nitrogen oxides concentration profiles obtained during the photo-degradation of gaseous NO under UV-Vis irradiation on sample A1. (b) NO conversion (%), NO₂ released (%), and NO_x conversion (%) for $\text{Fe}_2\text{O}_3/\text{SiO}_2$ composites. (c) Selectivity values (%) for $\text{Fe}_2\text{O}_3/\text{SiO}_2$ samples.

Under irradiation (30 min), the NO concentration decreased suddenly, being indicative of the existence of a light induced process. Thus, as the α -Fe₂O₃ sites are activated by the UV-vis light, the heterogeneous photocatalytic reaction takes place and the oxidation of NO begins. When illumination was shut down, the photochemical process stopped and the NO concentration returned to its initial value. The decrease of NO concentration values measured under light condition is related to the amount of removed NO. Sample A1, possessing the highest surface area, presented a maximum NO conversion value (Fig. 6b) close to 24%, this being almost double the efficiency of that previously reported for nanometric powdered hematite ²⁵. As expected ²⁴, the photocatalytic efficiency decayed as the surface area of the samples decreased, in the order sample A1 > A2 > B1.

However, the effective air quality improvement achieved by photocatalysis must take into account the appearance of the intermediate NO₂ during the photochemical De-NO_x process. This NO₂ is undesirable because is 8 to 25 times more dangerous than NO ⁵⁷. From Fig. 6a it can be seen that, even though in low amounts (6–9 ppb for A samples), some NO molecules were released again to the atmosphere as the highly toxic NO₂. Therefore, it is of high importance that this emission was lessened as much as possible by the photocatalyst. Thus, interest in a De-NO_x photocatalyst must

also be focused to achieve a high De- NO_x selectivity. As observed from Fig. 6b, the NO_2/NO ratios were different for each sample, affecting their whole De- NO_x ability. For a better comprehension, Fig. 6c shows the photocatalytic NO_x abatement selectivity (S) for $\text{Fe}_2\text{O}_3/\text{SiO}_2$ composites. This parameter expresses the ratio of degraded NO that is ultimately converted into harmless nitrate, rather than into toxic nitrogen dioxide. As observed, the selectivity was the highest in the case of sample A2, with a value of 72 %. Therefore, the best performance for the $\text{NO} \rightarrow \text{NO}_2 \rightarrow \text{NO}_3^-$ oxidation process (5) was achieved by this photocatalyst. The best S values measured for sample A2 could be associated with its peculiar particle shape. In other transition metal oxides, good catalytic activity of hexagonal plates compared to bulk material has previously been reported⁵⁸. Similarly, it is known that photocatalytic activity of hematite increases with crystallinity. Apart from crystallite size, the orientation plays a major role in enhancing photocatalytic properties²⁴. Even though hematite particles exhibiting {110} and {012} facets showed higher photocatalytic yields than those exhibiting {001} – the case of sample A2 –^{49-50, 59}, the ability of hematite hexagonal nanoplates in gas molecule reactant chemisorption and photocatalytic processes has been reported⁴⁹⁻⁵⁰. In consequence, the highest selectivity of sample A2 could be

accounted for by favoured NO₂ adsorption/oxidation on the surface of the hexagonal crystals.

Further experiments with samples composed only of hexagonal nanoplates must be performed in order to corroborate this initial evidence. Interestingly, for both samples A1 and A2, the *S* values exceeded that reported for the commercial Aeroxide® TiO₂ P25 (Evonik) – a material broadly used worldwide as reference in photocatalytic De-NO_x processes – and some modified TiO₂-based materials previously studied (*S* < 55%)⁶⁰⁻⁶². Moreover, on average, the Fe₂O₃/SiO₂ composites exhibited better NO conversion efficiency and selectivity than previous nanostructured Fe₂O₃, C-Fe₂O₃ and Fe₂O₃/TiO₂ hematite-based De-NO_x photocatalysts^{25, 63}. This validates the synthetic strategy studied here in the preparation of new composites as environmental friendly De-NO_x photocatalysts.

4.3.4. Conclusions

Fe₂O₃ catalysts supported on rice husk ash (RHA) prepared by a simple calcination procedure were found to be active for the photochemical oxidation of NO gas, a main pollutant in urban atmospheres. The catalyst was composed of pure hematite phase when obtained at 900 °C, with a minority presence of fayalite (Fe₂SiO₄) when prepared at 600 °C. The temperature and time of calcination determined the crystalline growth of the supported iron

oxide and surface area of the catalyst. After 1 h calcination, the large surface area of RHA favoured the crystallisation of irregular nano- (at 600 °C) and microparticles (at 900 °C), forming a film which covered the cob-shaped silica skeleton. Increasing the time of calcination to 4 h resulted in the appearance of hexagonal plates and large truncated pseudocube crystals at temperatures of 600 and 900 °C, respectively. Samples obtained at the lower temperature exhibited a microstructure comprised of meso- and macropores, with surface area values of 19.6 and 16.1 m²·g⁻¹. The use of RHA as support served to increase the surface area of hematite. However, calcination at 900 °C led to dense structures with very small surface area. All catalysts exhibited light absorption in the 300 to 900 nm UV-vis range. The photocatalytic abatement of NO gas was related to the surface area of the samples, decreasing in the order sample A1 > A2 > B1. The NO conversion value of 24% found for sample A1 is higher than that observed for nanostructured hematite De-NO_x photocatalyst previously reported. On the other hand, the selectivity of NO → NO₂ → NO₃⁻ oxidation process was enhanced by the presence of large hematite crystals. In summary, through the valorisation of the agricultural waste RH as catalyst support, iron oxide photocatalysts of enhanced De-NO_x activity can be prepared. The results obtained here open new interesting perspectives for its potential use in air remediation.

Appendix A. Supplementary Information

Supplementary Information accompanying this paper includes more information about: the morphology of the samples; N₂ isotherm for RHA; Kubelka-Munk transformed reflectance spectra; De-NO_x tests.

Acknowledgements

This work was financially supported by the Junta de Andalucía (Group FQM-175) and Universidad de Córdoba (XX PP. Modalidad 4.1). The authors thank to Herba Ricemills S.L.U. for the supply of RH samples.

References

1. United States Environmental Protection Agency. <http://www.epa.gov/> (accessed March 2017).
2. European Environment Agency. <http://www.eea.europa.eu> (accessed March 2017).
3. Williams, M. L.; Carslaw, D. C., New Directions: Science and policy – Out of step on NO_x and NO₂? *Atmos. Environ.* **2011**, *45* (23), 3911-3912.
4. Frampton, M. W.; Greaves, I. A., NO_x - NO_x: Who's There? *Am. J. Respir. Crit. Care. Med.* **2009**, *179* (12), 1077-1078.
5. Colls, J., *Air pollution*. 2nd ed.; Spon Press Taylor & Francis Group: London, 2002.
6. Nevers, N. d., *Air Pollution Control Engineering*. Second Edition ed.; McGraw-Hill: Illinois, 2000; p 586.
7. Devahasdin, S.; Fan Jr, C.; Li, K.; Chen, D. H., TiO₂ photocatalytic oxidation of nitric oxide: transient behavior and reaction kinetics. *J. Photochem. Photobiol. A* **2003**, *156* (1–3), 161-170.
8. Hunger, M.; Hüsken, G.; Brouwers, H. J. H., Photocatalytic degradation of air pollutants — From modeling to large scale application. *Cem. Concr. Res.* **2010**, *40* (2), 313-320.
9. Balbuena, J.; Cruz-Yusta, M.; Sánchez, L., Nanomaterials to combat NO_x pollution. *J. Nanosci. Nanotechnol.* **2015**, *15* (9), 6373-6385.

10. Chen, H.; Nanayakkara, C. E.; Grassian, V. H., Titanium Dioxide Photocatalysis in atmospheric chemistry. *Chem. Rev.* **2012**, *112* (11), 5919-5948.
11. Folli, A.; Campbell, S. B.; Anderson, J. A.; Macphee, D. E., Role of TiO₂ surface hydration on NO oxidation photo-activity. *J. Photochem. Photobiol. A* **2011**, *220* (2–3), 85-93.
12. Lackhoff, M.; Prieto, X.; Nestle, N.; Dehn, F.; Niessner, R., Photocatalytic activity of semiconductor-modified cement— influence of semiconductor type and cement ageing. *Appl. Catal. B: Environ.* **2003**, *43* (3), 205-216.
13. Sagrañez, R.; Álvarez, J. I.; Cruz-Yusta, M.; Mármol, I.; Morales, J.; Vila, J.; Sánchez, L., Enhanced photocatalytic degradation of NO_x gases by regulating the microstructure of mortar cement modified with titanium dioxide. *Build. Environ.* **2013**, *69*, 55-63.
14. Martinez, T.; Bertron, A.; Ringot, E.; Escadeillas, G., Degradation of NO using photocatalytic coatings applied to different substrates. *Build. Environ.* **2011**, *46* (9), 1808-1816.
15. Todorova, N.; Giannakopoulou, T.; Karapati, S.; Petridis, D.; Vaimakis, T.; Trapalis, C., Composite TiO₂/clays materials for photocatalytic NO_x oxidation. *Appl. Surf. Sci.* **2014**, *319*, 113-120.
16. Folli, A.; Bloh, J. Z.; Strøm, M.; Pilegaard Madsen, T.; Henriksen, T.; Macphee, D. E., Efficiency of solar-light-driven TiO₂ photocatalysis at different latitudes and seasons. Where and when does TiO₂ really work? *J. Phys. Chem. Lett.* **2014**, *5* (5), 830-832.

17. Bloh, J. Z.; Folli, A.; Macphee, D. E., Photocatalytic NO_x abatement: why the selectivity matters. *RSC Adv.* **2014**, *4* (86), 45726-45734.
18. European directives 78/176/EEC, 82/883/EEC and 92/112/EEC. <http://eur-lex.europa.eu/> (accessed March 2017).
19. Tobaldi, D. M.; Seabra, M. P.; Otero-Irurueta, G.; de Miguel, Y. R.; Ball, R. J.; Singh, M. K.; Pullar, R. C.; Labrincha, J. A., Quantitative XRD characterisation and gas-phase photocatalytic activity testing for visible-light (indoor applications) of KRONOClean 7000[registered sign]. *RSC Adv.* **2015**, *5* (124), 102911-102918.
20. Zamiri, R.; Tobaldi, D. M.; Ahangar, H. A.; Rebelo, A.; Seabra, M. P.; Belsley, M. S.; Ferreira, J. M. F., Study of far infrared optical properties and, photocatalytic activity of ZnO/ZnS hetero-nanocomposite structure. *RSC Adv.* **2014**, *4* (67), 35383-35389.
21. Li, H.; Liu, B.; Wang, Y.; Yin, S.; Ma, X.; Wang, X.; Wu, Q.; Shen, R.; Chen, H., A facile one-step hydrothermal synthesis of a B-doped graphene/rod-shaped TiO₂ nanocomposite. *RSC Adv.* **2014**, *4* (72), 37992-37997.
22. Kim, J. Y.; Kim, C. S.; Chang, H. K.; Kim, T. O., Synthesis and characterization of N-doped TiO₂/ZrO₂ visible light photocatalysts. *Adv. Powder Tech.* **2011**, *22* (3), 443-448.
23. Nie, H.; Ou, M.; Zhong, Q.; Zhang, S.; Yu, L., Efficient visible-light photocatalytic oxidation of gaseous NO with graphitic carbon nitride (g-C₃N₄) activated by the alkaline hydrothermal

- treatment and mechanism analysis. *J. Hazard. Mater.* **2015**, *300*, 598-606.
24. Mishra, M.; Chun, D.-M., α -Fe₂O₃ as a photocatalytic material: A review. *Appl. Catal. A: Gen.* **2015**, *498*, 126-141.
25. Sugrañez, R.; Balbuena, J.; Cruz-Yusta, M.; Martín, F.; Morales, J.; Sánchez, L., Efficient behaviour of hematite towards the photocatalytic degradation of NO_x gases. *Appl. Catal. B: Environ.* **2015**, *165*, 529-536.
26. Sugrañez, R.; Cruz-Yusta, M.; Mármol, I.; Morales, J.; Sánchez, L., Preparation of sustainable photocatalytic materials through the valorization of industrial wastes. *ChemSusChem* **2013**, *6* (12), 2340-2347.
27. Wheeler, D. A.; Wang, G.; Ling, Y.; Li, Y.; Zhang, J. Z., Nanostructured hematite: synthesis, characterization, charge carrier dynamics, and photoelectrochemical properties. *Energy Environ. Sci.* **2012**, *5* (5), 6682-6702.
28. Carraro, G.; Sugrañez, R.; Maccato, C.; Gasparotto, A.; Barreca, D.; Sada, C.; Cruz-Yusta, M.; Sánchez, L., Nanostructured iron(III) oxides: From design to gas- and liquid-phase photocatalytic applications. *Thin Solid Films* **2014**, *564*, 121-127.
29. Balbuena, J.; Cruz-Yusta, M.; Cuevas, A. L.; Lopez-Escalante, M. C.; Martín, F.; Pastor, A.; Sánchez, L., Enhanced activity of α -Fe₂O₃ for photocatalytic NO removal. *RSC Adv.* **2016**, *6* (95), 92917-92922.
30. Signoretto, M.; Ghedini, E.; Trevisan, V.; Bianchi, C. L.; Ongaro, M.; Cruciani, G., TiO₂-MCM-41 for the photocatalytic

- abatement of NO_x in gas phase. *Appl. Catal. B: Environ.* **2010**, 95 (1–2), 130-136.
31. Bellardita, M.; Addamo, M.; Di Paola, A.; Marci, G.; Palmisano, L.; Cassar, L.; Borsa, M., Photocatalytic activity of TiO₂/SiO₂ systems. *J. Hazard. Mater.* **2010**, 174 (1–3), 707-713.
 32. Adam, F.; Appaturi, J. N.; Thankappan, R.; Nawi, M. A. M., Silica–tin nanotubes prepared from rice husk ash by sol–gel method: Characterization and its photocatalytic activity. *Appl. Surf. Sci.* **2010**, 257 (3), 811-816.
 33. Li, Y.; Lan, J. Y.; Liu, J.; Yu, J.; Luo, Z.; Wang, W.; Sun, L., Synthesis of Gold Nanoparticles on Rice Husk Silica for Catalysis Applications. *Ind. Eng. Chem. Res.* **2015**, 54 (21), 5656-5663.
 34. Conradt, R.; Pimkhaokham, P.; Leela-Adisorn, U., Nano-structured silica from rice husk. *J. Non-Cryst. Solids* **1992**, 145, 75-79.
 35. Liou, T.-H., Preparation and characterization of nano-structured silica from rice husk. *Mat. Sci. Eng.: A* **2004**, 364 (1–2), 313-323.
 36. Estevez, M.; Vargas, S.; Castaño, V. M.; Rodriguez, R., Silica nano-particles produced by worms through a bio-digestion process of rice husk. *J. Non-Cryst. Solids* **2009**, 355 (14–15), 844-850.
 37. Jaroenworuluck, A.; Pijarn, N.; Kosachan, N.; Stevens, R., Nanocomposite TiO₂–SiO₂ gel for UV absorption. *Chem. Eng. J.* **2012**, 181–182, 45-55.
 38. Banu Yener, H.; Helvacı, Ş. Ş., Effect of synthesis temperature on the structural properties and photocatalytic activity of

- TiO₂/SiO₂ composites synthesized using rice husk ash as a SiO₂ source. *Sep. Purif. Technol.* **2015**, *140*, 84-93.
39. Mohamed, M. M.; Zidan, F. I.; Thabet, M., Synthesis of ZSM-5 zeolite from rice husk ash: Characterization and implications for photocatalytic degradation catalysts. *Microporous Mesoporous Mater.* **2008**, *108* (1–3), 193-203.
40. Chen, H.; Zhao, L.; Xiang, Y.; He, Y.; Song, G.; Wang, X.; Liang, F., A novel Zn–TiO₂/C@SiO₂ nanoporous material on rice husk for photocatalytic applications under visible light. *Desalin. Water Treat.* **2016**, *57* (21), 9660-9670.
41. Adam, F.; Muniandy, L.; Thankappan, R., Ceria and titania incorporated silica based catalyst prepared from rice husk: Adsorption and photocatalytic studies of methylene blue. *J. Colloid Interface Sci.* **2013**, *406*, 209-216.
42. Ahmed, A. E.; Adam, F., The benzylation of benzene using aluminium, gallium and iron incorporated silica from rice husk ash. *Micropor. Mesopor. Mat.* **2009**, *118* (1–3), 35-43.
43. Chang, F.-W.; Kuo, W.-Y.; Yang, H.-C., Preparation of Cr₂O₃-promoted copper catalysts on rice husk ash by incipient wetness impregnation. *Appl. Catal. A: Gen.* **2005**, *288* (1–2), 53-61.
44. Pandey, S. K.; Kim, K.-H.; Chung, S.-Y.; Cho, S. J.; Kim, M. Y.; Shon, Z.-H., Long-term study of NO_x behavior at urban roadside and background locations in Seoul, Korea. *Atmos. Environ.* **2008**, *42* (4), 607-622.

45. Real, C.; Alcalá, M. D.; Criado, J. M., Preparation of Silica from Rice Husks. *J. Am. Ceram. Soc.* **1996**, *79* (8), 2012-2016.
46. López, G. P.; Silvetti, S. P., Effect of milling time on Fe/SiO₂ system prepared by mechanical alloying. *Physica B: Condensed Matter* **2004**, *354* (1-4), 141-144.
47. Rochelle M. Cornell, U. S., *The Iron Oxides: Structure, Properties, Reactions, Occurrences and Uses*. 2nd ed.; Wiley: Weinheim, 2006; p 703.
48. Guo, H.; Barnard, A. S., Thermodynamic modelling of nanomorphologies of hematite and goethite. *J. Mater. Chem.* **2011**, *21* (31), 11566-11577.
49. Ouyang, J.; Pei, J.; Kuang, Q.; Xie, Z.; Zheng, L., Supersaturation-controlled shape evolution of $\alpha\text{-Fe}_2\text{O}_3$ nanocrystals and their facet-dependent catalytic and sensing properties. *ACS Appl. Mater. Interfaces* **2014**, *6* (15), 12505-12514.
50. Zhou, X.; Xu, Q.; Lei, W.; Zhang, T.; Qi, X.; Liu, G.; Deng, K.; Yu, J., Origin of tunable photocatalytic selectivity of well-defined $\alpha\text{-Fe}_2\text{O}_3$ nanocrystals. *Small* **2014**, *10* (4), 674-679.
51. Chen, L.; Yang, X.; Chen, J.; Liu, J.; Wu, H.; Zhan, H.; Liang, C.; Wu, M., Continuous shape- and spectroscopy-tuning of hematite nanocrystals. *Inorg. Chem.* **2010**, *49* (18), 8411-8420.
52. Reeves, N. J.; Mann, S., Influence of inorganic and organic additives on the tailored synthesis of iron oxides. *J. Chem. Soc., Faraday Trans.* **1991**, *87* (24), 3875-3880.
53. Mármol, I.; Ballester, P.; Cerro, S.; Monrós, G.; Morales, J.; Sánchez, L., Use of granite sludge wastes for the production of

- coloured cement-based mortars. *Cement Concrete Comp.* **2010**, *32* (8), 617-622.
54. Lever, A. B. P., *Inorganic Electronic Spectroscopy*. 2nd Revised edition ed.; Elsevier Science Ltd: Amsterdam, 1986; p 864.
55. Sivula, K.; Le Formal, F.; Grätzel, M., Solar Water Splitting: Progress Using Hematite (α -Fe₂O₃) Photoelectrodes. *ChemSusChem* **2011**, *4* (4), 432-449.
56. Lasek, J.; Yu, Y.-H.; Wu, J. C. S., Removal of NO_x by photocatalytic processes. *J. Photochem. Photobiol. C* **2013**, *14*, 29-52.
57. Lewis, R. J.; Sax, N. I., *Sax's Dangerous Properties of Industrial Materials*. 12th ed.; Van Nostrand Reinhold: New York, 2012; Vol. 5, p 5862.
58. Patra, A. K.; Kundu, S. K.; Kim, D.; Bhaumik, A., Controlled synthesis of a hexagonal-shaped NiO nanocatalyst with highly reactive facets {1 1 0} and its catalytic activity. *ChemCatChem* **2015**, *7* (5), 791-798.
59. Zhou, X.; Lan, J.; Liu, G.; Deng, K.; Yang, Y.; Nie, G.; Yu, J.; Zhi, L., Facet-mediated photodegradation of organic dye over hematite architectures by visible light. *Angew. Chem. Int. Edi.* **2012**, *51* (1), 178-182.
60. Ângelo, J.; Andrade, L.; Mendes, A., Highly active photocatalytic paint for NO_x abatement under real-outdoor conditions. *Appl. Catal. A: Gen.* **2014**, *484*, 17-25.

61. Ma, J.; Wu, H.; Liu, Y.; He, H., Photocatalytic Removal of NO_x over Visible Light Responsive Oxygen-Deficient TiO₂. *J. Phys. Chem. C* **2014**, *118* (14), 7434-7441.
62. Polat, M.; Soylu, A. M.; Erdogan, D. A.; Erguven, H.; Vovk, E. I.; Ozensoy, E., Influence of the sol-gel preparation method on the photocatalytic NO oxidation performance of TiO₂/Al₂O₃ binary oxides. *Catal. Today* **2015**, *241*, Part A, 25-32.
63. Balbuena, J.; Carraro, G.; Cruz, M.; Gasparotto, A.; Maccato, C.; Pastor, A.; Sada, C.; Barreca, D.; Sanchez, L., Advances in photocatalytic NO_x abatement through the use of Fe₂O₃/TiO₂ nanocomposites. *RSC Adv.* **2016**, *6* (78), 74878-74885.

Supplementary Information

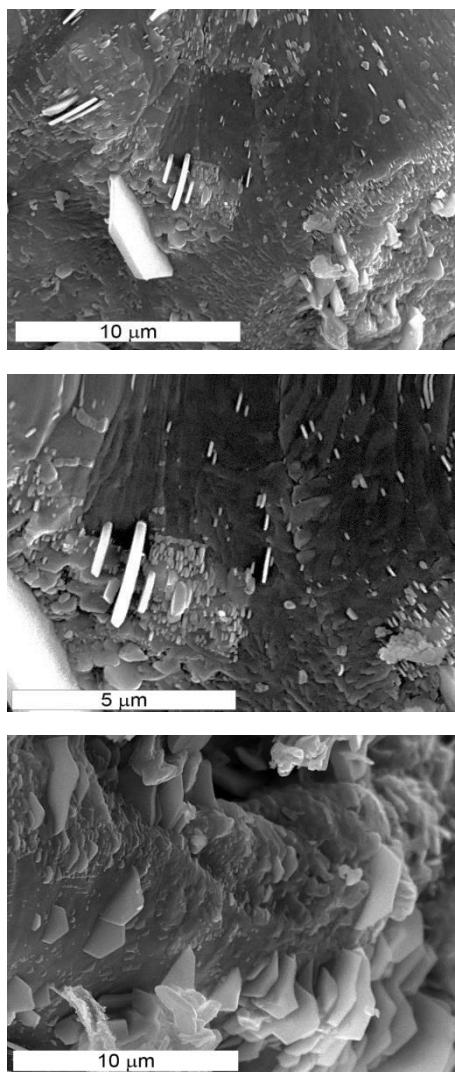


Figure SI-1. SEM images of samples A2. Detail of crystal growth.

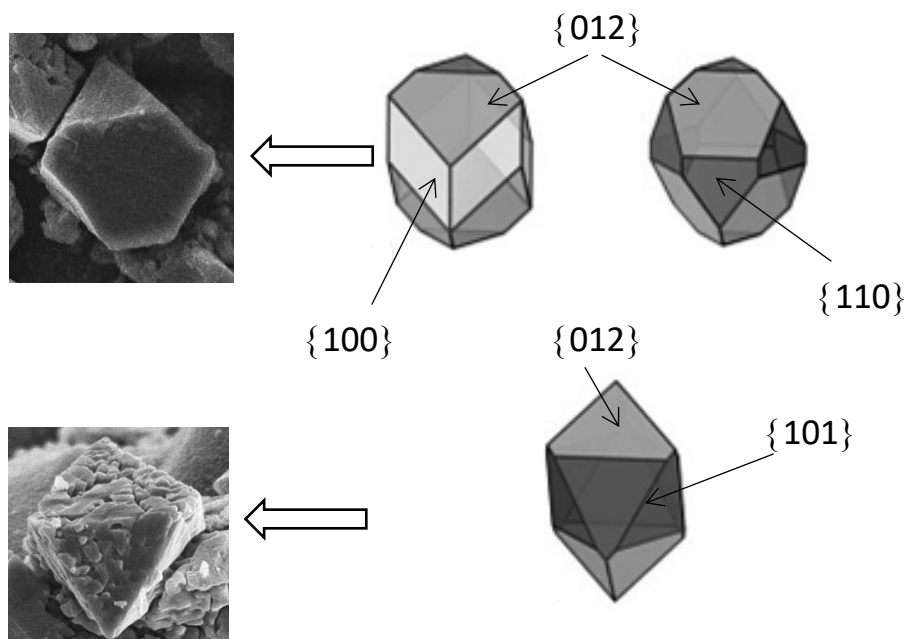


Figure SI-2. SEM images of samples B2 showing a detail of embryos crystalline particles growing as truncated pseudocubes. The geometrical figures are shown with their corresponding facet index.

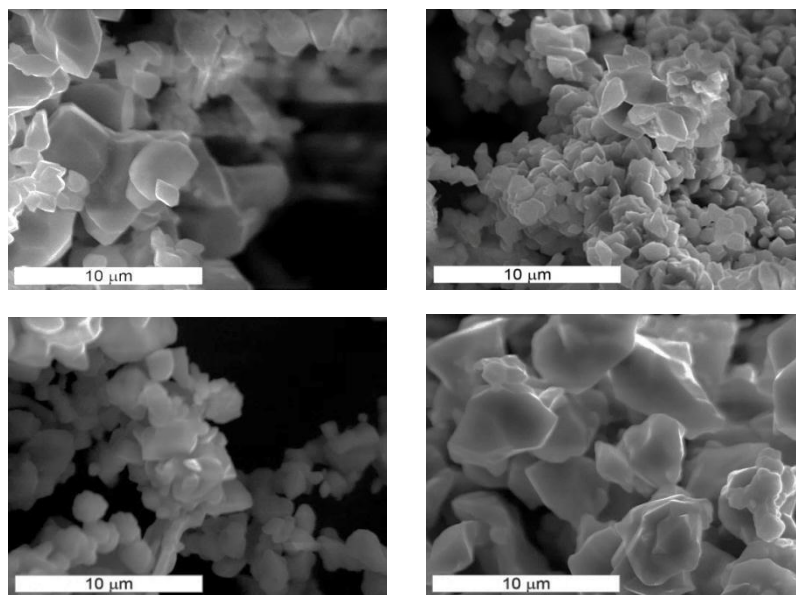


Figure SI-3. SEM images of samples obtained after calcination of FeCl₃ at (a) 600 °C, 1h; (b) 600 °C, 4h; (c) 900 °C, 1h; (d) 900 °C, 4h.

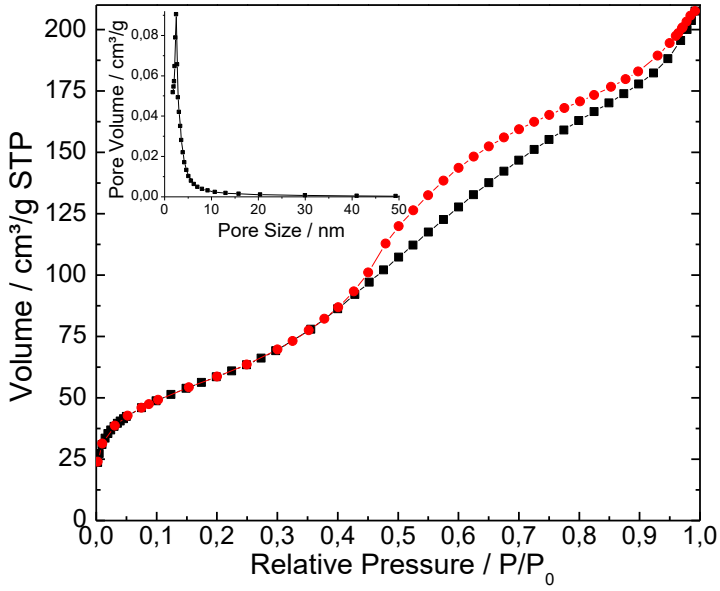


Figure SI-4. N_2 adsorption-desorption isotherm and pore size distribution for RHA.

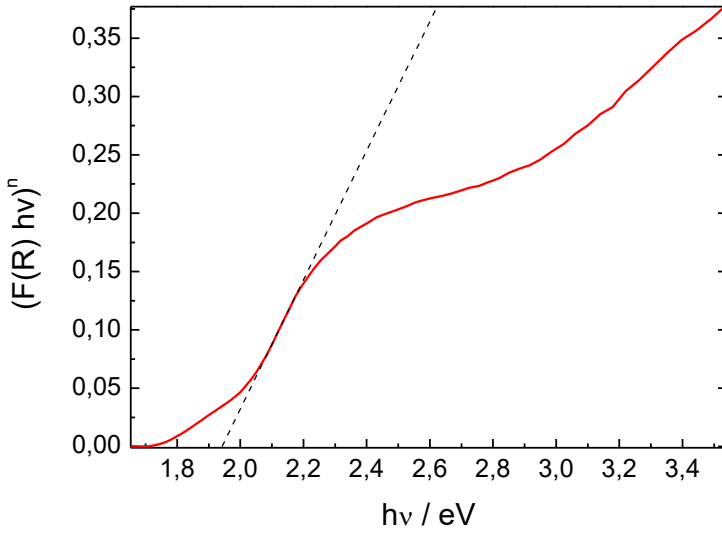


Figure SI-5. Kubelka-Munk transformed reflectance spectra of sample A1.

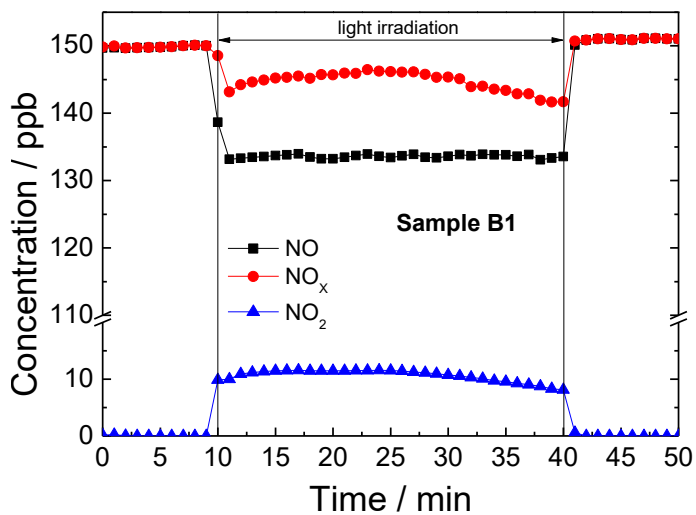
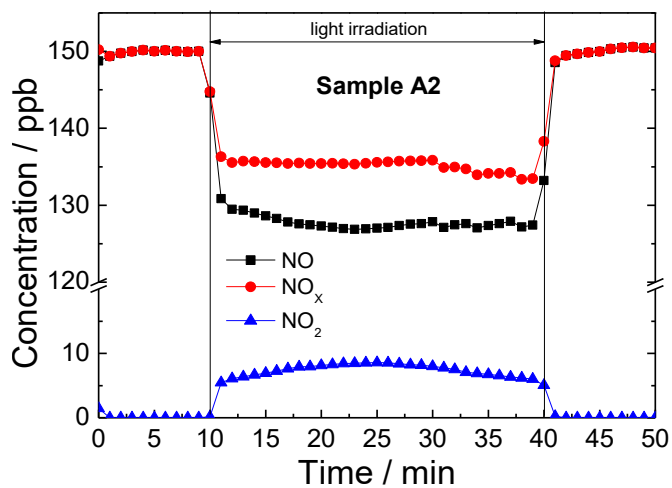


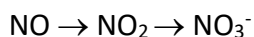
Figure SI-6. Nitrogen oxides concentration profiles obtained during the photo-degradation of gaseous NO under UV-Vis irradiation on samples A2 and B1.

5. Resumen general.

El desarrollo del presente trabajo de investigación ha permitido alcanzar las siguientes conclusiones generales.

a) En lo que respecta al diseño de nuevos materiales fotocatalizadores avanzados:

- Se demuestra la capacidad de la fase hematita del óxido de hierro, $\alpha\text{-Fe}_2\text{O}_3$, como fotocatalizador eficiente para la degradación de gases NO_x .
- Se ha confirmado que el mecanismo fotocatalítico De- NO_x conlleva el siguiente proceso de foto-oxidación:



- No obstante, y a pesar de su tamaño nanométrico, la eficiencia fotocatalítica de la hematita resulta ser pobre.
- La eficiencia fotocatalítica de la fase hematita se mejora al incrementar su superficie específica. En este sentido, estructuras unidimensionales constituidas por nanohilos nanocristalinos muestran una mejorada actividad De- NO_x .
- La fase $\alpha\text{-Fe}_2\text{O}_3$ se puede preparar por la técnica CVD con un control efectivo de su nano-organización estructural. De igual modo se pueden preparar depósitos de $\alpha\text{-Fe}_2\text{O}_3/\text{TiO}_2$ nanoestructurados. La fase $\alpha\text{-Fe}_2\text{O}_3$ actúa en sinergia con la

fase anatasa del TiO₂ obteniendo unas láminas delgadas muy eficientes en el proceso De-NO_x.

- Se demuestra que la actividad De-NO_x de la fase TiO₂ anatasa puede ser mejorada. La preparación de una estructura mesoporosa nanoparticulada conlleva a la obtención de un óxido TiO₂ no sólo activo a la luz UV sino también en el Visible, además de una sobresaliente mejora en la selectividad del proceso fotoquímico.
- b) Por otra parte, en relación al estudio de nuevos materiales fotocatalíticos obtenidos a partir de residuos sólidos procedentes de otras industrias:
- Se ha demostrado que se pueden realizar transformaciones adecuadas de los residuos industriales que les aporten un nuevo valor añadido y propiedades para la mejora de la calidad medioambiental.
 - Se ha optimizado el proceso de transformado de un residuo industrial en agente fotocatalizador.
 - Los residuos ricos en hierro son utilizados eficazmente como aditivos fotocatalizadores en materiales de construcción para aplicaciones de auto-limpieza y descontaminación de gases NO_x.
 - En los materiales de construcción que además de incorporar los residuos transformados también incorporan TiO₂, se

observa una acción sinérgica de ambos aditivos fotocatalizadores que conduce a una clara mejora de la eficiencia fotocatalítica última del material.

- Se ha demostrado que las cenizas de procedentes de la combustión de la cascarilla de arroz sirven de soporte útil de material fotocatalizador.
- El proceso térmico de preparación de composites $\text{Fe}_2\text{O}_3/\text{SiO}_2$ condiciona la morfología de la fase hematita soportada, así como su superficie específica.
- Los composites $\text{Fe}_2\text{O}_3/\text{SiO}_2$ presentan actividad De- NO_x mejorada respecto a la observada para la muestra de hematite nanocristalina en polvo.

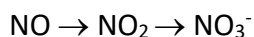
Todas las conclusiones anteriores evidencian que se pueden preparar nuevos materiales con propiedades fotocatalíticas mejoradas en lo que respecta a la eliminación de gases NO_x en atmósferas contaminadas, objetivo principal planteado al iniciar esta Tesis Doctoral.

Overall summary.

The development of this research work has led to the following general conclusions.

a) Regarding the design of new advanced photocatalyst materials:

- The ability of the hematite phase of iron oxide, $\alpha\text{-Fe}_2\text{O}_3$, as an efficient photocatalyst for degradation of NO_x gases is demonstrated.
- It has been confirmed that the photocatalytic mechanism De-NO_x carries the following photo-oxidation process:



- However, despite its nanometric size, the photocatalytic efficiency of the hematite evidences to be poor.
- The photocatalytic efficiency of the hematite phase is improved by increasing its specific surface area. In this sense, one-dimensional structures constituted by nanocrystalline nanowires show an improved De-NO_x activity.
- The $\alpha\text{-Fe}_2\text{O}_3$ phase can be prepared by the CVD technique with an effective control of its structural nano-organization. Similarly, nanostructured $\alpha\text{-Fe}_2\text{O}_3/\text{TiO}_2$ deposits can be prepared. The $\alpha\text{-Fe}_2\text{O}_3$ phase acts in synergy with the anatase

phase of TiO₂ obtaining thin films with high efficiency in De-NO_x process.

- It is demonstrated that the De-NO_x activity of the anatase TiO₂ phase can be improved. The preparation of a nanoparticulate mesoporous structure leads to the production of a TiO₂ oxide not only active in UV light but also in Visible, in addition to an outstanding improvement in the selectivity of the photochemical process.
- b) On the other hand, in relation to the study of new photocatalytic materials obtained from solid waste from other industries:
- It has been demonstrated that adequate transformations of the industrial waste can be carried out that give them a new added value and properties for the improvement of the environmental quality.
 - The process of transforming an industrial waste into a photocatalyst agent has been optimized.
 - Iron-rich wastes are effectively used as photocatalytic additives in building materials for self-cleaning and NO_x gases depollution applications.
 - In construction materials, which incorporate the transformed residues and TiO₂, a synergistic action of both photocatalytic

additives is observed that leads to a clear improvement of the last photocatalytic efficiency of the material.

- Ashes from the combustion of rice husk have been shown to serve as useful support for photocatalyst material.
- The thermal process of preparation of Fe₂O₃/SiO₂ composites determines the morphology of the supported hematite phase, as well as its specific surface.
- Fe₂O₃/SiO₂ composites have improved De-NO_x activity compared to that observed for the sample of nanocrystalline hematite powder.

All the above conclusions show that new materials with improved photocatalytic properties can be prepared regarding the elimination of NO_x gases in contaminated atmospheres, the main objective of this PhD Thesis.

6. Experimental techniques.

Subsequently, the theoretical bases of the different experimental techniques used throughout this Thesis are briefly described. The specific characteristics of the instruments and the working methods of each technique used have been mostly omitted in this section due to they were described in the experimental section of each published article, and are only included in those cases where they facilitate the explanation of its foundation.

A) Physical and morphological characterization

Thermogravimetric Analysis (TGA)

The thermogravimetric analysis¹ consists of recording the weight variation of a sample when is exposed to a heat treatment, and to relate this variation to the identification and quantification of the processes involved in the solid-gas reactions. Thus, this technique provides us with direct information on desorption, decomposition and oxidation processes. When the processes involved in mass variation are well identified (e.g., weight loss due to dehydration of a compound), TGA curves can be related to the kinetics of the reaction.

The instruments that perform this type of measures usually are equipped with (Figure 1): a sensitive analytical balance capable of providing quantitative and accurate information of the weight of

the sample, a furnace to heat the sample to the temperature required, a purge system to provide an inert atmosphere, typically using argon or nitrogen and a microprocessor for instrument control and data acquisition.

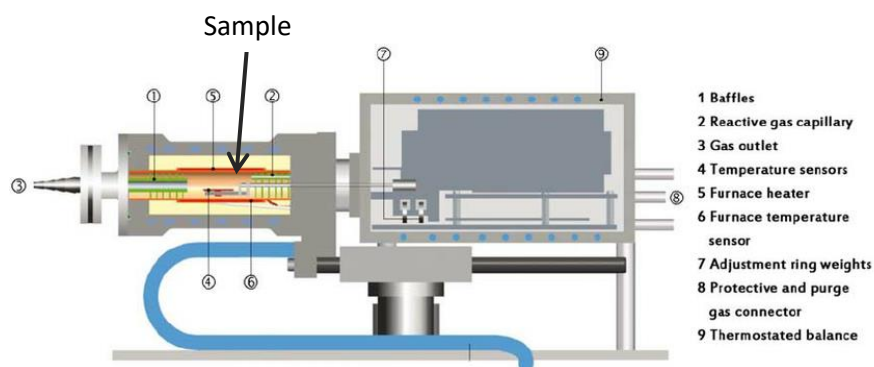


Figure 1. Scheme of thermogravimetric balance used in this Thesis (Mettler Toledo STARe TGA).

Nevertheless, in relation to the purging system to provide an inert atmosphere, sometimes an oxidizing atmosphere may also be of interest. For example, in the characterization of iron oxides, the structurally related phases such as magnetite and maghemite can be differentiated by this technique, e.g. magnetite, contrasting maghemite, will oxidize in the presence of air at 200-300 °C, which will result in an increase in weight in the thermogram.

Laser diffraction particle sizing technique.

The laser diffraction technique²⁻³ is used to determine the size of the particles and consists of illuminating them with a

monochromatic light source, so that they are dispersed in all directions with an intensity pattern which depends on their size (Figure 2). In this sense, small particles disperse light at large angles, while large particles disperse light at small angles.

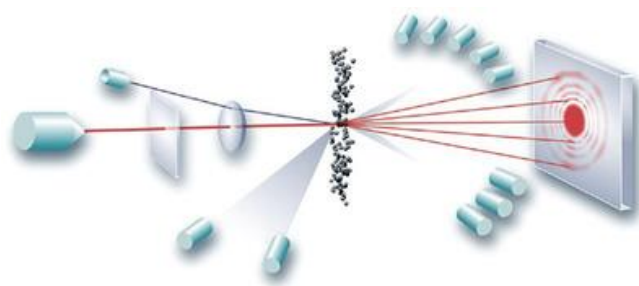


Figure 2. Laser diffraction particle sizing equipment scheme.

On the other hand, to determine the intensity of the dispersed radiation, optical detectors are used and, later, the information obtained by them is processed by applying different optical models. The model⁴⁻⁶ to be applied depends on the particle size being analysed, although, all have in common the fact that they consider the particles as spheres. Thus, when the size is approximately equal to that of the wavelength of the light source, Mie model is applied, if it is greater is used the Fraunhofer method, and if it is smaller the Rayleigh method.

Specific surface area determination.

The specific surface of a solid represents the area which material exhibit by gram of substance. In solids, the specific surface value is generally expressed in units of $\text{m}^2 \cdot \text{g}^{-1}$. For its determination, it is carried out by knowing the amount of molecules of an inert gas

(such as N₂) which are adsorbed on its surface at a determined pressure and temperature.

The specific surface of the material is closely related to its porosity; this means that its value will be greater when pore size is smaller and the number of pores larger. The pores, depending on their size, are classified into micropores, when their diameter is less than 2 nm, mesopores, when their diameter is between 2-50 nm, and macropores, when their diameter is greater than 50 nm, being the amount of micropores present that mainly determines the value of the specific surface of the solid.

Regarding the specific surface determinations performed in this Thesis, the Brunauer-Emmett-Teller⁷ (BET) method was applied. The central idea is, knowing the amount of adsorbed gas needed to form a monolayer (and therefore the number of molecules forming the monolayer) and the area occupied by one of these adsorbed molecules, it is possible to estimate the area of the solid.

Conversely, with the determination of the specific surface, the adsorption isotherms are obtained, which are curves that represent the quantity of gas molecules adsorbed at different pressures for the same temperature and are very useful in the characterization and type of pore which a solid has. The authors of the BET method proposed a classification of the isotherms obtained, known as BDDT⁸.

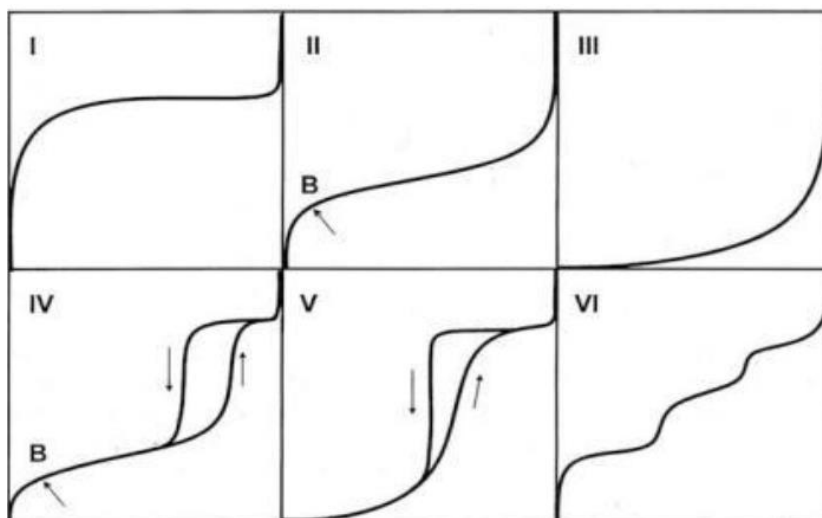


Figure 3. BDDT classification of isotherms.

Type I or Langmuir type: Characteristic of microporous solids.

Type II: Characteristic of adsorption processes in non-porous or macroporous solids.

Type III: Characteristic of adsorption processes in non-porous solids where adsorbent-adsorbate interaction is weak.

Type IV: Presence of hysteresis cycles. Characteristic of mesoporous systems. From the desorption branch of these isotherms the size distribution of the pores can be determined.

Type V: They are rare and the most difficult to interpret. The affinity of the adsorbent for the adsorbate is low and the hysteresis links with the filling of the pores.

Type VI: Characteristic of adsorption in multilayer on highly uniform surfaces. Each of the first layers is adsorbed within a certain range of pressures, each stage corresponding to the filling of a layer.

Adsorption isotherm and specific surface have a great importance in catalysis. These parameters have a direct relationship with catalyst efficiency.

Scanning Electron Microscopy (SEM)

Scanning electron microscopy (SEM)⁹⁻¹⁰ is a very useful tool for morphological characterization of the samples. In a scanning electron microscope, a beam of electrons called primary electrons are focused with high energy on the surface of the sample.

Consequently, different types of signals are produced, some of which are used to generate the image of the zone where the beam has affected. Thus, when projected on the sample, some of the primary electrons pass through it, but others interact with it. The interaction can be of two types, elastic, which would give to the backscatter of the electrons, or inelastic, in which case would occur the expulsion in all directions of the so-called secondary electrons with their corresponding electromagnetic radiation.

These secondary electrons are directed to a glittering counter that performs their photographic recording obtaining an image of the sample morphology.

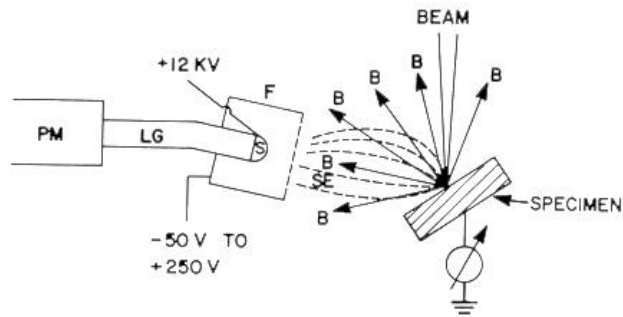


Figure 4. Scheme formation of secondary electrons (SE).

On the other hand, the sample surface on which the primary electron beam is projected is usually about 10 nm^2 , scanning this area in parallel strokes and with an energy from 5 to 50 KeV.

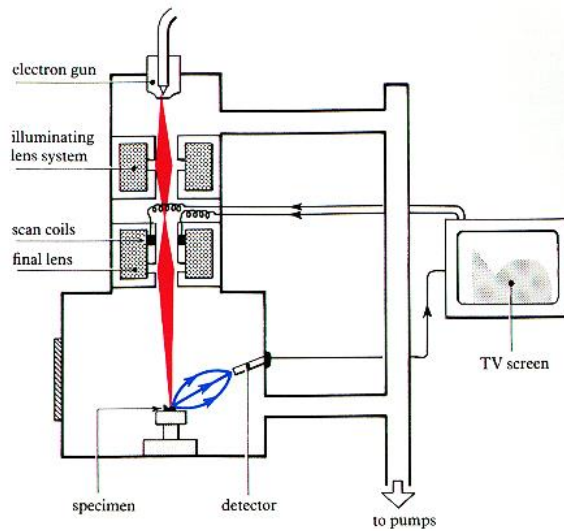


Figure 5. Scheme of SEM.

The preparation of the samples it is relatively easy, in the meantime they only are required to be conductive with the purpose of can absorb the electrons beamed and produce secondary electrons which will perform the image. Therefore, they are usually

coated with a layer of carbon or a thin layer of a metal such as gold to make them conductive.

Transmission Electron Microscopy (TEM)

Transmission electron microscopy is based on an electron beam which is manipulated through electromagnetic lenses and is projected onto a very thin sample located on a high vacuum column. The electrons pass through the sample or collide with its own atoms and end their travel. The source is a cathode made of a filament of incandescent tungsten (high vacuum).

Electrons are thermally pulled out at low speed and accelerated by the creation of a high potential (Wehnelt cylinder), which allows a rectilinear path of electrons of very low wavelength.

These electrons deviate from their trajectory by crossing an electromagnetic field (electromagnetic lens). This deviation is accentuated by the placement of several lenses.

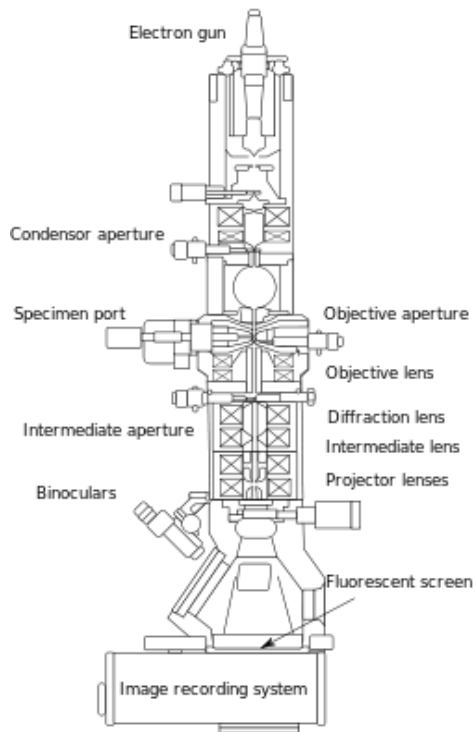


Figure 6. Transmission microscope scheme.

Finally, a very diverted beam, very open, is collected on a fluoroscopic screen to be visible to the human eye and thus obtain the images.

Atomic Force Microscopy (AFM)

Atomic force microscopy¹¹ (AFM) allows to examine the topography of the surface of the samples by providing information on the size, shape and distribution of nanostructures, and allows the calculation of the quadratic mean (RMS) of surface roughness.

The last parameter is of considerable importance as it can be related to the specific surface.

Basically, an AFM instrument is characterized by a flexible cantilever beam or cantilever (beam in which one of its ends is embedded while the other is free or cantilever) ending with a probe tip of 100 Å diameter (Figure 7). The probe tip, depending on the working mode, interacts in a concrete way with the surface of the sample, making a complete scan on the sample, obtaining a two-dimensional map of the intensity of the interaction with respect to each position on the surface. This allows to obtain an image of topography. The intensity of the interaction is given as a function of the deviation or alteration that this interaction causes in the cantilever.

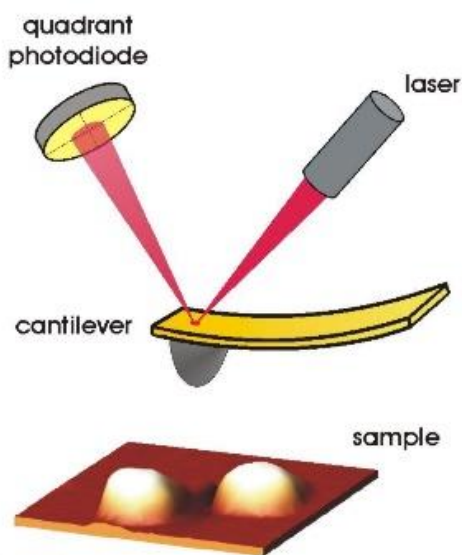


Figure 7. AFM scheme.

An example of a work modality is "non-contact". In this mode, attractive Van der Waals interactions between the probe tip and the surface of the sample are monitored, the distance between them being between 50 and 100 Å. The basis of this modality is because Van der Waals forces act by varying the resonant frequency of the cantilever, nevertheless, that frequency is kept constant by adjusting the distance between the probe tip and the surface, which is carried out by the instrument control system. The measurement of the adjusted distance to keep the resonance frequency constant at each point of the surface allows a topographic image of the surface to be obtained.

B) Chemical and electronic characterization

Energy Dispersive X-Ray Spectroscopy (EDAX)

The X-ray energy dispersion microanalysis consists of an electron excitation X-ray spectrometry technique whose excitation source is the same as that used in SEM, i.e. a high-energy electron beam incident on the sample. In fact, the instrument used to apply both types of technique is the same.

As discussed in the SEM technique description, by striking a beam of electrons (primary electrons) on the sample, the so-called secondary electrons are released. These electrons belong to the inner layers of the atoms present. These atoms, when they restructure their electronic shells, emit characteristic X radiation for

each type of element present (Figure 8), a phenomenon that can be used to analyse the chemical composition of the samples.¹²

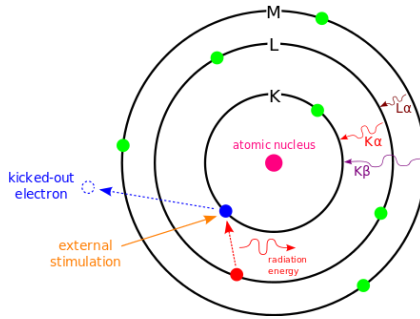


Figure 8. Restructuration of the electronic shell of an atom after fall upon a primary electron and expel a secondary electron releasing the corresponding characteristic X radiation.

In this way, the radiation pulses are detected by a silicon counter and separated per their wavelength by a multi-channel analyser. A spectrum is obtained in which the position of the peaks allows to identify the elements present in the sample, and their respective areas, to quantify them.

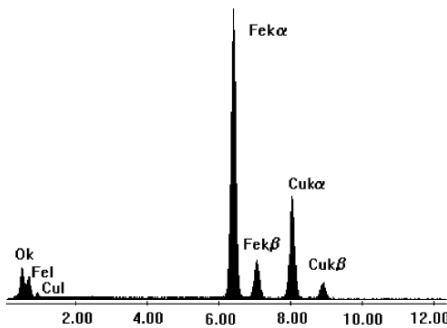


Figure 9. Typical EDAX spectra of iron oxide nanowires (Copper signal is from the sample holder).

X-Ray Fluorescence (XRF)

X-ray fluorescence¹³⁻¹⁴ is another X-ray spectrometry technique but in this case the excitation source is, not an electron beam as is the case with the EDAX technique, a source of x-ray radiation. When the sample is irradiated with this radiation, it emits secondary X-rays or fluorescence. The X-ray detectors collect all the photons emitted and analyse their energies.

Like in the EDAX technique, the energy of these photons is characteristic of each type of atom that compose the sample due to they are generated from the same principle, that is, transitions between the internal electronic levels of the atoms, being its intensity proportional to the present quantity of each one of them.

In this way, with this type of technique the type and proportion of each element present in the sample can be determined.

X-Ray Diffraction (XRD)

Diffraction is a phenomenon characteristic of the waves that is based on the deviation of them when they find an obstacle or cross a slit. X-ray diffraction technic¹⁵⁻¹⁶ is based, as its name implies, on X-ray diffraction, but for the case in which it touches crystalline solids.

In this type of technique, an X-ray beam interacts with a crystalline sample, which ideally must have the crystals oriented

randomly in all directions. The conditions necessary for X-ray diffraction to occur are analysed according to Bragg's law¹⁷:

$$n\lambda = 2d\sin\theta$$

where λ is the wavelength of the incident radiation, d is the spacing of the crystal lattice, n a number that always takes integer value ($n = 1, 2 \dots$) and θ the angle that forms the incident beam and the plane of reflexion.

Therefore, when X-ray radiation is incident on a crystalline powder sample and at different angles, only the positions of the sample in which the Bragg law is fulfilled will occur the diffraction phenomenon (Figure 10).

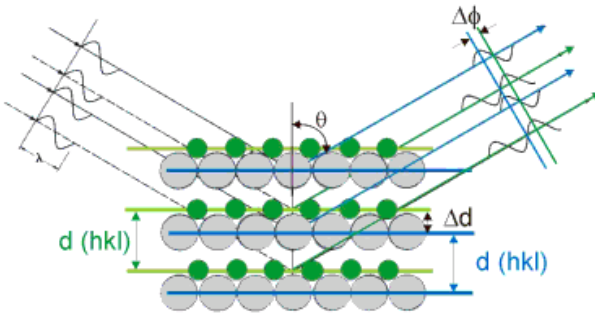


Figure 10. X-Ray diffracted by a crystalline solid.

The different diffracted radiations are collected in a detector, thus giving rise to the characteristic diffractogram of the sample studied. For each pair of values (incident angle 2θ , interplanar distance) that obeys with the Bragg law, we obtain a maximum of diffraction. For a pure sample, the intensity of the

peaks is given by the structural factors that are related to the different dispersion factors of each atom, like the crystalline structures (planes and distances) and other factors (scale, polarization, Lorentz correction). The study of the different lines that appear in the diffractogram is one of the best methods to obtain information about the crystalline phases present in the samples.

X-Ray Photoelectron Spectroscopy (XPS)

Photoelectron X-ray spectroscopy¹⁸ (XPS) is the most widely used surface characterization method nowadays. The popularity of this technique is due to the high content of information which provides and its flexibility to be used on a wide variety of samples. The most basic XPS analysis of a surface can provide qualitative and quantitative information of all the elements present, except H and He¹⁹. This is because this technique uses electrons from the inner layers of the electron cortex, whereas in these two elements there are only valence electrons. Valence electrons do not serve in XPS because the technique is based on studying the kinetic energy which electrons emerge when they are irradiated with X radiation, and in the case of valence electrons this energy is strongly influenced by the chemical environment (Being much less this influence in the inner), then cannot be well characterized. On the other hand, with more sophisticated applications of the technique

detailed information of the chemistry, organization and morphology of the surface is obtained.

The principle of this technique, as already mentioned, is based on the photoelectric effect and consists of the emission of an internal electron from the atomic cortex by interacting with a photon of X radiation with which it is irradiated (Figure 11), which transfers its energy.

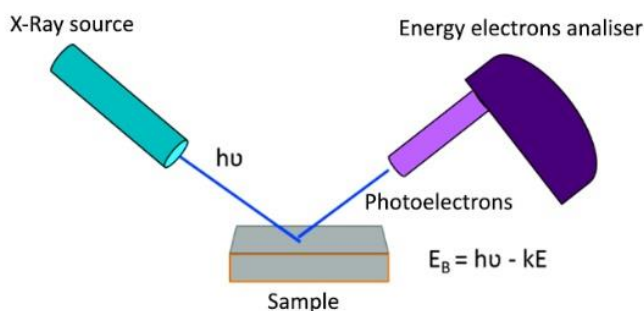


Figure 11. Photoelectrons generation in XPS technique.

The photoemission of the electron takes place because the energy that the photon transfers to it is superior to its binding energy, and allows him to acquire certain kinetic energy. For gases, the binding energy of an electron is equal to its ionizing energy, but in the solids, there is an influence on the part of the surface, so that an additional energy is necessary to make an electron out of it. This extra energy is called the work function. The photoemission process turns out to be extremely fast (10^{-16} s) and its basic physics is described by the Einstein Equation:

$$EB = h\nu - kE$$

where EB is the binding energy of the electron in the atom, h is the energy of the photons and kE is the kinetic energy that electron acquires. The set of kinetic energies of the photo-emitted electrons can be measured using a suitable electron energy analyser, and in this way, a photoelectronic spectrum is recorded.

Meanwhile for each element there is a characteristic binding energy associated with its internal atomic orbitals, each atom can be identified from a set of characteristic peaks in the photoelectronic spectrum.

UV-Vis-NIR spectroscopy

UV-Vis-NIR spectroscopy is one of the most widely used spectroscopic techniques to obtain information about the electronic structure of the samples. This technique uses electromagnetic radiation from the ultraviolet (200-380 nm), visible (380-700 nm) and near infrared (700 - 1000 nm) regions with which the samples are irradiated. From the relationship between the incident and the resulting radiation after interacting with the sample, the information of interest is obtained.

In this Thesis, the UV-Vis-NIR spectroscopy has been used by diffuse reflectance and by transmittance. Diffuse reflectance spectroscopy studies the radiation reflected by the samples, a

phenomenon from which information about their composition can be obtained and, also their colour.

The radiation reflected by a sample can be of two types, specular or diffuse (Figure 12).

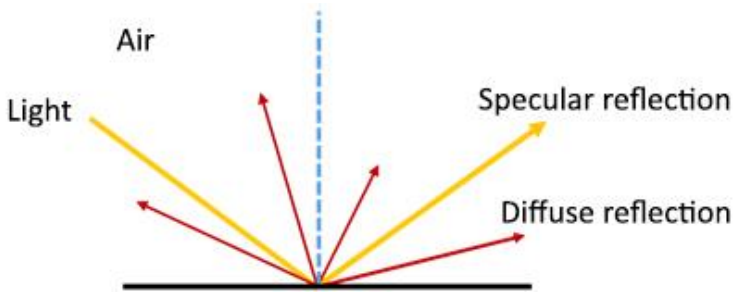


Figure 12. Reflected radiation when light touch the sample.

The specular reflectance follows the Fresnel laws and predominates when the material on which the reflection takes place has high values of the reflection coefficients for the incident wavelength. Diffuse reflectance occurs in all directions of the surface because of the absorption and dispersion processes (Kubelka-Munk theory²⁰), predominating when the materials of the reflecting surface are weakly absorbing at the incident wavelength and when the penetration of the radiation is large in relation to the wavelength.

In general, a measurement of reflectance contains both reflection components, however, it is tried to minimize the maximum by adjusting the position of the detector respect to the

sample, being the diffuse component the one that provides useful information.

In the spectrophotometers that carry out this type of measurements, the radiant energy emitted by the source passes through an optical system that connects the source to the monochromator. The monochromator disperses the radiation and transmits it as a narrow band of wavelengths through the exit slit which is optically communicated with the chamber containing the sample to be measured together with a standard. The detector system receives the radiation reflected by the sample and the standard and generates a quotient of the signals that is later transmitted to the computer for analysis and presentation.

On the other hand, in the transmittance mode is studied the relation between the incident radiation in the sample and the transmitted through it, in other words, the radiation absorbed by the sample is studied, which gives rise to different types of electronic transitions. The lessening in incident light intensity after interacting with the sample and crossing it can be described by Lambert-Beer law²¹, the law is given by the following expression:

$$I(\lambda) = I_0 e^{-\alpha(\lambda)t}$$

Where $\alpha(\lambda)$ is the absorption coefficient and t is the thickness of the sheet. The ratio between the transmitted and incident radiation (I/I_0), represents the transmittance, from which the absorbance can be calculated:

$$A(\lambda) = \ln\left(\frac{1}{T(\lambda)}\right) = -\ln\left(\frac{I}{I_0}\right) = \alpha t$$

The representation for a sample absorbance at each wavelength corresponding to its absorption spectrum, which can be used to identify the component elements of the sample, since each chemical element has specific absorption lines at certain wavelengths.

On the other hand, another application of special interest related to the UV-Vis-NIR spectroscopy is the calculation of the Band Gap value of semiconductors. In the case of the transmittance mode, for semiconductor materials, the absorption coefficient at the wavelength of maximum absorption can be expressed from the Tauc equation²²:

$$\alpha(h\nu) = (h\nu - E_G)^n$$

Where E_g represents the Band Gap energy and n depends on the nature of the electronic transition involved. Specifically, its value is 1/2, 3/2, 2 and 3 for direct permissible, indirect permissible, indirect, permissible and indirect permissible respectively. Typically, a Tauc plot represents the value of $h\nu$ (eV) on the abscissa axis versus the value $(\alpha h\nu)^n$ on the ordinate axis. The resulting curve has a characteristic linear regime whose interruption denotes the start of absorption. Therefore, the extrapolation of the linear region

for the abscissa axis ($(\alpha h\nu) n = 0$) gives the energy value E_g of the Band Gap of the semiconductor.

Infrared Spectroscopy

The interatomic bonds of molecules or crystals are not immobile, but are continually vibrating with a certain energy that defines a vibrational energy state. In polyatomic molecules, we can distinguish two basic categories of vibrations (or modes of vibration) called tension and flexion. A tension vibration assumes a continuous change in the interatomic distance along the bond axis of two atoms. The flexural vibrations instead are characterized by a change in the angle between two links.

Infrared spectroscopy²⁴ consists of irradiating the sample with this type of radiation to excite the vibrational energy states of the present species. Conversely, only the vibrations associated with a changing dipole moment (called active vibration modes) will be able to interact with the infrared radiation and therefore to modify its energy. The energy involved in this type of transitions is dependent on the interatomic forces within the molecule or crystal, and thus the position, symmetry, and relative intensity of the spectrum peaks give very useful information about the structure and composition of the sample.

C) Characterization of photocatalytic processes.

Colorimetry

The organic dyes degradation and their colour loss, is commonly used as standard assay for measure the photocatalytic activity of the materials. In this sense, a fine measurement of dye colour and its variation during the assay is required. The visual perception that an observer has about a colour is conditioned by many factors, such as the light source, the observer himself, the sample or object, or the way they are arranged in space. Thus, given the difficulty of evaluating a colour, measurement systems have been created with the purpose to allow quantification and numerical expression, whose principle is based on the amount of light reflected by the sample or object.

One of these systems is the CIE $L^*a^*b^*$ (CIELAB) system, which is the chromatic model normally used to describe all the colours that the human eye can perceive. It was developed specifically for this purpose by the Commission Internationale d'Eclairage (International Commission on Illumination), which is why it is abbreviated CIE. The CIELAB colour space is a Cartesian coordinate system defined by three colorimetric coordinates L^* , a^* , b^* (dimensionless quantities) (Figure 13).

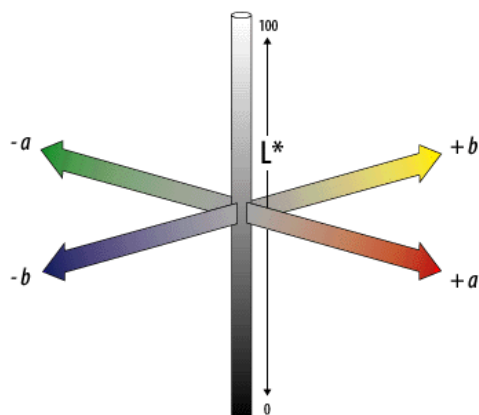


Figure 13. CIELAB colour space.

The L^* coordinate corresponds to the measure of brightness or clarity of a colour. The values on the L^* axis range from 0 (black) to 100 (white). The colorimetric coordinates a^* and b^* form a plane perpendicular to clarity. The coordinate a^* defines the deviation of the achromatic point corresponding to the brightness, towards red if $a^* > 0$ or towards the green if $a^* < 0$. Similarly, the coordinate b^* defines the deviation towards yellow if $b^* > 0$ or to the blue if $b^* < 0$. The set a^* , b^* is called Chromaticity and together with clarity define the colour of a stimulus.

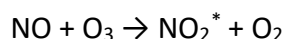
Chemiluminescence analysis of NO_x gases

The analyser used for the determination and quantification of NO_x ($NO + NO_2$) [Environnement S.A. AC32M, Figure 14], can measure the quantity of NO and NO_2 gases separately, from a gaseous flow taken as a model of contaminated air, this information is of great interest in relation to the thematic of study of this Thesis.



Figure 14. AC32M Analyser from Environnement S.A.

The principle in the detection and quantification of these gases is based on a chemiluminescence phenomenon²³ that occurs when the NO molecules are oxidized with O_3 to NO_2 , which, when formed initially, is in an excited state (NO_2^*). This process is carried out in the reaction chamber of the analyser:



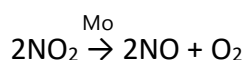
The transition to the fundamental state of NO_2 molecules occurs with the release of light radiation in the range of 600-1200 nm:



The detection and quantification of NO is performed indirectly by measuring the intensity of the radiation generated. To do this, the main reaction chamber is connected to the detection system through a filter that only passes radiation from 610 nm, thus eliminating possible interference due to other species that could be present such as certain hydrocarbons. On the other hand, to avoid that part of it is lost due to possible collisions between molecules

(quenching), pressure established throughout the system is sufficiently low.

According to the set of processes just described, in order to quantify the NO₂ molecules also present in the gaseous flow entering the analyser, they must be previously reduced to NO molecules. This process is carried out in a molybdenum furnace included in the analyser:



The difference between the number of NO and NO₂ molecules present in the gaseous flow is achieved from a series of successive steps which form a cycle. In this sense, it must be considered that the analyser works under continuous flow, so that the amount of gas used in each stage is rejected and does not participate in the successive stages of the cycle. The analyser is providing information at fixed time intervals showing the average value of the results obtained in the total cycles performed in that interval. The stages that constituting each cycle are as follows:

- The Reference Step (Step 1)

The inlet gaseous flow is passed through a pre-reaction chamber where the gas is mixed with O₃, with the purpose that whole NO molecules were oxidized to NO₂. The signal is not associated to the presence of NO molecules, because were completely oxidized to NO₂. Therefore, the signal obtained will be taken as a reference signal.

- The NO Step (Step 2)

At this step, the inlet gaseous flow is passed directly into the reaction chamber, so that all the NO molecules are going to be oxidized to NO_2 and the signal obtained will correspond only to the NO molecules.

- The NO_x Step (Step 3)

In the final period, the arriving gaseous flow is passed through the molybdenum furnace before entering the reaction chamber, so that all the NO_2 molecules present are reduced to NO. The signal is now due to the total NO_x molecules, i.e. the total amount of NO and NO_2 .

In summary, the signal obtained in step 2 is proportional to the concentration of NO molecules and the difference between the signals obtained in steps 2 and 3 is proportional to the concentration of NO_2 molecules. Previously, both signals are subtracted from the signal of step 1, i.e. the reference signal. A sketch of the composition of the analyser is shown in Figure 15. A scheme of complete De- NO_x system is shown in Figure 16. This system consists in carry through tubes a mix of gases to the reaction chamber which contains the photocatalyst sample; here sample is irradiated with simulated solar light and NO_x gases concentration is analysed by chemiluminescence.

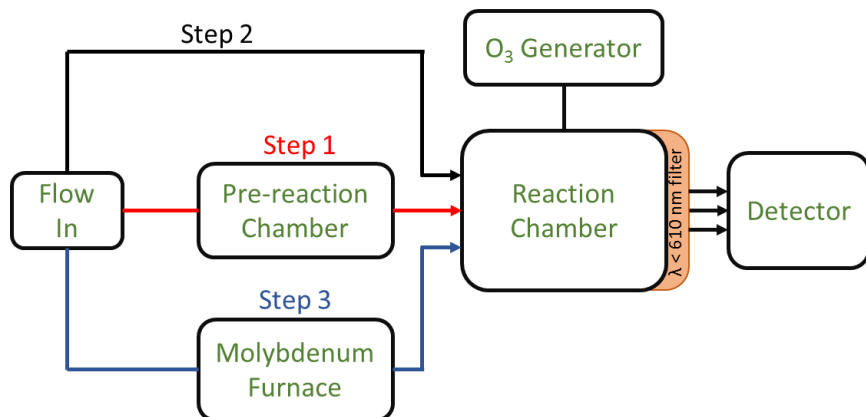


Figure 15. AC32M Analyser scheme.

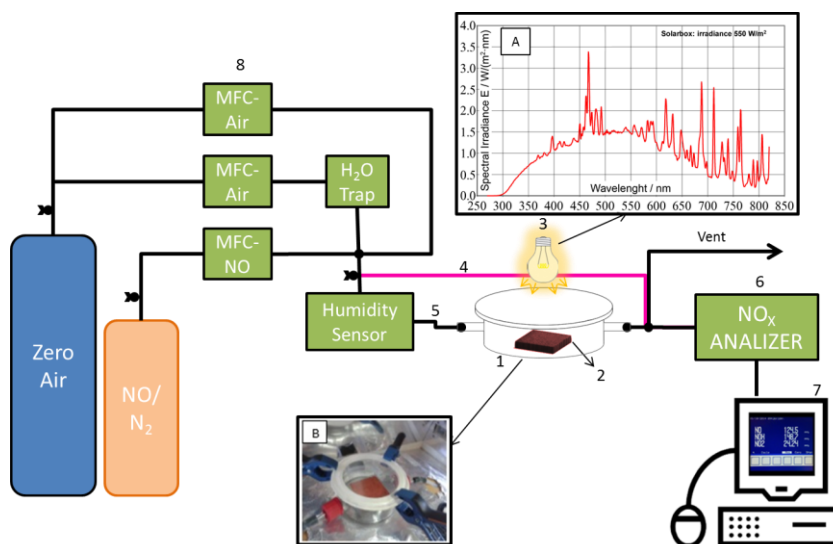


Figure 16. Complete De-NO_x system scheme.

References

1. Brown, M. E., *Introduction to Thermal Analysis: Techniques and applications*. Springer Netherlands: 2012.
2. Rawle, A., Basic of principles of particle-size analysis. *Surface coatings international. Part A, Coatings journal* **2003**, 86 (2), 58-65.
3. Allen, T., *Particle size measurement*. Springer US: 2013.
4. Etzler, F. M.; Deanne, R., Particle size analysis: A comparison of various methods ii. *Particle & Particle Systems Characterization* **1997**, 14 (6), 278-282.
5. Lee Black, D.; McQuay, M. Q.; Bonin, M. P., Laser-based techniques for particle-size measurement: A review of sizing methods and their industrial applications. *Progr. Energy Combust. Sci.* **1996**, 22 (3), 267-306.
6. Xu, R., *Particle Characterization: Light Scattering Methods*. Springer Netherlands: 2001.
7. Brunauer, S.; Emmett, P. H.; Teller, E., Adsorption of gases in multimolecular layers. *J. Am. Chem. Soc.* **1938**, 60 (2), 309-319.
8. Sing, K. S. W., Reporting physisorption data for gas/solid systems with special reference to the determination of surface area and porosity (Recommendations 1984). In *Pure Appl. Chem.*, 1985; Vol. 57, p 603.
9. Brundle, C. R.; Evans, C. A.; Wilson, S., *Encyclopedia of materials characterization: surfaces, interfaces, thin films*. Butterworth-Heinemann: 1992.

10. Zhang, S.; Li, L.; Kumar, A., *Materials Characterization Techniques*. CRC Press: 2008.
11. Haugstad, G., *Atomic Force Microscopy: Understanding Basic Modes and Advanced Applications*. Wiley: 2012.
12. Goodhew, P. J.; Humphreys, F. J., *Electron Microscopy And Analysis*. Taylor & Francis: 1988.
13. Bermúdez-Polonio, J., *Teoría y práctica de la espectroscopia de rayos X*. Alhambra: 1967.
14. Skoog, D. A.; Leary, J. J., *Análisis instrumental*. McGraw-Hill: 1998.
15. Azároff, L. V.; Buerger, M. J., *The powder method in X-ray crystallography*. McGraw-Hill: 1958.
16. Cullity, B. D., *Elements of X Ray Diffraction - Scholar's Choice Edition*. Scholar's Choice: 2015.
17. Ladd, M.; Palmer, R., *Structure Determination by X-ray Crystallography: Analysis by X-rays and Neutrons*. Springer US: 2014.
18. Moulder, J. F.; Chastain, J., *Handbook of X-ray Photoelectron Spectroscopy: A reference book of standard spectra for identification and interpretation of XPS data*. Physical Electronics: 1995.
19. Stojilovic, N., Why can't we see hydrogen in X-ray photoelectron spectroscopy? *J. Chem. Educ.* **2012**, 89 (10), 1331-1332.

20. Barrón, V.; Torrent, J., Use of the Kubelka—Munk theory to study the influence of iron oxides on soil colour. *Eur. J. Soil Sci.* **1986**, 37 (4), 499-510.
21. Atkins, P.; de Paula, J., *Atkins' Physical Chemistry*. OUP Oxford: 2010.
22. Stenzel, O., *The Physics of Thin Film Optical Spectra: An Introduction*. Springer International Publishing: 2015.
23. Kelly, T. J.; Stedman, D. H.; Ritter, J. A.; Harvey, R. B., Measurements of oxides of nitrogen and nitric acid in clean air. *Journal of Geophysical Research: Oceans* **1980**, 85 (C12), 7417-7425.
24. Colthup, N., *Introduction to Infrared and Raman Spectroscopy*. Elsevier Science: 2012.

7. Producción y Difusión Científica.

Como último capítulo, a continuación, se muestra un listado de las publicaciones realizadas, contribuciones a congresos científicos y referencias de los diferentes actos de difusión realizados en prensa y otros medios de comunicación, derivados de esta Tesis Doctoral o realizados durante el desarrollo de la misma, junto con información relevante acerca de los mismos.

- 5 artículos científicos
- 3 capítulos en libros científicos
- 19 comunicaciones a congresos científicos
- 10 Referencias de actos de difusión

7.1. Artículos publicados en revistas y libros científicos

Revistas científicas

Título: Enhanced activity of α -Fe₂O₃ for photocatalytic NO removal.

Autores: J. Balbuena, M. Cruz-Yusta, A. L. Cuevas, M. C. Lopez-Escalante, F. Martín A. Pastor and L. Sanchez

Revista: RSC Adv., 2016, 6, 92917

Editorial: ROYAL SOC CHEMISTRY

Código ISSN: 2046-2069

DOI: 10.1039/c6ra19167c

Base de datos en la que está indexada: Journal citation reports

Área temática de la base de datos de referencia: Chemistry, Multidisciplinary

Índice de impacto de la revista: 3,289

Posición que ocupa: 49 de 163

Cuartil: 2

Citado: 1 vez

Título: Advances in photocatalytic NO_x abatement through the use of Fe₂O₃/TiO₂ nanocomposites.

Autores: J. Balbuena, G. Carraro, M. Cruz, A. Gasparotto, C. Maccato, A. Pastor, C. Sada, D. Barreca y L. Sanchez

Revista: RSC Adv., 2016, 6, 74878–74885

Editorial: ROYAL SOC CHEMISTRY

Código ISSN: 2046-2069

DOI: 10.1039/c6ra15958c

Base de datos en la que está indexada: Journal citation reports

Área temática de la base de datos de referencia: Chemistry, Multidisciplinary

Índice de impacto de la revista: 3,289

Posición que ocupa: 49 de 163

Cuartil: 2

Citado: 3 veces

Título: Nanomaterials to Combat NO_x Pollution

Autores: J. Balbuena, M. Cruz-Yusta y L. Sánchez

Revista: J. Nanosci. Nanotechnol. 2015, Vol. 15, No. 9

Editorial: AMER SCIENTIFIC PUBLISHERS

Código ISSN: 1533-4880

DOI: 10.1166/jnn.2015.10871

Base de datos en la que está indexada: Journal citation reports

Área temática de la base de datos de referencia: Chemistry,
Multidisciplinary

Índice de impacto de la revista: 1,338

Posición que ocupa: 96 de 163

Cuartil: 3

Citado: 3 veces

Título: Efficient behaviour of hematite towards the photocatalytic degradation of NO_x gases

Autores: R. Sugr^ñez, J. Balbuena, M. Cruz-Yusta, F. Mart^ñ, J. Morales, L. S^ñchez

Revista: Applied Catalysis B: Environmental 165 (2015) 529-36

Editorial: ELSEVIER SCIENCE BV

Código ISSN: 0926-3373

DOI: 10.1016/j.apcatb.2014.10.025

Base de datos en la que est^a indexada: Journal citation reports

Área temática de la base de datos de referencia: Environmental Engineering

Índice de impacto de la revista: 7.435

Posición que ocupa: 1 de 47

Cuartil: 1

Citado: 13 veces

Título: Photocatalytic NO_x abatement by calcium aluminate cements modified with TiO₂: Improved NO₂ conversion.

Autores: M. Pérez-Nicolás, J. Balbuena, M. Cruz-Yusta, L. Sánchez, I. Navarro-Blasco, J.M. Fernández, J.I. Alvarez.

Revista: Cement and Concrete Research 70 (2015) 67–76

Editorial: ELSEVIER SCIENCE BV

Código ISSN 0008-8846

DOI: 10.1016/j.cemconres.2015.01.011

Base de datos en la que está indexada: Journal citation reports

Área temática de la base de datos de referencia: Materials Science, Multidisciplinary

Índice de impacto de la revista: 3.48

Posición que ocupa: 3 de 61

Cuartil: 1

Citado: 5 veces

Libros científicos

Título: New cement based mortar formulations as potential energetic efficiency building materials

Autores: J. Balbuena, M. Cruz-Yusta, I. Mármol, L. Sánchez

Libro: 3rd International Conference on Advances in Civil, Structural and Environmental Engineering.

Editorial: The IRED

ISBN: 978-1 -63248-065-1

D.O.I.: 10.15224/ 978-1 -63248-065-1 -88

Título: Síntesis y caracterización de fibras nanométricas de $\alpha\text{-Fe}_2\text{O}_3$ y su empleo como eficiente catalizador en la eliminación fotoquímica de gases NO_x .

Autores: J. Balbuena, A. Cuevas, M. Cruz-Yusta, F. Martín, J. Morales, L. Sánchez

Libro: XIII Congreso Nacional de Materiales

ISBN: 13978-84-617-0054-7

Editorial: Barceló Congresos

Título: Preparation of self-cleaning and de-polluting building materials through the valorization of industrial wastes

Autores: J. Balbuena, R. Sugr^oñez, M. Cruz-Yusta, I. M^ormol, J. Morales, D. Kovandzic, L. S^onc^ochez

Libro: 33rd Cement and Concrete Science Conference

Editorial: University of Portsmouth, United Kingdom

ISBN: 978-1-86137-642-8

7.2. Comunicaciones a congresos

J. Balbuena, J.M. Calatayud, M. Cruz-Yusta, P. Pardo, F. Martín, J. Alarcón and L. Sánchez

Mesoporous and visible light active TiO₂: a selective De-NO_x photocatalyst

Tipo de participación: Comunicación Oral

21st International Conference of Solid State Ionics

Fecha: 2017

Padua (Italia)

J. Balbuena, J.M. Calatayud, M. Cruz-Yusta, P. Pardo, F. Martín, J. Alarcón and L. Sánchez

TiO₂ mesoporoso como fotocatalizador uv-vis selectivo De-NO_x

Tipo de participación: Comunicación Oral

VI Encuentro NanoUCO

Fecha: 2017

Universidad de Córdoba

J. Balbuena, J. M. Calatayud, M. Cruz-Yusta, P. Pardo, J. Alarcón, L. Sánchez.

Anatasa con alta eficiencia y selectividad en la degradación fotocatalítica de NO_x.

Tipo de participación: Póster

11ª Reunión científica plenaria de química del estado sólido.

Fecha: 2016

Málaga

J. Balbuena, M. Cruz, A.L. Cuevas, M. C. López Escalante, F. Martín, A. Pastor y L. Sánchez.

Nuevas arquitecturas de α -Fe₂O₃ en su aplicación fotocatalítica De-NO_x

Tipo de participación: Comunicación Oral

XIV Congreso Nacional de Materiales.

Fecha: 2016

Gijón

J. Balbuena, M. Cruz-Yusta, I. Mármol, L. Sánchez.

New cement based mortar formulations as potential energetic efficiency building materials

Tipo de participación: Comunicación Oral

3rd International Conference on Advances in Civil, Structural and Environmental Engineering.

Fecha: 2015

Zurich

J. Balbuena, M. Cruz-Yusta, I. Mármol, L. Sánchez.

Materiales emergentes eficientemente energéticos para el ámbito de la edificación

Tipo de participación: Póster

XXXV Reunión Bienal RSEQ 2015

Fecha: 2015

A Coruña

J. Balbuena, J. M. Calatayud, M. Cruz-Yusta, N. Montoya, J. Alarcón,
L. Sánchez.

¿Mejoran las propiedades de-NO_x del TiO₂ mediante dopaje?

Tipo de participación: Póster

XXXV Reunión Bienal RSEQ 2015

Fecha: 2015

A Coruña

J. Balbuena, F. Martín, M. Cruz-Yusta, L. Sánchez

Nanofibras de Hematite (α -Fe₂O₃) para la eliminación de gases NO_x
mediante fotocatalisis.

Tipo de participación: Póster

NanoUCO V

Fecha: 2015

Córdoba

J. Balbuena

Preparación de nuevos materiales fotocatalizadores mediante la valorización de residuos industriales.

Tipo de participación: Comunicación Oral

IV Congreso Científico de Investigadores en Formación de la Universidad de Córdoba.

Fecha: 2014

Córdoba

J. Balbuena, A. Pastor, M. Cruz-Yusta, I. Mármol, J. Morales, L. Sánchez.

Use of industrial wastes as a resource for advanced photocatalytic materials.

Tipo de participación: Póster

NanotechItaly14

Fecha: 2014

Venecia

J. Balbuena, F. Martín, M. Cruz-Yusta, L. Sánchez

Hematite (α -Fe₂O₃) nanofibers for photocatalytic removal of NO_x gases.

Tipo de participación: Póster

NanotechItaly14

Fecha: 2014

Venecia

Pérez-Nicolás M., Fernández J.M., Balbuena J., Cruz-Yusta M., Sánchez L., Navarro-Blasco I., Álvarez J.I.

Preliminary study of photocatalytic NO_x degradation by different types of CAC incorporating TiO₂.

Tipo de participación: Póster

VII Jornada de Investigación en Ciencias Experimentales y de la salud de la Universidad de Navarra

Fecha: 2014

Navarra

J. Balbuena, R. SUGRÁÑEZ, F. Martín, M. Cruz-Yusta, J. Morales, L. Sánchez

Photocatalytic removal of NO_x with hematite (α -Fe₂O₃).

Tipo de participación: Póster

Sun New Energy Conference

Fecha: 2014

Sicilia

J. Balbuena, A. Cuevas, M. Cruz-Yusta, F. Martín, J. Morales, L. Sánchez

Síntesis y caracterización de fibras nanométricas de α -Fe₂O₃ y su empleo como eficiente catalizador en la eliminación fotoquímica de gases NO_x.

Tipo de participación: Comunicación Oral

XIII Congreso Nacional de Materiales

Fecha: 2014

Universidad de Barcelona

J. Balbuena, M. Cruz-Yusta, I. Mármol, J. Morales, D. Kovandzic, L. Sánchez

Use of Industrial Wastes in the Preparation of Advanced Photocatalytic Building Materials.

Tipo de participación: Comunicación Oral

Young Reserchers' Forum II: Construction Materials

Fecha: 2014

Escuela Universitaria de Londres

R. Sugr^{añ}ez, L. Sánchez, J. Morales, J. Balbuena, M. Cruz-Yusta

Tuning α -Fe₂O₃ particles size and morphology to obtain advanced photocatalyst materials

Tipo de participación: Póster

European Congress and Exhibitions on Advanced Materials and Processes

Fecha: 2013

Sevilla

J. Balbuena, R. Sugrañez, M. Cruz-Yusta, I. Mármol, J. Morales, D. Kovandzic, L. Sánchez

Preparation of self-cleaning and de-polluting building materials through the valorization of industrial wastes.

Tipo de participación: Póster

33rd Cement and Concrete Science Conference

Fecha: 2013

Universidad de Portsmouth

J. Balbuena, R. Sugrañez, M. Cruz-Yusta, I. Mármol, J. Morales y L. Sánchez

Obtención de óxidos de hierro con propiedades fotocatalíticas mediante la transformación de residuos

Tipo de participación: Comunicación Oral

IV Encuentro NanoUCO

Fecha: 2013

Universidad de Córdoba

J. Balbuena, R. Sugr^oñez, M. Cruz-Yusta, I. M^ormol, J. Morales y L. Sánchez

Transformación de residuos de fayalita en óxidos de hierro. Efecto de la molienda mecánica en sus propiedades fotocatalíticas

Tipo de participación: Póster

10^a Reunión científica plenaria de química del estado sólido- QIES12

Fecha: 2012

Universidad de Gerona

7.3. Referencias de los diferentes actos de difusión realizados en prensa y otros medios de comunicación

Referencia: Entrevista

Titular: "LA CANTERA DE LA INVESTIGACION - José Balbuena DEP. DE QUÍMICA INORGÁNICA E INGENIERÍA QUÍMICA: "En España se forma a muy buenos investigadores""

Medio de comunicación en donde se ha publicado la noticia:

Prensa (diario digital e impreso), Diario Córdoba



LA CANTERA DE LA INVESTIGACION

José Balbuena DEP. DE QUIMICA INORGANICA E INGENIERIA QUIMICA : "En España se forma a muy buenos investigadores"

T. C.
06/04/2016

Compartir:   



Objetivos Balbuena pretende finalizar su tesis doctoral y continuar investigando. - Foto: MIGUEL ANGEL SALAS

Fecha de publicación: 06-04-2016

Enlace web:

http://www.diariocordoba.com/noticias/universidad/jose-balbuena-dep-quimica-inorganica-ingenieria-quimica-en-espana-forma-buenos-investigadores_1031016.html

Referencia: Divulgación científica y acercamiento a la ciencia

Titular: “Cuando Superman y Ironman defienden sus poderes con ciencia”

Medio de comunicación en donde se ha publicado la noticia:
Noticiero Web.



eldiario.es

Fecha de publicación: 18-01-2016

Enlace web:

http://www.eldiario.es/andalucia/cordoba/superheroes-debaten-ciencia_0_473502772.html

La noticia fue difundida por otros medios de comunicación, entre ellos:

Titular: *“Ningún superhéroe puede con la ciencia”*

http://www.diariodenavarra.es/noticias/mas_actualidad/sociedad/2016/01/16/ningun_superheroe_puede_con_ciencia_384005_1035.html

Titular: *“La ciencia de los superhéroes enfrenta a Superman, Iron Man y Batman”*

<http://ecodiario.economista.es/ciencia/noticias/7283219/01/16/La-ciencia-de-los-superheroes-enfrenta-a-Superman-Iron-Man-y-Batman.html>

Referencia: Noticia

Titular: *“Un óxido de hierro para limpiar la atmósfera de las ciudades”*

Medio de comunicación en donde se ha publicado la noticia:

Unidad de Cultura Científica y de la Innovación de la [Universidad de Córdoba](#) y del [Campus de Excelencia Internacional Agroalimentario CeIA3](#).



Fecha de publicación: 18-05-2015

Enlace web:

<http://www.uco.es/uconews/es/article/un-oxido-de-hierro-para-limpiar-la-atmosfera-de-las-ciudades/>

La noticia fue difundida por otros medios de comunicación:

Titular: *“Usan por primera vez óxido de hierro para limpiar la contaminación atmosférica”*

Medio de comunicación: Web de Radio Televisión Española



Fecha de publicación: 19-05-2015

Enlace web:

<http://www.rtve.es/noticias/20150519/usan-primer-vez-oxido-hierro-para-limpiar-contaminacion-atmosferica/1147247.shtml>

Titular: *“La UCO estudia el uso de la hematita contra la contaminación”*

Medio de comunicación: Diario *El Día de Córdoba* (Edición digital)



Fecha de publicación: 19-05-2015

Enlace web:

<http://www.eldiadicordoba.es/article/cordoba/2032311/la/uco/estudia/uso/la/hematita/contra/la/contaminacion.html>

Titular: *“Óxido de hierro para limpiar la 'boina' de contaminación de las ciudades”*

Medio de comunicación: Diario *Libertad Digital*



Fecha de publicación: 20-05-2015

Enlace web:

<http://www.libertaddigital.com/ciencia-tecnologia/ciencia/2015-05-20/oxido-de-hierro-para-limpiar-la-boina-de-contaminacion-de-las-ciudades-1276548450/>

Titular: “Óxido de hierro para limpiar la atmósfera de las ciudades”

Medio de comunicación: Diario *El Correo* (Edición digital)

EL CORREO

Fecha de publicación: 19-05-2015

Enlace web:

<http://www.elcorreo.com/bizkaia/tecnologia/investigacion/201505/19/oxido-hierro-para-limpiar-20150519134333-rc.html>

Titular: “Óxidos de hierro, un nuevo aliado para limpiar la atmósfera de las ciudades”

Medio de comunicación: Servicio de Información y Noticias Científicas (SINC), plataforma multimedia de comunicación científica.

sinc
La ciencia es noticia

Fecha de publicación: 19-05-2015

Enlace web:

<http://www.agenciasinc.es/Noticias/Oxidos-de-hierro-un-nuevo-aliado-para-limpiar-la-atmosfera-de-las-ciudades>

Titular: *“Estudian el uso de un óxido de hierro para limpiar la atmósfera de ciudades”*

Medio de comunicación: Plataforma global de noticias y periodismo ambiental de la Agencia EFE (EFE verde)



Fecha de publicación: 18-05-2015

Enlace web:

<http://www.efeverde.com/noticias/oxido-de-hierro-limpiar-atmosfera-ciudades/>

Referencia: Artículo de divulgación

Título: *“Materiales de Construcción para Entornos Saludables y Limpios”*

Medio de comunicación en donde se ha publicado: Revista Aproin



Fecha de publicación: 05-2014

Enlace web:

http://www.revistaaproin.com/paginas/materiales_construccion.php

Referencia: Noticia en Telediario (RTV). Difusión de la investigación del Grupo FQM-175 sobre materiales de construcción en el Telediario 1 de RTVE

rtve



Fecha de la emisión: 27-11-2013

Enlace web:

<https://www.youtube.com/watch?t=173&v=7P9NRDhpNxs>
